On-Surface Synthesis of Porphyrin Functionalised Graphene Nanoribbons

A thesis for the degree of

Doctor of Philosophy

Conor McGeough B.Sc.

School of Physical Sciences

Dublin City University

Supervisors

Dr. A.A. Cafolla

Prof. Gregory Hughes

January 2022

Declaration

I hereby certify that this material, which I now submit for assessment on the programme of study leading to the award of Doctor of Philosophy is entirely my own work, that I have exercised reasonable care to ensure that the work is original, and does not to the best of my knowledge breach any law of copyright, and has not been taken from the work of others save and to the extent that such work has been cited and acknowledged within the text of my work.

Signed: ____________

ID No.: 57382618

Date: 10/01/2022

Acknowledgements

I would like to thank my co-supervisor Prof. Greg Hughes for providing the funding for this research and the memorable conferences and synchrotron runs. A great deal of thanks goes to my supervisor, Dr. Tony Cafolla for all the time, patience and advice given over the course of my Ph.D and the music and film recommendations.

To all my fellow Ph.D colleagues in DCU, specifically Ben, Cleo, Brian, Louis, Huw and Adam for all the help and fun times. And to the wider DCU School of Physical Sciences a big thank you to Pat Wogan, Dr. Justin Bogan, Prof. John Paul Mosnier and Lisa Peyton for helping things run as smoothly as possible. A special thanks goes to the Mountshannon crew, Ann, Dean and Seán for being great housemates over the years. And to Émilie for helping me see sense on several occasions.

To my family, my mother, father, sisters, and granny who I owe a great debt of gratitude for supporting me in many ways.

Ever tried.
Ever failed.

No matter.

Try again.
Fail again.

Fail better.

Samuel Beckett

Table of Contents

List of Tables

List of Figures

Abbreviations

AGNR	Armchair graphene nanoribbon
ARPES	Angle-resolved photoelectron spectroscopy
ARPUS	Angle-resolved ultraviolet photoelectron spectroscopy
cc-ZGNR	Cove-cape zig-zag graphene nanoribbon
CGNR	Chiral graphene nanoribbon
CVD	Chemical vapour deposition
DBBA	10,10'-Dibromo-9,9'-bianthracene
DFT	Density Functional Theory
FCC	Face centred cubic
FET	Field effect transistor
FT-STS	Fourier Transform- scanning tunnelling spectroscopy
GNR	Graphene nanoribbon
HOMO	Highest occupied molecular orbital
IMFP	Inelastic mean free path
LUMO	Lowest unoccupied molecular orbital
ML	Mono layer
nc-AFM	non-contact atomic force microscopy
Ni-DBTPP	Nickel 5,15dibromophenyl 10,20 tetra-phenylporphyrin
OBO	6,16-dibromo-9,10,19,20-tetraoxa-9a,19a-diboratetrabenzo[a,f,j,o] perylene
OSS	On-surface synthesis
PMMA	Poly-methyl methacrylate
STM	Scanning tunnelling microscopy
STS	Scanning tunnelling spectroscopy
TPP	Tetra-phenyl porphyrin
TSP	Titanium sublimation pump
UHV	Ultra-high vacuum
XPS	X-ray photoelectron spectroscopy
ZGNR	Zig-zag graphene nanoribbon

On-Surface Synthesis of Porphyrin Functionalised Graphene Nanoribbons

Conor McGeough

Abstract

In this thesis, routes toward Nickel-porphyrin functionalised graphene nanoribbon (GNR) formation on the Au(111) and Au(788) surface are investigated. The on-surface synthesis of 7-carbon atom-wide armchair graphene nanoribbons (7-AGNR) using 10,10'-dibromo-9,9'-bianthryl (DBBA) and the formation of (4,1) chiral graphene nanoribbons (CGNR) from an oxygen and boron (OBO) doped precursor molecules is achieved on both gold surfaces. The formation of these nanoscale structures holds promise for future molecular electronics and sensor technology.

The process of self-assembly, polymerisation, and covalent bonding of DBBA precursors to form 7-AGNRs and porphyrin functionalised 7-AGNR was studied using scanning tunnelling microscopy (STM). The DBBA molecules were found to self-assemble into rows on the Au(788) surface, while a mixture of rows and "florets" were observed on the Au(111) surface. Debrominated Ni-DBTPP formed porphyrin chains on the Au(111) surface. Under co-deposition of DBBA and Ni-DBTPP functionalised 7-AGNRs were formed on the Au(111). Different GNR-porphyrin-GNR heterojunction assemblies are identified on both gold surfaces. The impact of molecular surface coverage was studied, and the initial coverage of the precursor was found to play a role in the length of the ribbons formed on Au(111) while the templating effect of the vicinal Au(788) surface significantly increased the length and alignment of porphyrin functionalized 7-AGNR at monolayer coverage. The sublimation temperatures and deposition rates were found for DBBA, OBO and Ni(II) 5,15-dibromo-10,20-tetraphenyl porphyrin (Ni-DBTPP).

The transition of OBO precursor molecules from individual molecules to polymer chains and (4,1)-CGNRs on Au(111) surface was studied using STM. A model of the chemical environment of carbon atoms is developed and x-ray photoelectron spectroscopy (XPS) was employed to track the evolution of the C 1*s* core level in the OBO molecules following dehalogenation and cyclo-dehydrogenation. Partial debromination of OBO molecules was found to occur at lower temperatures than the debromination process in DBBA. Self-assemblies of OBO molecules are observed to be dominated by O – H interactions. A (2×1) reconstruction of both gold surfaces is observed for all three molecules when the surface is annealed. Porphyrin functionalised (4,1) CGNR were formed on both gold surfaces with a coverage of less than a monolayer. A double deposition protocol is described for growing long, aligned (4,1) CGNRs on the Au(788) surface.

Chapter 1: Introduction

1.1 Background

Graphene was first isolated in 2004 by Geim and Novoselov *et al.* [1] for which they were awarded the Nobel Prize in 2010. Graphene is a two-dimensional layer of carbon with a hexagonal crystal structure. It is a semimetal with zero bandgap. Carbon has four valence electrons, in graphene three of these electrons are covalently bonded in-plane in sp^2 hybridized orbitals as shown in figure 1.1. The remaining electron is in an out-of-plane p orbital and is effectively a delocalised electron. This delocalised electron gives graphene its extraordinarily large charge carrier mobility 200,000 cm^2/Vs [2] which is of great interest for electronic device research. This electrical property has been explored extensively for applications in field effect transistor (FET) technologies, mostly as a channel material between the source and drain electrodes [3]. An on/off current ratio of ~30 has been measured at room temperature [1] which effectively renders graphene "always on", meaning

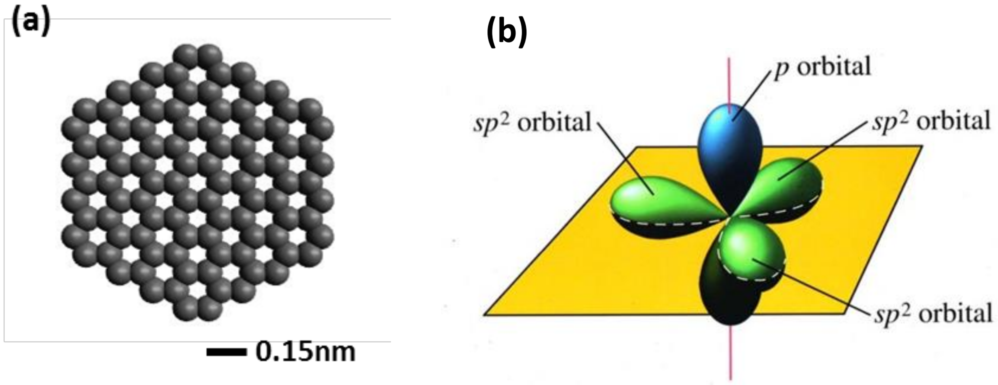

***Figure 1.1**: Illustrations of graphene: (a) Section of a graphene lattice. (b) Illustration of the hybridised in-plane sp2 orbitals that form covalent bonds and the out-of-plane p orbital.*

the flow electrons cannot be controlled sufficiently by the gate voltage ruling out applications in high frequency switching FETs [4][5]. This downside is a direct result of graphene having no bandgap. The question arises if it is possible to open a bandgap in graphene while still maintaining the high carrier mobility. A bandgap can be introduced in graphene through traditional top-down doping techniques such as boron or nitrogen ion implantation [6], wet chemical etching [7], and nitrogen annealing [8]. An alternative route to open a bandgap is to form narrow strips of graphene thus laterally confining electrons in the aptly named graphene nanoribbons (GNR). This latter bottom-up approach offers the possibility of engineering the bandgap of the nanoribbons to a desired value by selecting the width of the nanoribbon thus determining the size of the bandgap. This was theoretically proposed as far back as 1982 by Yamabe and Tanake *et al.* [9] [10] and confirmed experimentally in 2013 by Chen *et al.* [11]. Theoretical results for different GNRs show that in general the bandgap increases with decreasing width of GNRs as seen in figure 1.2 [4]. The various symbols in the figure are for different families of GNRs which are discussed in greater detail in section 1.2.1. The number of carbon atoms, N is used to indicate the width of GNRs.

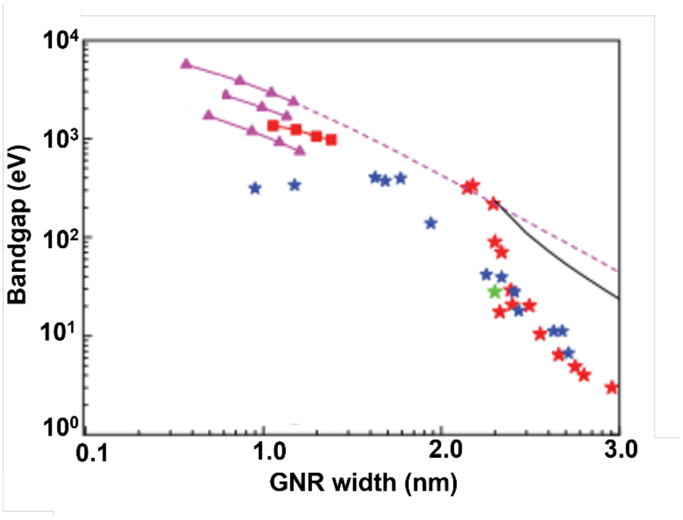

***Figure 1.2**: Bandgap versus GNR width: Compilation of bandgap values by Schwierz* [4]

As well as the width governing the size of the bandgap in GNRs the edge shape also plays an important role in their electronic structure. Graphene nanoribbons can have armchair, zig-zag or chiral edges as illustrated in figure 1.3 [12]. Chiral GNRs (CGNR) have a combination of zig-zag and armchair edges. They are defined by the lattice vector $\boldsymbol{C_h} = n\mathbf{a_1} + m\mathbf{a_2}$, where $\mathbf{a_1}$ and $\mathbf{a_2}$ are the lattice vectors of the graphene lattice. The electronic structure of GNRs is discussed in greater detail in section 1.5

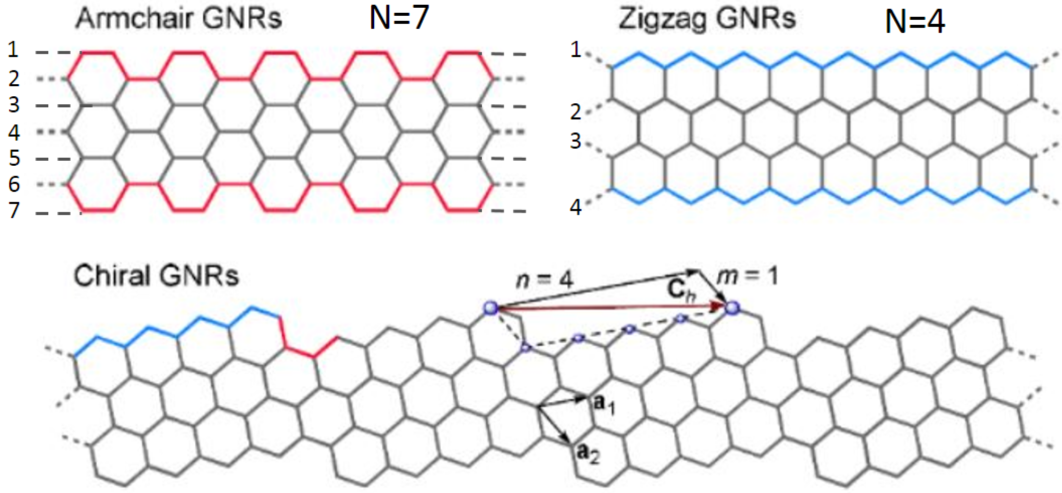

Figure 1.3: *Graphene nanoribbon edge shapes: (a) Armchair (b) zig-zag (c) Chiral (4,1) The edge geometry of chiral GNRs is defined by the lattice vector* [12]

There are two main avenues to forming GNRs; top-down and bottom-up approaches. The top-down approach starts with a large area of material and reduces the dimensions to the nanoscale. The bottom-up approach uses nanometre sized molecular building blocks to form GNRs. The top-down approach uses techniques already familiar to the microelectronic industry, moving from the macro-scale down to a nanoscale through lithography [13], solution-based chemistry[14], or unzipping of carbon nanotubes [15]. Several issues arise from the top-down approaches. Despite the fabrication of 10nm wide GNRs using lithography being recently reported [16] the critical matter of atomic precision at the edges of the ribbon still exists. Even small defects on the edges can cause electron scattering [17] thus reducing the charge mobility. The solution-based chemistry and unzipping methods also fail to achieve atomic precision at the edges and can leave the GNRs with unwanted carbonyl and carboxyl functional groups at the edges [15,18]. To address this problem, Cai *et al.* [19]

developed a bottom-up approach to produce atomically precise and reproducible GNRs. Their methodology is to deposit individual precursor molecules, dibromo-bianthracene (DBBA) onto a gold substrate and thermally activate a reaction to self-assemble the precursors into graphene nanoribbons. The result was atomically precise armchair graphene nanoribbons that are 7 carbon atoms wide (7-AGNR) as shown in figure 1.4. In the same paper Cai and co-workers described a different precursor, dibromo-tetraphenyl-triphenylene to grow chevron-type GNRs on Au (111), shown in figure 1.5(a).

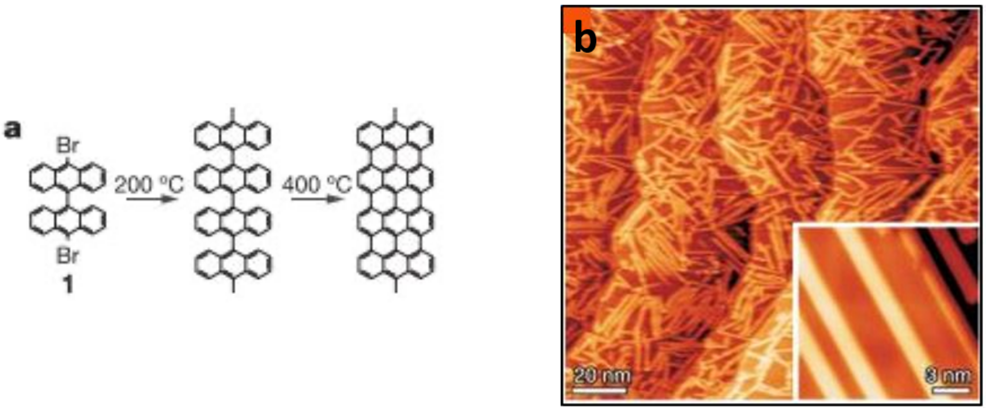

Figure 1.4: *Formation of GNRs on Au(111): (a) Diagram of the steps from DBBA (1) precursor to polymer chain to 7 carbon atom wide armchair GNR. (b) STM image (100 nm × 100 nm) of GNRs (Inset) STM image (15 nm × 15 nm) of three GNRs (V= -3.0 V, I=0.03 nA).* [19]

For these precursors the dehalogenation temperature is 250 °C and the dehydrogenation temperature is 440 °C on the Au(111) surface. In the same paper the group also incorporated tris-iodo-biphenylbenzene precursor to form a junction of three chevron-type GNRs as seen in figure 1.5 (b). By demonstrating the versatility of the on-surface synthesis pathway for forming molecular nanostructures this work opened up a new area of research that enables the controlled growth of graphene nanoribbons with defined widths, edge-shape and structure by designing the precursor molecules thus providing control of their optical and electrical properties.

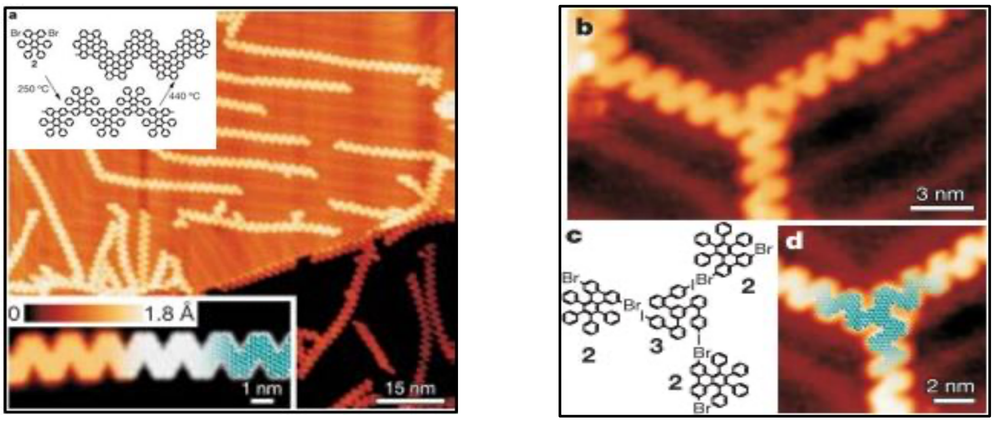

Figure 1.5: *Chevron and tri-junction GNRs. (a) STM image (80 nm × 80 nm) cheveron GNRs grown on Au(111) (V=-2.0 V, I=0.02 nA). (upper inset) Chemical pathway from monomer to GNR. (lower inset) STM image of single chevron ribbon with chemical structure overlay (V=-2.0 V, I=0.5 nA). (b) STM image (18 nm × 9 nm) of tri-junction by incorporating tris-iodo-biphenylbenzene with chevron GNRs (V=-2.0 V, I=0.02 nA) (c) Chemical structure of junction. (2 denotes dibromo-tetraphenyl-triphenylene). (3 denotes tris-iodo-biphenylbenzene) (d) 10 nm × 10 nm STM image of junction with chemical model overlay. Cai et al.* [19]

1.2 Properties of Graphene Nanoribbons

1.2.1 Electronic Bandgap

One of the main technological aims of GNRs is to combine the ballistic electronic transport properties of graphene, typically 2×10^5 cm^2/Vs [20] with a tunable bandgap for incorporation into present and post-silicon microelectronics. For this, bandgap engineering and measurements are key areas of research. Before GNRs were physically realized theorists predicted the electrical band gap using DFT [21,22], Clar Sextet Theory [23], many-body perturbation[24] and tight binding models [25]. A compilation of theoretical and experimental band gap measurements of 7-, 9-, 13-AGNR is summarised in table 1.1. The variation of theoretical predictions arises from the different models used and whether they include a correction for GNR/substrate interaction or model free standing GNRs [26]. An in-depth understanding of density functional theory and many-body perturbation theory is required to analyse the predictions and is beyond the scope of this thesis. Experimental methods have also been successful in measuring bandgaps of various AGNR widths using scanning tunnelling spectroscopy (STS) for probing local density of states and angular resolved photoelectron spectroscopy (ARPES) for area averaged measurements. Experimental results are also subject to variation as the GNR/substrate interaction effects the band gap due to metal reactivity and polarisation effects of the substrate [27].

Table 1.1: Theoretical and experimental bandgaps of armchair graphene nanoribbons

N	Theory (eV)	Experiment (eV)
7	1.6†[21], 1.3*[21], 1.6[24], 2.0[23]	2.3 [27] 2.4[11] 2.5[28]
9	0.7†[21], 0.9*[21], 2.0[24] , 1.8[23]	1.4 [29]
13	0.7[24], 1.4[23]	1.4 [11]

† denotes many-body perturbation GW approximation

* denotes tight-binding or DFT calculations

With more reactive substrates e.g. Cu, the greater the degree of band hybridisation between the GNR and Cu substrate results in a smaller band gap for similar GNRs. In addition to the metal surface the GNR/substrate interaction depends on the corrugation of the crystal plane of the surface and interaction with step-edges which also contributes to variations in the measured band gaps [30]. To this end it is an important to consider the measured band gap of a given GNR as a composite of both the GNR geometry and the substrate properties. All experimental results compiled in table 1.1 were conducted on the Au(111) surface.

Classifying armchair GNRs by bandgap, Son and co-workers [21] showed that AGNRs can be divided into three sub-categories; $N = 3p$, $N= 3p+1$, $N = 3p+2$ where p is an integer. The $N = 3p+1$ sub-category has larger bandgaps, the $N = 3p+2$ have relatively smaller bandgaps and $N = 3p$ have bandgaps in between these two sub-categories as shown in figure 1.6. By decreasing the widths of AGNRs atom by atom, the ribbon moves from one sub-category to another with a non-monotonous change in bandgap. Within each sub-category the bandgap increases monotonically with decreasing width.

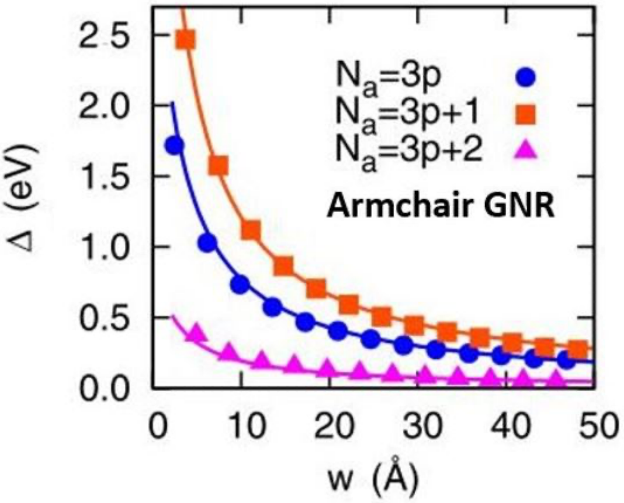

***Figure 1.6**: AGNR Bandgap as a function of width: First principle (Local density approximation) bandgap calculations of the 3 categories of armchair GNRs*[21]

How the bandgap of GNRs is affected on a semiconducting surface is critically important for the development of devices. Studies of AGNRs grown via chemical vapour deposition (CVD) on semiconducting Ge(001) substrates point toward a bandgap of ~0.8 eV for ribbons that are 4nm wide [31]. However, as discussed earlier top-down methods like CVD grown GNRs differ from ribbons grown via the on-surface synthesis (OSS) method as they lack atomically precise edges and thus have non-uniform electronic properties.

Theoretical predictions of zig-zag GNRs show that they do not fall into sub-categories like AGNRs but instead increases monotonically with decreasing width up to a critical point (~0.9 nm) where it falls off as shown in figure 1.7 [21]. The predicted presence of spin-polarized states on the zig-zag edges [32] has the potential for ZGNRs to be used for spintronic [33] and quantum computing applications [34]. Experimental work on ZGNRs has lagged behind AGNRs as the OSS methods previously mentioned are not directly suitable because the aryl-aryl coupling of the precursors takes place along the armchair orientation and top-down methods lack atomic precision on the edges.

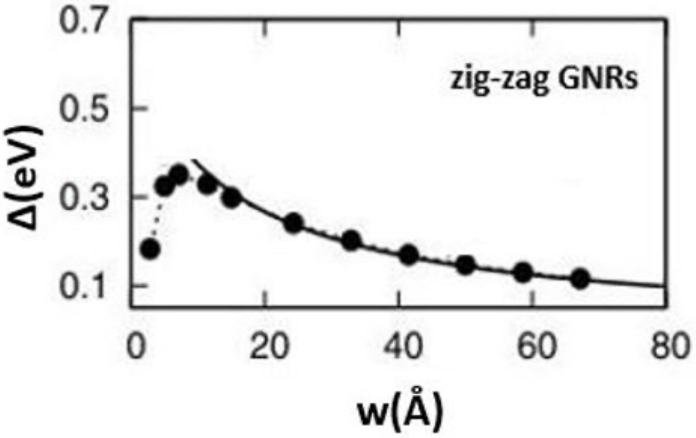

***Figure 1.7**: ZGNR bandgap as a function of width* [21]

However, the narrow end of AGNRs have zig-zag termination and have been used as a temporary solution for studying ZGNRs and electronic states near the edge have been identified 0.2 eV above the Fermi level [11]. Recently Ruffieux and co-workers [35] were successful in synthesising 12-ZGNRs on Au(111) using on-surface synthesis. They used T-shaped dimethyl-biphenyl which polymerises along the zig-zag direction. This protocol is illustrated in figure 1.8. The 12-ZGNR band structure was measured on a NaCl substrate to reveal energy gaps between filled and unfilled states of 1.4 eV and 1.7 eV [35]. The magnetic spin properties of ZGNRs that sets them apart from AGNRs remained a challenge to characterise due to chemical instability at the edges. Slota *et al.* [36] used a solution-based approach to grow functionalized 8-ZGNRs and characterised delocalised magnetic edge states. Solution-based methods were also used by Berezin *et al.* [37] to grow oxygen doped 6-ZGNR with a measured bandgap of 2.34 eV.

The electronic structure of CGNRs has not been explored as extensively as the armchair and zigzag GNRs, however, scanning tunnelling spectroscopy (STS) studies show CGNR with (3,1) and (4,1) edge chirality have bandgaps of 0.67 eV[38] and 0.5 eV[12] respectively.

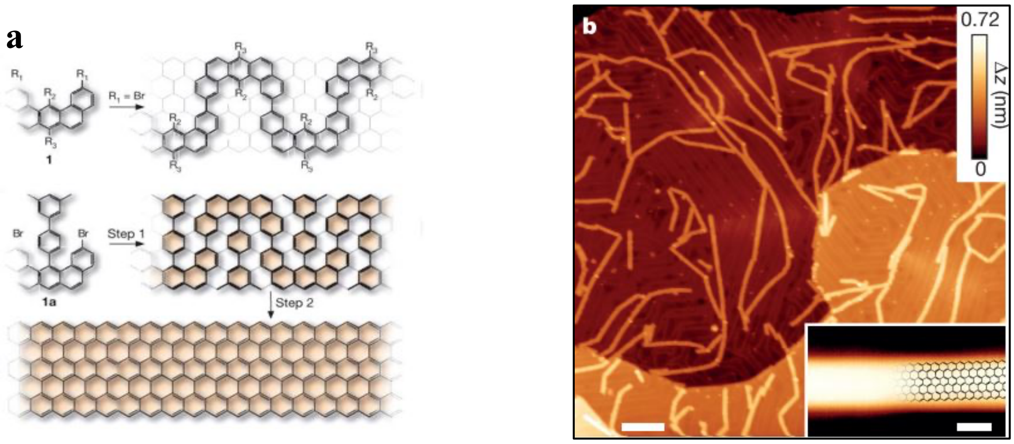

***Figure 1.8**: 6-zig-zag-GNR: (a) Illustration of polymerisation and cyclodehydrogenation of precursors dibenzo anthracene (1) and dimethyl-biphenyl (1a) to form 6 ZGNR. (a) 100 nm × 100 nm STM image of 6-ZGNR (V=-1.0 V, I=0.02 nA). Inset shows 5 nm × 3 nm STM image individual ribbon with 6 ZGNR superimposed structural model (V=-1.0, V, I=0.02 nA)* [35]

Notwithstanding the importance of width and edge-shape on the size of the band gap, it was recently demonstrated by Taleriz *et al.* that ribbon length and the number of hydrogen atoms at GNR termini can also have an effect the band gap by an order of hundreds of milli-electron volts [39]. For these reasons, correct interpretation of band gap measurements poses a challenge for researchers.

1.2.2 Electron Transport and Effective Mass

The electron effective mass, m^* determines the carrier mobility, a vital parameter for characterising the performance of electronic devices. The effective mass is the second derivative of the dispersion curve. For graphene, the slope of the Dirac cone at the point where the valence and conduction bands meet is zero resulting in a massless electron at this point. By extension, the effective mass can be determined by measuring the second derivative of the dispersion of electronic bands near the Fermi edge. Using angular resolved photoelectron spectroscopy (ARPES), Ruffieux *et al.*[27] measured an effective mass of 0.21 m_o at the top of the valence band, where m_o is the rest mass of the electron, and a charge carrier mobility of 8.2 x10^5 ms^{-1} in 7-AGNR aligned on the vicinal Au(788) surface. In a similar study, but using angular resolved ultraviolet photoemission spectroscopy (ARUPS) to probe aligned 7-AGNR on Au(788) Linden and co-workers[40] found the effective mass to be 1.07m_o in one electronic state and 0.83 m_o in another. Fourier transform scanning tunnelling spectroscopy (FT-STS) can also be used to measure the effective mass of electrons in individual GNRs. Using this technique Söde *et al.*[41] measured three effective masses; 0.41 m_o, 0.40 m_o and 0.20 m_o corresponding to the valence band maximum, conduction band minimum and a higher energy state in the conduction band respectively in 7-AGNRs. The disparity of effective mass values is evidence of the work required to fully understand the electronic properties of GNRs. For wider AGNRs, the band gap narrows, and the effective mass is expected to decrease, as is seen in extended graphene where the electron is effectively massless [42]. Electron transport experiments have been undertaken by several groups. Koch and co-workers [43] used an STM tip to pick up individual 7-AGNR and measured the current flowing between tip and substrate as a function of tip height and voltage. They found the greatest conductance values at electron energies near the highest occupied molecular orbital (HOMO) and the lowest unoccupied molecular orbital (LUMO) [43]. FETs using GNRs as the channel material between source and drain have shown electron transport is restricted by Schottky barriers at the electrodes [44]. In order to take full advantage of GNRs transport properties lower work function contacts are necessary.

1.3 Self-Assembly and On-Surface Synthesis

The self-assembly of molecules to form nano-structures is a key requirement for the realisation of molecular electronics and the miniaturisation of electronic devices and sensors [4,5]. A major consideration in forming nano-architectures is that the inter-molecular bonding must be strong enough to facilitate charge carrier transport and remain stable at room temperature [45, 46]. To this effect covalent bonding between molecular building blocks is vital. While non-covalent molecular self-assembly has been observed in different systems for decades [47] the first work that succeeded in forming covalently bonded self-assembled structures was performed by Grill and co-workers in 2007 [48]. This group used molecular building blocks with substituent elements in specific locations on the molecule which were thermally dissociated from the molecule allowing the core of the molecule to form covalent bonds in linear and 2D arrays on Au(111). An illustration of the processes with accompanying STM images of the molecular network is shown in figure 1.9.

Selection and design of the appropriate molecular building blocks is necessary as the connecting elements must be thermally dissociated from the molecule at a temperature that does not result in the decomposition of the core molecular structure or the desorption from the surface. For this reason, Grill *et al*. used halogenated porphyrins, specifically tetrabromophenyl-porphyrin (Br_4TPP) shown in the insert in figure 1.9(b). Similar molecular building blocks have been shown to self-assemble and form covalent bonded networks on Cu(111) through thermal activation [49] and also by using a scanning tunnelling microscope (STM) tip to induce dehalogenation [50]. However, using an STM tip to induce dehalogenation is not a viable option for mass production of covalently bonded molecular nanostructures. Another reason why halogenated porphyrins are suitable for on-surface synthesis (OSS) is that the halogen atom can be thermally dissociated from the molecule at a temperature that does not decompose the carbon-based core of the molecule. Controlling the shape and self-assembled structure can be achieved by designing the molecular precursor with specific geometry and placing halogen atoms at specific sites.

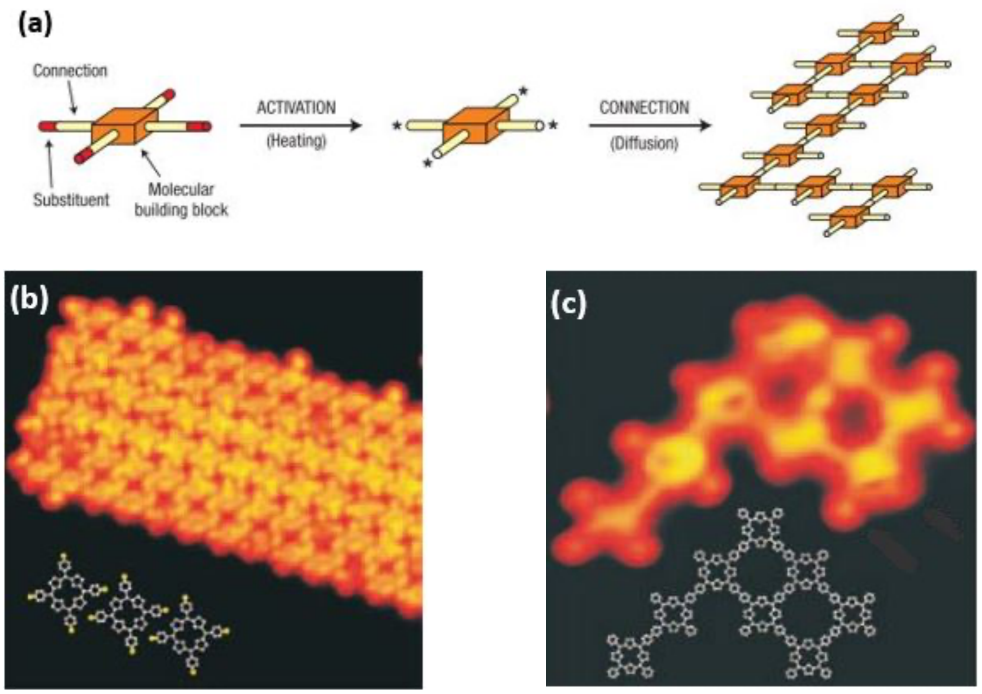

Figure 1.9*: Covalent bonding of Br_4TPP molecular networks (a) Schematic of the process (b) STM image (20 nm × 20 nm) of pre-activated molecules forming a supra-structure. Inset is an illustration chemical structure with bromine atoms coloured yellow. (c) STM image (8.5 nm × 8.5 nm) of covalent bonding of molecular building blocks. (Inset) Illustration of molecular structure after dehalogenation* [48] *(Authors did not report STM imaging parameters)*

This pioneering work was adopted by Cai and co-workers in 2010 [19]. They showed that using a specific halogenated building block, 10,10′-dibromo-9,9′-bianthracene (DBBA) it was possible to grow 7-AGNR graphene nanoribbons on the Au (111) surface.

An important series of reactions occur during on-surface synthesis, and it is important to understand the dynamics and contributing factors of each reaction. The order in which the stages occur is dependent on the substituent elements on the precursors and the reactivity of the substrate, which is discussed later in this section. Typically, the first chemical process to occur during OSS of GNRs is dehalogenation, whereby the halogen atoms are thermally cleaved from the precursor molecule. This process uses the Ullmann reaction or Ullmann coupling, first discovered by Ullmann and Bielecki in 1901, where they formed biphenyl from iodobenzene using copper powder as a catalyst [51] . The Ullmann reaction uses halogenated benzene and when supplied with sufficient thermal energy the halogen-carbon bond dissociates as the halogen bonds with copper and C-C bonding occurs forming a polymer as shown in figure 1.10.

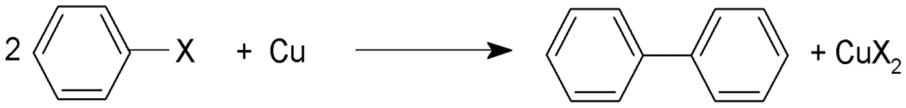

Figure 1.10*: Ullmann Reaction*: *The Ullman reaction using Cu as a catalyst forming two bonded benzene rings. X represents halogen atom (Br, Cl, I)*

Ninety years later the Ullmann reaction was adopted using a copper substrate to support and catalyse iodobenzene [52]. This reaction can be carried out in solution or on other metal substrates [52]. Cai *et al.* [19] used DBBA as the precursor molecule on the Au(111) surface to grow 7-AGNR. The two main factors affecting on-surface synthesis through Ullmann coupling are the metal substrate and the activation temperatures. For DBBA on Au(111) the dehalogenation occurs at 200 °C. The biradicals diffuse on the surface to form C-C bonds which results in a polymer chain. At this stage, the polymer chain is non-planar due to steric hinderance of the hydrogen bonds on the inner carbon atoms. As a result, each neighbouring anthracene unit is in an alternating up or down position as shown in figure 1.11.

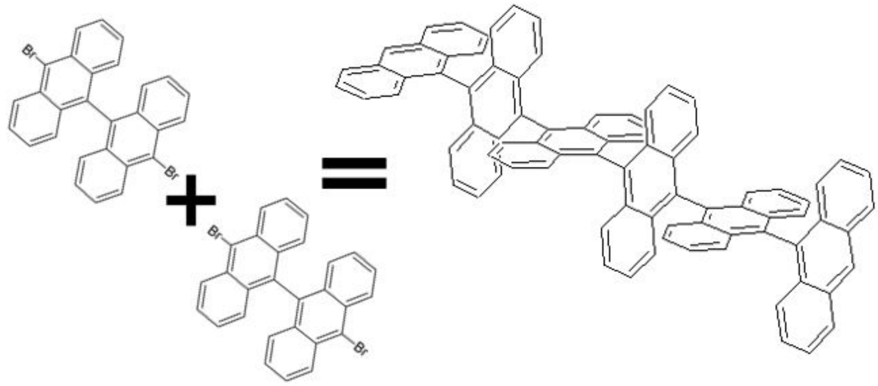

***Figure 1.11**: Ullmann coupling of DBBA (a) Chemical structure of DBBA (b) chemical structure of polymer DBBA chain with alternating up-down anthracene units*

The next process in the formation of GNRs is cyclodehydrogenation. This involves annealing the surface to a higher temperature, 400 ºC for DBBA on Au(111), to remove the hydrogen atoms from the inner carbon atoms to create covalent carbon-carbon bonds. The exact dynamics of the cyclodehydrogenation are not yet fully understood. The reaction pathway proposed by Blankenburg *et al.*[53] is illustrated in figure 1.12. The first step in this process is cyclization whereby upward and downward facing anthracene units rotate about the central C-C axis of the polyanthracene chain to form a new C-C bond while still retaining the hydrogen. This involves the carbon orbital transforming from sp^2 to sp^3 hybridization. As annealing temperature increases the hydrogen is eventually removed and aromatic rings of carbon form. There have been two routes for this reaction pathway proposed by Bjork *et al* [54] and observed by Blankenburg *et al.* [53]. In the illustrated example in figure 1.12, Blankenburg and co-workers observed cyclodehydrogenation along one side of the polymer chain then on the other side of the central axis to form GNRs. This experimental finding was accompanied by density functional theory (DFT) using van der Waals density function (vdW-DF) approximation. While Bjork reported the polyanthracene chain form a GNR in a zip-like fashion using the same computational approach [53]. The computational work of Bjork was recently supported by Xiao *et al.*[55] who predicted zip-like cyclodehydrogenation when in contact with the metal substrates but not when on top of a layer of GNRs. Contact between the polymer chain and a metallic substrate is essential for cyclodehydrogenation to occur.

X-ray photoelectron spectroscopy (XPS) is useful for tracking the evolution of the chemical state of carbon in deposited precursor monomers, polymer chains and GNRs as demonstrated by Simonov *et al.* and shown in figure 1.13 [56]. Following the deposition of DBBA on Au(111) at room temperature the carbon 1*s* spectrum is comprised of three components corresponding to the three chemical environments of carbon present for DBBA; carbon – bromine bonds, carbon - hydrogen bonds and all carbon bonds.

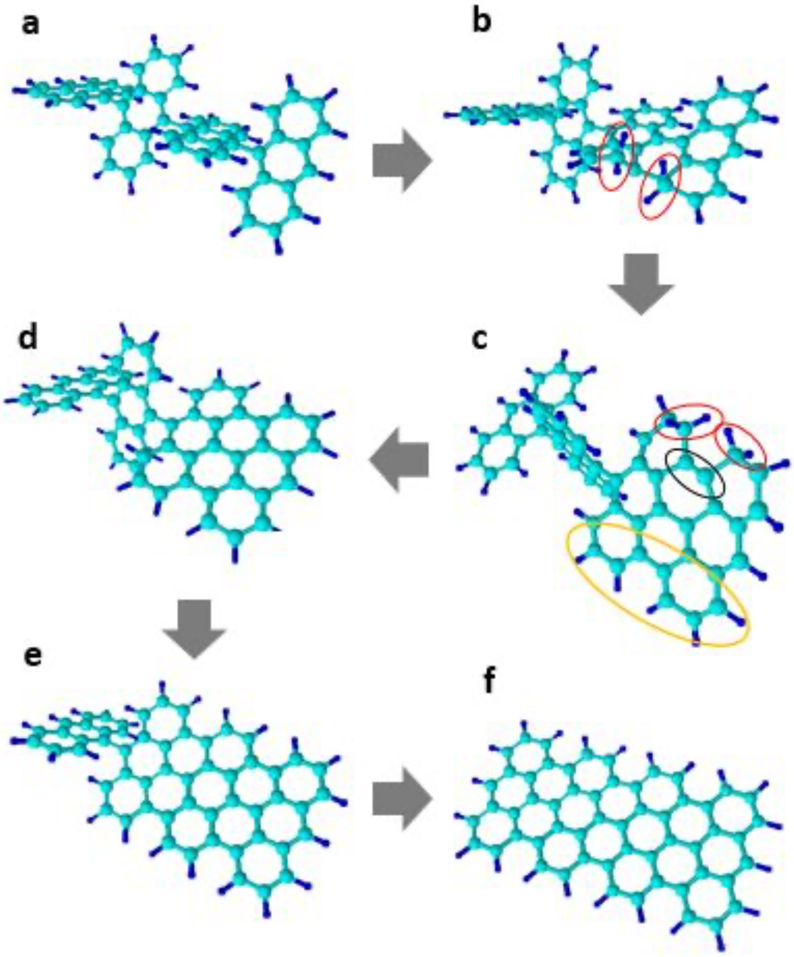

Figure 1.12: *Cyclo-dehydrogenation of DBBA: Steps a – f sequential removal of hydrogen from the inner then outer carbon atoms. (a) Polymer chain following C-C coupling (b) Red circles highlight outer carbons with two H bonds as inner carbons covalently bond. (c) One side of the central carbon axis is dehydrogenated (yellow circle). The opposite side covalently bonded C-C bonds (black circle) while outer carbons have two H bonds (red cicles) (d-f) Show the stepwise process resulting in 7-AGNR.*

In the carbon 1*s* XPS spectra shown in figure 1.13, these different carbon environments are highlighted by green, black, and cyan curves, respectively. Annealing the sample at 200 °C removes bromine from DBBA and forms polymer chains as evidenced by the absence of a higher binding energy component associated with the bromine bond (green curve). Annealing to higher temperatures instigates the cyclodehydrogenation process which manifests in the XPS spectra as a change in the ratio of C-C bonds to C-H bonds. At 400 °C the cyclodehydrogenation process is complete resulting in pristine 7-AGNRs. The corresponding spectrum is an XPS fingerprint of 7-AGNRs.

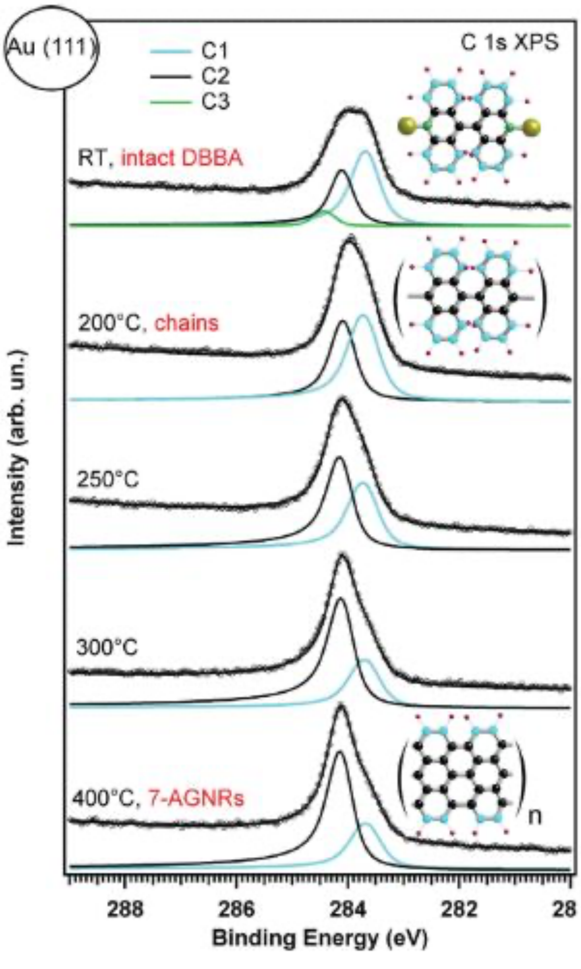

Figure 1.13: *XPS spectra of C1s evolution in DBBA to 7-AGNR* [56]

1.3.1 Substrates: Diffusion and Catalysis

Metal surfaces are required to induced cyclodehydrogenation in polymer chains. To this effect the substrate plays a key role in OSS affecting parameters such as catalysis and diffusion of molecules on the surface. However, not all metals are conducive for OSS. Polycyclic (hetero)aromatic hydrocarbons were shown to diffuse, polymerise and subsequently dehydrogenate on Au(111) whereas on Pt(111), a more reactive metal, the same precursor does not diffuse due to the greater adsorption energy of the substrate resulting in dehydrogenation alone [57]. Ourdjini *et al.*[58] conducted a comparative study of 1,4 benzenediboronic acid (BDBA) on coinage metals, namely Ag(100), Ag(111), Au(111) and Cu(111). Using the following expression for the rate of nucleation, n

$$n \propto Fe^{\frac{-E_d - E_s - E_g}{kT}} \tag{1.1}$$

where F is the deposition flux, E_d is the energy at which molecules are evaporated from the surface, E_s is the diffusion energy of the substrate, E_g is the nucleation energy, T is the substrate temperature and k is the Boltzmann constant. They found the diffusion of BDBA was limited on the copper surface and desorbed from the gold surface upon annealing to 350 °C suggesting that the Ag(100) and Ag(111) substrates offer the best compromise of diffusion and adsorption of all three metals.

Forming covalent structures from organic precursors on more reactive substrates, Ag and Cu can result in organometallic intermediates. Gutzler and co-workers[59] deposited brominated tetrathienoanthracene (TBTTA) on the Ag(111) and Cu(111) surfaces. TBTTA completely dibrominated upon deposition on the copper surface at room temperature leaving chemisorbed bromine on the substrate. After annealing the sample to 200 °C they observed the formation of organometallic structures with Cu adatoms linking the organic units. Subsequent annealing to higher temperatures did not result in full polymerisation. For TBTTA on Ag(111) however, organometallic and polymeric networks work formed after annealing to 300 °C and further annealing to 400 °C increased the number of polymer structures. The coexistence of both organometallic and polymer networks suggests the density of Cu adatoms on the surface affects the catalytic properties of the substrate. Similar work was conducted by Fan *et al.*[60] and Dai *et al.*[61] using 4,4”-dibromo-meta-terphenyl (DMTP), figure 1.14 (a), on low index copper substrates. They both found that the Br atoms dissociate from the molecule at room temperature and Cu adatoms then coupled with the precursor molecules forming organometallic chains. Depending on the surface coverage the organometallic chains can self-assembly into hyperbenzene macrocycles at low coverage and high-density zig-zag chains at higher coverages as shown in figures 1.14 (b) and (c) respectively.

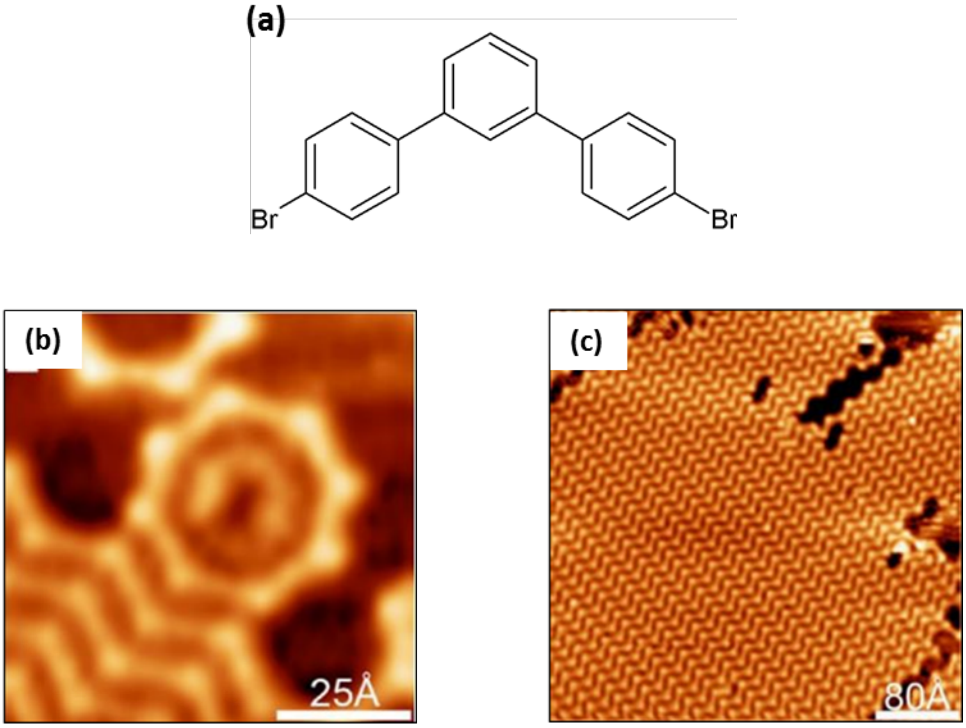

***Figure 1.14**: DMTP on Cu substrates. (a) Chemical structure of DMTP. (b) Hyperbenzene (V=-3.2 V, I=0.03 nA) (c) zig-zag self-assembly (V=-3.6 V, I=0.02 nA)* [62]

In a study closely related to the work in this thesis, Simonov and co-workers showed how the reactivity of the substrate metal effects the precursor monomers upon deposition. They used 10,10′-dibromo-9,9′-bianthracene (DBBA) on different coinage metal surfaces [63]. The XPS spectra in figure 1.15 shows the Br 3*d* doublet following sublimation of DBBA on the Au(111), Ag(111) and Cu(111) surfaces at room temperature. On the Au(111), the Br 3*d* doublet corresponding to bromine bonded to carbon is seen indicating the presence of fully intact DBBA on the surface. Whereas, on the silver crystal surface two doublets of equal intensity are seen which indicate partially dibrominated DBBA and chemisorbed bromine on the Ag(111) surface. Finally, on the Cu(111) substrate the spectrum contains a single doublet corresponding to bromine on the surface and inferring complete debromination of DBBA. This demonstrates the catalytic effect of metallic surfaces on the reaction pathway from precursor monomers to GNRs.

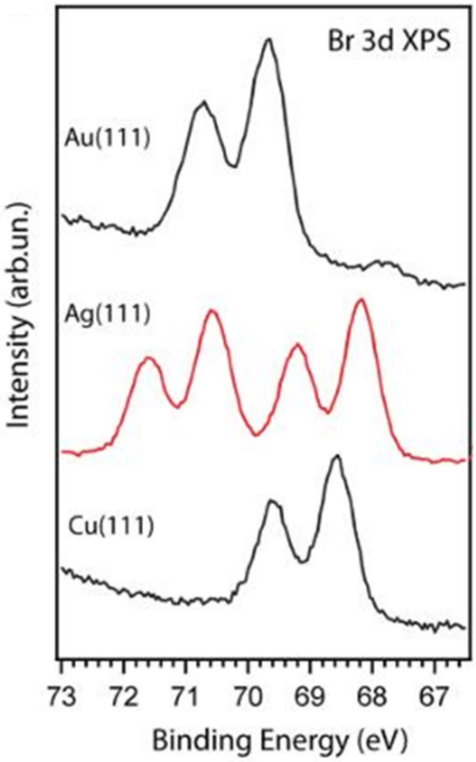

Figure 1.15: *Br 3d XPS spectra of DBBA on Au(111), Ag(111) and Cu(111) at room temperature.* [63]

In the same paper Simonov *et al.* also observed the formation of organometallic intermediates where silver atoms from the surface or adatoms intercalate between debrominated monomers to form organometallic chains. However, at elevated temperatures the metal atoms are removed from the structure and Ullmann coupling takes place to form polymer chains. Annealing the substrate at 350 ºC initiated cyclodehydrogenation leading to the formation of 7-AGNRs[63]. The same group demonstrated the synthesis of 7-AGNR from DBBA on Cu(111) with a Cu organometallic intermediate similar to that seen on the Ag(111) surface. However, on the anisotropic Cu(110) surface the molecules partially dehydrogenated but the higher adsorption energy of the Cu(110) plane restricts the diffusion of DBBA on the surface and instead they aligned along the $[1\bar{1}1]$ direction [64] and do not form nanoribbons These results show that not only does the coinage metal of the substrate affect the reaction pathway to the formation GNRs, but the crystal plane of the surface is also a key parameter.

1.3.2 Substrates: Orientation and Directional Growth

The inherent templating effect of some crystal planes promotes the alignment of precursor monomers in certain directions. Lafferentz and co-worker showed how the surface reconstruction influenced porphyrin orientation and controlled the direction of diffusion. The Au(100) surface arranges into a (5×1) reconstruction with top row protrusions 1.44 nm apart and corrugation of 70 pm, shown in figure 1.16(a). The deposited porphyrin molecules exhibited preferential alignment at approximately 51° to the direction of the gold rows, figure 1.16(b). The same group conducted a similar experiment on Au(111), the reconstruction of which leads to surface corrugation on the order of a few picometers, and no such preferential alignment was found [48]. Zhong *et al.* observed linear *n*-dotriacontontane monomers to align in the "missing-row" of the (1×2) reconstruction of the Au(110) surface. Annealing the substrate to 440 K, resulted in a phase transition from (1×2) to (1×3) reconstruction and the polymerization of the organic chains along the [110] direction [65]. [1]

Uniform alignment of graphene nanoribbons is required in order to probe the optical and electrical bandgaps and measurement of the electrons effective mass by means of non-local, area averaged techniques such as angular resolved photoelectron spectroscopy (ARPES) and inverse photoemission spectroscopy (IPS). Linden *et al.* used the Au(788) surface to grow aligned 7-AGNR and chevron GNRs from DBBA and 6,11-dibromo-1,2,3,4-tetraphenyltriphenylene, respectively [40]. The Au(788) vicinal surface has terraces with a typical width of 3.83 nm and parallel, monoatomic steps along the [111] direction which limits the diffusion of molecules and chains over the step edges. By using 4,4″-dibromoterphenyl (DBTP) as precursor monomers Merino-Díez *et al.* demonstrated the synthesis of GNRs by lateral fusion, a protocol

---

[1] Surface reconstruction, crystal planes and directions are discussed in greater detail in Chapter 2

that had not been realised until this study [30]. On the Au(111) surface, where diffusion is unrestricted by substrate geometry DBTP formed disordered 6-, 9-, 12- and greater AGNRs. However, on the vicinal Au(322) surface, which reconstructs with parallel terraces approximately 1.2nm wide as seen in figure 1.16(c), the DBTP dimers aligned along the $[11\bar{1}]$ direction and formed 6-AGNRs exclusively, corresponding to a width of 0.9nm approximately in line with the terrace dimensions, shown in figure 1.16(d). The nano-templating effect of an appropriate metallic crystal is an important factor for the growth and alignment of novel GNRs in order to investigate the band structure of the GNR and the electron effective mass.

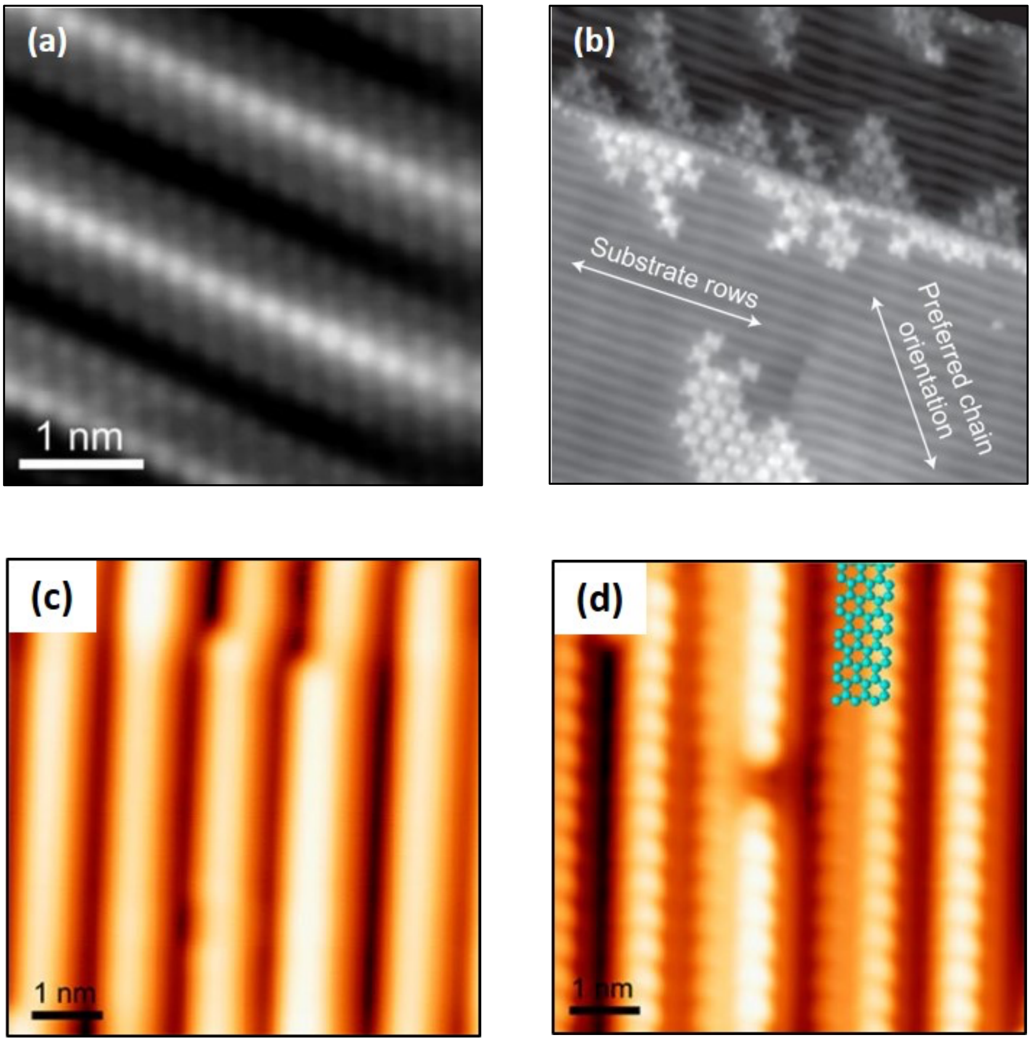

Figure 1.16*: STM images of precursor alignment on Au surfaces: (a) Clean Au(100) surface [66]. (b) Alignment of Br_2I_2TPP on Au(100) [66]. (c) Clean Au(322) surface.(V=-5.0 mV, I=2.0 nA)[30] (d) 6-AGNR aligned along rows of Au(322) reconstruction. (V=-1.5 V, I=0.5 nA) [30]. Authors did not report STM image parameters for (a) and (b)*

1.3.3 Substrates: Non-metallic surfaces and Transfer

It is necessary to transfer GNRs from metal surfaces to semiconducting surfaces to fabricate devices as the electric field can be modulated on semiconducting surfaces. SiO_2 is the most widely used insulating oxide as it readily grows on silicon. Kolmer *et al.* [67] attempted to grow GNRs from DBBA on insulating TiO_2 which resulted in polymerisation but not cyclodehydrogenation. Similarly, Xiao *et al.* [55] tried to grow GNR using DBBA on a layer of previously formed GNRs and failed to proceed passed the polymerisation stage. Both results strongly indicate that the metal surface lowers the energy needed to overcome the binding energies of hydrogen to carbon. This poses a potential roadblock for the growing of GNRs directly on semiconducting surfaces.

Transfer of GNRs to semiconductor surfaces has been achieved through several strategies. Wang *et al.* [68] transferred individual 7-AGNR from Au(111) onto NaCl by dragging them with an STM tip. For large area transfer, Bennet *et al* [44] grew GNRs on Au/Mica, then coated the surface in poly-methyl methacrylate (PMMA) creating a stacked structure. Through a series of mica delamination and gold etching the PMMA/GNR was then drawn onto SiO_2/Si substrate. The PMMA was rinsed with acetone leaving GNRs on the silicon substrate. This technique has limitations as the PMMA can contaminate/damage the GNRs. Barin *et al* [69] developed a similar large area technique and transferred 7- and 9-AGNRs from Au(111) onto Al_2O_3, SiO_2/Si and CaF_4 substrates without coating the GNRs with a polymer resulting in fewer defects in the GNRs. However, the gold substrate is also removed by an etchant in the method, which is both costly and can damage the GNR edges. An etchant-free transfer method was developed by Yamamoto *et al.* [70] to transfer aligned 7-AGNRs from Au(788) to SiO_2/Si. In this procedure GNRs are grown on gold surfaces and coated in a nanoporous film of hydrogen silsesquioxane (HSQ). The sample is then added to alkanethiol solution. The alkanethiol quasi-covalently bonds with the gold and form a self-assembled monolayer which mechanically cleaves the 7-AGNRs from the Au (788) surface. The GNRs now transferred to the HSQ can subsequently be transferred to SiO_2/Si. The HSQ is removed by rinsing in tetramethylammonium hydroxide (TMAH). The process is illustrated in figure 1.17.

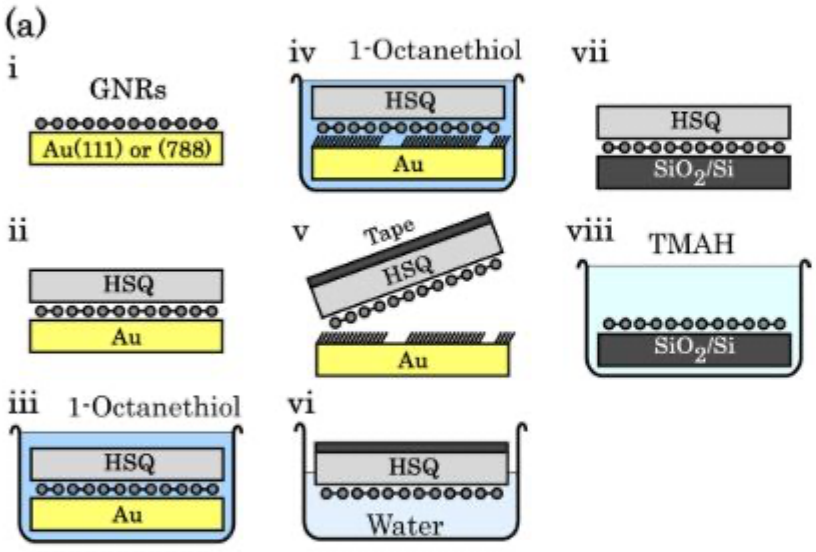

***Figure 1.17**: Etchant-free transfer of GNRs from Au(788) to SiO_2/Si* [70]

1.3.4 Temperature Dependent Reactions

The general rule of thumb in forming covalently bonded structures via OSS is a given precursor molecule determines the geometry of the GNR. However, this idea was recently challenged by conflicting results from two groups using the same precursors and substrates. In 2014 Simonov *et al.* reported the growth of 7-AGNR from DBBA on Cu(111), figure 1.18(a) [56]. Using XPS they found the DBBA dehalogenated on contact with the copper surface upon deposition at room temperature. Polymerisation and cyclodehydrogenation occurred at 100 °C and 200 °C, respectively. Later the same year, Han and co-workers published a similar study but found DBBA formed (3,1) chiral-GNR on Cu(111) shown in figure 1.18(b) [71]. This disparity was settled by the Fasel/Müllen group in 2016. By using a non-contact atomic force microscope (nc-AFM) with a carbon monoxide functionalised tip they were able to unambiguously image the chiral step of (3,1) CGNR as seen in figure 1.18 (c) [72]. This result appears to confirm the rule of thumb. However, Jacobse *et al.*[73] showed that one precursor, 10,10′-dichloro-9,9′-bianthryl (DCBA), analogous to DBBA but with chlorine as the halogen substituent, could form both 7-AGNRs and (3,1) CGNRs side by side on Ag(111) through different annealing protocols shown in figure 1.18(d). DCBA formed 7-AGNR when the substrate is slowly heated to 570 K, whereas rapidly heating the substrate to 600 K resulted in the presence of both chiral and armchair GNRs, a result which disproves the general understanding of precursor geometry determining the GNR shape and may help explain the initial results obtained by Simonov *et al.* The rate of heating of the sample is another parameter effecting the reaction pathways, when combined with coinage metal and crystal plane of the substrate, offers another controllable variable for OSS device fabrication.

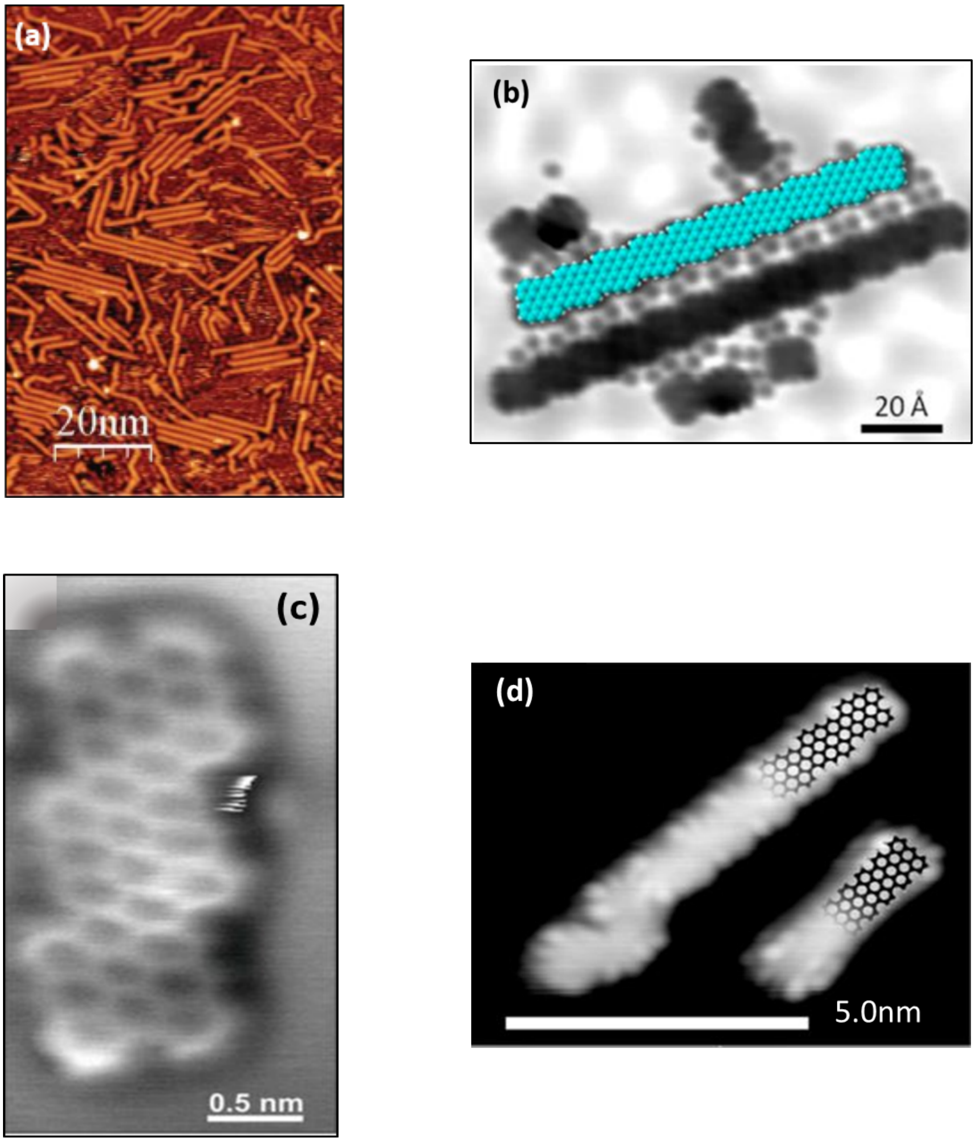

***Figure 1.18**: 7-AGNR and (3,1) chiral GNR. (a) 60 nm × 100 nm STM of 7-AGNR on Cu(111)(V=1.5 V, I=0.04 nA)* [56]*. (b) 10 nm × 8 nm STM of (3,1) CGNR on Cu(111) with space filling model overlayed (V=10 mV, I=0.35 nA)* [71] *(c)1.5 nm × 2.5 nm nc-AFM of (3,1) CGNR on Cu(111) (z=-40 pm, V=10 mV, I=2 pA)* [72]*. (d) 7 nm × 8 nm 7-AGNR and (3,1) CGNR on Ag(111)(V=-1.0 V, I=20 pA)* [73]*.*

1.4 Novel GNR Structures

Further tailoring of GNR properties can be achieved by forming heterojunctions, incorporating doped precursors, or designing GNRs with novel edge architectures. Molecular bandgap engineering was achieved by Chen *et al*. by growing a GNR structure of two different widths [74]. A heterojunction was formed between 7- and 13-AGNR segments. DBBA was used to form the 7-AGNR and the 13-AGNR segments were grown using di-phenyl-dibromo biantracene precursors as shown in figure 1.19. Scanning tunnelling spectroscopy (STS) reveal the HOMO and LUMO separation is greater in the narrower *N* = 7 segment compared to the *N* = 13 segment suggesting the *N* = 7 segment might serve as an energy barrier to charge transfer from the *N* = 13 section. Such heterojunctions have applications in solar cell technology[75] and graphene quantum-dot-based systems [76].

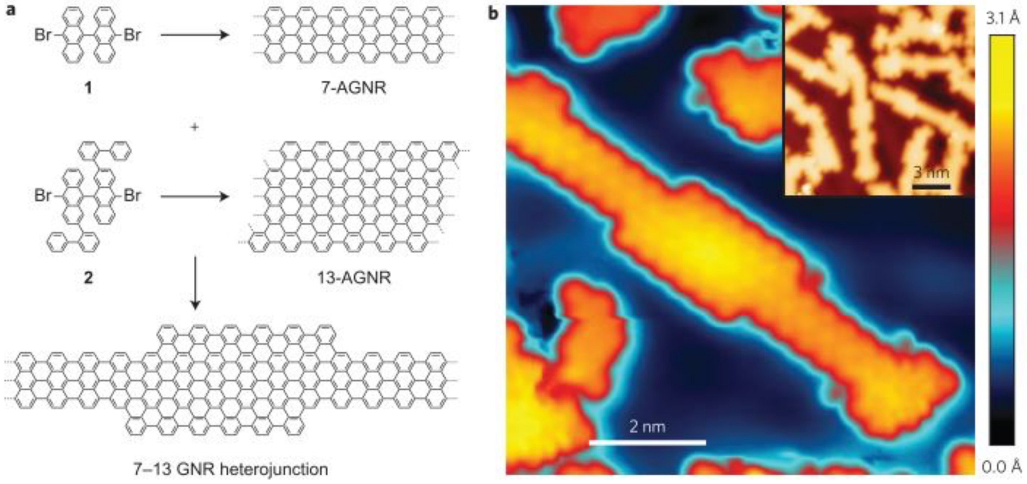

***Figure 1.19**: Heterojunction formation between 7- and 13-AGNRs: (a) Schematic diagram of DBBA and di-phenyl-dibromo biantracene precursor molecules. (b) 8 nm × 8 nm STM topography image of GNR heterojunction.(V=60 mV, I=0.2 nA) (inset) 12 nm × 12 nm of several GNR heterojunctions (V=0.5 V, I=2.0 pA)* [74]

The edge shape of GNRs also impacts the electronic structure. Liu *et al.* [77] grew 0.9nm GNRs with cove-type edges on Au(111), shown in figure 1.20. DFT calculations predict a bandgap of 1.9 eV for this GNR. Despite having comparable widths, this is much lower than the reported band gap of 2.3 eV for the 7-AGNR[11] which are 0.73 nm wide, highlighting the influence edge structure has on electronic states of GNRs.

Band gap engineering can also be achieved by replacing carbon atoms within the precursor monomers with dopants for example, B, N, O or S atoms [76]. This substitutional doping mechanism was implemented to form the precursor monomer 6,16-dibromo-9,10,19,20-tet-raoxa-9a,19a-diboratetrabenzo[a,f,j,o]perylene, (here abbreviated to OBO), by Wang and Narita and co-workers [78]. The result was a (4,1) CGNR with oxygen and boron dopants shown in figure 1.20. The inclusion of the heteroatoms increased the bandgap to 3.33 eV. DFT calculation of OBO doped (4,1) CGNR and undoped, all-carbon (4,1) in vacuum have band gaps of 1.50 eV and 0.50 eV, respectively. Chemical synthesis of doped precursors offers further controllability of GNR properties.

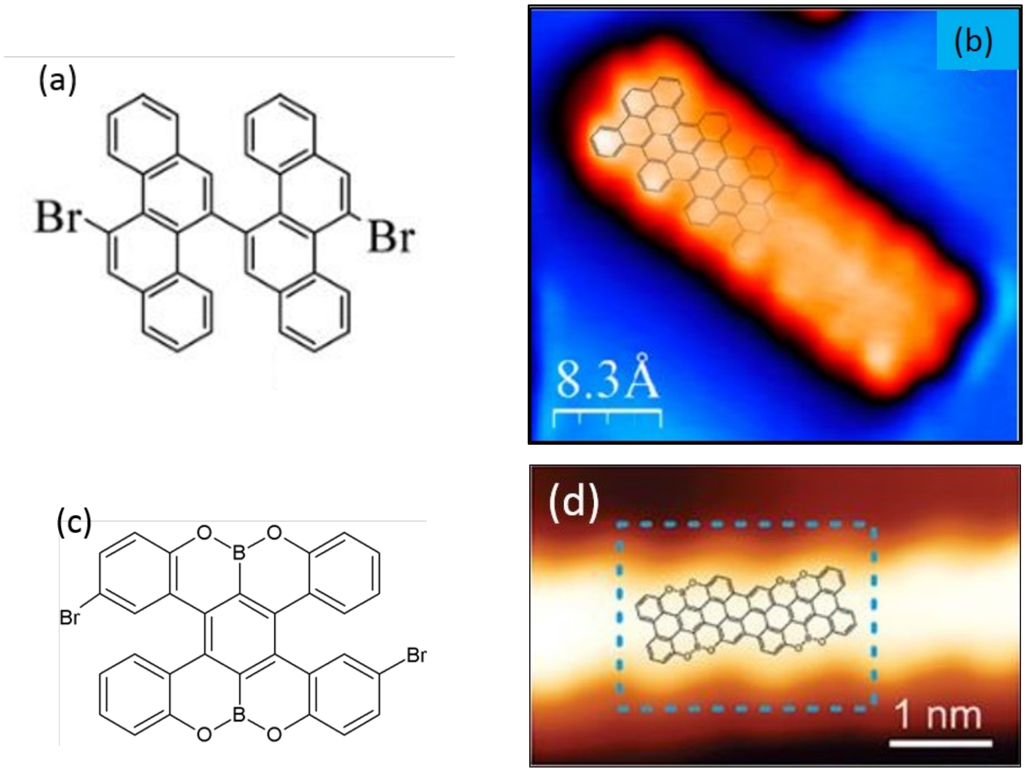

***Figure 1.20**: Novel GNR structures: (a) Pathway of monomer synthesis leading to cove-type GNR (b) STM image of GNR with cove-type edges (V=-0.9 V, I=0.4 nA) (c) The chemical structure of OBO monomer. (d) 5 nm × 4 nm STM image of OBO (4,1) CGNR with chemical structure overlay (V=-1.5 V, I=50 pA)* [12]

1.5 Porphyrin molecules

Porphyrins are a group heterocyclic aromatic molecules that are ubiquitous in the natural world. Fe-porphyrins form the core of the heme molecule present in red blood cells and are responsible for electron and oxygen transfer in the body [79]. Chlorophyll contains a Mg porphyrin that is formed through several proto-porphyrin stages [80]. The wide range of porphyrin HOMO-LUMO bandgaps means that they display exceptional electronic and optical properties [81]. There are many applications of porphyrins as the functional component in molecular electronics across many disciplines [82]. The optical band gap of porphyrins is utilised in photodynamic therapy [83] and dye-sensitive solar cells [84], while the electrical properties have applications in catalysis [85] and as chemical detecting sensors [86]. The simplest porphyrin is the unsubstituted parent compound, porphine. Figure 1.21 shows the Fe- and Mg-porphyrin cores. When used as sensors, transition metal porphyrins (TM-Py) either exhibit changes in electrochemistry or colour variation upon binding with different chemical compounds [87][81]. Fe-Py derivatives π-π stacked on a graphene FETs show sensitivity to nitric oxide [88] and dopamine detectors have been demonstrated using porphyrins with chromium ligands non-covalently bonded to graphene [89].

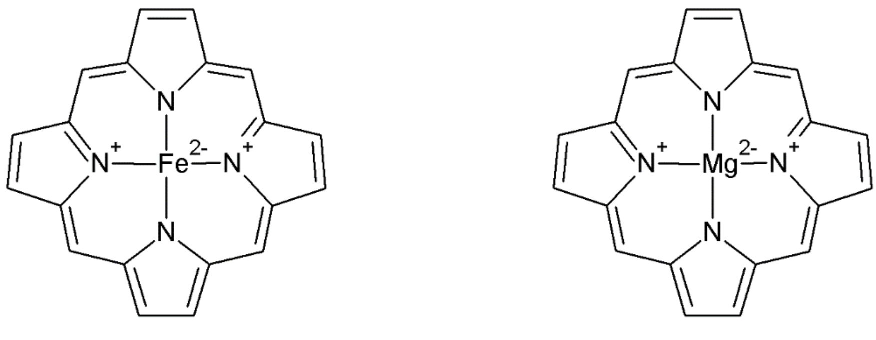

***Figure 1.21**: Chemical structure of porphine: (left) The Fe-porphyrin bases of the haemoglobin molecule. (Right) The Mg-porphyrin present within chlorophyll*

However, the lack of covalent bonds affects the stability of these devices. Further controllability of the opto-electronic properties of the porphyrin can be achieved by adding a transition metal to the core of the porphyrin and thus the functionality of a device can be tailored by coupling different transition metal porphyrins with specific GNR geometries.

A clear understanding of how porphyrins behave on surfaces is required if they are to be incorporated in the GNR devices. As mentioned in section 1.3, Grill *et al.* were the first to demonstrate the formation of covalently bonded networks using tetra(4-bromophenyl)porphyrin (Br_4TPP) on Au(111) via OSS. The chemical structure of Br_4TPP is shown in figure 1.22. In 2001, using DFT calculations Yokoyama and co-workers showed that the phenyl rings of non-brominated tetra-phenyl porphyrins (TPP) are rotated approximately 63° away from the planar macrocycle of the porphyrin core due to steric hindrance between the hydrogen atoms. This prediction roughly agreed with STM measurements in the same paper [90].

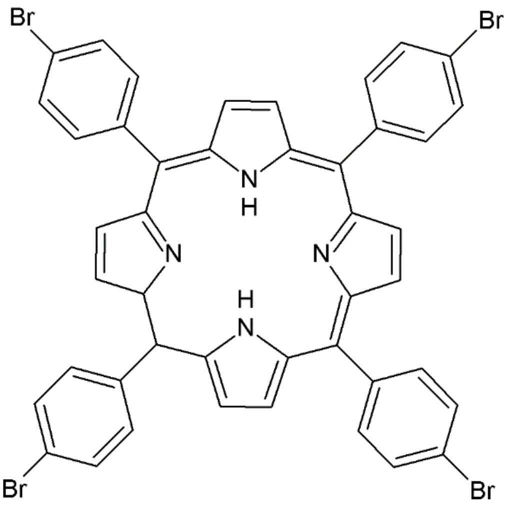

Figure 1.22*: tetra(4-bromophenyl)porphyrin (Br_4TPP)*

This rotation effectively raises the porphyrin 0.1 nm relative to the surface. The height of the halogen substituent with respect to the substrate is an important consideration for forming networks via OSS as the dangling bonds formed following dehalogenation of porphyrins and polymer chains need to be sub-nanometre height apart to form a bond to the extent that if the height separation is too great bonds cannot be formed. In a comparative study of TPP and Br_4TPP on the Ge(001) surface by Berner *et al.* all four bromine atoms in Br_4TPP were observed to strongly interacted with the surface resulting in little diffusion on the surface but also form two distinct flat formations; symmetric (square shaped) and asymmetric (rectangular)[91]. Similar orientations of porphyrins were observed by Iancu *et al.* when they deposited Br_4TPP with Co- and Cu- cores, respectively on Cu(111) [92]. However, the similarity was due to a different porphyrin/substrate interaction. In this case the porphyrin also took on a planar formation when all four bromine atoms interacted with the substrate but a non-planer structure when only two of the bromines interacted with the surface and the other bromo-phenyl rings raised of the surface in a saddle-like shape. Using a 2.2 V pulse from an STM tip the group could change the conformation of the porphyrin from saddle-like to planar, the reverse, from planar to saddle-like may also be possible by STM tip induction.

1.6 Functionalisation of GNRs

Functionalisation involves incorporating additional molecules into the GNR structure for a specific purpose. Functionalising graphene nanoribbons offers further control over the electronic, chemical, optical properties of GNRs increasing the range of possible applications. Herein, attempts to form functional graphene nanoribbons (f-GNRs) via different strategies and for different purposes are discussed.

Kosynkin *et al.* created GNRs by unzipping carbon nanotubes (CNT) in an acidic solution [15]. This top-down method produced inherently functionalised GNRs as the acidic solution leaves the ribbon edges with epoxides, carbonyls, carboxyls and hydroxyls present. The familiar drawbacks of forming GNRs via this top-down technique remain, namely the lack of atomic precision at the ribbon edges. For functionalisation purposes this method is also unsuitable due to the arbitrary nature at which the edges may be functionalised with oxygen and hydrogen groups. Various strategies for unzipping CNTs and doped CNTs in acids resulted in many different functionalised GNRs. A major flaw with this type of edge functionalisation is the lack of long-term stability due to the nature of the non-covalent bonds. Zhu and co-workers formed f-GNRs with covalently bonded out-of-plane aryl dizonium salts in a top-down solution-based technique shown in figure 1.23(a) [93]. In a similar study by the same group, the authors covalently bonded 4-nitrophenyl groups to top-down GNRs which resulted in sp^3 hybridisation of the bonded carbon atom thus reducing the conductivity of the GNRs [18]. In work by Zhang *et al.,* GNRs functionalised via non-covalent π-π stacking with Fe-porphyrins exhibited catalytic behaviour for oxygen reduction, illustrated in figure 1.23(b) [86]. By using this device as an electrode, it was demonstrated that the f-GNR could function as a glucose biosensor. This work showed that using porphyrin functionalised GNRs could act as detectors sensitive to any number of molecules and compounds. However, for long term stability covalent bonds between the GNR and the functional molecule are necessary. Another obvious hindrance of these routes toward f-GNR is the use of top-down solution-based approaches which fails to ensure atomic precision of GNRs which is key to tailoring the device properties.

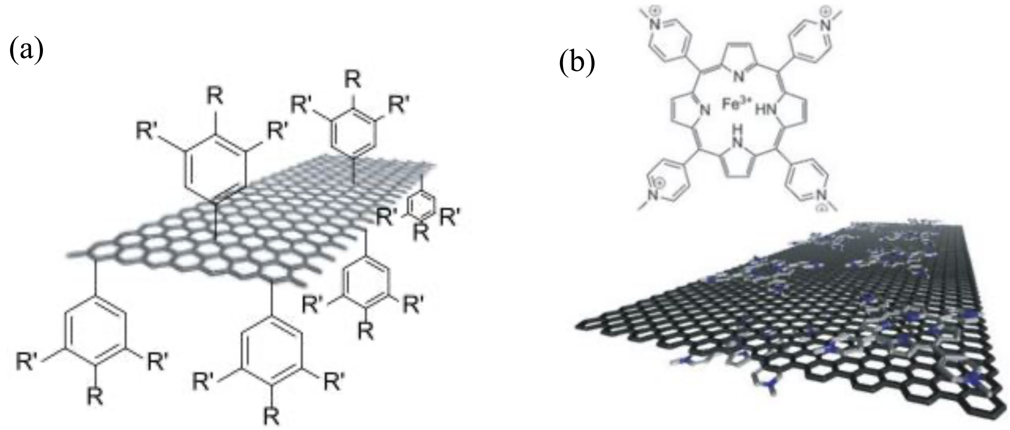

***Figure 1.23**: Functionalised Graphene nanoribbons: (a) GNR with out of plane covalent bonds with aryl moieties* [94]*. (b) π – π stacking of Fe-porphyrin on GNRs* [86].

In one of the first papers to report GNR-porphyrin hybrid structures, de Oteyza *et al.* co-deposited 2,2′- dibromo-9,9′-bianthracene (DBBA), which forms (3,1) CGNRs [95] and Fe-tetra(4-bromophenyl)porphyrin chloride (Br_4-FeTPP(Cl)) onto Au(111) and formed a porphyrin with three chiral GNRs covalently bonded to it shown in figure 1.24(a) and (b) [96]. The Fe- core of the porphyrin maintained its magnetic properties when incorporated into hybrid structure. One drawback of this work is the degrees of freedom displayed at the GNR/porphyrin junction and between the phenyl ring and macrocycle whereby following cyclodehydrogenation different combinations of five-membered rings are formed. The electron transport within a molecular electronic device is greatly dependent on the geometry of the five-membered rings [97].

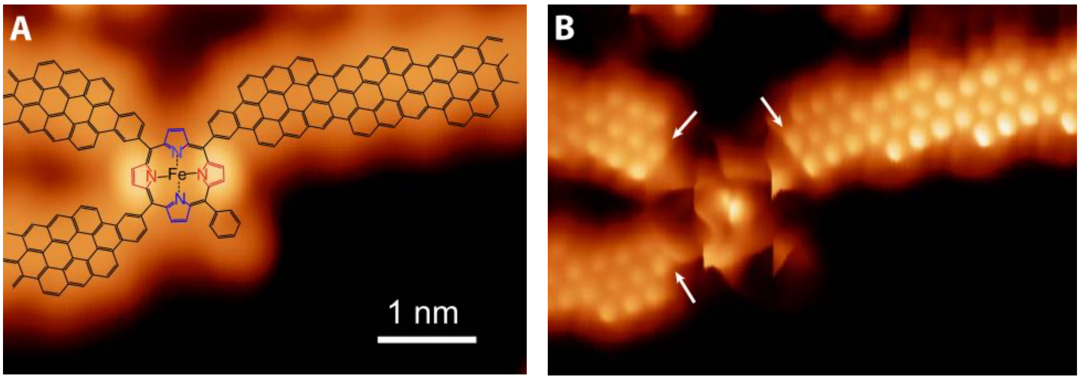

***Figure 1.24**: GNR-porphyrin hybrid. (a) STM image of Fe-TPP with three GNRs bonded. Chemical structure overlayed.(V=0.21 V, I=16 pA) (b) dI/dV of (a) arrows highlight newly formed membered rings (V=0 V, V_{ac}=2 mV_{rms} R_t~1 GOhm)* [96].

1.6 Thesis Outline

The work in this thesis utilises on-surface synthesis to grow GNRs and functionalised GNRs with Ni-dibromo-tetraphenyl porphyrin (Ni-DBTPP) on the Au(111) and Au(788) surfaces. This involves finding the appropriate temperature for sublimating GNR precursor molecules and porphyrins at a suitable rate and the necessary temperatures to facilitate dehalogenation and cyclo-dehydrogenation. All steps and processes are observed by scanning tunnelling microscopy (STM) and for the OBO functionalised porphyrins on Au(111), x-ray photoelectron spectroscopy (XPS) characterisation is also used.

In Chapter 2, scanning tunnelling microscopy and x-ray photoelectron spectroscopy experimental techniques are described from both a theoretical and a technical standpoint. The molecular precursor materials and the Au crystal surfaces are discussed as is the ultra-high vacuum environment, deposition and sample preparation methods.

Chapter 3 describes the formation of Ni-porphyrin functionalised 7-AGNR on the Au(111) and Au(788) surfaces. Ni-DBTPP is deposited on the Au(111) surface and porphyrin chains are formed to observe the behaviour of porphyrin in isolation from GNRs. Co-deposition of DBBA and Ni-DBTPP resulted in funtionalised 7-AGNR and an investigation into the effect of surface coverage on length and alignment of the functionalised ribbons for both surfaces is conducted.

In Chapter 4, (4,1) chiral GNRs and porphyrin functionalised CGNRs are formed on the Au(111) ad Au(788) surfaces. The oxygen and boron doped 10, 10-dibromo-9,9 bianthracene (OBO) precursor molecule is deposited on the Au(111) surface and a comparison of 0.5 ML and ~1 ML are carried out. A statistical comparison of length and angles of nanostructures on the Au(111) and Au(788) surfaces is conducted. Finally, a protocol for achieving long and aligned (4,1) CGNRs on the Au(788) surface is described.

The final chapter includes a summary of the results and proposes future work that would complement the research in this thesis and discusses recent developments and breakthroughs in the field of on-surface synthesis.

1.7 References

1. Novoselov, K. S. *et al.* Electric field effect in atomically thin carbon films. *Science* **306**, 666–669 (2004).
2. Bolotin, K. I. *et al.* Ultrahigh electron mobility in suspended graphene. *Solid State Commun.* **146**, 351–355 (2008).
3. Wang, X. *et al.* Room-Temperature All-Semiconducting Sub-10-nm Graphene Nanoribbon Field-Effect Transistors. *Phys. Rev. Lett.* **100**, 206803 (2008).
4. Schwierz, F. Graphene Transistors. *Nat. Nanotechnol.* **5**, 4–5 (2010).
5. Schwierz, F. Graphene transistors: Status, prospects, and problems. *Proc. IEEE* **101**, 1567–1584 (2013).
6. Bangert, U. *et al.* Ion implantation of graphene - Toward IC compatible technologies. *Nano Lett.* **13**, 4902–4907 (2013).
7. Bae, S. *et al.* Roll-to-roll production of 30-inch graphene films for transparent electrodes. *Nat. Nanotechnol.* **5**, 574–578 (2010).
8. Guo, B. *et al.* Controllable N-Doping of Graphene. *Nano Lett.* **10**, 4975–4980 (2010).
9. Yamabe, T., Tanaka, K., Ohzeki, K. & Yata, S. Electronic structure of polyacenacene. A one-dimensional graphite. *Solid State Commun.* **44**, 823–825 (1982).
10. Tanaka, K., Yamashita, S., Yamabe, H. & Yamabe, T. Electronic properties of one-dimensional graphite family. *Synth. Met.* **17**, 143–148 (1987).
11. Chen, Y.-C. *et al.* Tuning the Band Gap of Graphene Nanoribbons Synthesized from Molecular Precursors. *ACS Nano* **7**, 6123–6128 (2013).
12. Wang, X.-Y. *et al.* Bottom-Up Synthesis of Heteroatom-Doped Chiral Graphene Nanoribbons. *J. Am. Chem. Soc.* **140**, 9104–9107 (2018).
13. Han, M. Y., Zyilmaz, B. O., Zhang, Y. & Kim, P. Energy Band-Gap Engineering of Graphene Nanoribbons. *Phys. Rev. Lett.* **98**, 206805 (2007).
14. Jishan Wu, † *et al.* From Branched Polyphenylenes to Graphite Ribbons. (2003). doi:10.1021/MA0257752
15. Kosynkin, D. V. *et al.* Longitudinal unzipping of carbon nanotubes to form graphene nanoribbons. *Nature* **458**, 872–876 (2009).
16. Woo, J. Y., Jo, S., Oh, J. H., Kim, J. T. & Han, C. S. Facile and precise fabrication of 10-nm nanostructures on soft and hard substrates. *Appl. Surf. Sci.* **484**, 317–325 (2019).
17. C. Joachim, J. K. Gimzewski, A. A. Electronics using hybrid-molecular and mono-molecular devices. *Nature* **408**, 541–548 (2000).
18. Sinitskii, A. *et al.* Kinetics of diazonium functionalization of chemically converted graphene nanoribbons. *ACS Nano* **4**, 1949–1954 (2010).
19. Cai, J. *et al.* Atomically precise bottom-up fabrication of graphene nanoribbons.

Nature **466**, 470–473 (2010).

20. Mir, S. H., Yadav, V. K., & Singh, J. K. Recent Advances in the Carrier Mobility of Two-Dimensional Materials: A Theoretical Perspective. *ACS Omega* **5**, 14203–14211 (2020).

21. Son, Y.-W., Cohen, M. L. & Louie, S. G. Energy Gaps in Graphene Nanoribbons. *Phys. Rev. Lett.* **97**, 216803 (2006).

22. Barone, V., Hod, O. & Scuseria, G. E. Electronic structure and stability of semiconducting graphene nanoribbons. *Nano Lett.* **6**, 2748–2754 (2006).

23. Wassmann, T., Seitsonen, A. P., Saitta, A. M., Lazzeri, M. & Mauri, F. Clar's theory, π-electron distribution, and geometry of graphene nanoribbons. *J. Am. Chem. Soc.* **132**, 3440–3451 (2010).

24. Yang, L., Park, C. H., Son, Y. W., Cohen, M. L. & Louie, S. G. Quasiparticle energies and band gaps in graphene nanoribbons. *Phys. Rev. Lett.* **99**, 6–9 (2007).

25. Brey, L. & Fertig, H. A. Electronic States of Graphene Nanoribbons. *Phys. Rev. B - Condens. Matter Mater. Phys.* **73**, 2–6 (2006).

26. Kharche, N. & Meunier, V. Width and Crystal Orientation Dependent Band Gap Renormalization in Substrate-Supported Graphene Nanoribbons. *J. Phys. Chem. Lett.* **7**, 1526–1533 (2016).

27. Ruffieux, P. *et al.* Electronic Structure of Atomically Precise Graphene Nanoribbons. *ACS Nano* **6**, 6930–6935 (2012).

28. Nguyen, G. D. *et al.* Atomically precise graphene nanoribbon heterojunctions from a single molecular precursor. *Nat. nan* **12**, 1077–1083 (2017).

29. Talirz, L. *et al.* On-Surface Synthesis and Characterization of 9-Atom Wide Armchair Graphene Nanoribbons. *ACS Nano* **11**, 1380–1388 (2017).

30. Merino-Díez, N. *et al.* Switching from Reactant to Substrate Engineering in the Selective Synthesis of Graphene Nanoribbons. *J. Phys. Chem. Lett.* **9**, 2510–2517 (2018).

31. Kiraly, B. *et al.* Sub-5 nm, globally aligned graphene nanoribbons on Ge(001). *Appl. Phys. Lett.* **108**, 213101 (2016).

32. Meunier, V., Souza Filho, A. G., Barros, E. B. & Dresselhaus, M. S. Physical properties of low-dimensional sp2 -based carbon nanostructures. *Rev. Mod. Phys.* **88**, 1–50 (2016).

33. Wang, Z.-Q. *et al.* Controlling the conductance of single-molecule junctions with high spin filtering efficiency by intramolecular proton transfer. *Org. Electron.* **64**, 7–14 (2019).

34. Trauzettel, B., Bulaev, D. V., Loss, D. & Burkard, G. Spin qubits in graphene quantum dots. *Nat. Phys.* **3**, 192–196 (2007).

35. Ruffieux, P. *et al.* On-surface synthesis of graphene nanoribbons with zigzag edge topology. *Nature* **531**, (2016).

36. Slota, M. *et al.* Magnetic edge states and coherent manipulation of graphene nanoribbons. *Nature* **557**, 691–695 (2018).

37. Berezin, A., Biot, N., Battisti, T. & Bonifazi, D. Oxygen-Doped Zig-Zag Molecular Ribbons. *Angew. Chemie Int. Ed.* **57**, 8942–8946 (2018).

38. Néstor Merino-Díez, N. *et al.* Unraveling the Electronic Structure of Narrow Atomically Precise Chiral Graphene Nanoribbons. *J. Phys. Chem. Lett.* **9**, 25–30 (2017).

39. Talirz, L. *et al.* Band Gap of Atomically Precise Graphene Nanoribbons as a Function of Ribbon Length and Termination. *ChemPhysChem* **20**, 2348–2353 (2019).

40. Linden, S. *et al.* Electronic Structure of Spatially Aligned Graphene Nanoribbons on Au(788). *Phys. Rev. Lett.* **108**, (2012).

41. Söde, H. *et al.* Electronic band dispersion of graphene nanoribbons via Fourier-transformed scanning tunneling spectroscopy. *Phys. Rev. B* **91**, 45–49 (2015).

42. Novoselov, K. S. *et al.* Two-dimensional gas of massless Dirac fermions in graphene. *Nature* **438**, 197–200 (2005).

43. Koch, M., Ample, F., Joachim, C. & Grill, L. Voltage-dependent conductance of a single graphene nanoribbon. *Nat. Nanotechnol.* **7**, 713–717 (2012).

44. Bennett, P. B. *et al.* Bottom-up graphene nanoribbon field-effect transistors. *Appl. Phys. Lett.* **103**, 253114 (2013).

45. Nitzan, A. & Ratner, M. A. Electron Transport in Molecular Wire Junctions. *Science (80-.).* **300**, 1384–1389 (2003).

46. Joachim, C. & Ratner, M. A. Molecular electronics: Some views on transport junctions and beyond. *Proc. Natl. Acad. Sci. U. S. A.* **102**, 8801–8808 (2005).

47. Barth, J. V. Molecular Architectonic on Metal Surfaces. *Annu. Rev. Phys. Chem.* **58**, 375–407 (2007).

48. Grill, L. *et al.* Nano-architectures by covalent assembly of molecular building blocks. *Nat. Nanotechnol.* **2**, 687–691 (2007).

49. Stöhr, M. *et al.* Controlling molecular assembly in two dimensions: The concentration dependence of thermally induced 2D aggregation of molecules on a metal surface. *Angew. Chemie - Int. Ed.* **44**, 7394–7398 (2005).

50. Hla, S. W., Meyer, G. & Rieder, K. H. Selective bond breaking of single iodobenzene molecules with a scanning tunneling microscope tip. *Chem. Phys. Lett.* **370**, 431–436 (2003).

51. Ullmann, F. & Bielecki, J. Ueber Synthesen in der Biphenylreihe. *Berichte der Dtsch. Chem. Gesellschaft* **34**, 2174–2185 (1901).

52. Xi, M. & Bent, B. E. Mechanisms of the Ullmann coupling reaction in adsorbed monolayers. *J. Am. Chem. Soc.* **115**, 7426–7433 (1993).

53. Blankenburg, S. *et al.* Intraribbon Heterojunction Formation in Ultranarrow Graphene Nanoribbons. *ACS Nano* **6**, 2020–2025 (2012).

54. Björk, J., Stafström, S. & Hanke, F. Zipping up: Cooperativity drives the synthesis of graphene nanoribbons. *J. Am. Chem. Soc.* **133**, 14884–14887 (2011).

55. Xiao, Z. *et al.* Ab initio investigation of the cyclodehydrogenation process for

polyanthrylene transformation to graphene nanoribbons. *npj Comput. Mater.* 1–6 (2019). doi:10.1038/s41524-019-0228-6

56. Simonov, K. A. *et al.* Effect of Substrate Chemistry on the Bottom-Up Fabrication of Graphene Nanoribbons: Combined Core-Level Spectroscopy and STM Study. *J. Phys. Chem. C* **118**, (2014).

57. Pinardi, A. L. *et al.* Tailored formation of n-doped nanoarchitectures by diffusion-controlled on-surface (Cyclo)Dehydrogenation of heteroaromatics. *ACS Nano* **7**, 3676–3684 (2013).

58. Ourdjini, O. *et al.* Substrate-mediated ordering and defect analysis of a surface covalent organic framework. *Phys. Rev. B* **84**, 125421 (2011).

59. Gutzler, R. *et al.* Ullmann-type coupling of brominated tetrathienoanthracene on copper and silver. *Nanoscale* **6**, 2660–2668 (2014).

60. Fan, Q. *et al.* Surface-assisted formation, assembly, and dynamics of planar organometallic macrocycles and zigzag shaped polymer chains with C-Cu-C bonds. *ACS Nano* **8**, 709–718 (2014).

61. Dai, J. *et al.* The role of the substrate structure in the on-surface synthesis of organometallic and covalent oligophenylene chains. *Phys. Chem. Chem. Phys.* **18**, 20627–20634 (2016).

62. Fan, Q. *et al.* Surface-assisted organic synthesis of hyperbenzene nanotroughs. *Angew. Chemie - Int. Ed.* **52**, 4668–4672 (2013).

63. Simonov, K. A. *et al.* Synthesis of armchair graphene nanoribbons from the 10,10′-dibromo-9,9′-bianthracene molecules on Ag(111): the role of organometallic intermediates. *Sci. Rep.* **8**, 3506 (2018).

64. Simonov, K. A. *et al.* From Graphene Nanoribbons on Cu(111) to Nanographene on Cu(110): Critical Role of Substrate Structure in the Bottom-Up Fabrication Strategy. *ACS Nano* **9**, 8997–9011 (2015).

65. Zhong, D. *et al.* Linear Alkane Polymerization on a Gold Surface. *Science (80).* **334**, 213–216 (2011).

66. Lafferentz, L. *et al.* Controlling on-surface polymerization by hierarchical and substrate-directed growth. *Nat. Chem.* **4**, 215–220 (2012).

67. Kolmer, M. *et al.* Polymerization of polyanthrylene on a titanium dioxide (011)-(2×1) surface. *Angew. Chemie - Int. Ed.* **52**, 10300–10303 (2013).

68. Wang, S. *et al.* Giant edge state splitting at atomically precise graphene zigzag edges. *Nat. Commun.* **7**, (2016).

69. Borin Barin, G. *et al.* Surface-Synthesized Graphene Nanoribbons for Room Temperature Switching Devices: Substrate Transfer and ex Situ Characterization . *ACS Appl. Nano Mater.* **2**, 2184–2192 (2019).

70. Ohtomo, M., Sekine, Y., Hibino, H. & Yamamoto, H. Graphene nanoribbon field-effect transistors fabricated by etchant-free transfer from Au(788). *Appl. Phys. Lett.* **112**, (2018).

71. Han, P. *et al.* Bottom-Up Graphene-Nanoribbon Fabrication Reveals Chiral Edges and Enantioselectivity. *ACS Nano* **8**, 9181–9187 (2014).

72. Sánchez-Sánchez, C. *et al.* Purely Armchair or Partially Chiral: Noncontact

Atomic Force Microscopy Characterization of Dibromo-Bianthryl-Based Graphene Nanoribbons Grown on Cu(111). *ACS Nano* **10**, 8006–8011 (2016).

73. Jacobse, P. H. *et al.* One Precursor but Two Types of Graphene Nanoribbons: On-Surface Transformations of 10,10′-Dichloro-9,9′-bianthryl on Ag(111). *J. Phys. Chem. C* **123**, 8892–8901 (2019).

74. Chen, Y. C. *et al.* Molecular bandgap engineering of bottom-up synthesized graphene nanoribbon heterojunctions. *Nat. Nanotechnol.* **10**, 156–160 (2015).

75. Guter, W. *et al.* Current-matched triple-junction solar cell reaching 41.1% conversion efficiency under concentrated sunlight. *Appl. Phys. Lett* **94**, 223504 (2009).

76. Wang, X.-Y., Yao, X., Narita, A. & Mü, K. Heteroatom-Doped Nanographenes with Structural Precision. *Acc. Chem. Res.* **52**, 2491–2505 (2019).

77. Liu, J. *et al.* Toward Cove-Edged Low Band Gap Graphene Nanoribbons. *J. Am. Chem. Soc.* **137**, 6097–6103 (2015).

78. Wang, X.-Y., Narita, A., Zhang, W., Feng, X. & Mü, K. Synthesis of Stable Nanographenes with OBO-Doped Zigzag Edges Based on Tandem Demethylation-Electrophilic Borylation. *J. Am. Chem. Soc.* **138**, 9021–9024 (2016).

79. Collman, J. P., Boulatov, R., Sunderland, C. J. & Fu, L. Functional Analogues of Cytochrome c Oxidase, Myoglobin, and Hemoglobin. *Chem. Rev.* **104**, 561–588 (2004).

80. Beale, S. I. Enzymes of chlorophyll biosynthesis. *Photosynthesis Research* **60**, 43–73 (1999).

81. Di Natale, C., Monti, D. & Paolesse, R. Chemical sensitivity of porphyrin assemblies. *Mater. Today* **13**, 46–52 (2010).

82. Jurow, M., Schuckman, A. E., Batteas, J. D. & Drain, C. M. Porphyrins as molecular electronic components of functional devices. *Coord. Chem. Rev.* **254**, 2297–2310 (2010).

83. Moreira, L. M. *et al.* Photodynamic therapy: Porphyrins and phthalocyanines as photosensitizers. *Aust. J. Chem.* **61**, 741–754 (2008).

84. Campbell, W. M. *et al.* Highly efficient porphyrin sensitizers for dye-sensitized solar cells. *J. Phys. Chem. C* **111**, 11760–11762 (2007).

85. Barona-Castaño, J. C. *et al.* Porphyrins as catalysts in scalable organic reactions. *Molecules* **21**, (2016).

86. Zhang, S., Tang, S., Lei, J., Dong, H. & Ju, H. Functionalization of graphene nanoribbons with porphyrin for electrocatalysis and amperometric biosensing. *J. Electroanal. Chem.* **656**, 285–288 (2011).

87. Auwärter, W., Écija, D., Klappenberger, F. & Barth, J. V. Porphyrins at interfaces. *Nat. Chem.* **7**, 105–120 (2015).

88. Xie, H. *et al.* Real-Time Monitoring of Nitric Oxide at Single-Cell Level with Porphyrin-Functionalized Graphene Field-Effect Transistor Biosensor. *Anal. Chem.* **88**, 11115–11122 (2016).

89. Wu, L., Feng, L., Ren, J. & Qu, X. Electrochemical detection of dopamine using

porphyrin-functionalized graphene. *Biosens. Bioelectron.* **34**, 57–62 (2012).

90. Yokoyama, T., Yokoyama, S., Kamikado, T. & Mashiko, S. Nonplanar adsorption and orientational ordering of porphyrin molecules on Au(111). *J. Chem. Phys.* **115**, 194708 (2001).

91. Berner, N. C. *et al.* Adsorption of 5,10,15,20-tetrakis (4-bromophenyl)porphyrin on germanium(001). *Phys. Status Solidi Curr. Top. Solid State Phys.* **9**, 1404–1407 (2012).

92. Iancu, V., Deshpande, A. & Hla, S. W. Manipulating Kondo temperature via single molecule switching. *Nano Lett.* **6**, 820–823 (2006).

93. Zhu, Y., Higginbotham, A. L. & Tour, J. M. Covalent functionalization of surfactant-wrapped graphene nanoribbons. *Chem. Mater.* **21**, 5284–5291 (2009).

94. Sinitskii, A. *et al.* Kinetics of diazonium functionalization of chemically converted graphene nanoribbons. *ACS Nano* **4**, 1949–1954 (2010).

95. de Oteyza, D. G. *et al.* Substrate-Independent Growth of Atomically Precise Chiral Graphene Nanoribbons. *ACS Nano* **10**, 9000–9008 (2016).

96. Li, J. *et al.* Survival of spin state in magnetic porphyrins contacted by graphene nanoribbons. *Sci. Adv.* **4**, (2018).

97. Sedghi, G. *et al.* Comparison of the Conductance of Three Types of Porphyrin-Based Molecular Wires: *β,meso,β-* Fused Tapes, *meso* -Butadiyne-Linked and Twisted *meso-meso* Linked Oligomers. *Adv. Mater.* **24**, 653–657 (2012).

Chapter 2: Experimental Methods and Materials

All experimental results in this thesis were acquired using an ultra-highvacuum system in Dublin City University. This chapter will describe the experimental techniques of scanning tunnelling microscopy (STM) and x-ray photoelectron spectroscopy (XPS) from both a practical and theoretical point of view. The analysis of data from these techniques and the software used to do so is discussed. The materials, substrates, deposition apparatus, and preparation procedures are discussed as well as brief introduction to vacuum technology.

2.1 Omicron Ultra-High Vacuum System

Ultra-high vacuum (UHV) systems operate in the of 10^{-9} to 10^{-11} mbar pressure regime. A UHV system provides the necessary conditions to operate scanning tunnelling microscopy (STM) and x-ray photoelectron spectroscopy experiments (XPS). UHV are also needed to maintain a contaminant free environment for surface science studies. The system used in this thesis is an Omicron UHV system. The technical drawings and labelled photographs of the system are shown in figures 2.1 and 2.2 respectively [1].

The two main components of the system are the analysis chamber (1) and the preparation chamber (2). The analysis chamber contains the scanning tunnelling microscope, the x-ray source, and the hemispherical analyser of the XPS system. The base pressure of the analysis chamber is approximately $1\text{x}10^{-10}$ mbar, maintained by a 45 Litres/sec (L/s) ion-pump in conjunction with a titanium sublimation pump (TSP) (10). The preparation chamber has four ports for holding home-made cells for evaporating molecules on to substrates and an argon gun for cleaning crystals. The preparation chamber uses a 30 L/s ion-pump and TSP to maintain a base pressure of $2.3\text{x}10^{-9}$ mbar.The fast entry load-lock (3) is connected to a rotary pump and a turbo molecular pump (9) via the angle valve (8). The load-lock is separated from the pumping system by thepneumatic gate valve (6) and from the preparation chamber by the manual gate valve(7). The samples and STM tips are moved from load-lock to the preparation chamber and from here to the analysis chamber by two separate magnetic drives (13). Each chamber has a multi-axis manipulator (11) with filaments for sample heating and thermocouples mounted into the stages. The analysis chamber has a wobble stick (12) for loading and unloading samples and tips from the manipulator into the STM tip assembly. All the mentioned apparatus is held on a frame (5) with built-in heaters (14) for baking for when the UHV system is exposed to contaminants.

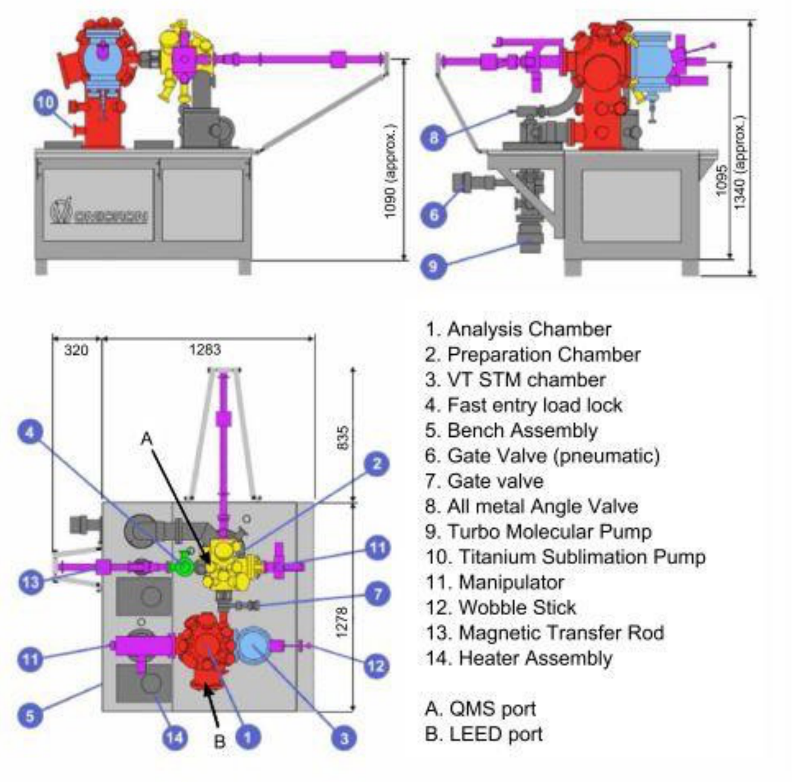

Figure 2.1*: Omicron UHV system. Side and top views of the vacuum system from the OEM manual* [2]*. The numbered areas correspond to the parts discussed in the body of the text*

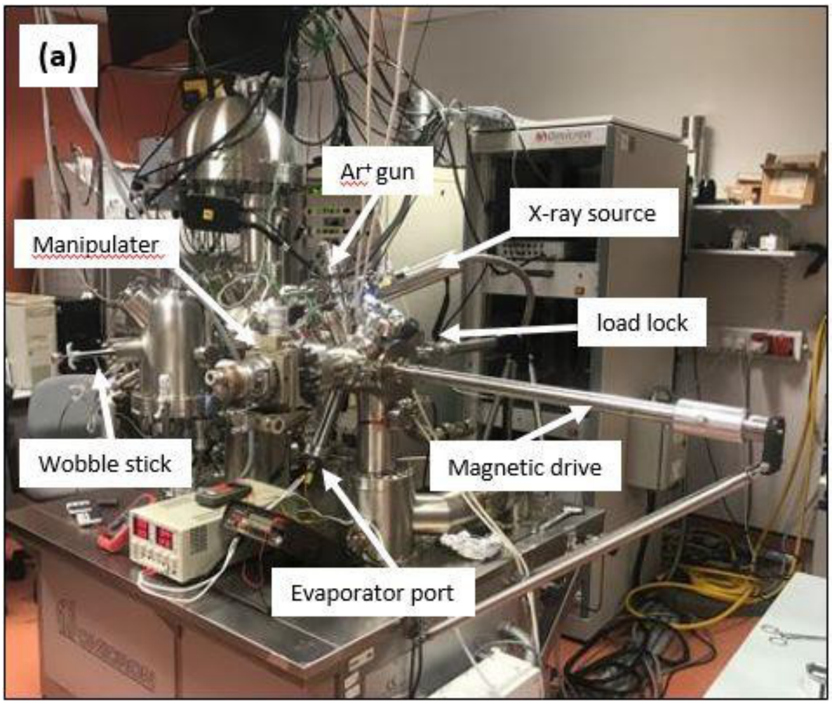

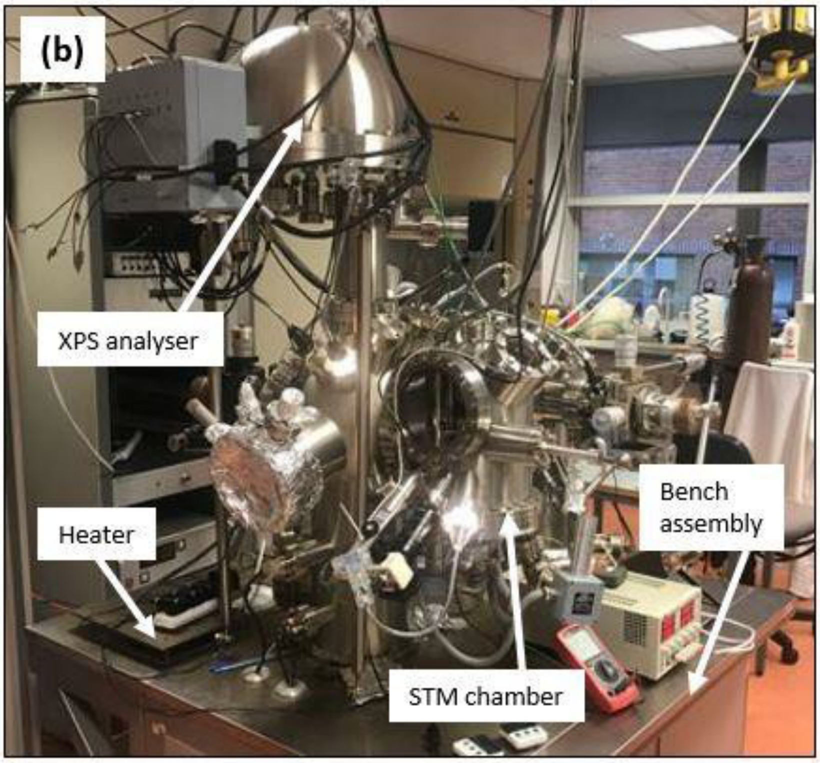

Figure 2.2*: UHV System (a) Photograph of the preparation chamber (b) Photograph of analysis chamber*

Controls for the vacuum pumps, gate valves and argon sputter gun are housed on a rack adjacent to the UHV system. The UHV system was modified by placing a spacer on the XPS lens stack to allow for more efficient sample transfer. This has an effect on the resolution of the XPS spectra as the sample could no longer be placed in the focal plane of the XPS lens.

2.1.1 Vacuum Pumps

Four types of pumps are necessary for the UHV system to operate. The rotary and turbo molecular pumps are mechanical pumps and in general, work by moving a rotating vein about a cavity. The rotary pump can create a vacuum of 10^{-2} mbar. The turbo molecular pump has a similar mode of operation, though there are many variations. This pump has many rotating veins arranged to form a turbine rotating at higher speeds thus producing a greater vacuum in the region of $10^{-7} – 10^{-8}$ mbar.

The titanium sublimation pump (TSP) uses resistive heating of a titanium alloy filament to sublimate titanium on to the walls of the chamber. Gases in the chamber are then chemisorbed onto the film creating low vapor pressure compounds [3]. TSPs are not run continuously but on a timer or after molecule depositions. The TSPs are not run while the sample crystal is in the chamber as it can contaminate the crystal.

Ion pumps consist of two parallel cathodes with cylindrical anodes in-between them. The electrodes are in a large magnetic field (~0.1 T) from permanent magnets. A large voltage of 3-7 kV is applied to the electrodes. Free electrons are attracted to the anode and get trapped in the magnetic field. They rotate about the magnetic field until they collide with a gas molecule, thereby ionizing the molecule which is then accelerated toward the Ti cathode [3]. The ions are implanted into the cathode and sputter Ti onto the surfaces of the pump/chamber trapping additional gas molecules much like the TSP.

2.2 Scanning Tunnelling Microscopy

The scanning tunnelling microscope (STM) was developed by Gerd Binning and Heinrich Rohrer at IBM [4]. They were awarded the Nobel Prize in Physics in 1986 for its invention. The STM is capable of imaging topographical details with atomic resolution. The basic operation of the STM is straightforward; a voltage is placed across a metallic tip and a conducting sample separated by several angstroms resulting in electrons quantum mechanical tunnelling between filled electronic states in the tip and empty states in the sample, or vice-versa depending on the bias direction [5]. The tip-sample distance is maintained by means of a feedback loop which in turns is used to provide topographical measurements. An Omicron variable temperature STM was used in this work.

2.2.1 Theory of Scanning Tunnelling Microscopy

For quantum mechanical tunnelling to occur three criteria must be meet; a distance of ~1 nm or less between the STM tip and sample, empty states for electrons to tunnel into and filled states for electrons to tunnel out of, and a finite potential barrier for electrons to tunnel through. This potential barrier is provided by the vacuum gap between the tip and sample. In reality the STM tip and sample is a three-dimensional system, however Tersoff and Hamann demonstrated that solving the Schrödinger equation for a one-dimensional case using some approximations[2] is sufficient to model the tip-sample interaction [6]. For a one-dimensional case, if an electron with mass m and energy E, experiences a potential U as a function of distance z, it can be described by the Schrödinger equation as follows

$$-\frac{\hbar^2}{2m}\frac{d^2}{dz^2}\Psi(z)+U(z)\Psi(z)=E\Psi(z) \tag{2.1}$$

where $\Psi(z)$ is the electron wave function and $\hbar = h/2\pi$ and h is the Planck constant.

---

[2] Approximations: Tip modelled as a spherical potential well. Work function of tip equal to that of the surface. Model neglects any non-perpendicular tunnelling between surface and tip

The simple one-dimension model of two classically allowed regions separated by a potential barrier *d* as shown in figure 2.3

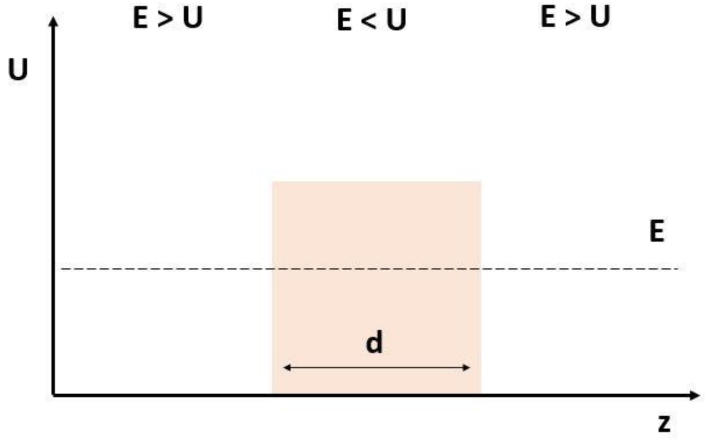

***Figure 2.3**: 1-D model of potential barrier*

The solutions to the Schrödinger equation in the $E > U$ regions take the form

$$\Psi(z) = \Psi(0)\, e^{\pm ikz} \tag{2.2}$$

where

$$k = \frac{\sqrt{2m(E-U)}}{\hbar} \tag{2.3}$$

This represents a standing wave. In the classically forbidden regions, $E < U$, the solutions to the Schrödinger equation are of the form

$$\Psi(z) = \Psi(0)\, e^{\pm \alpha z} \tag{2.4}$$

where

$$\alpha = \frac{\sqrt{2m(U-E)}}{\hbar} \tag{2.5}$$

This is known as the decay constant. The solution in the - z direction describes the electron wavefunction decaying exponentially into the barrier region as in equation 2.6, while the solution in the + z direction represents a travelling wave in the tip (or sample).

$$\Psi(z) = \Psi(0)\, e^{-\alpha z} \tag{2.6}$$

Equation 2.6 allows electrons to tunnel from one classically allowed region to the other through the barrier on the condition the barrier is sufficiently narrow [7]. The square of the wavefunction gives the probability density of an electron occupying a certain region in space. Therefore, the probability, P of an electron tunnelling through the barrier is proportional to the square of the wavefunction in equation 2.6.

$$P \propto |\, \Psi(0)\, |^2 e^{-2\alpha z} \tag{2.7}$$

By extending this one-dimensional model to that of the STM tip and sample surface, the tunnel current I is related exponentially to the vacuum gap d.

$$I \propto e^{-2\alpha d} \tag{2.8}$$

The tunnel current changes by an order of magnitude for every angstrom change in tip-sample separation [8]. Conversely, in order to maintain a constant current betweentip and sample, d varies on the order of picometers [9]. This sensitivity to tip-sample separation is what enables the STM to produce images of surfaces with atomic resolution.

A true description of electron tunnelling requires full knowledge of the filled and unfilled electronic states in the tip and the sample. Tersoff and Hamann simplified this interaction by modelling the tip as a point source of current [8]. In addition to the tip-sample separation they found the tunnel current was dependent on the local density of states (LDOS) of the sample, ρ at the Fermi level, E_F measured at a given tip position r_t such that

$$I \propto \rho(r_t, E_F) \tag{2.9}$$

In figure 2.4 an electron tunnels from the tip through the vacuum gap of width d to the sample. The work function, Φ is defined as the minimum energy required to excite an electron to the vacuum level. The work function of the tip and sample are assumed to be equal. In relation to the vacuum level the Fermi level, $E_F = -\Phi$. When the tip and sample are grounded the Fermi levels are aligned and there is no tunnel current. However, by negatively biasing the tip, the E_F of the tip shifts relative to the E_F of the sample by eV as shown in figure 2.4. Electrons in the tip with energies between $E_{F\ tip}$ and $E_{F\ tip} - eV$ can tunnel into empty states in the sample between $E_{F\ sample}$ and $E_{F\ sample} + eV$. Reversing the bias shifts the $E_{F\ tip}$ to a lower energy relative to the $E_{F\ sample}$ and allow for electrons to tunnel from the sample into the tip.

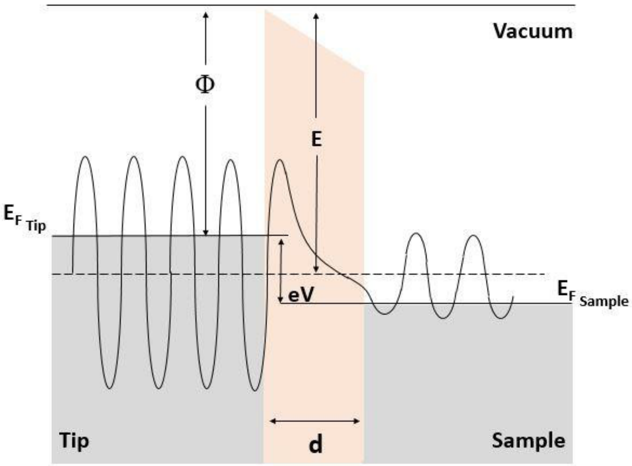

***Figure 2.4**: Schematic of electron tunnelling from tip to sample.*

2.2.2 Operation of STM

The STM tip is mounted on a three-axis piezo tube scanner. The tip is scanned across the surface in the x-y plane. Topographical information can be collected in two modes: constant height mode and constant current mode. In constant height mode the tip-sample separation is fixed and the tunnel current is measured as the tip scans. This mode runs the risk of colliding the tip with protruding features on the surface. To avoid this, all STM experiments were conducted in constant current mode. By using a feedback loop to maintain a constant tunnel current between tip and sample, topographical information of the surface can be revealed by measuring the adjustments to the piezo in the z- direction. The feedback electronics are provided in the Omicron VT controller unit and SCALA software. The basic STM setup is shown in figure 2.5.

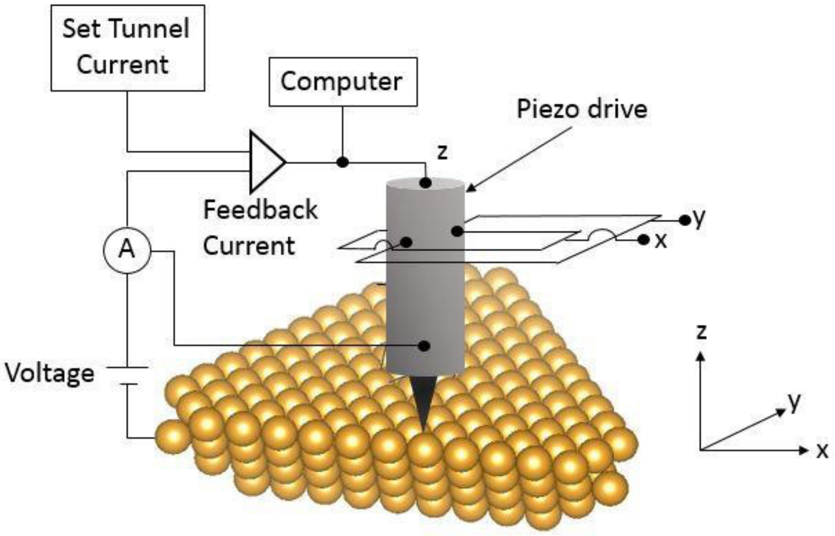

Figure 2.5: *Diagram of STM setup*

STMs typically have lateral resolution of <10 Å and vertical resolution of 0.01 Å [8]. To achieve atomic resolution tip-sample separation must be of the order of 0.1 Å. It is therefore necessary to remove external vibrations from affecting the tip- sample separation. In the experimental apparatus the STM tip and sample holder assembly are suspended from the STM chamber by metal springs. A magnetic eddy current damping system is used to further reduce oscillations from the metal springs [7].

The preparation of STM tips is vital as the tip geometry plays an important role in image resolution. The tip should come to a fine point to approximate Tersoff and Hamann model [9]. Blunt or double ended tips can result in false imaging [10]. The tips in this work were prepared using an electrochemical etch process using an Omicron Tip Etching Kit [11]. To make the tips, 7 mm of 0.15 mm diameter tungsten wire is cut and inserted into STM tip holder. The tip holder is mounted onto a variable height retort stand. The wire is lowered in a 2.5 molar sodium hydroxide (NaOH) solution such that 2 mm of the wire are immersed in the liquid. The wire is surrounded by a stainless-steel ring also submerged in the solution. The etching process begins by biasing the stainless-steel ring with 6 V with respect to the wire. The tungsten wire is etched at the meniscus and after several minutes the submerged part of the wire breaks off due to its weight, leaving a sharp point on the remaining piece of tungsten wire that will be used as the tip. The tip is removed from the NaOH solution and rinsed several times in deionised water before being placed in an Omicron sample holder and loaded into the fast entry load lock. The tip is conditioned on a clean Au(110) surface. This involves applying 5 V and 10 V pulses to the tip using the Nanostructuring feature of the SCALA PRO 5.0 software to remove any contaminates. The tip can also be conditioned by operating it at relatively high currents ~5 nA at 1 V for extended periods of time, typically 30 minutes.

2.2.3 STM Data Analysis with WSxM Software

All STM images were acquired at room temperature. STM images were analysed using the scanning probe microscopy image analysis software, WSxM [12]. For illustrative purposes images are visually enhanced by plane subtraction and contrast adjustment to highlight features within the image. In figure 2.6 molecules of Perylenetetracarboxylic dianhydride are deposited on the Au(111) crystal. Figure 2.6 shows the STM image of the individual molecules as acquired without image enhancement. In figure 2.6 (b) the image is adjusted by increasing the contrast between height positions of the STM tip. The individual PTCDA molecules are still clearly identifiable but now the Au(111) surface reconstruction underneath the molecules is also visible. The Au(111) surface reconstruction is discussed in more detail in section 2.4.

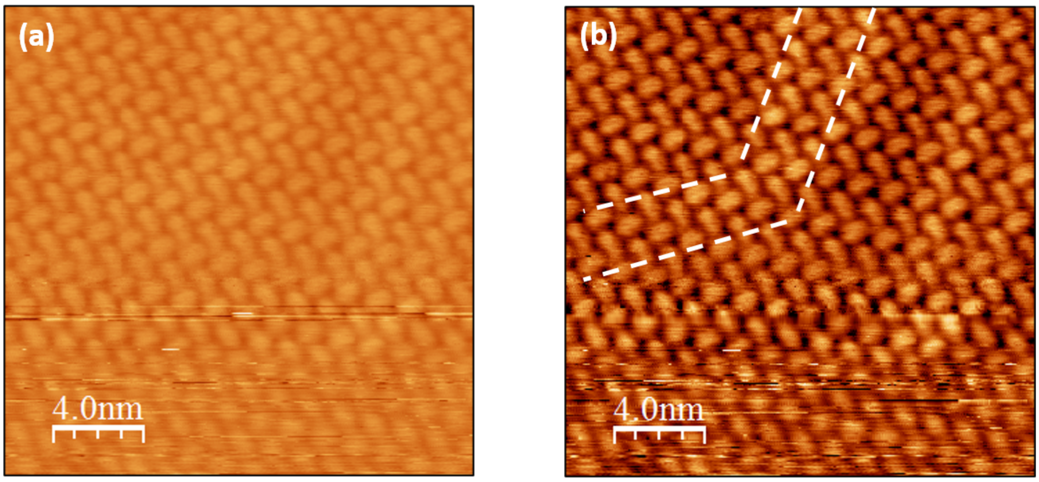

***Figure 2.6**: PTCDA molecules on Au(111) (a) 20 nm × 20 nm STM image of PTCDA molecules on Au(111) (b) Contrast enhancement of (a) shows visible reconstruction (dashed line as guide). V =0.1 V, I = 0.2 nA.*

For images with periodic features the Fast Fourier Transform (FFT) function is used to convert an image from real-space to reciprocal-space allowing for lattice parameters and distances to be measured. This function takes the FFT of every line in the image to produce the reciprocal space image. A 10 nm × 10 nm STM image of the highlyordered pyrolytic graphite (HOPG) surface is shown in figure 2.7(a), which has a hexagonal lattice. The FFT of 2.7(a) is shown in figure 2.7(b). The reciprocal lattice of a hexagonal lattice is also a hexagonal lattice. The lattice parameter of graphite can be measured from the power spectral density (PSD) plot of the FFT image. The PSD plot is shown in figure 2.8 and the reciprocal lattice parameter of 0.44 Å^{-1} equates to a lattice parameter in real-space of 0.24 nm, which is consistent with the literature [13].

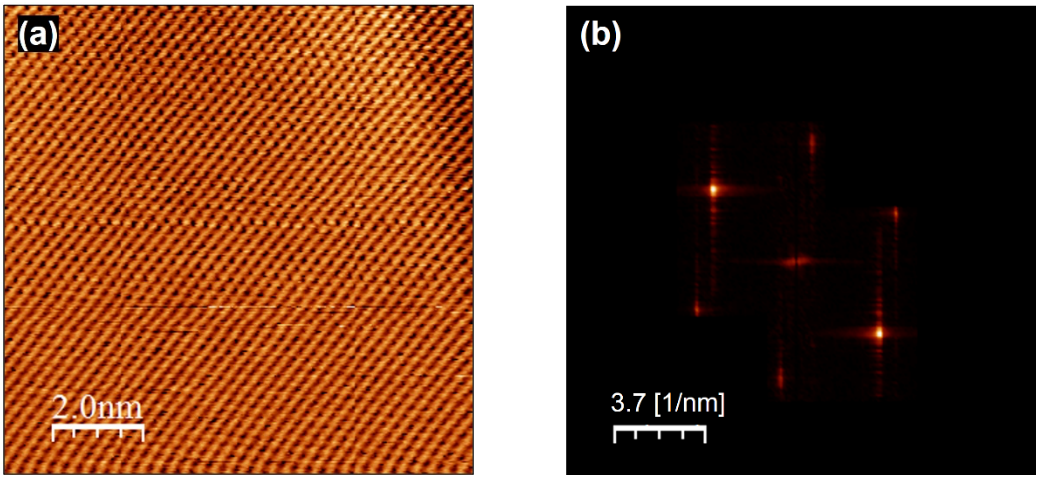

Figure 2.7: *STM and FFT of HOPG (a) 10 nm × 10 nm of graphite, V=1.0 V; I=1.0 nA (b) FFT of (a) shows hexagonal reciprocal lattice.*

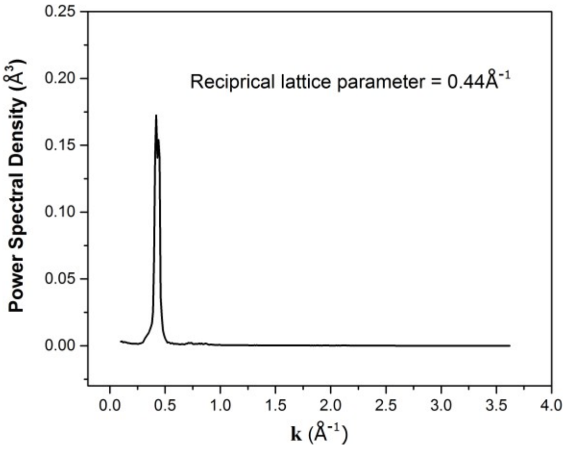

Figure 2.8*: Power Spectral Density of FFT of HOPG.*

WSxM features a line profile tool which is used for measuring distances and heights and depths of protrusions in acquired images. Figure 2.9 shows an STM image of polymer chains formed from 10,10'-Dibromo-9,9'-bianthracene (DBBA) with protruding anthracene units. The line profile in figure 2.10 shows the distance between adjacent anthracene units to be 0.95 nm.

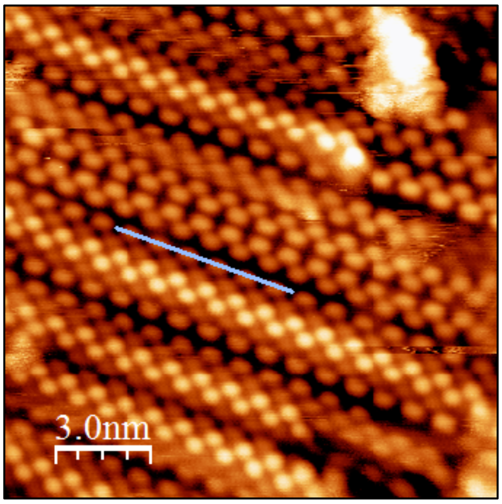

Figure 2.9: *Polymer chains of DBBA molecules. Line profile taken over anthracene segments*

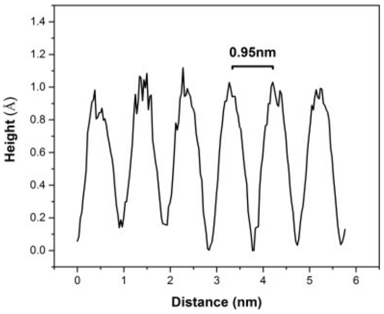

Figure 2.10: *Height and distance of DBBA protrusions. Distance between segments is approximately 0.95 nm*

The flooding tool feature on WSxM is used to estimate the surface coverage of deposited material. The image processor finds low lying areas called holes which correspond to the surface or topographical hills which correspond to adsorbents. Images can be filtered by adjusting the minimum size area (in nm^2), the minimum height of features when finding the area of holes and the maximum height of adsorbents when finding the area covered by material. Figure 2.11 (a) shows functionalised porphyrinGNRs on the Au(111) surface. Figure 2.11 (b) shows the area of the image corresponding to the structures while figure 2.11 (c) shows the area of the bare gold surface. Taking both areas of hills and holes is used to estimate the surface coverage.In the example given the area of material is 0.46 ML ±0.04 ML and the area of the surface is 0.52 ML ±0.04 ML.

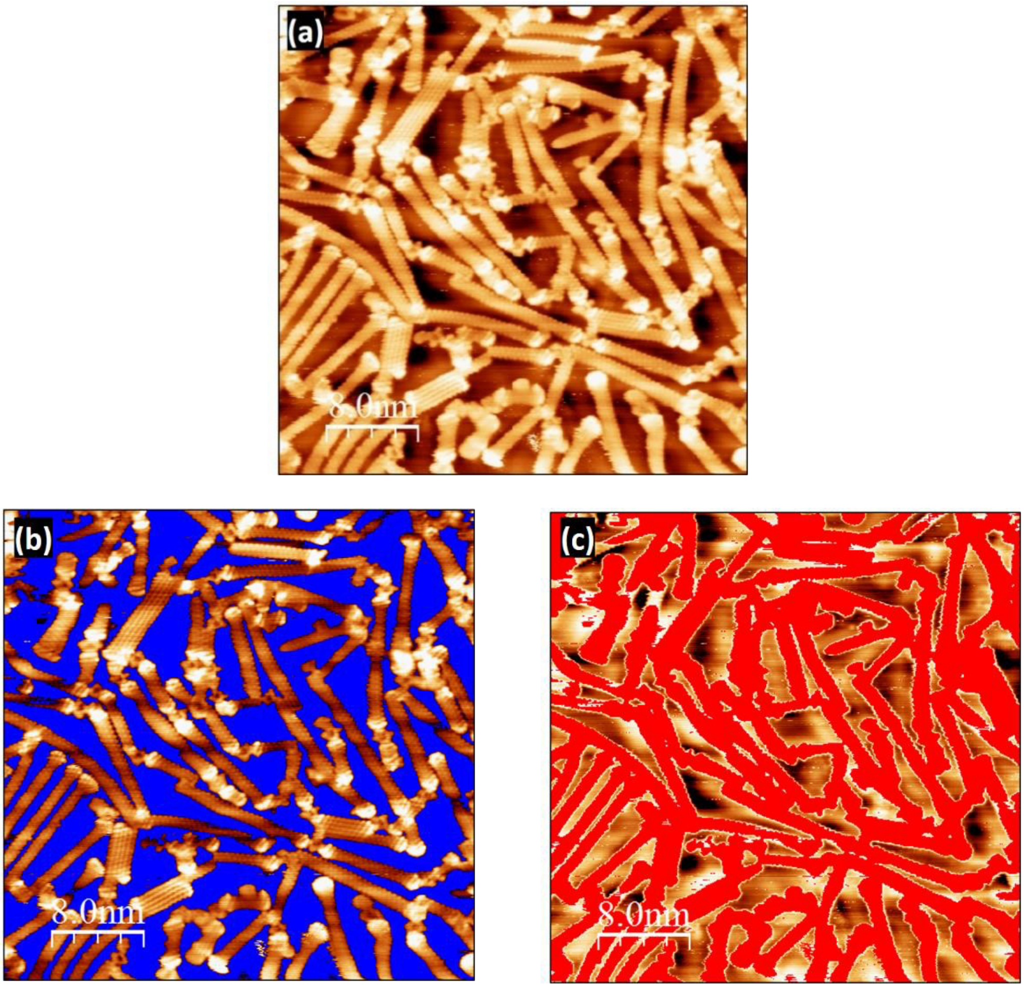

Figure 2.11*: Flooding tool for surface coverage estimates. (a) 40 nm × 40 nm image of Por/7-AGNR on Au(111) (b) Flooding tool for finding hills. (c) Floodingtool for finding holes. (All images acquired at V=0.03 V, I=3.66 nA)*

2.3 X-Ray Photoelectron Spectroscopy

X-ray photoelectron spectroscopy (XPS) is a non-local experimental technique that provides information on the elemental composition and chemical environment of elements within the surface of a sample. XPS utilises the photoelectric effect whereby electrons are emitted from a surface upon irradiation with x-rays. Hertz, Planck and Einstein were all responsible for developments in the underlying physical principles of the photoelectric effect, for which Einstein was awarded the Nobel Prize in physics in 1921. XPS began to be used as an analytical tool from the 1950s onwards thanks in part to improved vacuum systems and instrumentation developed by Kai Siegbahn earning him the Nobel Prize in physics in 1981.

X-ray photoelectron spectroscopy has a wide range of applications. In this thesis XPS is used and to characterise the chemical state of polymers, nanoribbons and functionalised GNRs and to verify molecular deposition and estimate surface coverage. This section discusses the theoretical and instrumental considerations necessary for XPS experiments and XPS data analysis methods.

2.3.1 Theory of XPS

When matter is irradiated with x-rays the photon energy can be transferred to an electron. If the energy of the x-ray is greater than the binding energy (E_B) of the electron in the solid, the electron will be emitted from the solid with a kinetic energy (E_K) relative to the vacuum level such that

$$E_K = hv - E_B - \Phi_s \tag{2.10}$$

where h is the Planck constant, ν is the photon frequency (in Hz) and Φ_S is the work function of the sample (in eV). The work function is the amount of energy needed to excite an electron from the Fermi level (E_F) to the vacuum level (i.e. $E_K = 0$ eV). The process is illustrated in figure 2.12 which also shows the binding energy spectrum of emitted photoelectrons (PE) from the valence band, core levels and secondary photoelectrons.

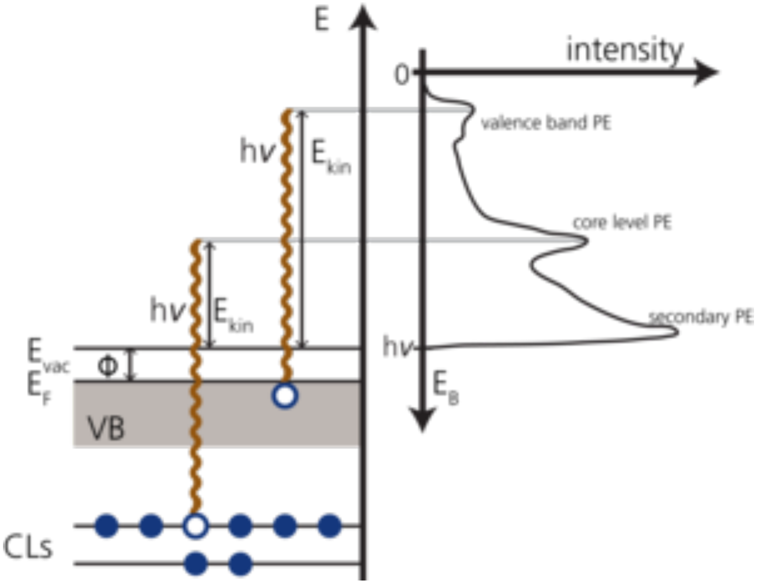

***Figure 2.12**: The Photoelectric effect. Incoming photons (hv) ejecting electrons from a core levels (CLs) and the valence band (VB) with kinetic energy with respect to the vacuum level (Evac)* [14]

In the XPS system the sample and the spectrometer share a common ground, as shownin figure 2.13, the work function in equation 2.10 is no longer the work function of the sample but now that of the spectrometer, $\Phi_{Sp,}$ such that,

$$E_B = hv - E_K - \Phi_{sp} \tag{2.11}$$

It is the work function of the spectrometer that is necessary for calculating the binding energy of electrons. The work function of the spectrometer is calibrated by the system manufacturer using a clean gold sample by aligning the Fermi Level to 0eV and the Au $4f_{7/2}$ binding energy to 83.96 eV. For a known photon energy and Φ_{Sp} and by measuring the E_K of emitted electron the binding energy of a core level electron can be calculated using equation 2.11

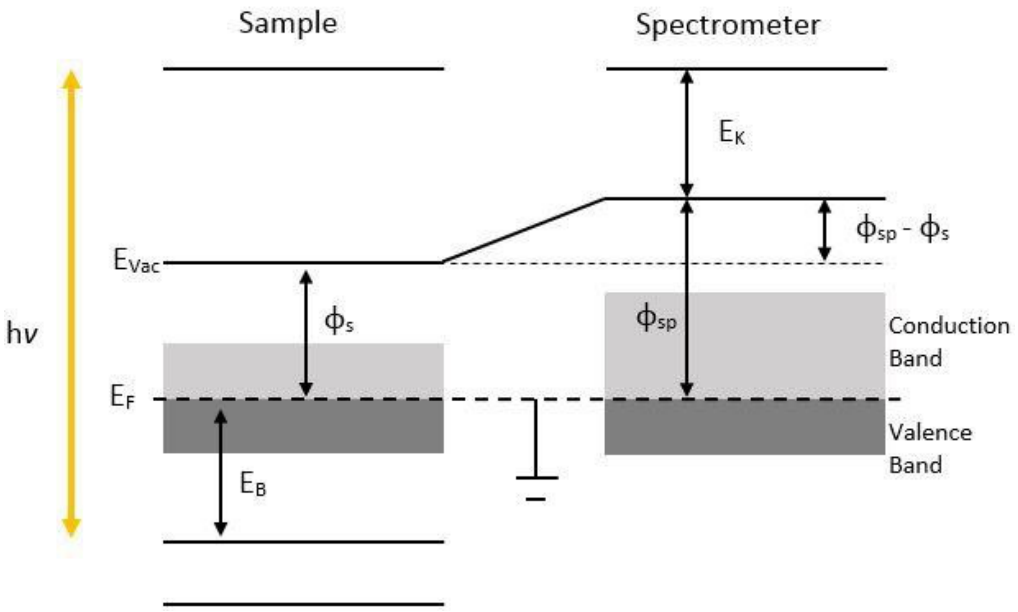

***Figure 2.13**: Schematic of photoelectric process in XPS system.*

This photoelectric effect model is based on Koopman's Theorem which assumes that the binding energy of the electron is the difference between the initial and the final energy states of the electron [3]. Koopman's theorem neglects to take into consideration the rearrangement of electrons in the sample following photoemission and relativistic effects. However, both effects are typically very small and their contribution to the measured binding energy is negligible and can be ignored. A model based on a core-hole and electron pair provides a more accurate description of the photoelectric process, however the single electron model presented here is adequate for analysing the data presented in this thesis.

2.3.1.1 XPS surface sensitivity

A major factor for the use of XPS to study nanoscale structures is due to the surface sensitivity of the technique. X-ray sources in typical XPS systems generate photons with energies of 1253.6 eV for the Mg Kα and 1486.6 eV for the Al Kα anodes, respectively. X-rays with this wavelength penetrate hundreds of nanometres into the surface. However, the escape depth for electrons at these energies is considerably less (~10 nm) due to photoelectrons losing kinetic energy via inelastic collisions with atomic nuclei. The escape depth of photoelectrons is determined by the inelastic mean free path (IMFP). The IMFP, λ, is the average distance an electron travels between collisions and is dependent on the kinetic energy of electrons and the composition of the surface [14]. The IMFP for several elements as a function of electron energy is shown in the universal mean free path curve in figure 2.14. This curve shows the IMFP is approximately 1.5-2.0 nm for electrons with kinetic energy of the order of 1 keV.

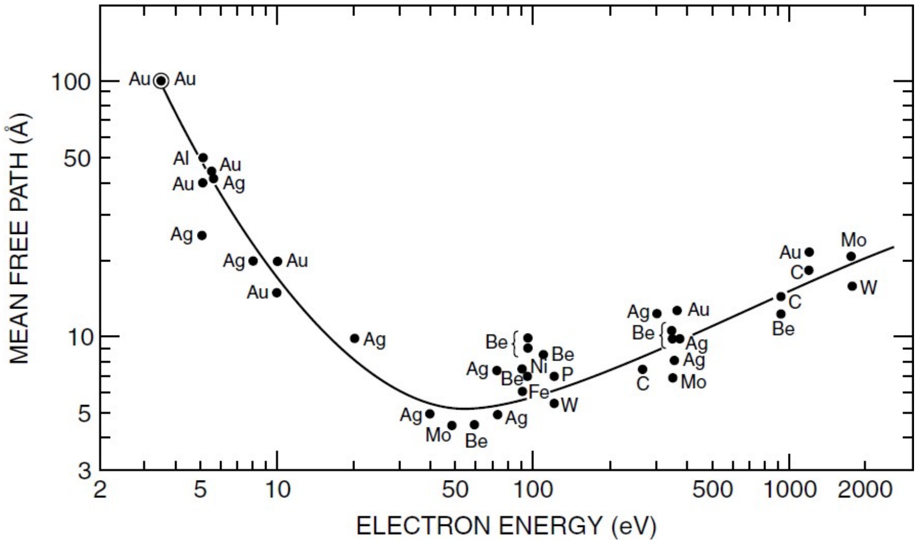

Figure 2.14: *Universal mean free path curve* [15]

From this empirical data, the IMFP can be approximated using the equation 2.12

$$\lambda = \frac{143}{E^2} + 0.054\sqrt{E} \tag{2.12}$$

where E is the energy of the electron.

The probability of a photoelectron exiting a sample can be calculated by the following equation

$$P(d) = e^{-\frac{d}{\lambda}} \tag{2.13}$$

where d is the distance travelled by an electron in a solid in nm. As d increases the probability of a photoelectron exiting the surface reduces. 68% of photoelectrons that enter the XPS analyser originate within a depth of 1 λ of the sample surface i.e do not undergo energy lose collisions. As such, these electrons form sharp, well-defined peaks in the XPS spectra and provide binding energy information of the chemical state. The remaining 32% of photoelectrons that enter the XPS detector are scattered electrons and contribute to the background signal. From the universal mean free path curve, the sampling depth for carbon and gold is between 2-5 nm approximately, highlighting the surface sensitivity of XPS.

2.3.2 XPS Spectral Features

The XPS spectra contains many features and understanding the nature of these features is important for accurately determining the chemical composition and chemical environment of samples. In order to correctly interpret XPS data, curve fitting of peaks and appropriate background subtraction is required. XPS data analysis is discussed in section 2.3.3. Herein, the main spectral features are discussed.

2.3.2.1 Survey Scans

When undertaking an XPS experiment a survey or wide scan, typically within an electron binding energy range of 0 to 800 eV – 1,200 eV is taken to ascertain the composition of the sample. In figure 2.15, a survey scan of a gold sample mounted on a tantalum holder is presented. It is convention to label the x-axis from high to low binding energy. The y-axis is the number of detected photoelectrons, shown here as total counts although counts per second is often used. The binding energy position of the peaks is referenced to values in the Handbook of X-ray Photoelectron

Spectroscopy by Moulder *et al.* [16] which contains XPS data for all elements from lithium to uranium including Auger electron data, which will be discussed further in this section. The spectrum is comprised mostly of photoemission lines from core levels of gold and tantalum with the presence of carbon and oxygen evident and labelled accordingly. For more detailed spectra narrow scans of photoemission lines are acquired.

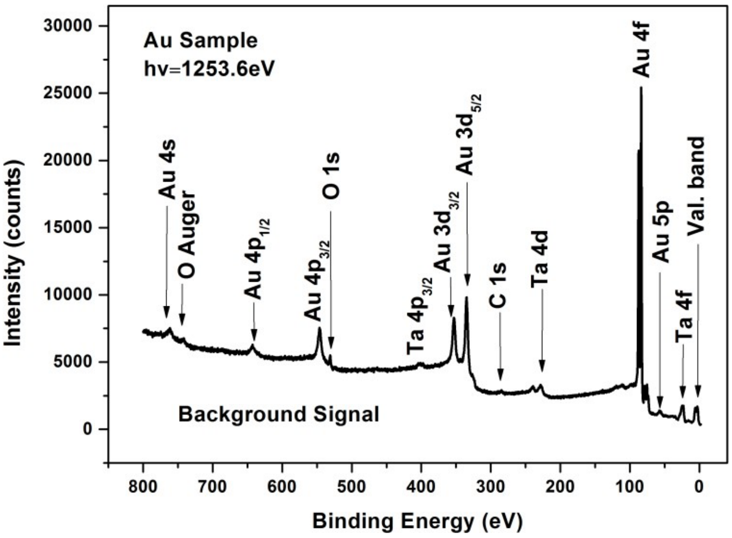

***Figure 2.15**: Survey scan of Au sample.*

2.3.2.2 Photoemission lines

Core level electrons in the *s* orbital, where the orbital angular momentum *l* is equal to zero, have one peak in the XPS spectrum as seen for the O 1s in figure 2.16. For electrons in core levels with orbital angular momentum greater than zero (i.e. the *p, d* and *f* orbitals), the electron spin, m_s ($m_s = \pm½$) can couple with the orbital angularmomentum resulting in two energetically separated energy levels with $j = l + m_s$ and thus two corresponding peaks in the spectrum. This is known as spin-orbit splitting or *j-j* coupling. Each state has a degeneracy of $2j + 1$ and the ratio of the number of electrons in one state to another determines the relative areas of peaks in a spin-orbit doublet. For example, in the *p* orbitals, *j* is equal to $^1/_2$ or $^3/_2$ resulting in a

1:2 ratio between the area of the $p_{1/2}$ and $p_{3/2}$ components of the spin-orbit pair. Figure 2.17 shows the titanium 2*p* spin-orbit pair with a spin-orbit splitting of 5.5 eV taken from a TiO_2 sample. Subsequently, the ratios between spin-orbit pairs in *d* and *f* orbitals is 2:3 and 3:4, respectively. The binding energy separation of spin-orbit pairs can vary slightly depending on the chemical environment however the ratio of the areasbetween spin-orbit pairs remains fixed.

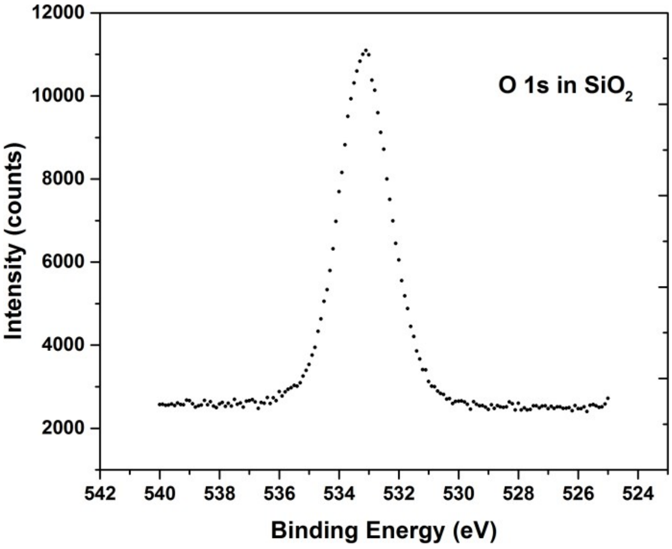

Figure 2.16: *O 1s photoemission line in* SiO_2 *has a binding energy of 531.9 eV*

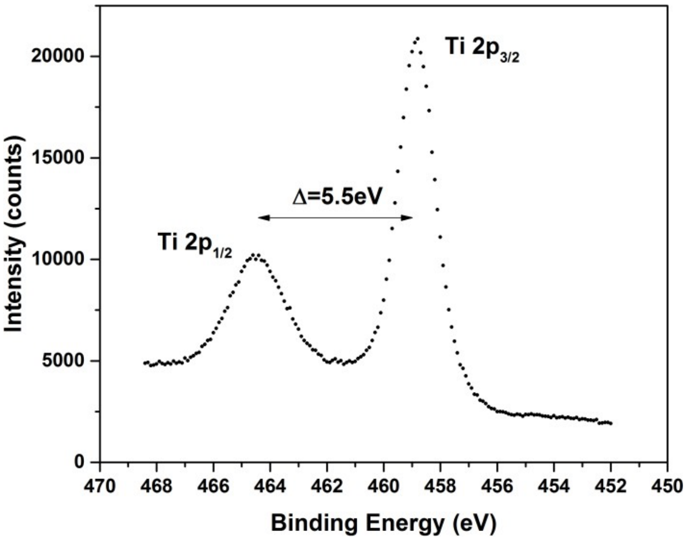

Figure 2.17: *Ti* $2p_{3/2}$ *and Ti* $2p_{1/2}$ *peaks from a* TiO_2 *sample have binding energy of 458.8 eV and 464.3 eV with spin-orbit splitting of 5.5 eV.*

2.3.2.3 Chemical shifts

In addition to identifying elements within a sample it is necessary to determine the chemical environment of elements. In compounds and molecules electrons are shared between atoms forming chemical bonds. The binding energy of an electron in an atom is dependent on the electronegativity of the element the atom is bonded to and the strength of the bond; single, double or triple bond. Electronegativity χ, is an empirical value of the tendency of an atom to attract electrons. Electronegativity affects the electron density around atoms resulting in a chemical shift of the binding energy of electrons. The greater the difference in electronegativity between two bonding atoms the greater the shift of binding energy. This will be described using the Mo *3d* and the S 2*s* photoemission lines in the clean and oxidised MoS_2 spectra in figure 2.18. For homogenous molybdenum, the 3*d* spin-orbit pair have a binding energy at 228 eV with spin-orbit splitting of 3.1 eV. However, in MoS_2 each molybdenum atom bonds with four sulfur atoms. Sulfur has an electronegativity of 2.58 compared to 2.16of molybdenum which leads to a higher charge density around the sulfur atoms. Withlower electron density surrounding the Mo atoms, photoelectrons must overcome a greater potential to reach the vacuum level. Thus, photoelectrons are emitted from the Mo 3*d* orbital in MoS_2 with lower kinetic energy resulting in ~1 eV shift to higher binding energy from 228 eV to 229 eV as seen in the clean MoS_2 spectrum in figure 2.18. Conversely, the 2*s* sulfur peak shifts by 1.6 eV from 228.0 eV in homogenous sulfur to 226.2 eV in MoS_2.

Oxygen is one of the most electronegative elements, $\chi = 3.44$. When MoS_2 is exposed to atomic oxygen molybdenum readily oxidises while sulfur does not. Mo now exists in two chemical environments; Mo bonded to S and Mo bonded to O. The Mo-S bonds have previously been discussed. Photoelectrons from molybdenum oxide however are chemically shifted to higher binding energy. In the oxidised MoS_2 spectra in figure 2.18, the 3*d* doublet from Mo-S bonds are present together with another doublet from the Mo atoms bonded to O. The evidence for molybdenum oxidation appears as an increase in the height of the Mo $3d_{3/2}$ peak and the presence of an additional peak at 235.6 eV. The spin orbit splitting of 3.1 eV for the Mo 3*d* doublet remains the same in both chemical environments. The values for electronegativity are compiled in Lange's Handbook of Chemistry [17].

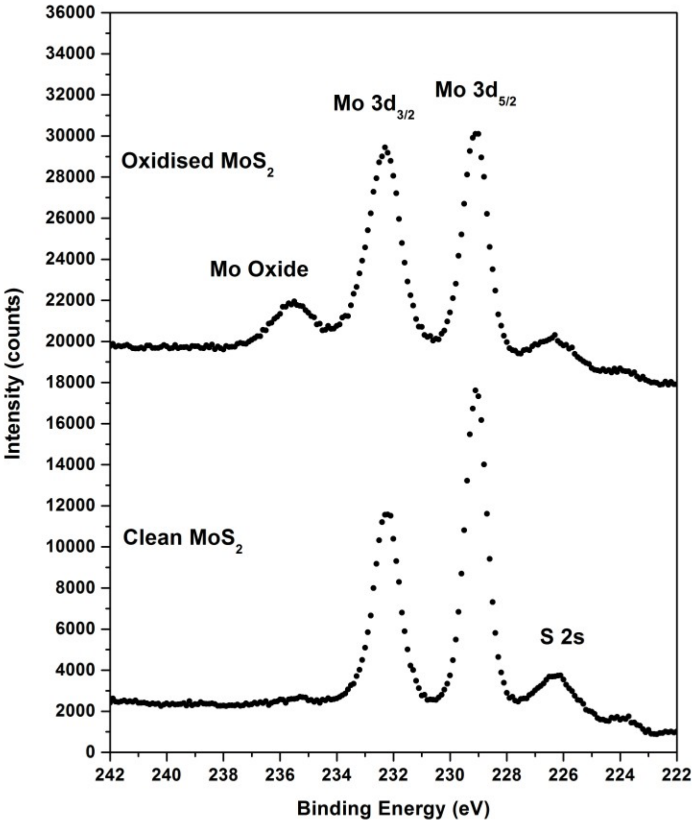

***Figure 2.18**: Clean MoS_2 and oxidised MoS_2. Mo $3d_{5/2}$ and $3d_{3/2}$ present at 229.0 eV and 232.1 eV, respectively and S 2s at 226 eV. The oxidised MoS_2 has an additional doublet peak attributed to Mo bonded to O at 232.5 eV and 235.6 eV*

2.3.2.4 Auger Electrons

Auger electrons also generate sharp photoemission peaks in the XPS spectra. Auger lines are a result of multi-electron and photon interactions. When an x-ray ionises a core level electron emitting it from the atom a core-hole is created. The core-hole is then filled by an electron from a higher energy level. The transition between energy levels releases energy which can ionise an electron in the same atom, emitting it from the sample. Unlike photoemission lines, Auger lines are independent of x-ray source. Therefore, when changing between Mg and Al x-ray sources, Auger lines will remain at the same binding energy position while photoemission lines will change allowing Auger lines to be readily identified. Auger electron spectroscopy is a powerful analytical tool and although it is not utilised in this work it is important to identify Auger lines in the XPS spectra to avoid confusion with photoelectron lines.

2.3.2.5 Other Spectral Features

Photoelectrons that undergo inelastic scattering can couple with bulk or surface plasmons resulting in minor peaks at higher binding energy (lower kinetic energy) to the photoemission line creating what are known as plasmon peaks. These are often much weaker in intensity to photoemission and Auger lines.

As mentioned previously the single electron model is adequate for interpreting most XPS data. However, certain spectral features arise from core-level and outer shell electron pair coupling and from energy transfer between photoelectrons and valence electrons. Multiplet splitting or electrostatic splitting arises following photo-ionisation when the core level electron couples with unpaired electrons in the outer shell which can create several final states resulting in multiple peaks in the spectra.

Shake-up satellite peaks occur when photoelectrons lose kinetic energy due to collision with valence electrons, exciting the valence electron to an unoccupied orbital. Unlike typical energy loss collisions that contribute to the continuous background signal, shake-up satellites peaks have energy losses equivalent to specific energy transitions.

All spectral features discussed thus far are due to photoelectrons leaving the sample however certain peaks are a result of the x-ray source itself. The XPS system used in this thesis is equipped with two anodes for generating x-rays; a magnesium and aluminium anode. X-ray generation is discussed in more detail in section 2.3.4. Non-monochromatic x-ray sources produce characteristic $K\alpha_{1,2}$ x-rays and a number of smaller intensity x-rays with higher photon energy. These higher energy photons give rise to satellite peaks at lower binding energy relative to the main photoemission peak with a spacing and intensity characteristic of the x-ray source photon energy as shown in table 2.1. The satellite peaks of Au 4*f* associated with Kα_3 and Kα_4 are shown in figure 2.19.

Table 2.1: *Energy displacement and relative height with respect to photoemissionlines for Mg and Al anodes*

	$\alpha_{1,2}$	α_3	α_4	α_5	α_6	β
Mg Displacement (eV)		8.4	10.1	17.6	20.6	48.7
Relative Height	100	8.0	4.1	0.6	0.5	0.5
Al Displacement (eV)		9.8	11.8	20.1	23.4	69.7
Relative Height	100	6.4	3.2	0.4	0.3	0.6

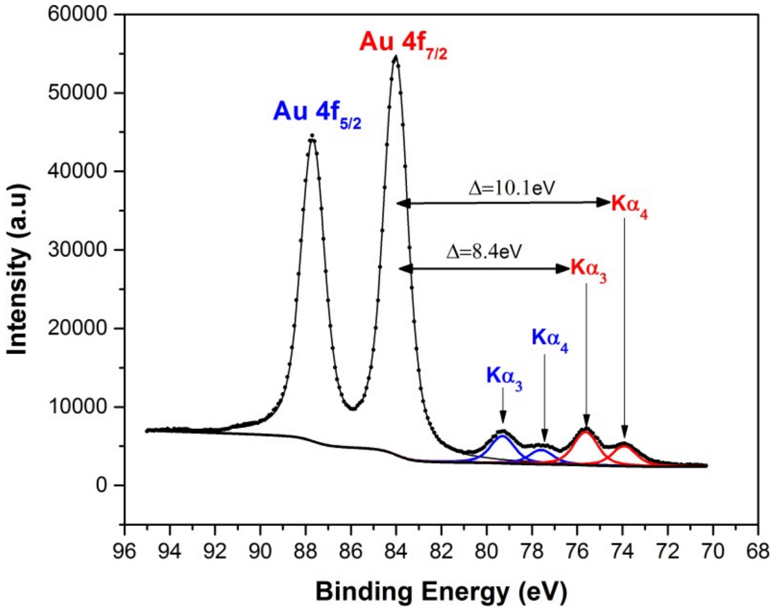

Figure 2.19: *Au 4f peaks and satellite peaks associated with Kα_3 and Kα_4 x-rays*

Other spectral features include ghost lines where the Al anode can become contaminated by the Mg anode and vice versa or due to exposed copper from the anode base or by oxidation generating unwanted x-rays producing ghost lines in spectrum.

2.3.3 Spectrum Analysis

Spectral analysis is a key component of XPS experiments. Understanding the underlying physics is required and has been discussed in previous sections. Herein, the analytical tools for studying spectra are discussed.

2.3.3.1 Background Signal

As mentioned previously in section 2.3.1 photoelectrons that undergo scattering contribute to the XPS background signal. As a result, the intensity of the background signal is greater at the higher binding energy side of a photoelectron peak due to energy loss collisions of photoelectrons from the given subshell. For accurate quantification of XPS spectra, background subtraction is required. Several methods have been developed for background subtractions through the years [18]. The workin this thesis uses a method first developed by Shirley in 1972 [19] and subsequently improved by Végh [20], then Salvi and Castle [21] and is referred to henceforth as the Shirley-type background.

The method uses the ratio of the number of electrons with binding energy greater than the central peak binding energy to the total number of electrons from the peak to fit a background. For a photoemission peak centred at energy *E* with an energy distribution to E_{left} and E_{right} and assuming the background is proportional to the number of electrons with energy greater than *E* the background signal can be expressed by

$$B(E) = kY_0 \int_{E}^{E_{left}} y(E')\,dE' \tag{2.14}$$

So that

$$B\left(E_{left}\right) \approx kY_0 \tag{2.15}$$

And

$$B\left(E_{right}\right) \approx 0 \tag{2.16}$$

Where k is the scattering factor and can be interpreted as the ratio between the difference of intensity at E_{left} and at E_{right} to the height of the peak, Y_0. The measured photoemission peak takes the form

$$Y'(E) = Y_0\left(y(E) + k\int_{E}^{E_{left}} y(E')dE'\right) \tag{2.17}$$

The Shirley background uses the ratio of the number of photoelectrons with energy greater than E to the total numbers of emitted photoelectrons to construct a background. Where a measured spectrum with a first approximation background subtraction can be written as

$$Y''(E) = Y'(E) - Y_0'\left(\frac{\int_{E}^{E_{left}} Y'(E')dE'}{\int_{E_{right}}^{E_{Left}} Y'(E')dE'}\right) \tag{2.18}$$

Where Y'_0 is the difference in intensities either side of the peak. By rearranging equation 2.18, the Shirly background $S(E)$ is expressed as

$$S(E) = Y'(E) - Y''(E) = Y_0'\left(\frac{\int_{E}^{E_{left}} Y'(E')dE'}{\int_{E_{right}}^{E_{Left}} Y'(E')dE'}\right) \tag{2.19}$$

In practice, this procedure is iterated until the difference between $Y'(E)$ and $Y''(E)$ are negligible which is where the scattering factor k has converged [22].

Figure 2.20 shows the bottom portion of a hafnium 4*f* doublet fit with a Shirly-type background. It can be seen from the figure where the fitted curve (red line) and the background (black line) converge at E_{right} the difference between the background andthe baseline are effectively zero while at E_{left} is approximately Y'_0.

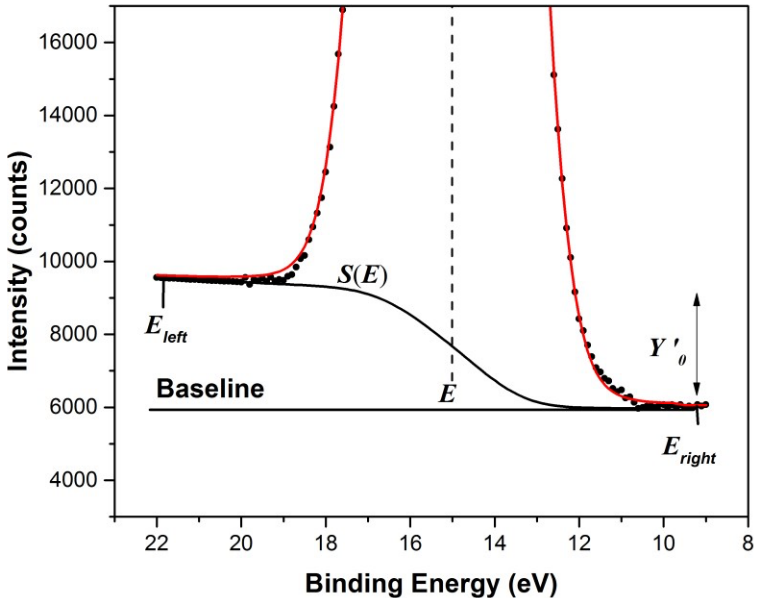

***Figure 2.20**: Shirley Background, S(E), on Hf 4f spectrum.*

2.3.3.2 Line Shapes

The line shape of XPS photoemission peaks is due to two factors; the lifetime of the core-hole and the instrumental resolution. The core-hole lifetime is an intrinsic property. The peak width Γ in eV due to the core-hole lifetime can be written as

$$\Gamma = \frac{h}{\tau} \tag{2.20}$$

where h is the Planck constant in units of eV.s and τ is the lifetime in seconds. The line shape associated with the core-hole lifetime is assumed to be Lorentzian in nature[18]. Instrumental broadening arises from the resolution of the analyser and the energy distribution of the incident x-ray beam. These effects can be reduced by adjusting the analyser aperture and by using monochromated x-rays. Instrumental broadening is typically fit with Gaussian line shapes [23]. The full width at half maximum (FWHM) of a photoemission peaks can be expressed by

$$FWHM = \sqrt{G^2 + L^2} \tag{2.21}$$

where G is the Gaussian component and L is the Lorentzian component of the XPS peak. For XPS data the Gaussian component is greater than the Lorentzian component in the above expression. In order to account for both Gaussian and Lorentzian components when fitting XPS data, a Voigt function is used. The Voigt function is a convolution of both line shapes.

2.3.3.3 XPS peak fitting and A-Analyzer

The A-Analyzer software package was used to fit XPS data presented. The software was developed by A. Herrera-Gomez at the Center for Research and Advanced Studies of the National Polytechnic Institute (CINVESTAV) at Querétaro, Mexico [24]. The program offers background and Shirley-type approximation fits. The XPS peaks are fit with Voigt line shapes with adjustable Gaussian and Lorentzian components. For doublet peaks, the spin-orbit splitting energy separation and area ratios can be set. When fitting the data all peak parameters can either be fixed, free, limited or correlated to other parameters. From the fits the area of each peak is calculated. The Mo 3*d* and S 2*s* peaks of a MoS_2 are shown in figure 2.21 to display the functionality of A-Analyzer.

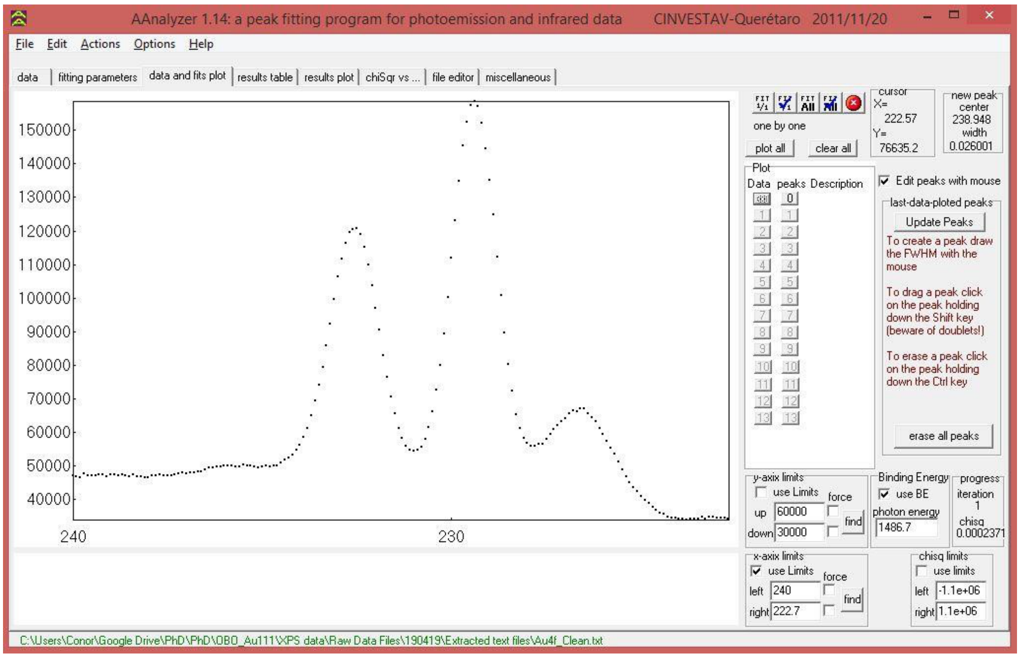
AAnalyzer 1.14: a peak fitting program for photoemission and infrared data CINVESTAV-Querétaro 2011/11/20

cursor X= 222.57 Y= 76635.2

new peak center 238.948 width 0.026001

☑ Edit peaks with mouse

To create a peak draw the FWHM with the mouse

To drag a peak click on the peak holding down the Shift key (beware of doublets!)

To erase a peak click on the peak holding down the Ctrl key

y-axix limits ☐ use Limits up 60000 down 30000 force ☐ ☐

Binding Energy ☑ use BE photon energy 1486.7

progress iteration 1 chisq 0.0002371

x-axix limits ☑ use Limits left 240 right 222.7 force ☐ ☐

chisq limits ☐ use limits left -1.1e+06 right 1.1e+06

C:\Users\Conor\Google Drive\PhD\PhD\OBO_Au111\XPS data\Raw Data Files\190419\Extracted text files\Au4f_Clean.txt

Figure 2.21: *Screen grab of A-Analyzer data plot of Mo 3d and S 2s peaks*

The parameters window is shown in figure 2.22. In the area highlighted by the black box, three check boxes are selected for each of the peaks in the spectrum: S 2*s* singlet, the Mo 3*d* doublet and Mo oxide peak. Peaks are selected as singlet or doublet accordingly. Here, the Mo 3*d* has spin-orbit energy splitting of 3.18 eV and ratio of 0.655. The Voigt line shapes can be adjusted by changing the Gaussian and Lorentzian components. In the final column, the area of each peak is calculated. Thisis used for compositional analysis. In the red box, selected parameters can be optimized by using fixed values or allowing parameters to be freely adjusted as the software optimizes the fit. The tolerance of the fit and the number of iterations can also be adjusted. The background settings are found in the highlighted blue box. The Shirley value relates to the scattering factor, *k* discussed previously in section 2.3.3.1. Figure 2.23 shows the same data from figure 2.21 fitted with parameters shown in figure 2.22. A new section is visible below the spectra showing the residual, that is thedifference between the data and the fit. This is the residual and indicates to how accurate the fit is to the data.

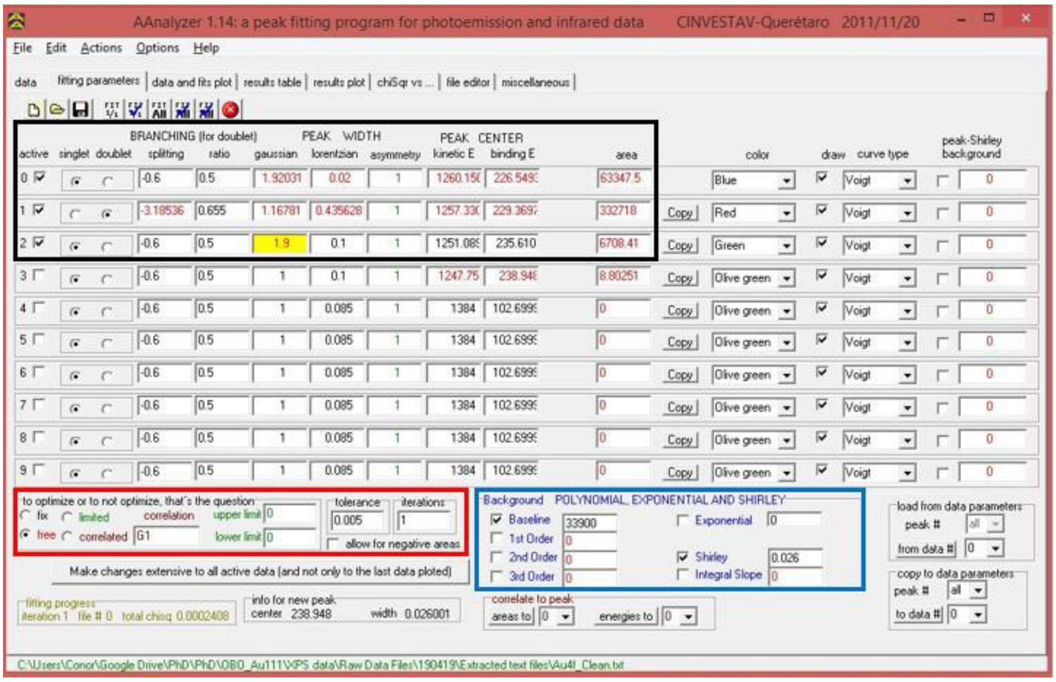

active	singlet	doublet	BRANCHING (for doublet) splitting	ratio	PEAK WIDTH gaussian	lorentzian	asymmetry	PEAK CENTER kinetic E	binding E	area	color	draw	curve type	peak-Shirley background	
0 ☑	●	○	-0.6	0.5	1.92031	0.02	1	1260.15	226.549	63347.5	Blue	☑	Voigt	☐	0
1 ☑	○	●	-3.18536	0.655	1.16781	0.435628	1	1257.33	229.369	332718	Red	☑	Voigt	☐	0
2 ☑	●	○	-0.6	0.5	1.9	0.1	1	1251.08	235.610	6708.41	Green	☑	Voigt	☐	0
3 ☐	●	○	-0.6	0.5	1	0.1	1	1247.75	238.94	8.80251	Olive green	☑	Voigt	☐	0
4 ☐	●	○	-0.6	0.5	1	0.085	1	1384	102.699	0	Olive green	☑	Voigt	☐	0
5 ☐	●	○	-0.6	0.5	1	0.085	1	1384	102.699	0	Olive green	☑	Voigt	☐	0
6 ☐	●	○	-0.6	0.5	1	0.085	1	1384	102.699	0	Olive green	☑	Voigt	☐	0
7 ☐	●	○	-0.6	0.5	1	0.085	1	1384	102.699	0	Olive green	☑	Voigt	☐	0
8 ☐	●	○	-0.6	0.5	1	0.085	1	1384	102.699	0	Olive green	☑	Voigt	☐	0
9 ☐	●	○	-0.6	0.5	1	0.085	1	1384	102.699	0	Olive green	☑	Voigt	☐	0

to optimize or to not optimize, that´s the question
○ fix ○ limited correlation upper limit 0
● free ○ correlated G1 lower limit 0
tolerance 0.005
iterations 1
☐ allow for negative areas

Background POLYNOMIAL, EXPONENTIAL AND SHIRLEY
☑ Baseline 33900
☐ 1st Order 0
☐ 2nd Order 0
☐ 3rd Order 0
☐ Exponential 0
☑ Shirley 0.026
☐ Integral Slope 0

load from data parameters
peak # all
from data # 0

copy to data parameters
peak # all
to data # 0

fitting progress
iteration 1 file # 0 total chisq 0.0002408

info for new peak
center 238.948 width 0.026001

correlate to peak
areas to 0 energies to 0

C:\Users\Conor\Google Drive\PhD\PhD\OBO_Au111\XPS data\Raw Data Files\190419\Extracted text files\Au4f_Clean.txt

Figure 2.22: *Screen grab of A-Analyzer parameters window*

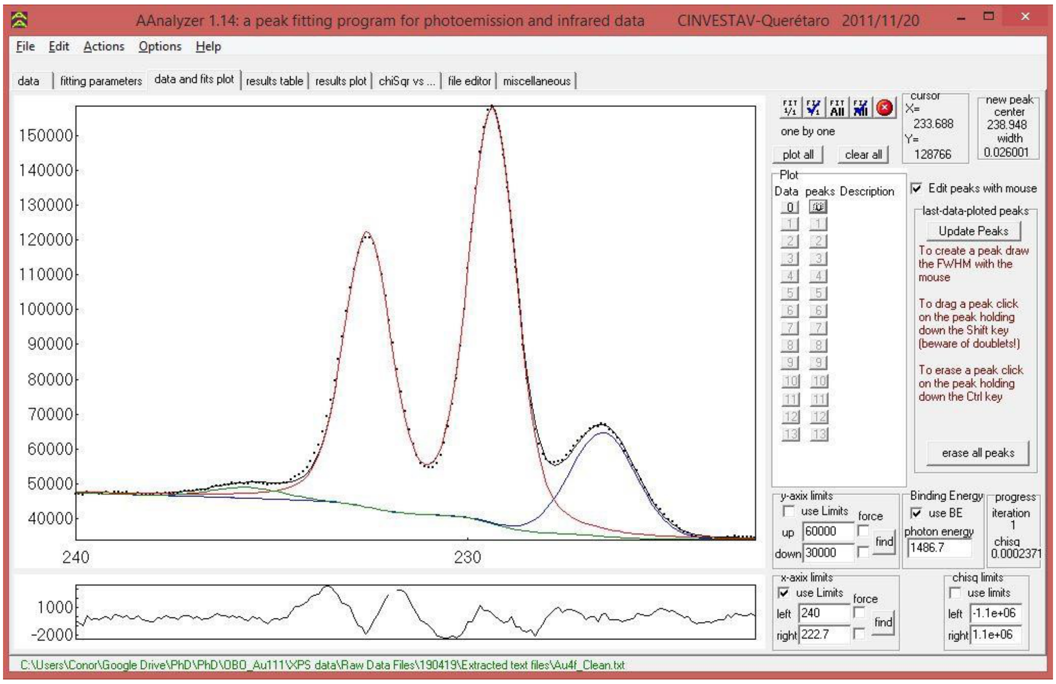

cursor
X= 233.688
Y= 128766

new peak
center 238.948
width 0.026001

☑ Edit peaks with mouse

last-data-ploted peaks

To create a peak draw the FWHM with the mouse

To drag a peak click on the peak holding down the Shift key (beware of doublets!)

To erase a peak click on the peak holding down the Ctrl key

y-axix limits
☐ use Limits force
up 60000 ☐
down 30000 ☐

Binding Energy
☑ use BE
photon energy 1486.7

progress
iteration 1
chisq 0.0002371

x-axix limits
☑ use Limits force
left 240 ☐
right 222.7 ☐

chisq limits
☐ use limits
left -1.1e+06
right 1.1e+06

C:\Users\Conor\Google Drive\PhD\PhD\OBO_Au111\XPS data\Raw Data Files\190419\Extracted text files\Au4f_Clean.txt

Figure 2.23: *Screen grab of A-Analyzer plot with fitted data*

2.3.4 XPS System Hardware

The XPS system used for this body of work consists of a dual anode x-ray source, a grounded sample, a electrostatic lens and a concentric hemispherical analyser (CHA) with entrance and exit slits, a five-channel electron detector[‡], five fibre optic cables to carry signal to amplifier, a signal amplifier and a computer to control the system and record the electron counts as illustrated in figure 2.26. In this section, each major component will be discussed. Data can be acquired in two modes: constant analyser energy (CAE) and constant retard ratio (CRR). All data acquired in this thesis used CAE mode.

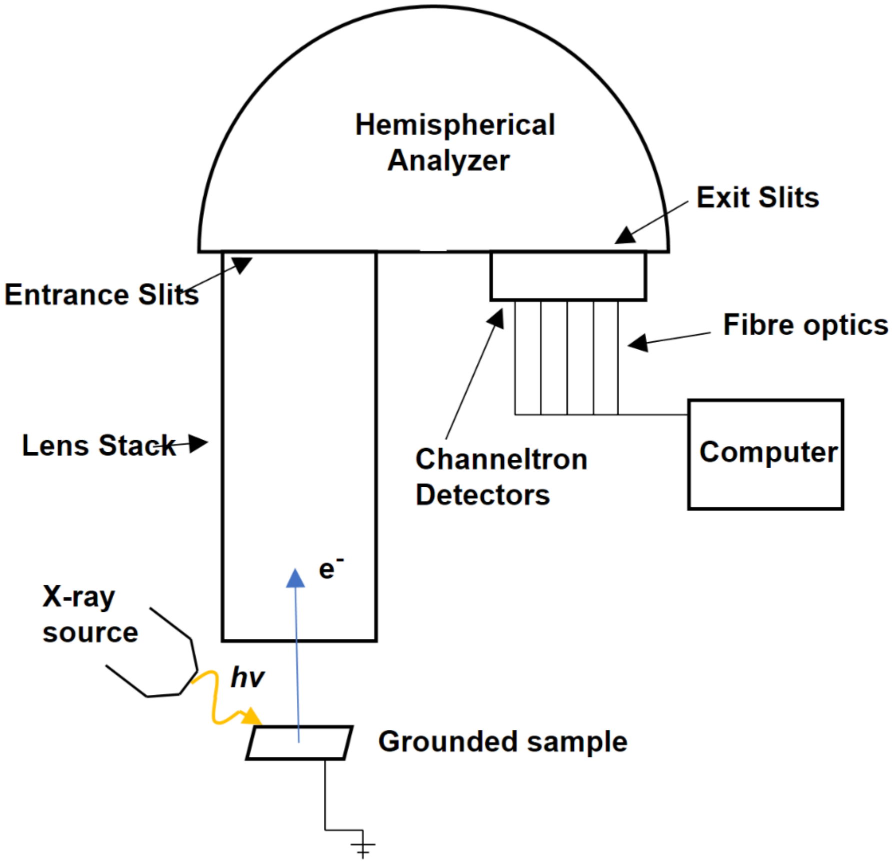

Figure 2.26: *Illustration of XPS system*

[‡] The Channeltron has an analog to digital convertor which converts the electrical signal created by electrons to a digital optical signal.

The x-ray source comprises of a copper anode with Al and Mg targets, tungstenfilaments for the cathode and exit aperture covered by aluminium foil as shown in figure 2.27. A voltage of 14 kV is applied across the cathode and the anode accelerating electrons from the heated filament toward the selected target. The accelerating electrons impinge on the anode material and excite inner shell electrons to higher energy levels. The core-hole is filled with an electron from a higher energy level thusradiating an x-ray. The strongest transitions are from the $2p_{1/2}$ and $2p_{3/2}$ orbitals to the$1s$ subshell known as the $K\alpha_1$ and $K\alpha_2$ transitions. The x-rays from Mg and Al targets have a photon energy of 1253.6 eV and 1486.7 eV, respectively. Other transitions occurproducing additional higher energy x-rays as previously discussed in section 2.3.2.5. The generation of characteristic x-rays also produces Bremsstrahlung and the aluminium foil acts as a high energy filter to reduce these x-rays impinging on the sample. High temperatures are generated at the anode when producing x-rays and water cooling is required to prevent overheating and melting.

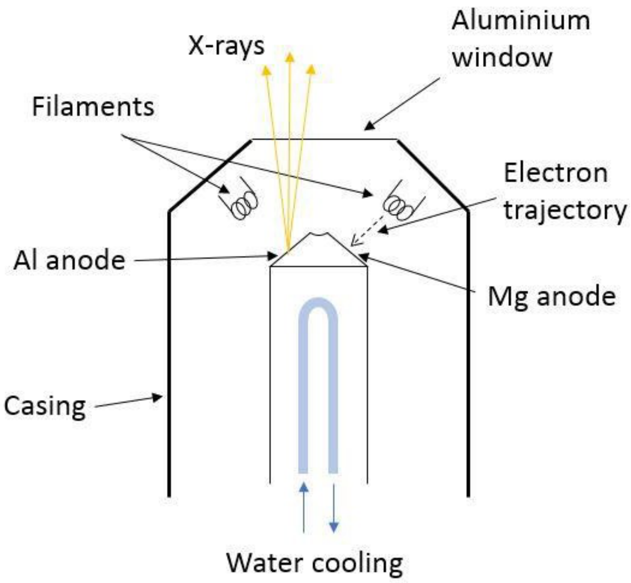

Figure 2.27*: Dual anode x-ray source*

The electrostatic lens has a twofold function in CAE mode; it collects and focuses photoelectrons from the sample onto the analyser entrance slits while also acting as a filter to allow only photoelectrons with kinetic energy equal to the pass energy of the analyser be transmitted through the CHA to the detectors. The pass energy of the analyser is the energy an electron requires to complete a trajectory around the hemisphere to the detectors. The photoelectrons are accelerated or retardedby the electrostatic lens to equal the pass energy. The CHA consists of two concentric hemispheres, the inner hemisphere with a radius R_1 and the outer hemisphere with R_2. The outer hemisphere is negatively biased with respect to the inner. Photoelectrons with kinetic energy equal to the pass energy, E_P travel a trajectory R_0 as shown in figure 2.28 such that,

$$e\Delta V = E_P\left(\frac{R_2}{R_1} - \frac{R_1}{R_2}\right) \tag{2.22}$$

where e is the electron charge and ΔV is the voltage across the inner and outer hemispheres. As per equation 2.16 the pass energy of the analyser is set by the voltage across the two hemispheres, ΔV. During experiments the pass energy is fixed and the voltage across the electrostatic lens sweeps through a set of user defined values allowing photoelectrons with a range of kinetic energies impinge on the detectors forming a spectrum.

The resolution ΔE, of the analyser is given by

$$\Delta E = E_P\left(\frac{d}{2R_0} + \alpha^2\right) \tag{2.23}$$

where d is the slit width and α is the aperture half-angle as illustrated in figure 2.21. From equation 2.17 the pass energy and the resolution are directly proportional. Photoelectrons within 10% of the pass energy reach the detectors [9]. Therefore, increasing the pass energy increases the number of photoelectrons counted by the detectors improving the signal-to-noise ratio. However, at higher pass energy the larger energy distribution ΔE, which reduces the analyser resolution. A compromise must be found between counts and resolution. A pass energy of 25 eV, an entrance slit width a 2 mm diameter and an acceptance angle ~0.2° were used for acquiring data for this thesis resulting in a detector resolution of ~1.2 eV.

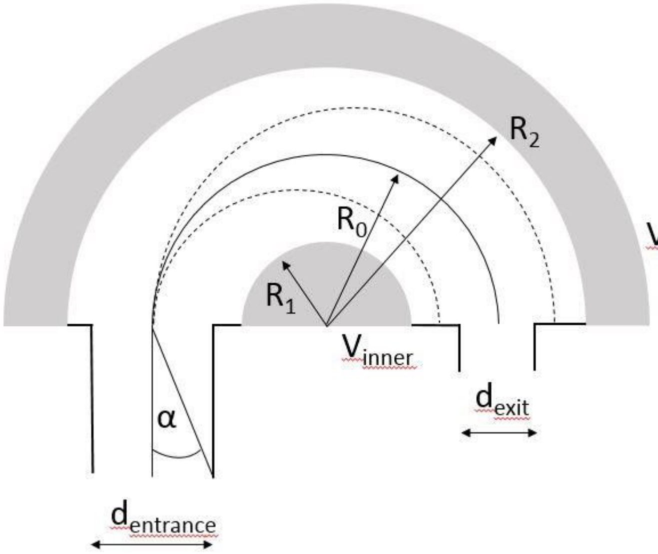

Figure 2.28: *Concentric hemispherical analyser*

The photoelectrons that reach the five-channel detector generate secondary electrons that are then accelerated through a positive voltage of +2-3 kV creating an electron avalanche effect multiplying the electron count by a factor of approximately 10^7 [28]. A preamplifier removes system noise and the signal is sent via fibre optic to a receiving unit which counts the number of photoelectrons received. Data is recorded using EIS software supplied by Omicron with the EA 125 Analyser [25].

2.4 Gold Crystal Substrates

As discussed in section 1.3 metallic surfaces are necessary for facilitating the diffusion of deposited molecules and the catalytic effect they have in the dehalogenation and cyclodehydrogenation processes. The nanotemplating effect of the surface reconstruction also plays a role in the direction of GNR growth and alignment.

The Au(111) and Au(788) crystals were used for all the deposition experiments and the Au(110) surface was used for STM tip conditioning. Gold is an inert face-centred cubic (fcc) crystal with a lattice constant of a = 4.06 Å. As with all crystalline materials the surface is different from the crystal structure in the bulk. Crystals have periodic structure throughout but on the surface the atoms experience unbalanced forces from the bulk. The surface atoms relax or reconstruct to regain equilibrium with the bulk. Reconstruction results in a change in the surface atoms relative position to bulk atoms while the bulk unit cell is preserved. Surface reconstructions result in patterned surface with steps, terraces and corrugations that can contribute to molecular alignment of adsorbents. All crystals were purchased from Surface Preparation Laboratory in The Netherlands [26]

2.4.1 Au(111) Reconstruction

The (111) crystal plane of gold is shown in figure 2.29(a) and three direction at 120° to each other are shown in figure 2.29(b). The Au(111) is unique to other (111) planes in fcc metals as the surface has a $22 \times \sqrt{3}$ reconstruction, producing a "herringbone" pattern shown in figure 2.22(b). The herringbone pattern is a combination of competing fcc and hexagonal closed packed (hcp) domains first verified with STM by Wöll *et al.* [27]. The surface has regions of compression along the <110> direction, forming a ripple like effect on thesurface [28] A schematic drawing of the "herringbone" structure is shown in figure 2.29(c). The corrugation on the surface has a height of ~12 pm and this flatness of the surface allows for a greater amount of molecular diffusion compared to other gold planes. Figure 2.29 (d) shows a 100 nm × 100 nm STM imageof the Au(111) surface with three directions highlighted.

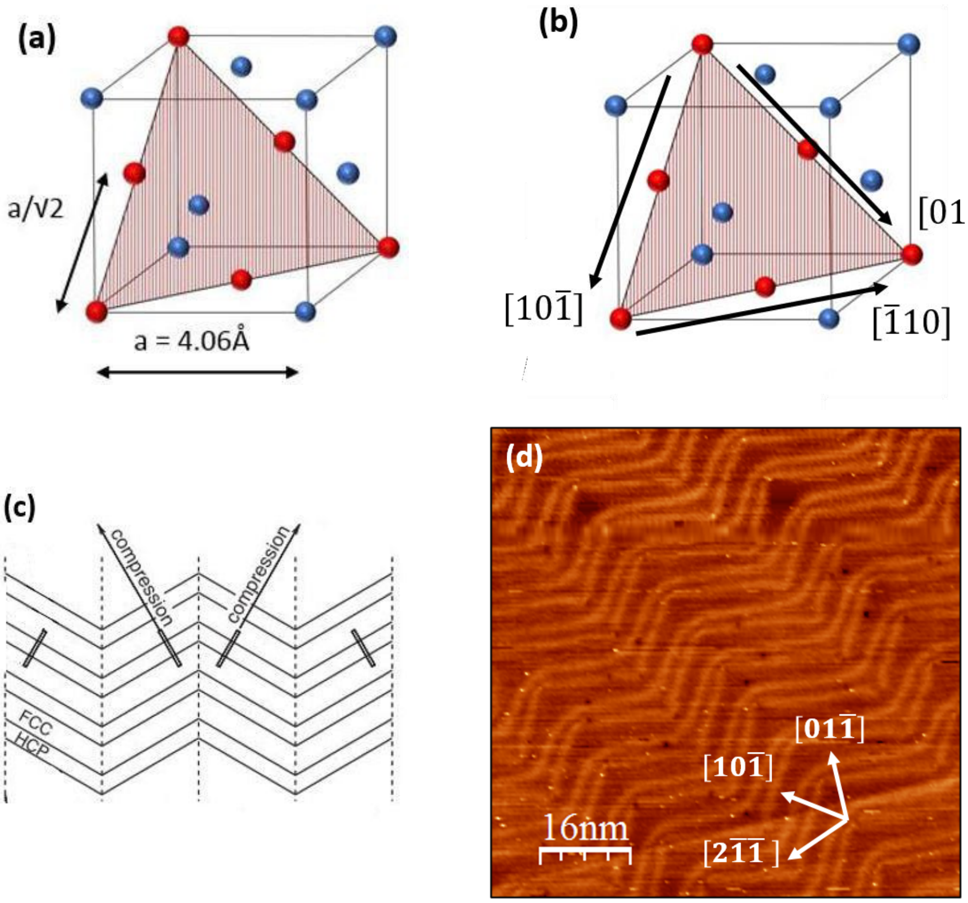

***Figure 2.29**: Au(111) crystal and surface reconstruction: (a) Unit cell of fcc crystal showing the (111) plane with gold lattice parameter (b) Au(111) with threedirections highlighted. (c) Schematic drawing of Au(111) surface from Reinert et al.* [28] *who show regions of compression perpendicular to ripples and fcc and hcpregions.(d) 100 nm × 100 nm STM image of the (111) surface with three directions at 60º to each other. (V =1.0 V, I = 0.5 nA)*

2.4.2 Au(788) Surface

The Au(788) surface is created by cutting the (111) plane at an angle of 3.5° in the $[\bar{2}11]$ direction. The result is a stepped surface with a 1:16 atom step to terrace ratio resulting in parallel terraces with an average width of 4.8 nm and height of 0.4 nm [29] A diagram of the vicinal surface is shown in figure 2.30(a) the [788] direction perpendicular to the (788) plane is highlighted in blue. A 50 nm × 50 nm STM image displaying the parallelterraces is shown in figure 2.30 (b) and a profile verifying terrace width is shown in figure 2.30(c). The terraces of the (788) crystal are of the (111) plane.

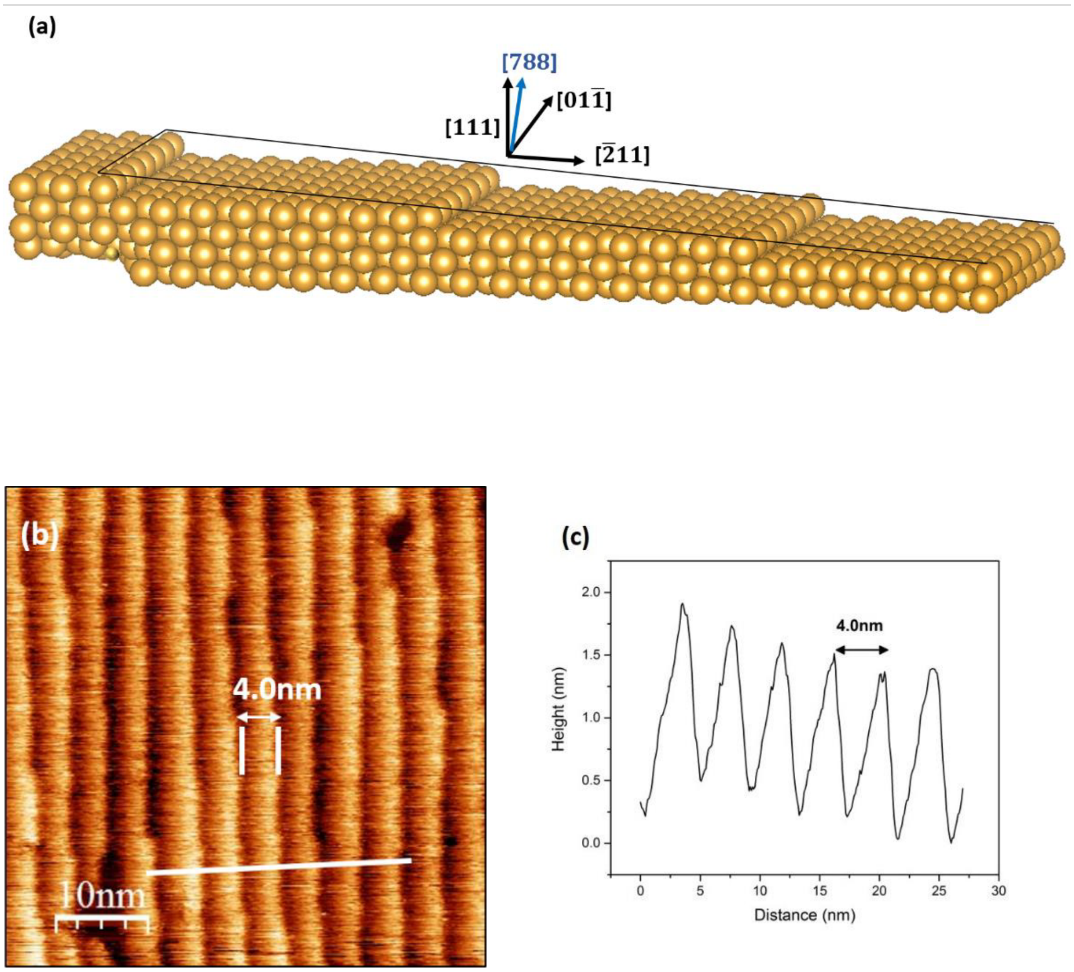

***Figure 2.30:** Au(788) crystal and reconstruction. (a) Drawing of the (788) surfacewith labelled directions. The cut angle is illustrated by the plane outlined in black. (b)50 nm × 50 nm STM image of the (788) surface (V=1.0 V, I= 0.25 nA) (c) Lineprofile from (b) showing the average terrace width to be 4.0 nm*

2.4.3 Sample Preparation

Samples are mounted on tantalum spades and held in place by a tantalum sheet spot welded to the spade. The tantalum sheet has an opening to expose the sample surface for STM measurements and XPS. The gold samples are prepared *in situ* by argon bombarding the surface for 30 minutes at room temperature and annealing to 400 °C. The process is repeated until the sample is clean. The cleanliness of the sample is verified by XPS and STM.

2.5 Precursor Molecules for formation of GNRs

The molecules 6,16-dibromo- 9,10,19,20-tetraoxa-9a,19a-diboratetrabenzo (OBO) and 10,10'-Dibromo-9,9'-bianthracene (DBBA) were used as precursors to form (4,1) chiral GNRs and 7-Armchair GNRs, respectively. Chapter 3 will discuss GNR formation with DBBA and in chapter 4, the growth of (4,1) chiral GNR and 5,15 dibromophenyl 10,20 tetra-phenylporphyrin heterojunctions are discussed. All precursor molecules are named and labelled according to the International Union of Pure and Applied Chemistry (IUPAC) nomenclature.

2.5.1 DBBA precursor

The 10,10'-Dibromo-9,9'-bianthracene (DBBA) precursor was used in the first bottom-up on surface synthesis of graphene nanoribbons reported by Cai *et al.* [34] This molecule was purchased from Tokyo Chemical Industry [35] (product number D4254)It has the chemical formula of $C_{28}H_{16}Br_2$ shown in figure 2.33. The anthracene units are rotated about the central C-C axis due to steric hindrance from the hydrogen atoms.

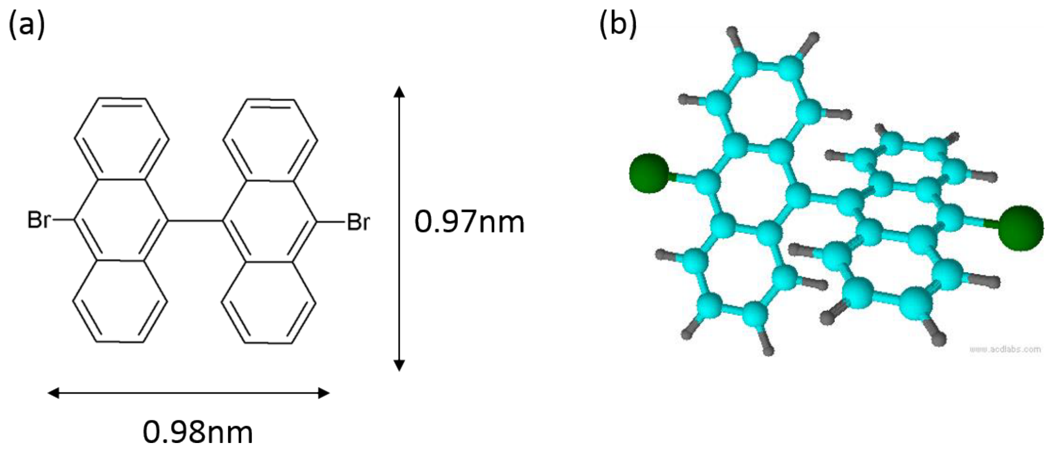

***Figure 2.33**: Drawing of 10,10'-Dibromo-9,9'-bianthracene (DBBA) (a) Chemical sketch of DBBA with dimensions. (b) Ball and Stick drawing of DBBA with H included showing the angle between anthracene units*

2.5.2 OBO doped precursor

The precursor molecular 6,16-dibromo-9,10,19,20-tetraoxa-9a,19a-diboratetrabenzo[a,f,j,o] perylene (OBO) was synthesised by Akimitsu Narita from the Müllen research group at Max Planck Institute for Polymer Research [30] by means of the synthesis procedure presented in figure 2.32(a) and is not commercially available. It has the chemical formula $C_{30}H_{14}B_2Br_2O_4$. The motivation of Narita *et al.* was to synthesis a molecular precursor that would form chiral GNRs (c-GNR) as only the (3,1) c-GNR had been realised at this time [31]. However, an all-carbon bistetracene precursor molecule that ideally could yield (4,1) c-GNR is unstable. By introducing the oxygenand boron substituent atoms into the synthesis produced the stable precursor molecule.Using bottom-up on-surface synthesis techniques, discussed in chapter 1, this molecule forms chiral (4,1) chiral graphene nanoribbons on the Au(111) surface [32]. The zig-zag edges of the CGNR have an oxygen-boron-oxygen segment and isreferred to as OBO precursor molecules. The dimensions of the molecule are estimated using the Chemsketch molecular drawing freeware from ACD Labs [33] The dimensions are shown in figure 2.32 (b) and a stick and ball model shown in figure 3.32 (c).

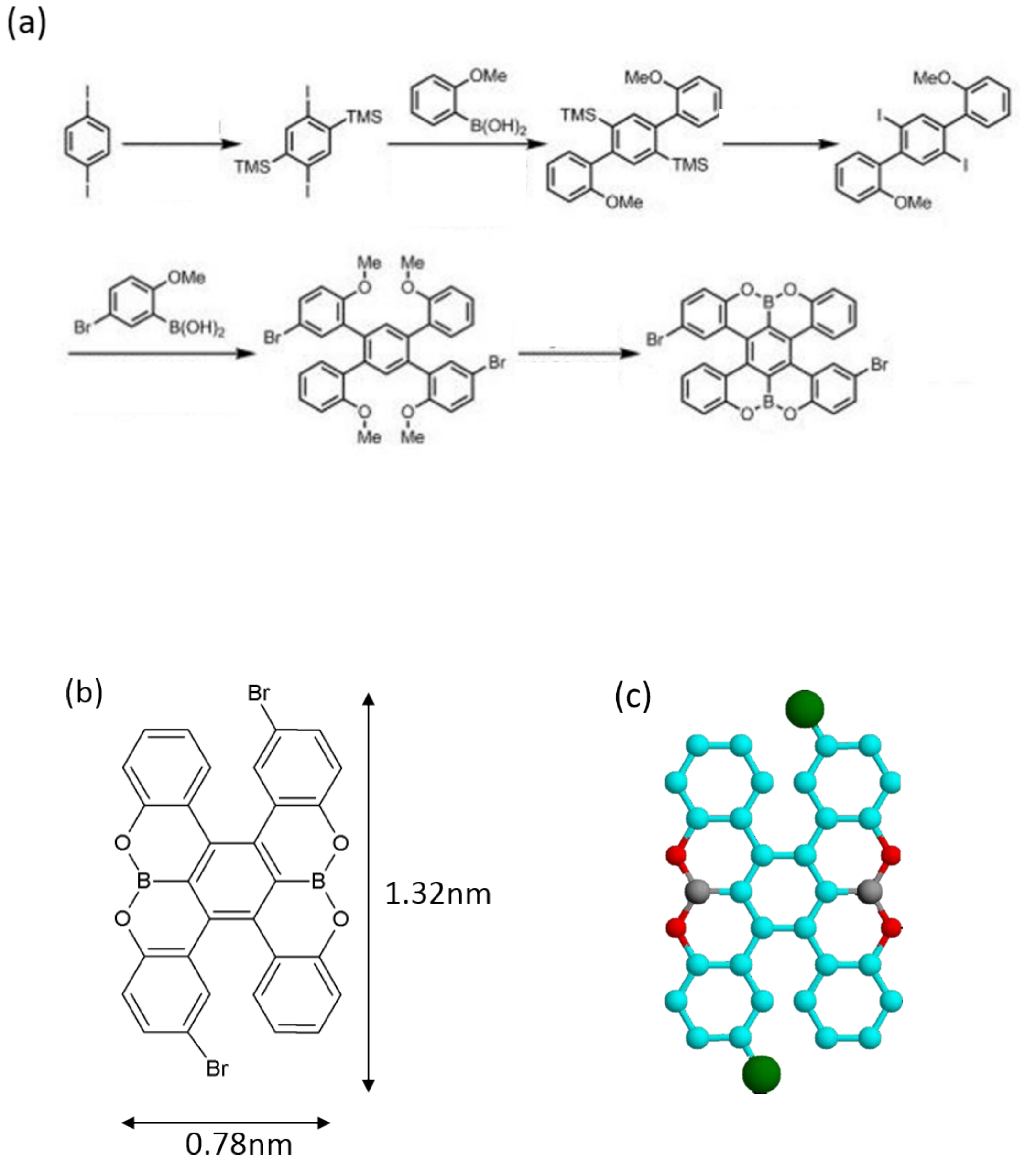

Figure 2.32: OBO precursor molecule. (a) Synthesis of 6,16-dibromo- 9,10,19,20-tetraoxa-9a,19a-diboratetrabenzo OBO [30] *(b) Sketch and lateral dimensions of OBO. (c) Stick-and-ball model of OBO molecule.*

2.5.3 Porphyrin Molecule

The 5,15dibromophenyl 10,20 tetra-phenylporphyrin with Ni (Ni-DBTPP) was synthesised by Dr. Aoife Ryan from Prof. Mathias Senge's group in Trinity College Dublin [36]. The molecule has an organometallic porphine parent compound atthe centre as shown in figure 2.34 (a) with all *beta* and *meso* positions of the structurenumbered. Four phenyl rings are covalently bonded to the central structure at the 5, 10, 15 and 20 positions, two of which are brominated as illustrated in figure 2.34 (b) and (b). The molecule has the chemical formula $C_{44}H_{26}Br_{2}N_{4}Ni$. As mentioned in section 1.5, using DFT the rotation between the phenyl rings and the porphine core was calculated to be approximately 63°, using the 3D visualization feature on Chemsketch software an angle of 65° was measured in good agreement with published results.

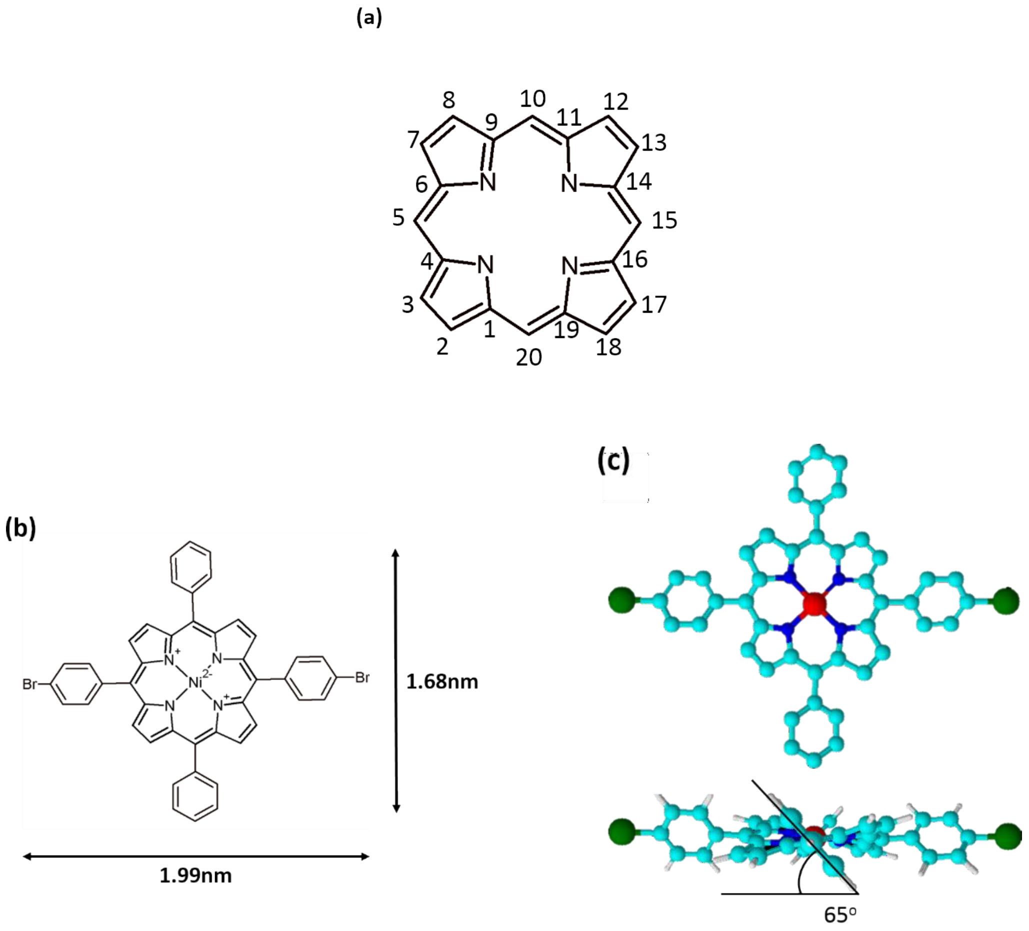

Figure 2.34: Porphine and porphyrin (a) Drawing of porphine core. (b) Drawing of DBTPP with length and width. (b) Chemical structure of DBTPP showing the twisting of phenyl rings and the 65° rotation of phenyl rings

2.6 Deposition and Knudsen Cells

Knudsen cells (K-cell) are used to evaporate molecules onto the substrates. The K-cell is made up of a tungsten wire filament wrapped around a molybdenum crucible connected to a power supply to control the current and voltage. The temperature of the crucible is monitored by a thermocouple spot welded to the underside of the crucible. The assembly is picture in figure 2.35. The molybdenum crucible does not have catalytic effect on the molecules allowing them to evaporate attemperatures higher than the molecules debromination temperature on gold of ~180 °C.The deposition rate of molecules from the K-cell is controlled by two variables; temperature and duration. A table of sublimation temperatures and corresponding current and voltages required to deposit 1 monolayer (1 ML) of material is tabulated inTable 2.3 It should be noted that heating the crucible to excessive temperatures abovethe evaporation temperature can cause the molecules to decompose in the crucible resulting in poor control over the deposition rate.

Table 2.3*: Approximate deposition temperatures and duration for 1ML of molecules*

Precursor	*Sublimation temp. °C* **(±2° C)**	*Time for 1 ML (mins)*
DBBA	195	50
OBO	260	180
Ni-porphyrin	335	90

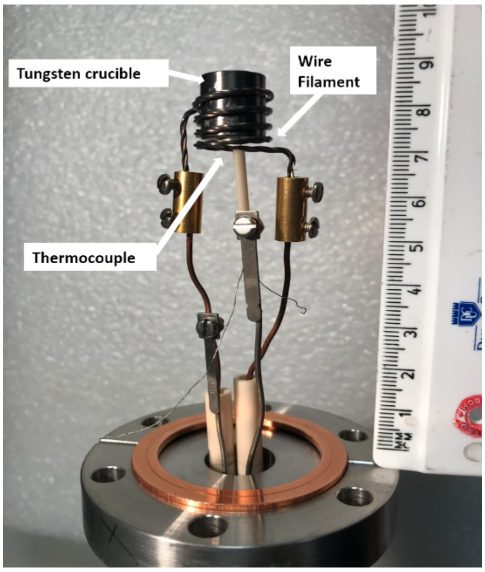

***Figure 2.35**: Photograph of Knudsen cell*

2.7 References

1. Omicron NanoTechnology GmbH,. *URL http//www.omicron.de/en/products/ Var. Temp.*
2. Doyle, C. An investigation of the structural and electronic properties of covalently bonded molecular networks on metal surfaces formed through debromination reactions. *Ph.D Thesis DCU* 232 (2013).
3. Leggett, G. J. *Surface Analysis– The Principal Techniques: Scanning Probe Microscopy*. *Surface Analysis– The Principal Techniques* (Wiley, 2009).
4. G. Binning, H. Rohrer, C. Gerber, E. W. Surface Studies by Scanning Tunneling Microscopy. *Phys. Rev. Lett.* **49**, 57–61 (1982).
5. Wiesendanger, R. Scanning Probe Microscopy and Spectroscopy: Methods and Applications, 1st ed. *Cambridge Univ. Press.* (1994).
6. Tersoff ', J. & Hamann, D. R. *Theory of the scanning tunneling microscope*. *Physical Review B* **31**, (1985).
7. Chen, C. . Introduction to Scanning Tunneling Microscopy, 2nd ed. *Oxford Sci. Publ. New York* (2008).
8. Woodruff D.P. and Delchar, T. A. Modern Techniques of Surface Science, 2nd ed. *Cambridge Univ. Press.* (1994).
9. Tersoff, J. & Hamann, D. R. Theory of the scanning tunneling microscope. *Theory scanning tunneling Microsc.* **6**, 59–67 (1985).
10. Zhang, R. & Ivey, D. G. Preparation of sharp polycrystalline tungsten tips for scanning tunneling microscopy imaging. *J. Vac. Sci. Technol. B Microelectron. Nanom. Struct.* **14**, 1–10 (1996).
11. Tip Etching Kit User Manual, 1st ed.,. *Omi. Nanotechnology, Taunusstein, Ger.* (1998).
12. Horcas, I. *et al.* WSXM: A software for scanning probe microscopy and a tool for nanotechnology. *Rev. Sci. Instrum.* **78**, (2007).
13. Gray, D., Mccaughan, A. & Mookerji, B. *Crystal Structure of Graphite, Graphene and Silicon*. (2009).
14. Seah, M. P. & Dench, W. A. Quantitative Electron Spectroscopy of Surfaces : *Surf. Interface Anal.* **1**, 2–11 (1979).
15. Magnuson, M. *Electronic structure studies using resonant x-ray and photoemission spectroscopy*. (1999).
16. Chastain, J. F. M. J. Handbook of X-ray Photoelectron Spectroscopy AReference Book of Standard Spectra for Identification and Interpretation of XPS Data. *Eden Prairie, Minn. Phys. Electron. Div. Perkin-Elmer Corp* (1992).

17. Dean, J. A. *LANGE'S HANDBOOK OF CHEMISTRY 15th Edition*. *Applied Engineering in Agriculture* **18**, (McGRAW-HILL, INC, 1972).

18. Proctor, A. & Sherwood, P. M. A. Data analysis techniques in x-ray photoelectron spectroscopy. *Anal. Chem.* **54**, 13–19 (1982).

19. Shirley, D. A. High-resolution x-ray photoemission spectrum of the valence bands of gold. *Phys. Rev. B* **5**, 4709–4714 (1972).

20. Végh, J. The analytical form of the Shirley-type background. *J. Electron Spectros. Relat. Phenomena* **46**, 411–417 (1988).

21. Salvia, A. M. & Castle, J. E. The intrinsic asymmetry of photoelectron peaks : dependence on chemical state and role in curve fitting . **95**, 45–56 (1998).

22. Querétaro, U. & Herrera-gomez, A. The Peak-Shirley Background. (2012).

23. Jain, V., Biesinger, M. C. & Linford, M. R. The Gaussian-Lorentzian Sum, Product, and Convolution (Voigt) functions in the context of peak fitting X-ray photoelectron spectroscopy (XPS) narrow scans. *Applied Surface Science* **447**, 548–553 (2018).

24. Herrera-Gómez, A., Hegedus, A. & Meissner, P. L. Chemical depth profile of ultrathin nitrided SiO_2 films. *Appl. Phys. Lett.* **81**, 1014–1016 (2002).

25. EIS/EIS Sphera Software User Guide, 2nd ed. *Omi. Nanotechnology, Taunusstein, Ger.* (2008).

26. Surface Preparation Laboratory. *Oct 2019* Available at: https://spl.eu.

27. Woll, C., Chiang, S., Wilson, R. J. & Lippel, P. H. Determination of atom positions at stacking-fault dislocations on Au(111) by means of STM. *Phys. Rev. B* **39**, 7988–7991 (1989).

28. Reinert, F. & Nicolay, G. Influence of the herringbone reconstruction on the surface electronic structure of Au(111). *Appl. Phys. A Mater. Sci. Process.* **78**, 817–821 (2004).

29. Mugarza, A. *et al.* Electron Confinement in Surface States on a Stepped Gold Surface Revealed by Angle-Resolved Photoemission. (2001).

30. Wang, X.-Y. *et al.* Bottom-Up Synthesis of Heteroatom-Doped Chiral Graphene Nanoribbons. *J. Am. Chem. Soc.* **140**, 9104–9107 (2018).

31. de Oteyza, D. G. *et al.* Substrate-Independent Growth of Atomically Precise Chiral Graphene Nanoribbons. *ACS Nano* **10**, 9000–9008 (2016).

32. Müllen, K. *et al.* Heteroatom-Doped Perihexacene from a Double Helicene Precursor: On-Surface Synthesis and Properties. *J. Am. Chem. Soc.* **139**, 4671–4674 (2017).

33. Labs, A. ACD/ChemSketch. *Adv. Chem. Dev. Inc., Toronto, ON, Canada, www.acdlabs.com* (2021).

34. Cai, J. *et al.* Atomically precise bottom-up fabrication of graphene nanoribbons. *Nature* **466**, 470–473 (2010).

35. Tokyo Chemical Industry. Available at: https://www.tcichemicals.com/. (Accessed: 5th November 2019)

36. Ryan, A., Cafolla, A. A. & Senge, M. O. Chemical synthesis in solution and porphyrin nanostructures on surfaces - Similar concepts, different results. *ECS Trans.* **45**, 77–90 (2013).

Chapter 3: Porphyrin Functionalised 7-AGNRs on Au(111) and Au(788)

3.1 Introduction

The formation of atomically precise graphene nanoribbon-based structures through the process of "bottom-up" on-surface synthesis is the basis of the work in the chapter. The seminal work by Cai *et al.* [1] in 2010 using 10,10'-dibromo-9,9'-bianthryl (DBBA) molecules to form 7-carbon atom wide armchair graphene nanoribbons (7-AGNR) built on the previous work of Grill *et al.* [2] who first demonstrated covalently bonded nano-architectures via on-surface synthesis. To recap the work in the paper of Cai *et al.*, the process involves the sublimation of DBBA molecules onto the Au (111) surface and annealing the sample at 200 ^{o}C to thermally activate diffusion of the molecules on the surface and dehalogenation of the bromine atoms from the molecule to form covalently bonded chains. Further annealing at 400 ^{o}C initiates cyclo-dehydrogenation resulting in 7-AGNR. This process is illustrated in figure 3.1 The work in Cai's paper was successfully replicated in our lab and the STM results are summarised in figure 3.2.

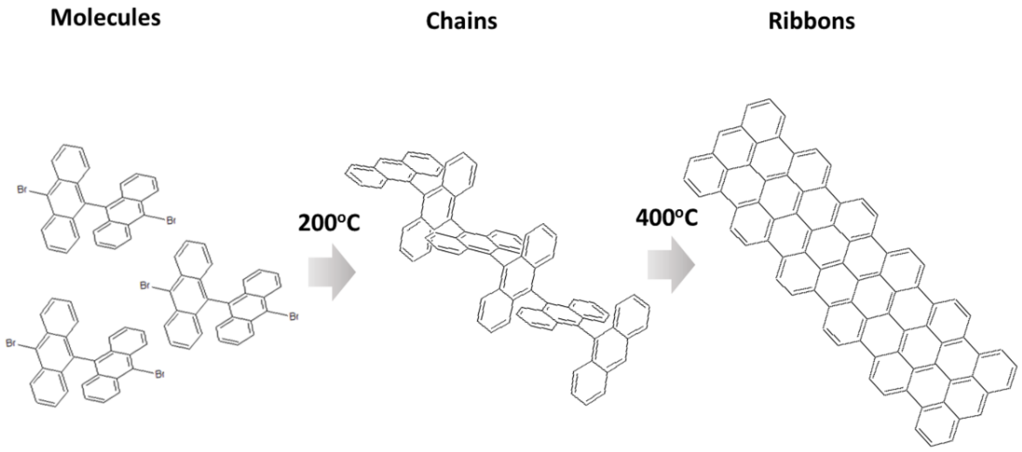

Figure 3.1: *Chemical models of the stages of 7-AGNR formation from DBBA molecules on the Au (111) surface.*

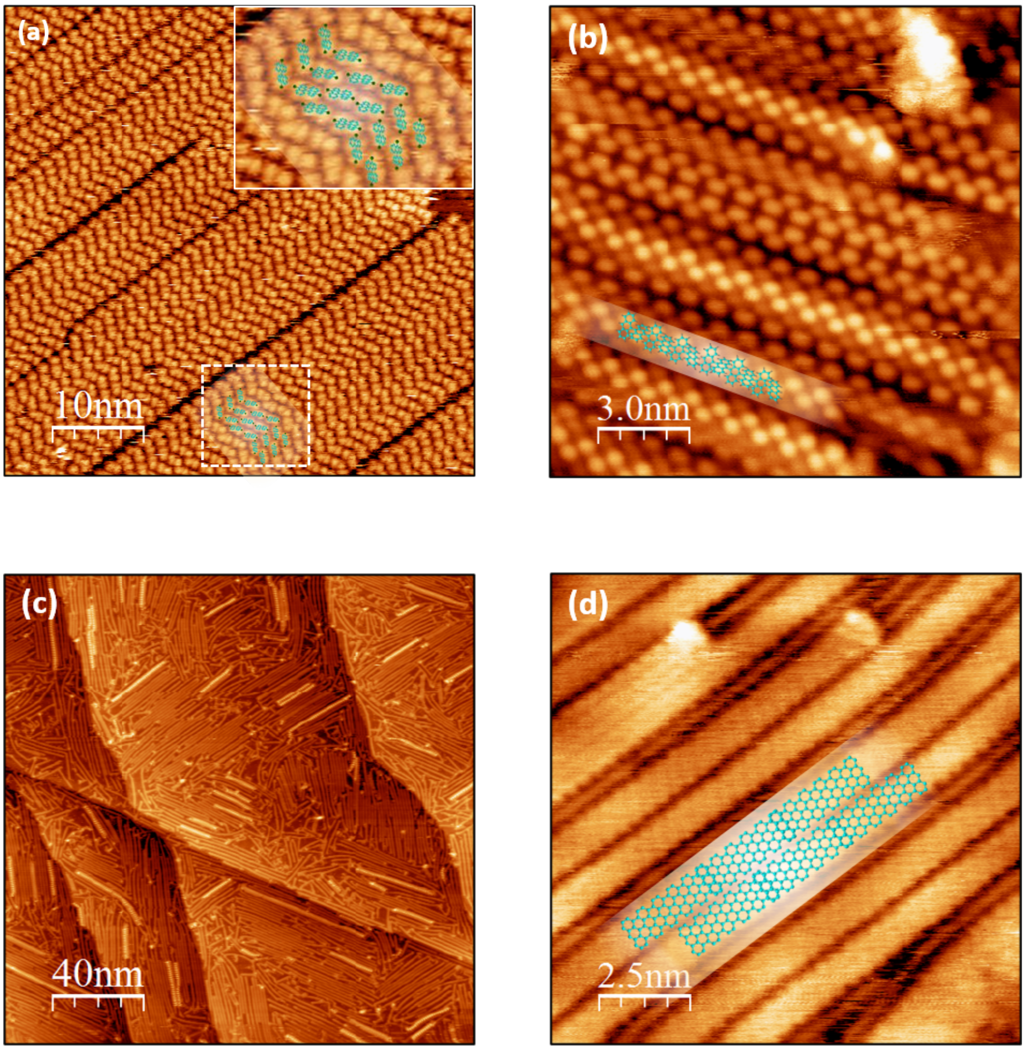

Figure 3.2*: STM of 7-AGNR from DBBA on Au (111). (a) 50 nm × 50 nm image of self-assembled DBBA (V=1.0 V I=0.21 nA). (b) 15 nm × 15 nm image polymer chain phase with chemical model overlayed. The bright lobes are due to protruding anthracene units. (V=0.6 V, I=0.47 nA) (c) 200 nm × 200 nm of 7-AGNR. (V=1.0 V I=0.31 nA) (d) 12.5 nm × 12.5 nm image of 7-AGNRs. The molecular structure of the ribbons can be seen. (V=0.2 V I=0.12 nA)*

This chapter builds on the work of Cai *et al.* by integrating nickel 5,15 dibromophenyl 10,20 phenylporphyrin (Ni-DBrTPP) with DBBA through the on-surface synthesis process to form heterojunction structures, as shown schematically in figure 3.3. The overarching aim of this research is to create molecular electronic devices such as FETs, energy harvesters, switches and chemical sensors with the porphyrin molecule as the active component and the GNRs acting as wires. The road map for this work among the research community is to first demonstrate the feasibility of forming such devices; followed by electronic and chemical characterisation of these porphyrin functionalised GNRs, and finally implementation of functioning devices onto a semiconducting platforms. The work contained in this this thesis is concerned with the feasibility of forming covalently bonded structures through on-surface synthesis on gold surfaces.

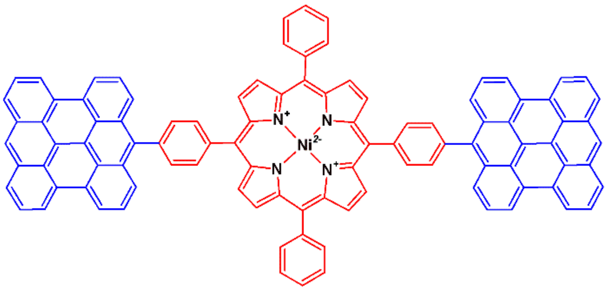

Figure 3.3: *Hetero-junction of Ni-porphyrin with 7-AGNR*

This chapter is focused on scanning tunnelling microscopy imaging of Ni-DBrTPP on Au (111) and the formation of porphyrin integrated 7-AGNRs on gold surfaces. The effect the substrate has on alignment of the structures is compared for Au(111) crystal and Au(788) vicinal surface. Having unidirectional GNRs and heterojunctions is necessary for angle resolved characterisation techniques such as ARPES. Alignment of the GNRs is also desirable for transferring and integrating the structures on semiconducting surfaces for device fabrications.

3.2 Experimental Details

The evaporation temperatures and deposition rates of Ni-DBrTPP were calibrated by sublimation of the molecules onto a pristine Au (111) surface from a homemade K-cell at 330 °C ±2 °C for 15 minutes in a preparation chamber with a base pressure of $1x10^{-8}$ mbar. The surface coverage is then estimated from analysis of STM images using the flooding tool in the WSxM software. The deposition conditions used in this experiment yielded approximately 0.1 monolayers (ML). At this coverage and at room temperature individual Ni-DBrTPP molecules cannot be imaged on the Au(111) surface due to the diffusion on the surface. The substrate was then annealed at 200 °C to debrominate the porphyrins resulting in chain-like structures. The sample cooled to room temperature and STM images of the porphyrin chains on the Au(111) surface were collected.

The second experiment involved a co-deposition of DBBA and Ni-DBrTPP simultaneously onto a clean Au (111) crystal. The DBBA and Ni-DBrTPP were sublimated at 200 ± 2 ° C and 330 ± 2 ° C, respectively, from separate K-cells for 15 minutes. The estimated surface coverage for this deposition is 0.9 – 1.1 ML with an approximate composition of 60% DBBA and 40% porphyrin. After deposition the sample was annealed at 100 °C for ten minutes to uniformly diffuse material on the crystal. The sample was then annealed at temperatures of 200 °C, 300 °C, and 400 °C for ten minutes at each step to instigate the different stages of GNR formation. The sample was cooled to room temperature after each annealing stage before collecting STM images.

For the Au(788) crystal two separate co-depositions of DBBA and Ni-DBTPP were carried out to achieve a ~0.5 ML and ~1.0 ML surface coverage with a 3:2 ratio of DBBA to porphyrin. The sublimation temperatures of the K-cell were the same as those used for the depositions on Au(111). Material was sublimated for 7.5 minutes to acquire the 0.5 ML coverage and 15 minutes for the monolayer. The annealing procedure described for the Au(111) sample was repeated for the Au(788) crystal.

3.3 Results and Discussion

3.3.1 NiDBTPP on Au(111)

The individual NiDBTPP molecules cannot be imaged at room temperature due to molecules diffusing on the surface and tip-molecule interaction. Therefore, the porphyrins must be dehalogenated to allow neighbouring porphyrins to form covalent bonds resulting in porphyrin chains, the additional mass of the nanostructure reduces the diffusion for the porphyrin chain on the surface, allowing the STM tip to image the structure at room temperature. Dehalogenation occurs by annealing at 200 °C. The dibrominated Ni-TPP molecules bond together and the increase in mass of the molecular structure reduces the level of diffusion on the surface allowing STM imaging. At this stage, the porphyrins form semi-linear 1-D chains as shown in figure 3.4. Another effect caused by the H-H repulsion is the rotation of the phenyl rings effectively raising the porphyrin macrocycles on the surface.

The STM images in figure 3.5 show the porphyrin chains on the Au(111) surface following annealing at 200 °C. The estimated surface coverage for figure 3.5 (a) is approximately 0.07 ML ± 2%. The porphyrins can be seen to preferentially align along the step-edges. The step-edges have a higher surface energy and act as nucleation sites for the molecular nanostructures [3].

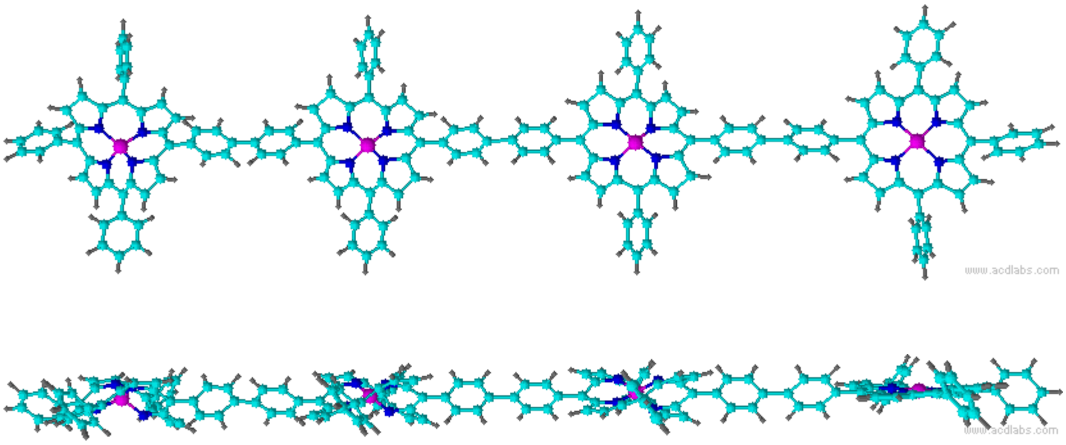

***Figure 3.4**: (top) Ball and stick model of debrominated porphyrins in a semi-rigid linear chain. (Bottom) Side-view of porphyrin chain shows the non-planarity of the chain caused by the rotated phenyl rings. Colour code: C: cyan, H: grey, N: blue, Ni: magenta*

The image in figure 3.5 (b) shows six porphyrin chains on the lower terrace anchored to the step-edge. Chains are also observed forming on the terraces. The porphyrin molecules have formed semi-rigid 1-D chains. In some cases the short chains are imaged as fan-like structures This so-called "Christmas tree effect" has been observed by Lafferentz *et al.* [4] and is due to the chain anchoring at one of end of the structure while the un-anchored end oscillates about the anchor point at a rate faster than the scan rate of the STM tip (532.67 nm.s^{-1}). This "Christmas tree effect" is seen on both the lower and upper sides of the step-edge which is evidence of weak interaction between the porphyrin and the gold atoms on the terrace.

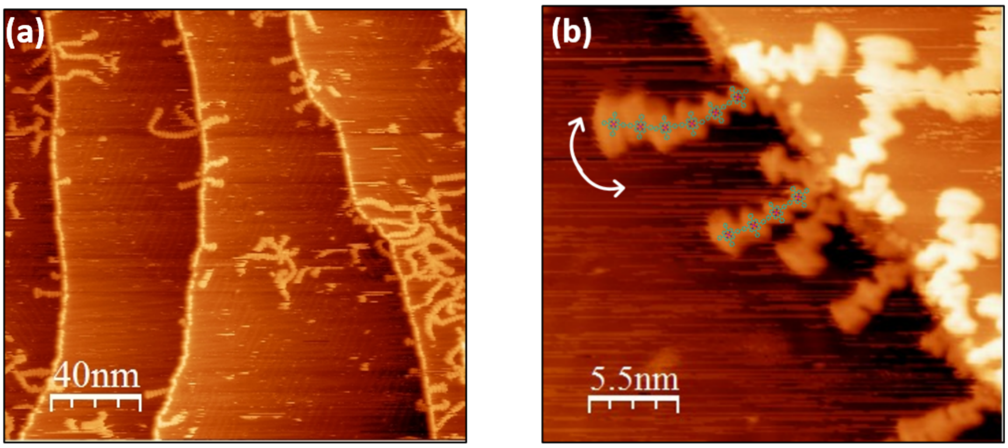

Figure 3.5: *Porphyrin chains on Au (111). (a) 200 nm × 200 nm image with 0.07 ML (V=-0.82 V, I=0.12 nA) (b) 27.5 nm × 21.5 nm image of porphyrin chains on step-edge with chemical model overlayed. (V=0.61 V, I=0.12 nA)*

Ni-TPP molecules undergo cyclo-dehydrogenation at approximately 300 °C. The dissociation of hydrogen allows additional bonds to form between the porphyrin macrocycle and the phenyl rings as shown in figure 3.6 The result of cyclo-dehydrogenation in this context is the formation of five-membered rings which disrupts the aromatic nature of the porphyrin. Disrupting the aromaticity of the structure by forming five membered rings may have a negative effect on the transport properties, with respect to applications such as a chemical sensor device, by reducing the conductivity at the junction between the GNR and the active sensing component, the porphyrin.

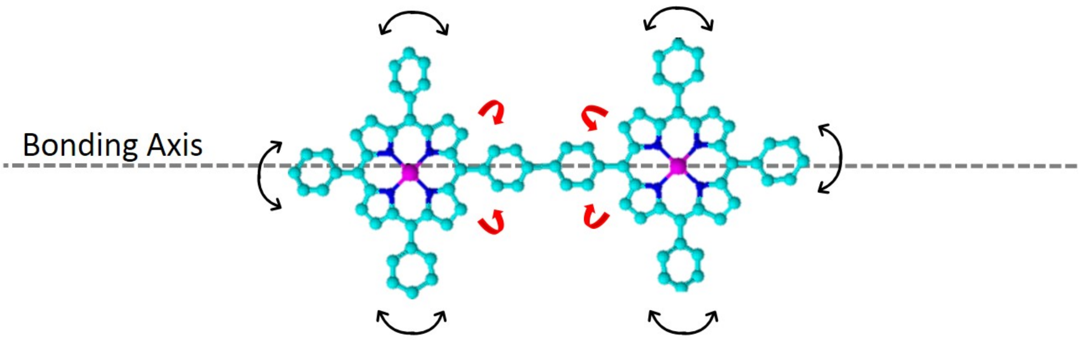

Figure 3.6*: Chemical model of two bonded porphyrins. Red arrows show the possible bending at the junction and black arrows show degrees of freedom of phenyl rings.*

Figure 3.7 shows the two possible orientations of a two-porphyrin homo-junction. The model in figure 3.7 (a) is an example of both phenyl rings at the junction forming five-membered rings at the 8 and 2 beta positions on the macrocycle. In figure 3.7 (b) the junction phenyl rings bond to 8 and 18 beta positions on the macro-cycle. A single, isolated dehydrogenated porphyrin has four variables (four phenyl rings) with two degrees of freedom, meaning there are 16 possible orientations for a single Ni-TPP molecule. However, because the porphyrin has four-fold symmetry only a quarter of these orientations are unique, the rest are mirror images, which leaves four possible configurations.

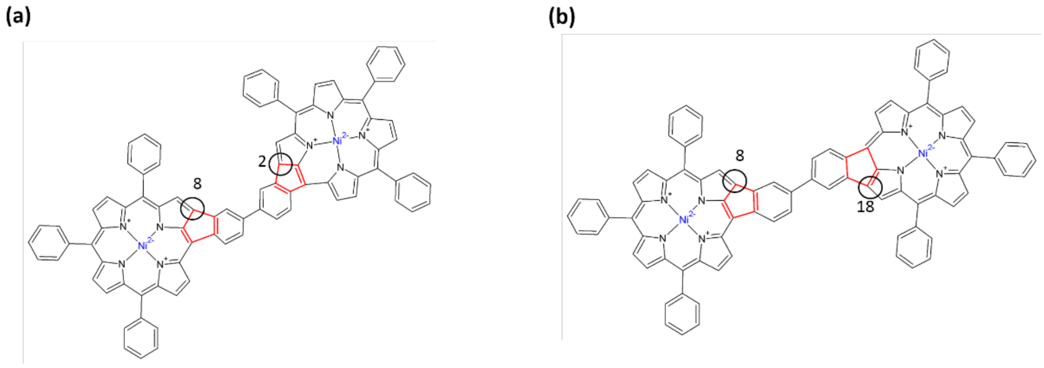

Figure 3.7*: Porphyrin homo-junctions. (left) Phenyl ring bonding to equivalent positions on the macrocycle (right) Bonding of phenyl rings to non-equivalent positions on the macro cycle of the porphyrin*

Figure 3.8 shows images of dehydrogenated TPP chains following annealing at 300 ^{o}C. In figure 3.8 (a) a linear chain in the centre of the image is similar to the rigid chains with hydrogen intact as seen in figures 3.5. However, on the left side of the image a disordered chain is clearly seen and is indicative of dehydrogenated porphyrin chains. This is further exemplified in figure 3.8 (b) where two porphyrin chains containing several units form corrals. The "herringbone" surface reconstruction of the Au (111) surface is visible outside of the porphyrin rings, while inside the corral of porphyrins a different surface reconstruction is observed.

Unambiguously distinguishing the orientation of porphyrin chains can be challenging due to the small differences between similar structures. Using the distance between the phenyl rings at the 5 and 15 positions as a metric to ascertain the geometry of a dehydrogenated porphyrin chain is not ideal as the distance between these phenyl rings when bonded to the 3 and 17 beta positions is 1.71 nm ±0.15 nm while the distance between phenyl rings bonded at the 3 and 13 positions is 1.75 nm ±0.15 nm, as shown in figure 3.8 (c), making the two orientations unresolvable with the STM tip. A plot of the line profiles indicated in figure 3.8 (b) is displayed in figure 3.8 (e) and shows the range of values for distances between the phenyl rings on opposite sides of the bonding axis. Alternatively, measuring the distance from the phenyl rings at the 5 or 15 positions to the bonding axis of the chains provides a better metric for distinguishing orientations as displayed in the chemical model in figure 3.8 (d). Three distinct lengths are identified; 0.39 nm ±0.10 nm, 0.79 nm ±0.10 nm and 1.16 nm ±0.10 nm which are resolvable with the STM tip. The coordination geometry of four units in a porphyrin chain are unambiguously identified using this method as shown in figure 3.8 (f).

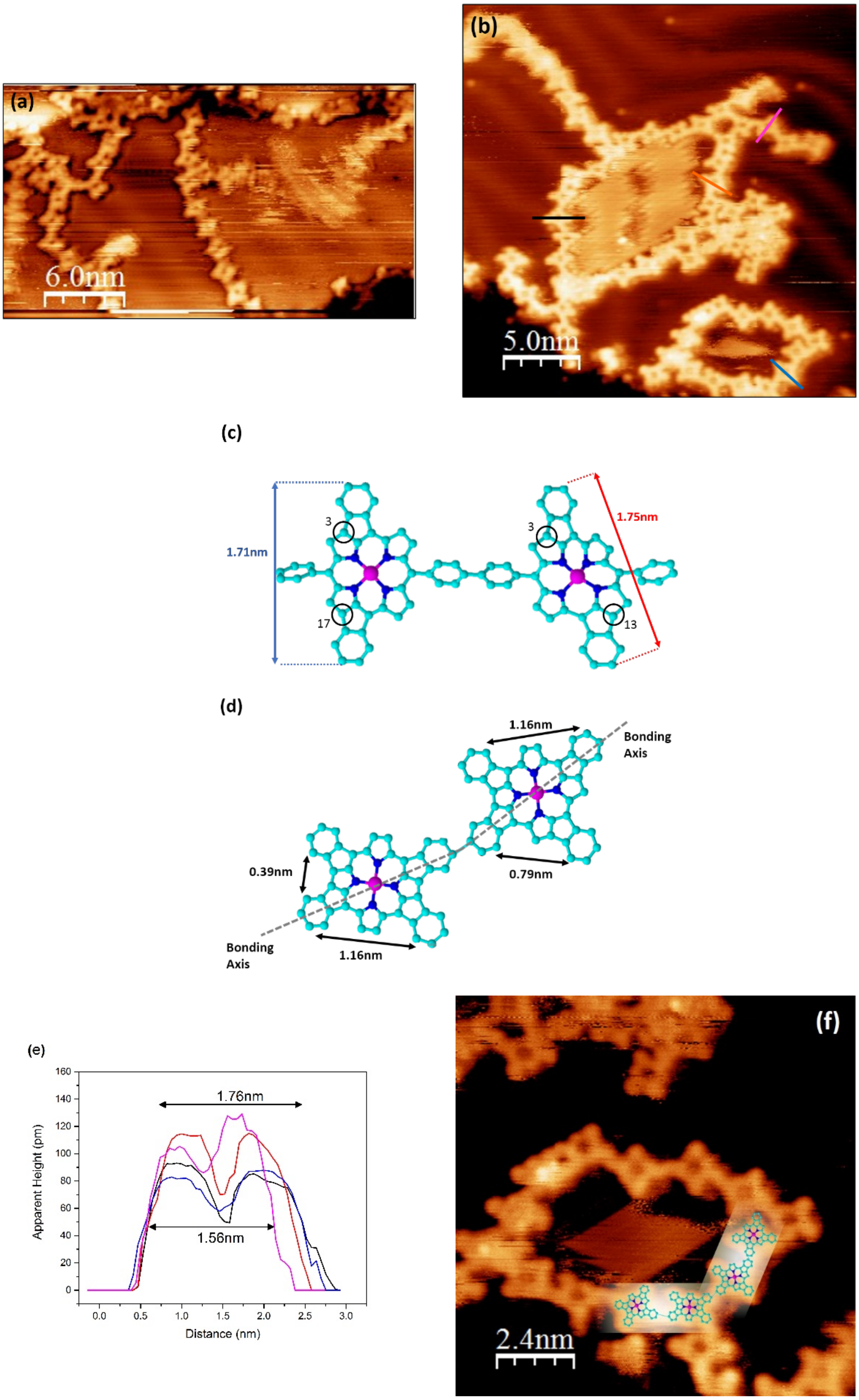

Figure 3.8: *TPP Chains. (a) TPP chains (V=-0.37 V, I=0.07 nA) (b) TPP chains in corrals with line profiles (V=0.39 V, I=0.07 nA) (c) Distance between phenyl rings in the 3 and 17, 3 and 13 positions. (d) Distances between phenyl rings and bonding axis. (e) Line profiles from (b). (f) STM image with model of four-unit TPP chain overlaid. (V=-0.35 V, I=0.07 nA)*

The surface reconstruction observed inside the corrals shown in figure 3.8 (b) is observed for other enclosed regions and further examples are shown in figure 3.10 (a) and (b). This 2×1 reconstruction is only observed in areas enclosed by porphyrins. Three reconstructed domains can be seen in the region of figure 3.10 (a) highlighted by the blue box. The adjacent domains are at an angle of 120^o with respect to each other reflecting the three prominent crystal directions of Au (111) surface. There is also a limit to the size of the 2×1 domains. The white dashed lines in figure 3.10 (a) highlight the width of these regions is 4.8 nm ±0.3 nm. Figure 3.10 (b) is an enlarged area of the white box in figure 3.10 (a) and shows a phase mismatch between adjacent domains of 0.2 nm ±0.05 nm. The line profile of the white dashed line in figure 3.10 (b) is shown in figure (c) and shows the spacing between rows is 0.49 nm ±0.05 nm. The nature of this phenomenon is unclear, however, from several observations the reconstruction is independent of deposited molecules as it has been observed for DBBA, OBO (see section 4.3.4). It is also independent of the STM tip bias. To our knowledge no reports of reordering of the Au(111) surface are found in the literature although it has been confirmed through private correspondence with L. Grill and presented in Ph.D theses by T. Carpy and C. Doyle [5, 6]. Surface reordering of the Au(110) surface in the presence of organic molecule adsorbents has been noted in the literature [7, 8]. The mechanism behind this reordering is unknown. It is possibly due to local changes of the electronic structure of the surface gold atoms due to charge transfer with the deposited molecules or a result of an energetically favourable reconstruction in the presence of molecules after the surface is annealed at 300 ^{o}C. This is still an open question and further study into this phenomenon is needed.

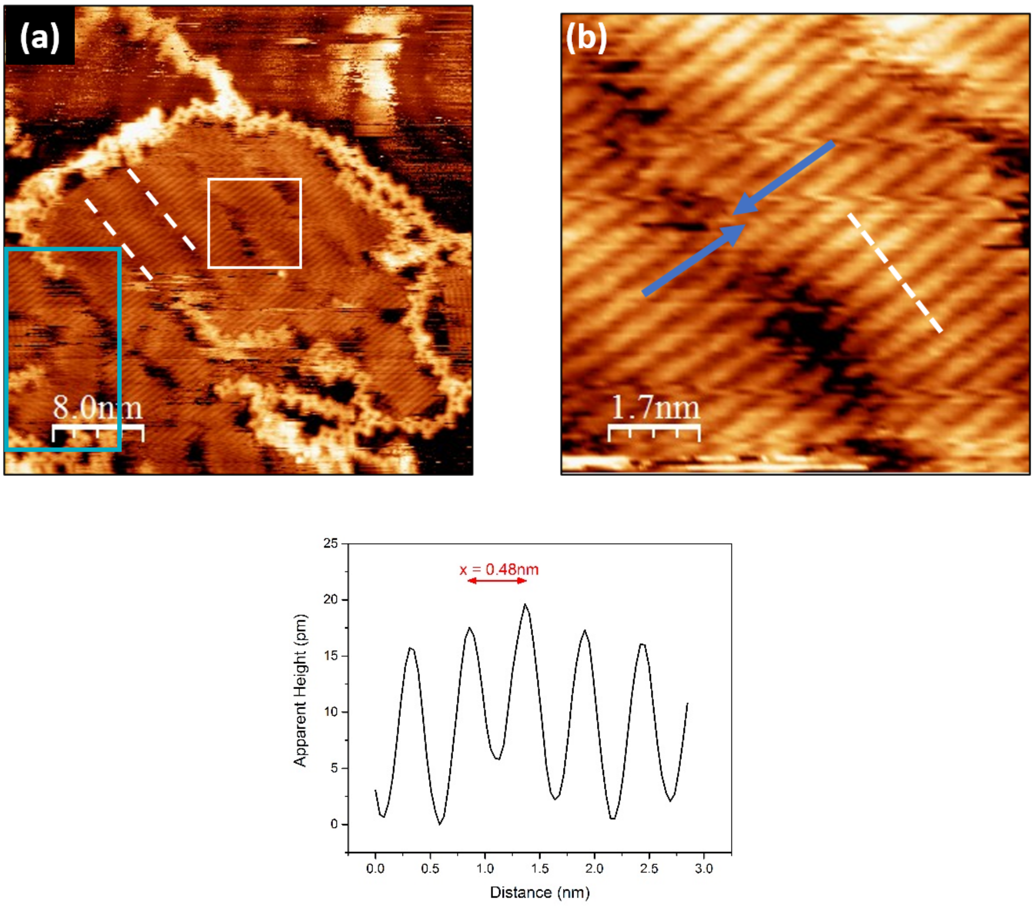

Figure 3.9: *Porphyrin chains and surface reconstruction. (a) 40 nm × 40 nm of TPP chains (V=-0.5 V, I=0.1 nA). (b) Magnified region of (a) (V=-0.51 V, I=0.10 nA). (c) Line profile from (b).*

3.3.2 Co-Deposition of DBBA and NiDBTPP on Au(111)

Figure 3.10 (a) shows a large area STM image of DBBA and NiDBTPP co-deposited on the Au(111) surface. Four domains of self-assembled material are identified. Regions labelled 1 and 4 are parallel with each other while 2 and 3 form rows at 120° with respect to regions 1 and 4, respectively. This is likely due to the molecules aligning along the three prominent directions of the Au(111) surface which are at 120° to one another. At the boundaries of these domains there is a phase boundary between both species of molecules which the STM tip images poorly. Figure 3.10 (b) shows in greater detail the well-defined phase separation of self-assembled DBBA molecules while the porphyrins are not sufficiently ordered to be imaged. From figure 3.10 (a) an estimated 1.1 monolayer of material is deposited and the ratio of surface coverage of DBBA to NiDBTPP is approximately 3:2 for the deposition parameters outlined in section 3.2. Figure 3.10 (c) shows a high resolution STM image of densely packed rows of DBBA with an inset of the Fast Fourier Transform (FFT). The distance between adjacent rows is 4.1 nm ±0.1 nm as indicated by the white dashed lines in the figure and the average intermolecular distance is 1.5 nm ± 0.08 nm. These measurements were taken with line profiles and verified with the FFT calculation. The individual DBBA molecules are resolved in figure 3.10 (d). Two rows are overlaid with a ball-and-stick chemical model where three molecules are identified in each row. The two outer molecules of each row are parallel to each other and form a 120° angle with the centre molecule as shown in the model in figure 3.10 (e). The unit cell is highlighted by the blue rectangle in figure 3.10 (d), with unit cell vectors **a** and **b** of length 8.5 nm and 1.5 nm, respectively. The area of the gold surface covered by a single DBBA molecule is calculated by measuring the area of a row and dividing by the number of monomers contained within. Given that a row is 4.1 nm ±0.10 nm wide and the intermolecular distance within a row is 1.5 nm ±0.08 nm the area occupied by 30 DBBA molecules is 61.5 nm^2 ±0.33 nm^2 therefore in this self-assembly configuration a single DBBA molecule occupies an area of 2.06 nm^2 ± 0.03 nm^2. This self-assembly differs from the previously observed monolayer of DBBA on Au(111) shown in figure 3.2 (a) where surface density is 1.8 nm^2 ± 0.02 nm^2 per DBBA molecule. The reason for the discrepancy could either be due to the quantity of material deposited or the presence of the Ni-porphyrins. The self-assembled orientation and surface coverage of molecules on surfaces has been shown to be coverage dependent with Tian *et al.* showing two unique orientations resulting from a 0.8 ML and 1.2 ML surface coverage of DBBA on Au (111) [9]. In this paper the authors also showed that over time the adsorbents can reassemble into more stable orientations.

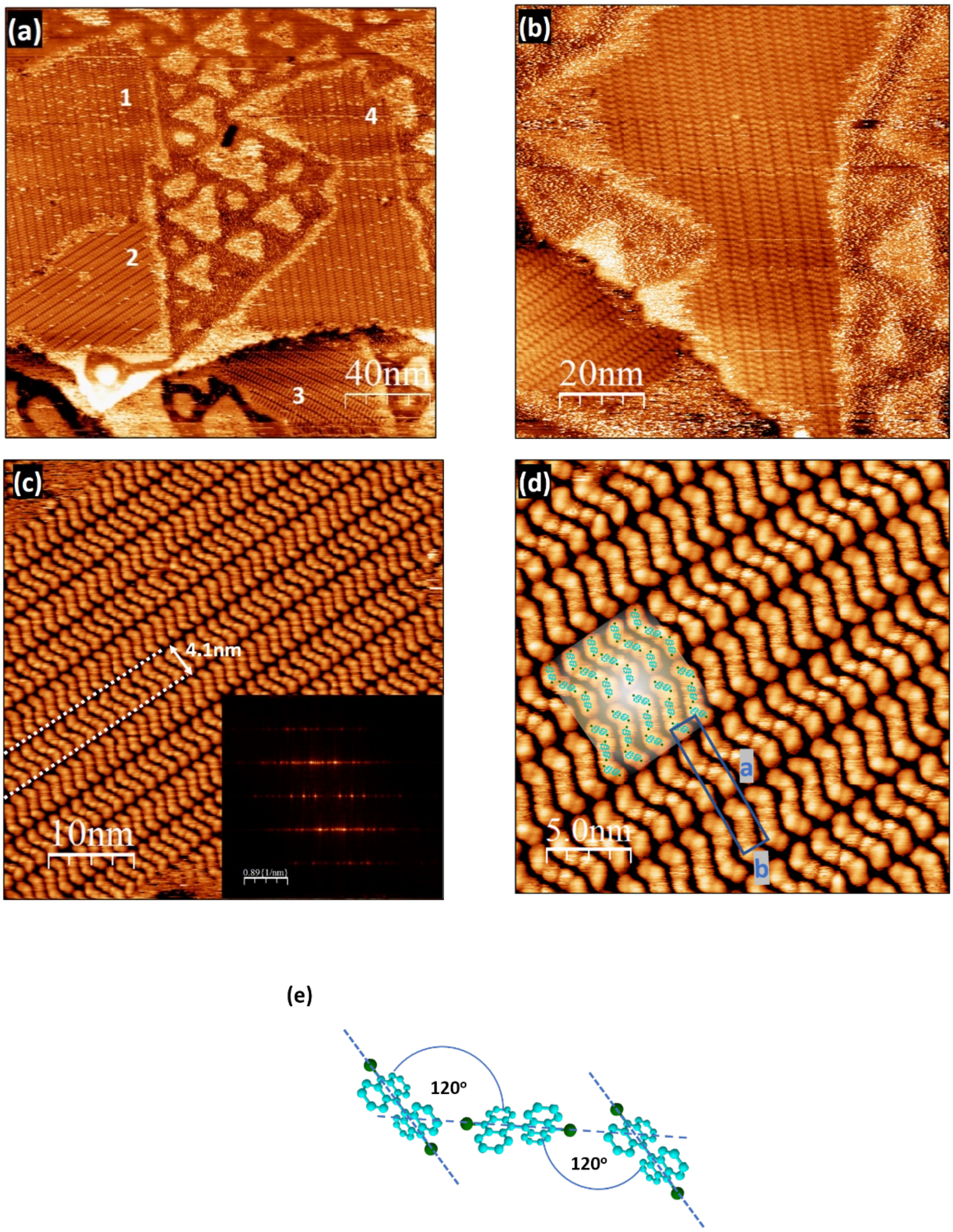

***Figure 3.10**: DBBA and Ni-DBTPP co-deposited on Au(111). (a) 200 nm × 200 nm (V=-1.0 V I=0.10 nA). (b) 100 nm × 100 nm (V=-1.48 V I=0.3 6nA). (c) 50 nm × 50 nm V=1.5 V I=36 pA) with FFT inset. (d) 25 nm × 25 nm (V=-1.5 V I=22 pA). (e) Model of DBBA self-assembly.*

Figure 3.11 (a) and (b) show the effect of tip bias on STM imaging. Figure 3.11 (a) was taken with a positive voltage applied to surface and therefore shows the unoccupied states in the molecules. Figure 3.11 (b) was recorded with a negative biased on the sample and therefore it is imaging filled states in the molecule. These figures exemplify how identifying DBBA imaged under different tip parameters can be non-intuitive. These images also demonstrate the importance of STM data interpretation as the local density of states and not specifically topographical information.

A second self-assembled DBBA structure is also observed on this surface in the form of hexamer 'florets' as shown in figure 3.11 (c) and (d). Figure 3.11 (c) shows these hexamers forming alongside rows of DBBA that are one, two and four molecules wide. These hexamer structures have been observed previously on the Ag(111) surface by Simonov *et al.* [10] and Shen *et al.* [11] and on the Au(111) in the presence of a monolayer of bismuth [12][9]. To the best of our knowledge this hexamer orientation has not been reported previously for Au(111). The rows of DBBA molecules in between the hexamers have a different orientation to that shown in figures 3.11 (a) and (b). Figure 3.11 (e) shows an example of two hexamer rows side by side. The model in figure 3.11 (f) exemplifies the self-assembly of the hexamers and rows. The hexamers all appear to have the same orientation with respect to the surface while the individual DBBA molecules in rows either align perpendicular to the direction of the hexamers as illustrated by the red dash line in figure 3.11 (f) or form parallel pairs at a 60° angle to the hexamers, shown by the blue dash line in the figure. The distance between the parallel pairs of DBBA molecules is between 0.45 and 0.55 nm. The area occupied by individual DBBA molecules under the different self-assembled structures is compiled in Table 3.1. All images appear to have local surface coverage of at least 1 monolayer. This may be due to the molecule having a degree of freedom about the central axis of the molecule where the anthracene units are connected. An illustration of the large and small footprints of DBBA is shown in figure 3.12.

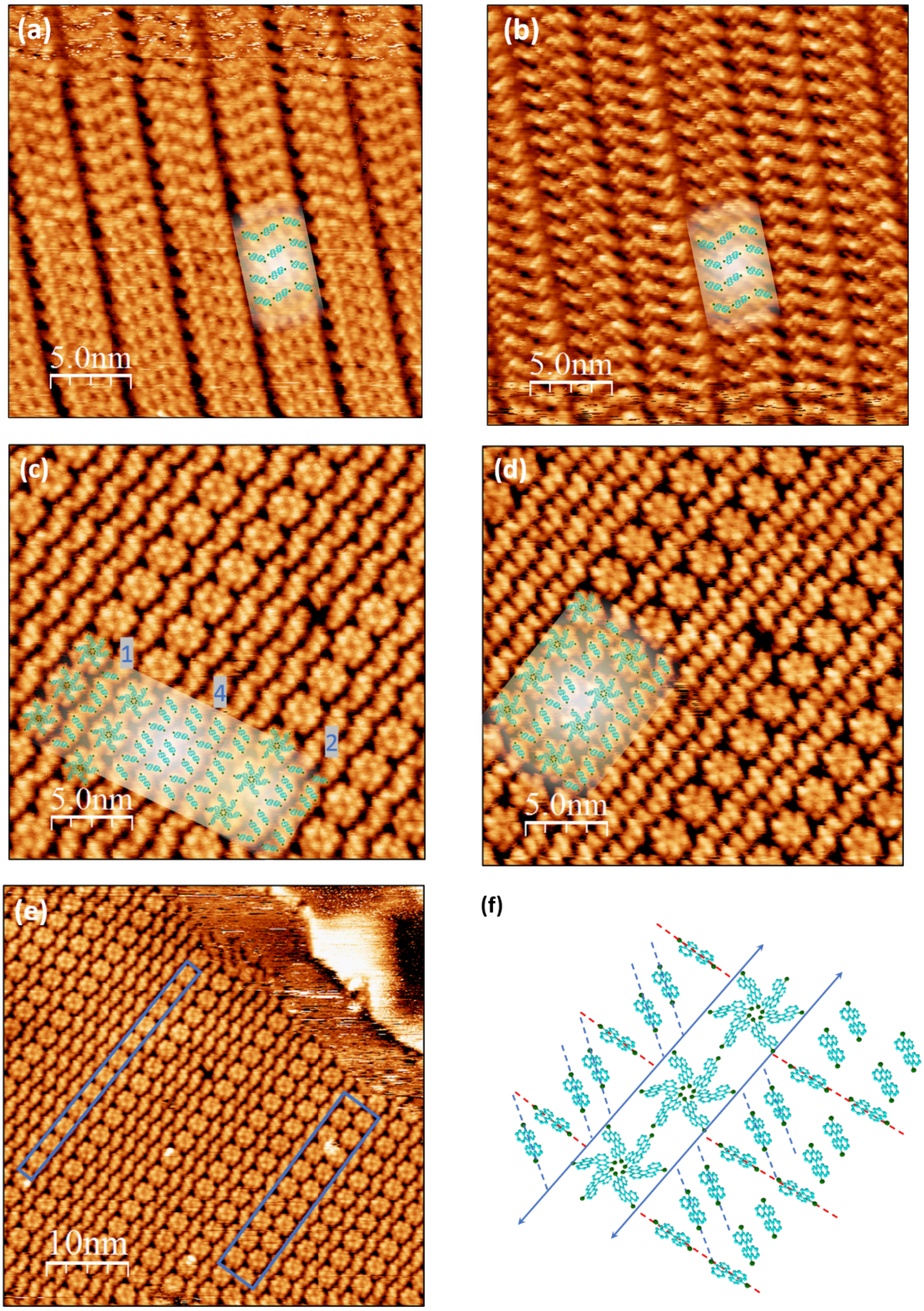

Figure 3.11: *DBBA self-assembly in Au(111): (a) 25 nm × 25 nm (V=1.48 V, I=36 pA). (b) 25 nm × 25 nm (V=-1.48 V, I=36 pA). (c) 25 nm × 25 nm (V=-1.50 V, I=84 pA) (d) 25 nm × 25nm (V=1.50V, I=84pA). (e) 50nm × 50nm (V=-1.50 V, I=86 pA) (f) Chemical model of hexamer and rows.*

***Table 3.1:** Table of surface area occupied by DBBA molecule*

Self-assembly	**Figure**	**Area Occupied (nm^2/DBBA)**	**Environment**
Self-assembly A	Fig. 3.2 (a)	1.566	DBBA
zig-zag rows	Fig. 3.11 (d)	2.081	DBBA + Por.
Parallel/Perp.	Fig. 3.12 (c)	1.623	DBBA + Por.
Hexamer (single row)	Fig. 3.12 (e)	1.039	DBBA + Por.
Hexamer (double row)	Fig. 3.12 (e)	0.976	DBBA + Por.

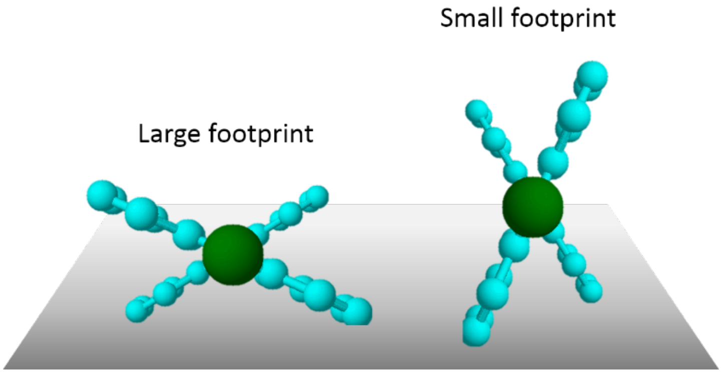

***Figure 3.12**: Drawing of large and small DBBA footprints.*

Annealing the sample at 200 °C breaks the C-Br bond on the DBBA and the Ni-DBTPP molecule and results in the formation of polyanthracene chains with integrated porphyrins as shown in the model in figure 3.13. The steric hindrance caused by the repulsion between hydrogen atoms on the porphyrin and polyanthracene restricts the degrees of freedom of the heterojunction to one linear chain orientation. Although the chains are not rigid, curved chains are seen when neighbouring chains grow into each other. In the STM images shown in figure 3.14 (a) – (e) the porphyrins that can be unambiguously identified are highlighted in white. It is clear from figure 3.14 (a) – (d) that there are more polyanthracene units in the chains than porphyrins. This is because annealing the sample not only debrominates the molecules, but also desorb the more weakly bonded porphyrins from the surface. As was shown in section 3.3.1, the porphyrin has a weak interaction with the Au(111) surface and as a result fewer porphyrins remain on the surface. Further to this point, due to the non-planar nature of the chain/porphyrin, the structure weakly interacts with the surface and as was seen with porphyrin chains in section 3.3.1, can diffuse on the surface, as highlighted in blue in figures 3.14 (a) and (d).

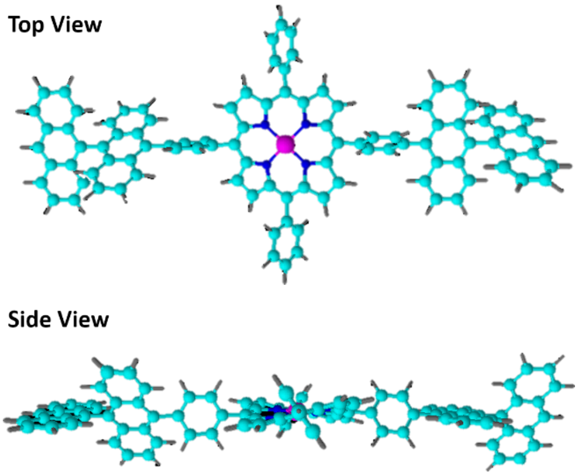

***Figure 3.13**: Chemical drawing of polymer chains with integrated porphyrin*

As with the self-assembly of the precursor molecules, the polymer chains are aligned along three directions at 120° to each other. There is also evidence of chains growing in the second layer where the brighter of the chains appear to sit on top of a layer in contact with surface. The characteristic alternating anthracene feature of DBBA-chains in the second layer is identified in the white box in figure 3.14 (d) and shown in greater detail in figure 3.14 (e). A line profile of figure 3.14 (d) is shown in figure 3.14 (f) and shows that the separation of protrusions is 0.88 nm ± 0.02 nm of in agreement with similar studies who reported a value of 0.90 nm for the separation [10].

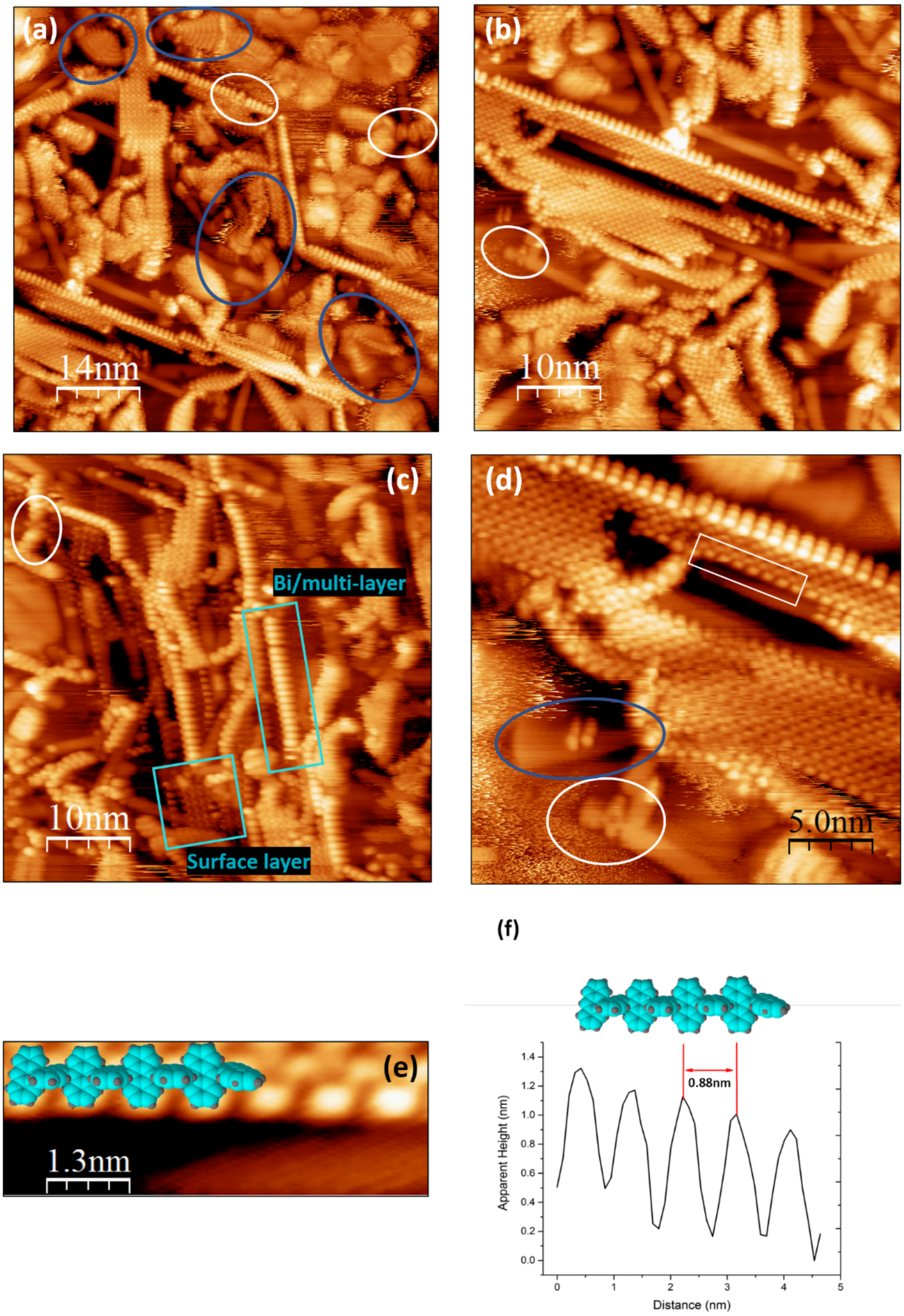

***Figure 3.14**: Functionalised polymer chains on Au(111). (a) 70 nm × 70 nm (V=-0.23 V, I=28 pA). (b) 50 nm × 50 nm (V=-0.28 V, I=22 pA) (c) 50 nm × 50 nm (V_t=-0.20 V, I=20 pA) (d) 25 nm × 25 nm (V=-0.06 V, I=17 pA) (d) 8.0 nm × 2.6 nm (V=-0.06 V, I=17 pA) (e) Line profile of (e).*

Polymer chains with integrated porphyrins can adopt only one configuration, however after cyclo-dehydrogenation the number of orientations that the 7-AGNR-porphyrin structure can form increases considerably. To differentiate between the different orientations the structures can be classified as symmetrical and non-symmetrical predicated by which porphyrin macrocycle coordinate the dibrominated phenyl ring bonds to when forming a 5-membered ring. Symmetrical junctions are formed at the 2 (18) and 8 (12) beta positions on the macrocycle, while the non-symmetrical junction forms at the 18 (2) and 8 (12) positions as illustrated in figure 3.15[4]. Further to this, a fluoranthene unit is always formed at the heterojunction between the 7-AGNR and the porphyrin phenyl ring. The fluoranthene unit contains a 5-membered ring as shown in figure 3.16.

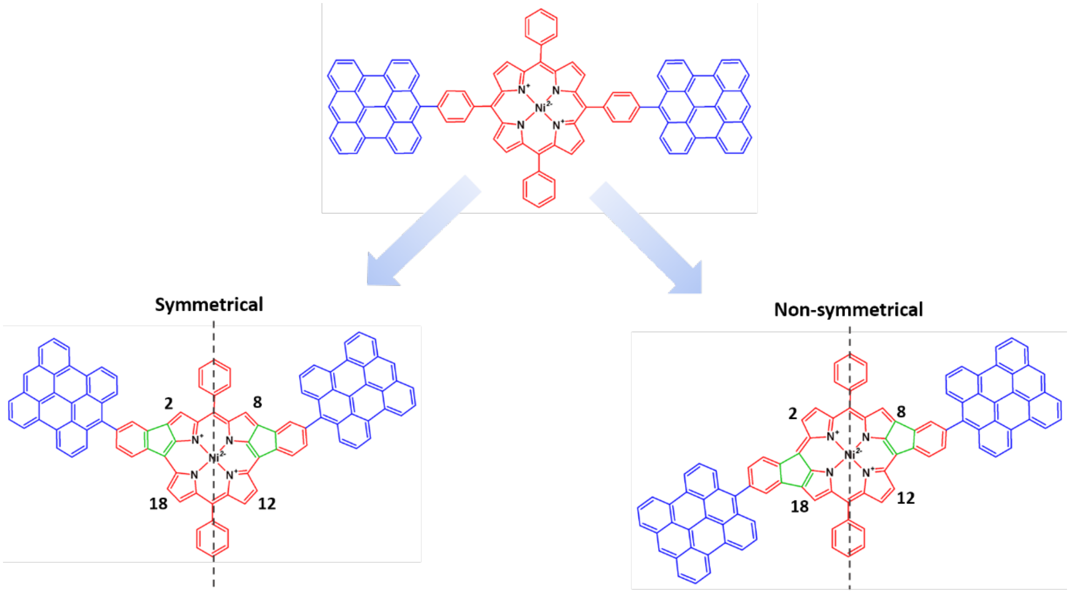

Figure 3.15: *Symmetrical and non-symmetrical heterojunctions*

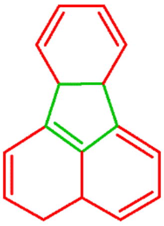

Figure 3.16: *Fluoranthene unit*

---

[4] Numbers in parentheses represent equivalent coordinates.

As with the junctions on porphyrin chains, these 5 membered rings disrupt the aromaticity which may result in a change of the transport properties at both the GNR-phenyl ring junction and the phenyl ring-macrocycle junction. The phenyl rings at the 5 and 15 positions on the macrocycle may also bond to the macro cycle at the 3 or 7 and the 13 or 16 coordinates, respectively. Although the phenyl rings are not part of the heterojunction their bonding to the macrocycle may affect the energetic position of the HOMO and LUMO in the porphyrin. These structures can be classified according to the angle formed by the GNR arms with the porphyrin at the apex or by the offset between the ribbons. Figure 3.17 shows the possible orientations associated with the symmetrical structure, where the number in parentheses beneath each structure denotes the number of unique orientations taking into consideration the phenyl ring positions and the 5-memebered rings are shown in green. Angles and offsets were measured using the Chemsketch software package. For the non-symmetrical heterojunctions, both linear and angled structures are possible. The linear arrangements can have an offset of 0.31 nm or 0.26 nm ±0.01 nm as shown in figure 3.18. The non-symmetrical orientation can form angles of 145.6° or 148.8° and with the addition of the 5,15 phenyl ring orientations there are seven possible structures. Overall there are 21 possible orientations for the Ni-TPP 7-AGNR junction.

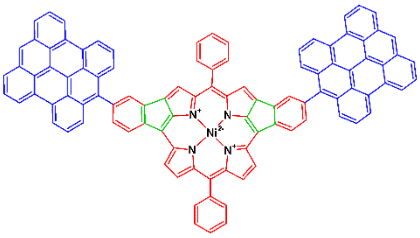

97.6°	**122.3°**	**180°**
1 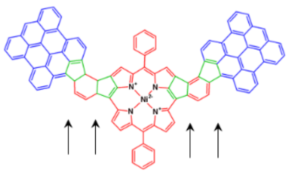 (2)	**2** 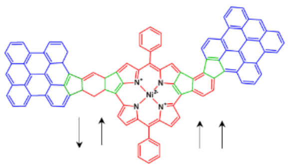 (4)	**3** 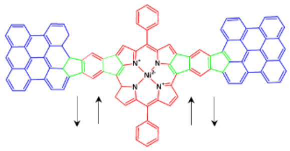 (2)

Figure 3.17: *Possible structures for symmetrical heterojunctions.*

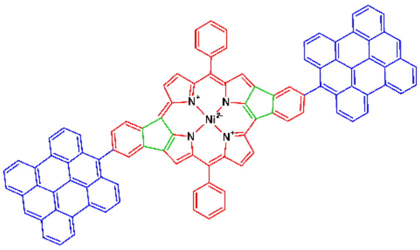

Offset: 0.31 nm	Offset: 0.26 nm
4 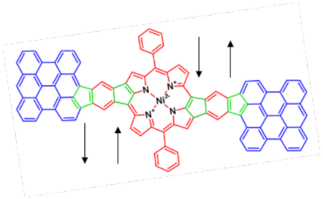 (3)	**5** 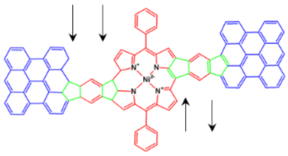 (3)

Figure 3.18: *Possible structures for linear non-symmetrical heterojunctions*

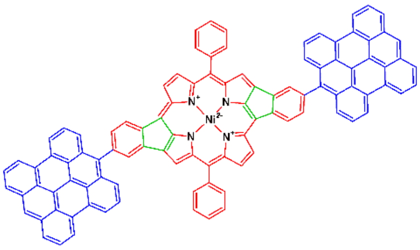

145.6º	148.8º
6 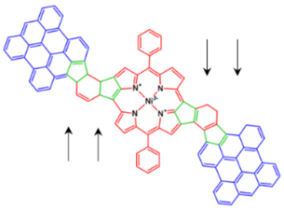 (3)	**7** 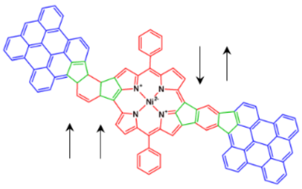 (4)

Figure 3.19: *Possible arrangements for angled non-symmetrical heterojunctions.*

Figures 3.20 (a), (b) and (c) shows Ni-TPP functionalised 7-AGNRs after annealing the sample at 300 °C for 15 minutes. In figure 3.20 (a) the surface coverage is estimated at 0.90-0.96 ML with no evidence of bi- or multi – layer material. while figure 3.20 (b) shows a different region with a small amount of polymer chains remaining in the second layer. Without the catalytic effect of the metal surface the chains in the second layer cannot undergo cyclodehydrogenation. This requirement for a metal surface for on-surface synthesis of devices has been reported in the literature [13], specifically by Xiao *et al.* who attempted unsuccessfully to grow GNR from DBBA on a layer of previously formed GNRs [14] and Berner *et al.* who attempted a similar procedure on the Ge(001) surface [15]. Figure 3.20 (c) shows a 100 nm x 100 nm image with a large number of porphyrin functionalised GNRs. The highlighted regions in the figure are to guide the eye to particularly high-density regions of porphyrins. The length of the functionalised ribbons in figure 3.20 (c) are represented by histograms in figure 3.20 (d) [5]. The average length lying in the 11-15 nm category while the longest ribbon in the region shown in figure 3.20 (c) is 31 nm ±1 nm.

---

[5] Error bars in Figure 3.30 (d) calculated using the Standard Error Formula $S.E = \frac{\sigma}{\sqrt{N}}$ where σ is the standard deviation of the lengths and N is the number of counts

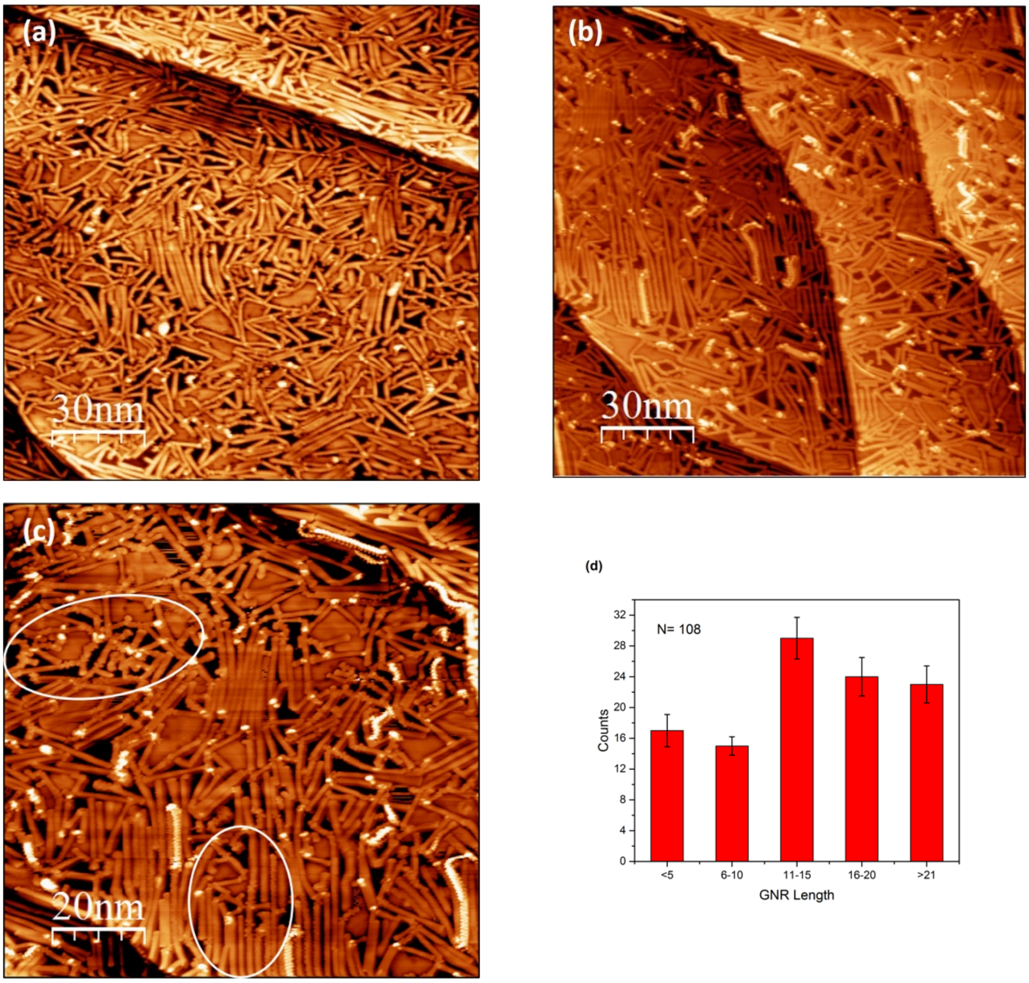

Figure 3.20: *Porphyrin Functionalized 7-AGNR on Au(111). (a) 200 nm × 200 nm (V=-1.0 V, I=48 pA) (b) 200 nm × 200 nm (V=1.0 V, I=119 pA) (c) 100 nm × 100 nm (V=1.0 V, I=1.2 nA). (d) Histogram of GNR lengths.*

In figure 3.21 (a) four polymer chains are observed on a layer of GNRs. The appear much brighter by virtue of their height compared to surround GNRs in contact with the gold surface, which supports the assertion that metallic contact is necessary to induced cyclodehydrogenation. Figure 3.21 (b) shows 16 nm × 16 nm area where porphyrin-GNR heterojunctions can unambiguously be identified. Porphyrins are highlight in green to guide the eye. A linear porphyrin functionalised GNR is identified and highlighted by the white dashed line with a measured offset of 0.27 nm ±0.05 nm. The STM image resolution is insufficient to determine whether the linear heterojunction corresponds to orientation 4 or 5 in figure 3.18 which have offsets of 0.31 nm and 0.26 nm, respectively. In figure 3.21 (c), two heterojunctions are identified, and the angle formed by the GNR arms is measured and indicated. In the centre of the image a junction with an angle of 144° ±1° is highlighted which can be identified as orientation 6 in figure 3.19 The other measured heterojunction in the figure forms an angle of 104° ±1°. The closest model to this is orientation 1 in figure 3.17 which has an angle of 97.6°. The cause for the 6.4° discrepancy is possibly due to other GNRs on the surface limiting directions of growth. Figure 3.21 (c) also shows the characteristic "cat paws", highlighted in blue, associated with 7-AGNR terminations due the high local density of states (LDOS) located at the ends of the ribbon [16].

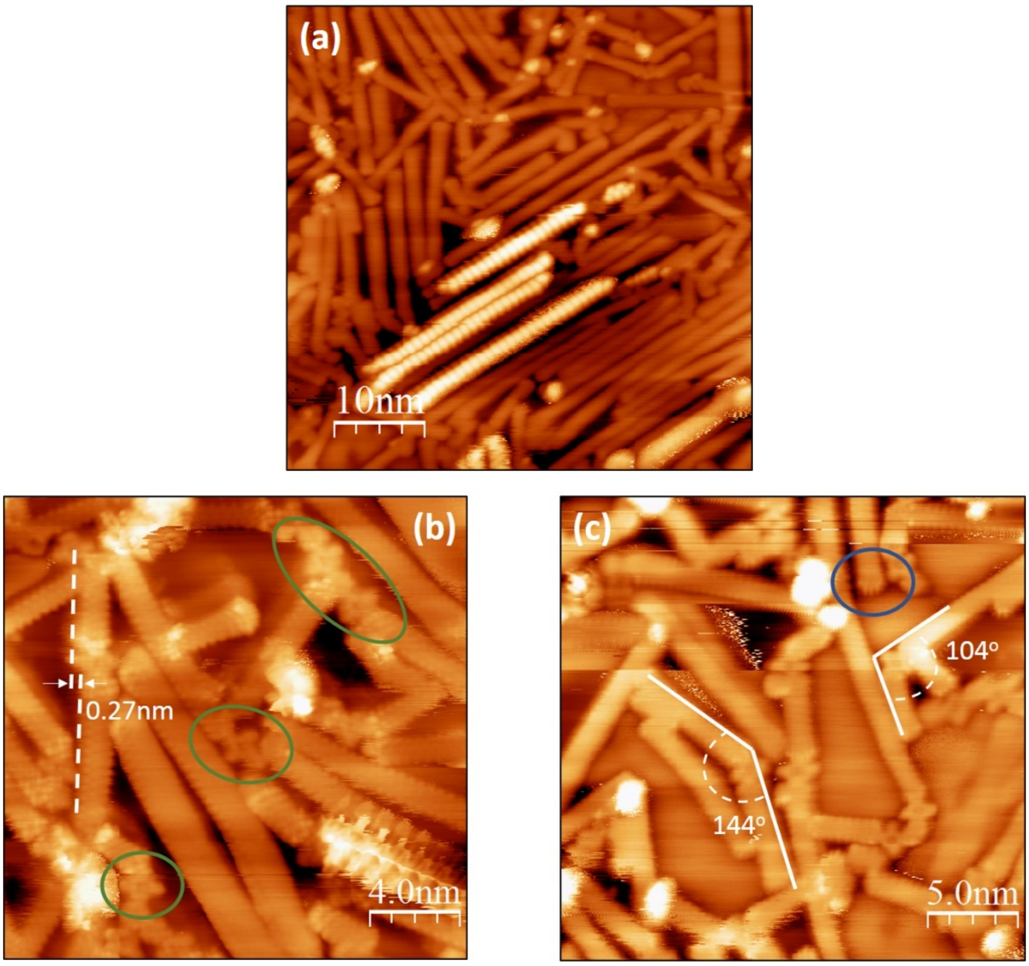

***Figure 3.21**: (a) 50 nm × 50 nm (V=1.00 V, I=80 pA) (b) 20 nm × 20 nm (V=-0.01 V, I=80 pA) (c) 25 nm × 25 nm (V=-0.37 V, I=0.9 nA)*

Figure 3.22 (a) shows a large area 200 nm × 200 nm STM image of porphyrin functionalised GNRs after annealing the sample at 400 ^{o}C. Local alignment can be seen in some regions but over the entire area the GNRs are disordered as shown by the FFT in figure 3.22 (b). The majority of bi-layer material has either desorbed or diffused on the surface as only two polymer chains are seen in the image. Figure 3.22 (c) a shows 40 nm × 40 nm region with 31 aligned GNRs. The area enclosed by the white dashed box is shown in figure 3.22 (d). The 10mV change in the imaging parameters between 3.22 (c) and (d) enhances the atomic resolution of the ribbons. Two functionalised GNRs are highlighted by the blue box and exhibit offsets of 0.22 nm ±0.05 nm and 0.28 nm ±0.05 nm respectively. An example of a distorted heterojunction is shown in the white box in figure 3.22 (d) where the surrounding GNR growth has clearly had an effect on the orientation of the heterojunction. Another feature of the GNRs observed following the high temperature annealing is dehydrogenation resulting in the lateral fusing of 7-AGNR into 14-AGNR. This was first observed by Cai *et al.* [1]. The width of 7-AGNR is 1.07 nm ±0.05 nm while the width of the 14-AGNR is 2.05 nm ±0.05 nm as measured from figure 3.22 (d). An example of the changing band structure between 7- and 14-AGNR is exemplified in figure 3.22 (e) where two 7-AGNRs overlap and fuse together forming a 5.1 nm long 14-AGNR segment. In this figure the differences in the structure of the 7- and 14-atom wide segments reflect the change in the local density of states of the ribbons. Figure 3.22 (f) shows the fusion of several 7-AGNRs to form 14-, and 21-AGNRs.

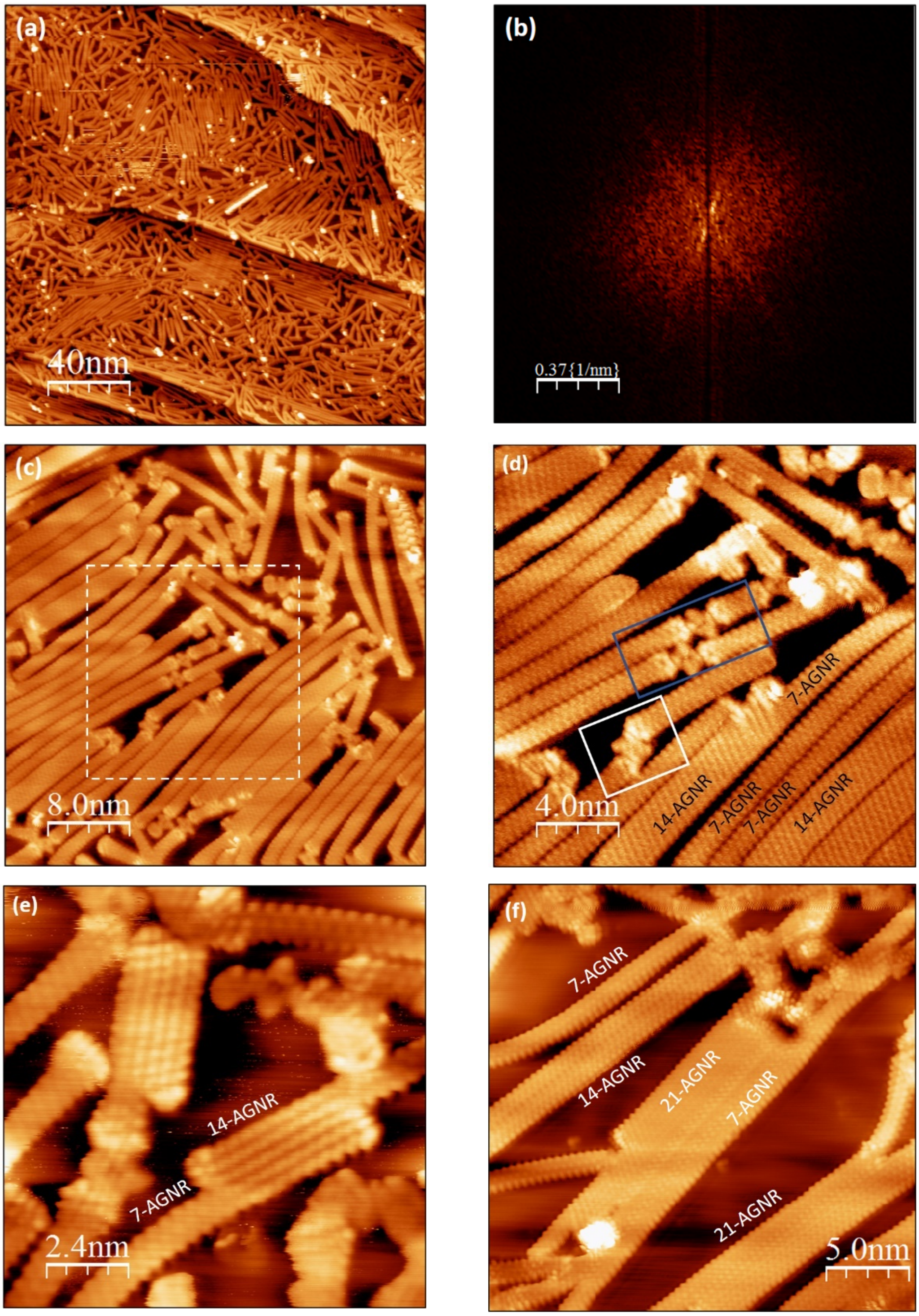

***Figure 3.22**: Ni-TPP functionalised GNRs following annealing at 400 °C (a) 200 nm × 200 nm (V=-1.00 V, I=0.10 nA) (b) FFT of (a). (c) 40 nm × 40 nm (V=-0.61 V, I=77 pA). (d) 16 nm × 16 nm (V=-0.60 V, I=77 pA). (e) 12 nm × 12 nm (V=-0.03 V, I=0.37 nA) (f) 25 nm × 25 nm (V=-0.38 V I=0.10 nA)*

Under the same deposition conditions local distribution of material varies from region to region. Figure 3.23 (a) and (b) both show 40 nm × 40 nm areas with surface coverages of 0.46 ML and 0.62 ML respectively while the number of porphyrins is approximately the same for both figures; 29 and 31 respectively. An analysis of the length distributions are shown in figures 2.23 (c) and (d) respectively. Comparing the two histograms show that both surfaces have a similar proportion of GNRs less than 10 nm long: 70% for the low-density region and 60% for the high-density region. However, there is only one GNR greater than 20 nm in the highly populated region which has a length of 22.4 nm ±0.05 nm. While in the lower coverage region eight GNRs are recorded with lengths over 20 nm with the longest GNR measured at 39.2 nm ±0.05 nm. This suggests that the more space that is available on the surface for the DBBA molecules to diffuse results in longer GNRs and there is an optimal surface density to achieve long (>20 nm) GNRs.

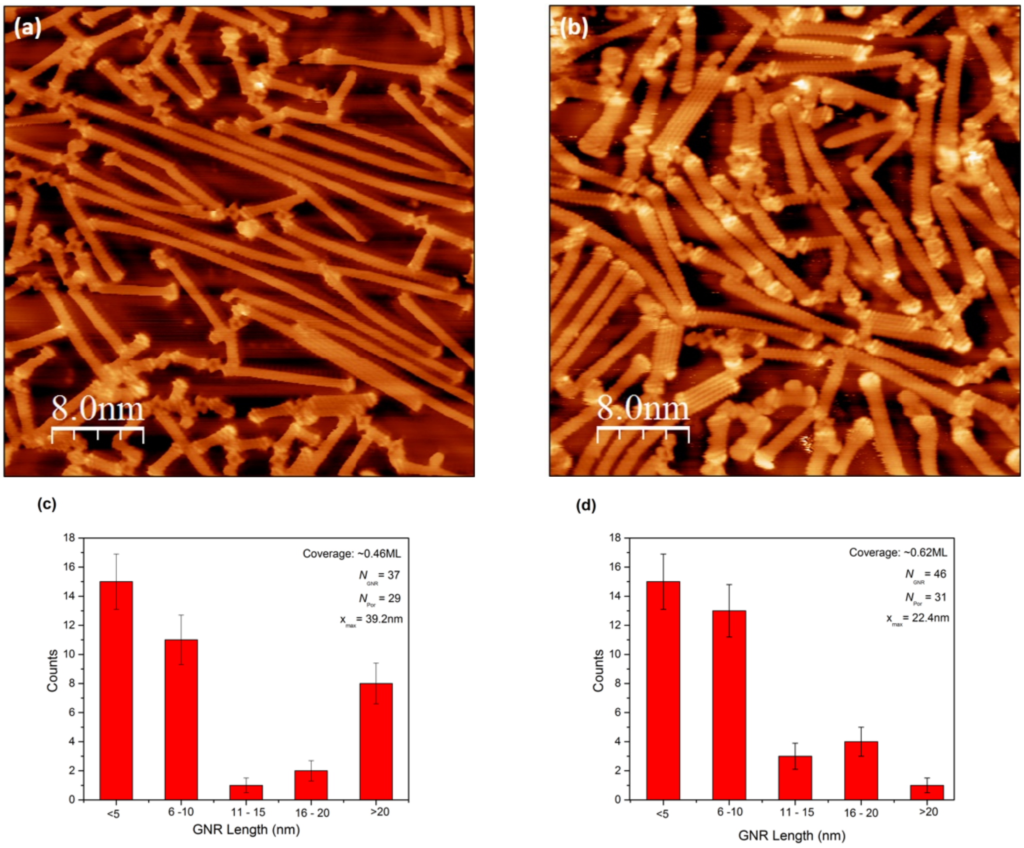

Figure 3.23*: Comparison of GNR density with length. (a) 40 nm × 40 nm (V=0.50 V I=77 pA). (b) 40 nm × 40 nm (V=0.03 V I=0.37 pA) (c) Histogram of GNR length from (a). (d) Histogram distribution of GNR lengths from (b).*

Figure 3.24 shows high resolution images of a linear functionalised 7-AGNR. The structure in figure 3.24 (a) is overlaid with a ball-and-stick chemical model of orientation **4** from figure 3.18. Atomic resolution within the ribbon can be seen in figure 3.24 (b) with bright lobes at the two junctions. Under the imaging parameters these lobes represent the HOMO at these positions, which corresponds to the location of the fluoranthene unit. These features support the hypotheses the high LDOS at the five-membered rings results in high resistance between the 7-AGNR and the porphyrin however, further studies are needed to confirm this prediction.

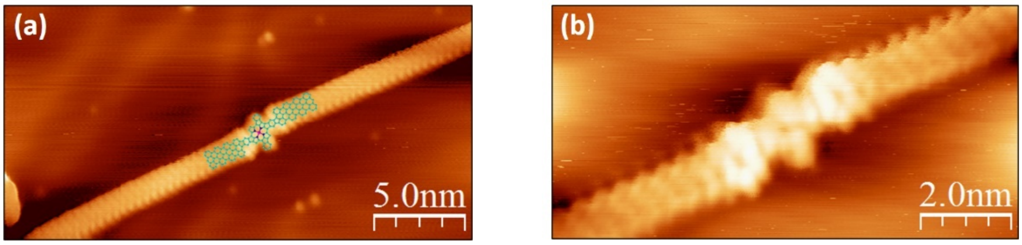

***Figure 3.24**: Porphyrin functionalised 7-AGNR on Au(111). (a) 15 nm × 25 nm (b) 6 nm × 10 nm. Both images acquired at V=-0.30 V, I=0.10 nA*

3.3.3 Co-Deposition of DBBA and NiDBTPP on Au(788)

The STM images in figure 3.25 show the evolution of DBBA and Ni-DBTPP molecules into chains and functionalised ribbons on the Au(788) surface following an initial co-deposition of material which resulted in a coverage of approximately 0.5 ML. Figure 3.25 (a) shows a 50 nm × 50 nm area with molecules accumulated on the step-edges of the vicinal surface. The line profile in figure 3.25 (b) shows that the average spacing between the rows is 4.3 ± 0.8 nm which is in agreement with the accepted value of 3.9 ± 0.8 nm for the terrace width of Au(788) [17]. The individual DBBA and porphyrin molecules cannot be identified in figure 3.25 (a) and due to the low surface coverage, the material is free move and images poorly. Figure 3.25 (c) was acquired after dehalogenation and the material on the step-edges forms polymer chains although the orientation of the chains on the step-edge and/or imaging parameters does not present the characteristic alternating protrusions associated with chains formed from DBBA. Figure 3.25 (d) shows a composite image of (c) and the derivate of (c) which shows segments of chains with integrated porphyrins. The region highlighted in the figure is attributed to porphyrin molecules incorporated in the chains. Despite the poor image quality, the Au(788) vicinal surface appears to have a templating effect on the formation of the polymer chains. Figure 3.25 (e) and (f) were recorded following cyclo-dehydrogenation. The structures shown on the surface in figure 3.25 (e) are disordered and no longer aligned along the step-edges. Two 7-AGNR segments are identified in figure 3.25 (f), one ribbon lies perpendicular to the step-edge and the other ribbon crosses the step edge at a shallow angle. A three-porphyrin chain bonded to a 7-AGNR is identified in the image and appears as a the fan-like structure similar to that observed in figure 3.6 (b). The mechanism that results in the chains aligned parallel to the step edges becoming disordered ribbons is not fully understood, however the density of material on the surface appears to play a role.

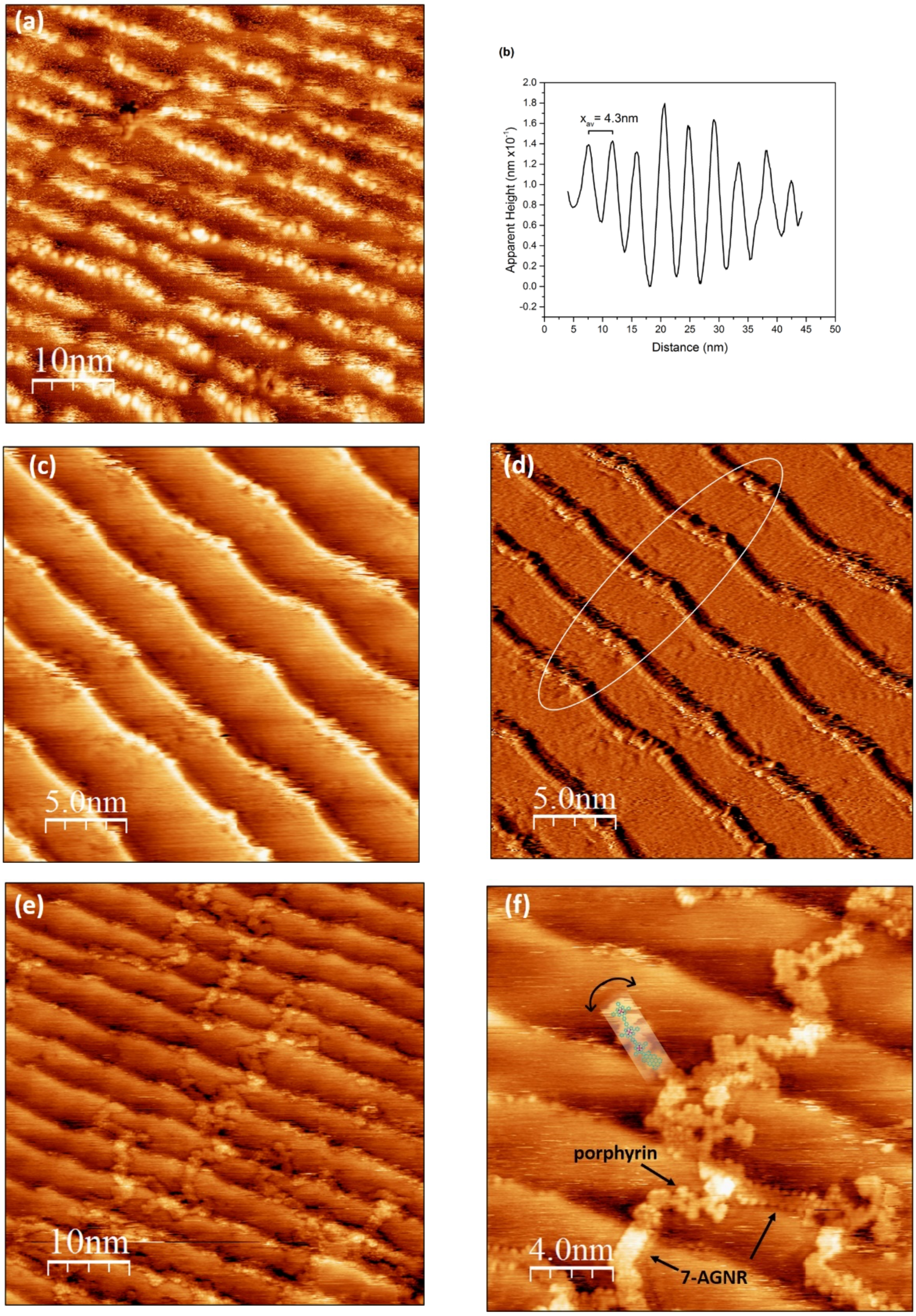

***Figure 3.25**: Formation of functionalised 7-AGNRs on Au(788). (a) 50 nm ×50 nm (V=-1.54 V, I=46 pA). (b) Y-average of (a). (c) 25 nm × 25 nm (V=-0.86 V, I=28 pA). (d) Composite image of (c) with derivative image of (c). (e) 50 nm x 50 nm (V=-0.17 V, I=2.1 nA) (f) 20 nm × 20 nm (V=-0.17 V, I=2.1 nA)*

Figure 3.26 (a) shows a large area of both self-assembled and disordered material after depositing a monolayer of DBBA and Ni-porphyrin on the Au(788) surface and annealing at 100 °C. Figure 3.26 (b) shows a 25 nm × 25 nm area of self-assembled molecules with an inset FFT . This molecular arrangement is reminiscent of the DBBA self-assembled structure shown in figure 3.10 (d). There is no evidence of porphyrin molecules incorporated in the array which suggest it is composed of entirely of DBBA. Proposed molecular models are overlayed on two regions in the figure labelled 1-6 and **a**-**f**. The presence of bright rows along rows **c** and **f** and also row 2 may be caused DBBA on the Au(788) step-edge either due to the topographic height difference of the edge in relation to the terrace or the way the DBBA interacts and sits on the step-edge. The distance between rows **c** and **f** is 4.8 nm ±0.05 nm which coincides with the terrace width on Au(788) as discussed in section 2.4.2. The apparent height difference between molecules in rows **c** and **f** and molecules in rows **d** and **e** would support the self-assembly model proposed, although more evidence is needed to be definitive. From the FFT image the unit cell vectors are 1.29 nm ±0.09 nm and 8.28 nm ±0.10 nm. Rows 1 and 2 have the same orientation as rows **a** and **b** appear to occupy a larger area than the molecules in other rows. The area occupied by the molecules is estimated to be between 1.96 nm^2 and 2.17 $nm^2 \pm 0.01$ nm^2 which makes it less densely packed than the self-assembled molecules on Au(111).

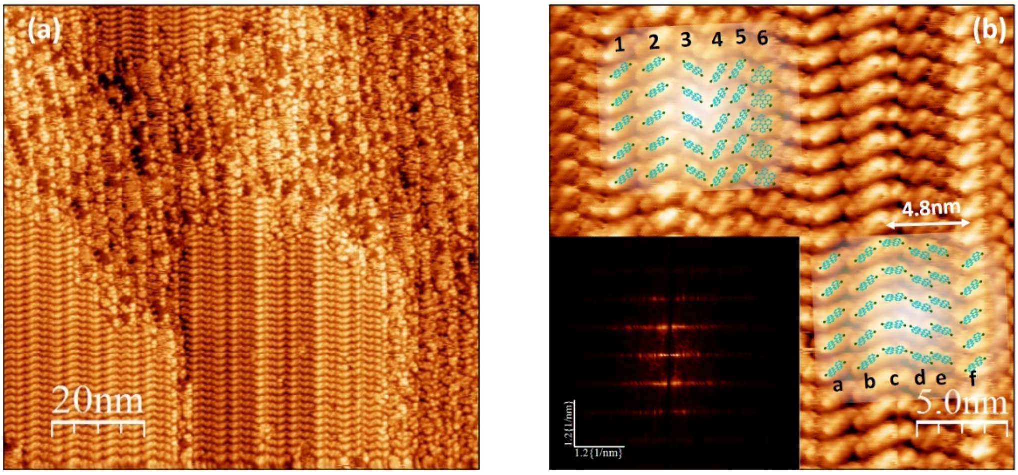

Figure 3.26: *Au (788) after co-deposition of porphyrin and DBBA. (a) 200 nm × 200 nm (V=1.45 V, I=86 pA). (b) 25 nm × 25 nm (V=1.4 V, I=42 pA)*

The sample was annealed 200 ^{o}C to induce dehalogenation. Figure 2.27(a) is a large area STM image showing parallel aligned chains. An FFT of the image in figure 3.27(a) is shown in 3.27(b). The presence of bright lobes along a straight line through the origin in the FFT image is indicative of unidirectional growth. A line profile of the FFT is displayed in figure 3.27 (c) and shows the distance, in *k*-space, between bright lobes and the origin. The measurements 0.176 nm^{-1}, 0.288 nm^{-1}, and 0.344 nm^{-1} correspond to distance, in real space of 5.6 nm, 3.5 nm, and 2.8 nm, respectively. The width of a DBBA polymer chains is 1.4 nm ±0.06 nm as determined from the line profile in figure 3.27 (d), therefore tightly packed parallel chains the distance between each row is approximately 1.4 nm and the distance between multiple close packed chains is an integer (n) multiple of 1.4 nm, which accounts for the distances of 2.88 nm (n=2) and 5.68 nm (n=4) measured from the FFT image. However, the peak at 0.288 nm^{-1} is remains unaccounted for. A line profile of figure 3.27 (a) is taken and shown in figure 3.27 (d) which shows distances between rows of 0.7 nm, 1.4 nm, 2.1 nm, 2.8 nm and 3.5 nm, all multiples of 0.7 nm, which is half the width of a DBBA chain. A model of second layer material is proposed to account for the rows separated by non-integer number of DBBA rows in figure 3.27 (d). The orientation of the polymer chains caused by the steric hindrance of the hydrogen atoms on the anthracene units (see figure 3.1) results in a criss-cross structure on the surface. The second layer of polymer chain rows straddles the surface row with an offset of 0.7 nm as shown in the by the side-view in figure 3.27 (e). This model is supported by the fact that all peaks are separated by multiples of 0.7 nm thus corresponding to either a single layer of chains or a bilayer. Also, in the line profile in an apparent height difference is seen between rows separated by 0.7 nm and 0.21 nm and as labelled 1st and 2nd row.

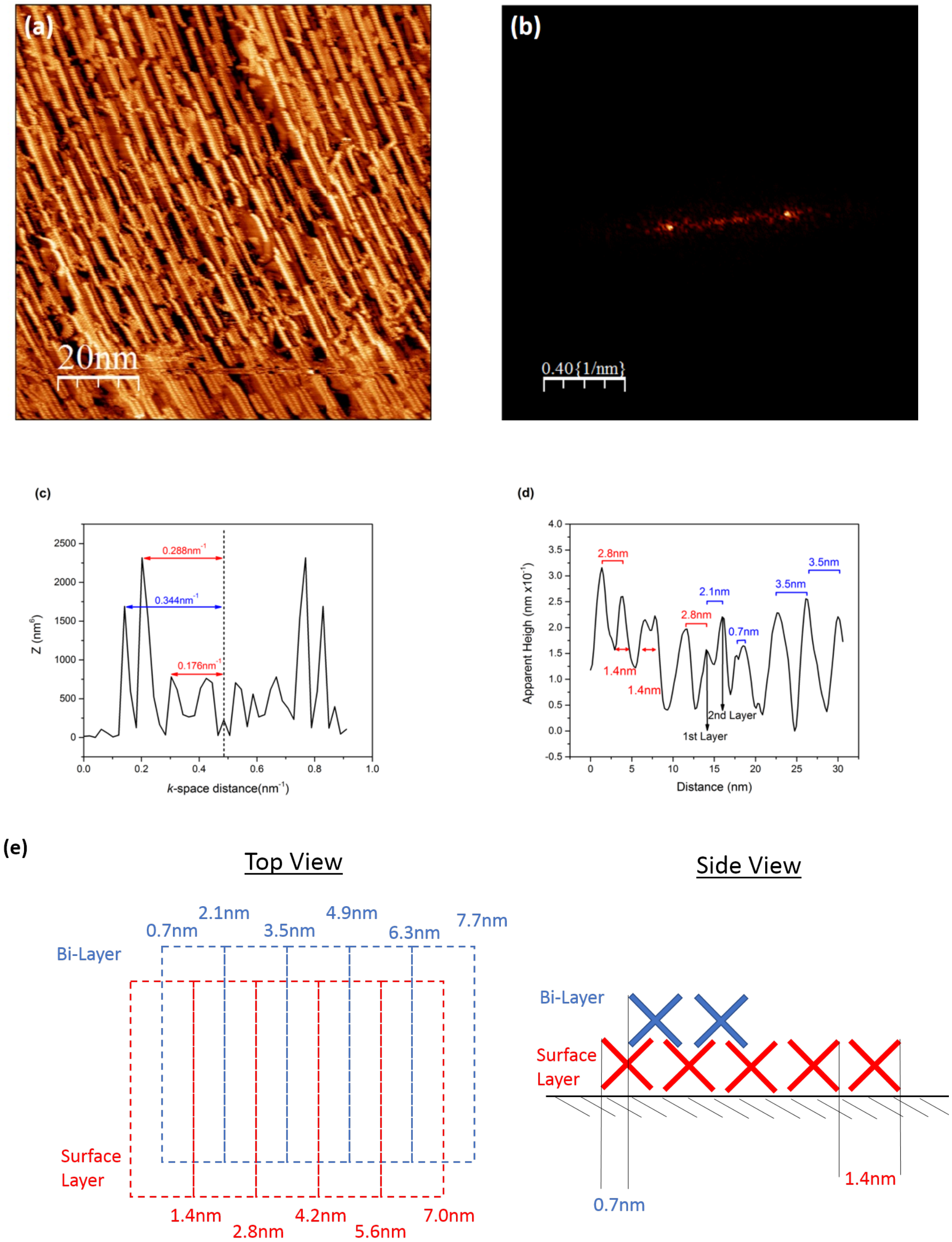

Figure 3.27: *Polymer chains on Au(788) with FFT and Line profile. (a) 100 nm × 100 nm (V=1.0 V, I=0.1 nA). (b) FFT of (a). (c) Line profile of FFT. (d) Y-average line profile of polymer chains in (a). (e) Model of surface and bi-layer interaction.*

The images in figure 3.28 (a) and (b) were acquired after the sample was annealed at 300 °C to initiate the cyclodehydrogenation process. Most of the material shown in figure 3.28 (a) is in the polymer phase although some ribbons are visible as highlighted in the figure. Porphyrin-chain heterojunctions are identified with arrows; blue arrows pointing to those with a bend at the junction and the green arrows identify linear chains or offset junctions. Similarly, in figure 3.28 (b) both chains and ribbons are seen alongside each other and porphyrin-7-AGNR heterojunctions are identified with the same colour scheme as with figure 3.28 (a). Two distinctive patterns are seen when imaging the chains: the characteristic bright lobes shown in the figure with the black trace line through it and a more complex structure with the red line through it. Both line profiles are shown in figure 3.28 (c) and colour coded, both are unmistakably polymer chains as the distance between anthracene protrusions is 0.88 nm ± 0.02 nm for both. The difference of the imaging of the two chains could be due to a tip-effect but it is more likely due to a second layer of material. In figure 3.28 (b) the line profile shown in blue captures both images of the chains. The separation between protrusions remains the same, however there is an apparent height difference of 0.6 nm ± 0.02 nm which would suggest a double layer of chains and the more complex features in the top layer are a result in the change of the band structure of the bi-layer chains. Another line profile from figure 3.28 (b) as shown by the white dashed line. It shows the height difference between single- and double-layer chains. Both chains appear to be the same height but considering that the distance between the chains is approximately 4.6 nm and the width of Au(788) terraces is 4.0 nm the single row may lie on the step edge and the double layer is on the terrace. Further studies are needed to see exactly how chains aligns on the step-edges.

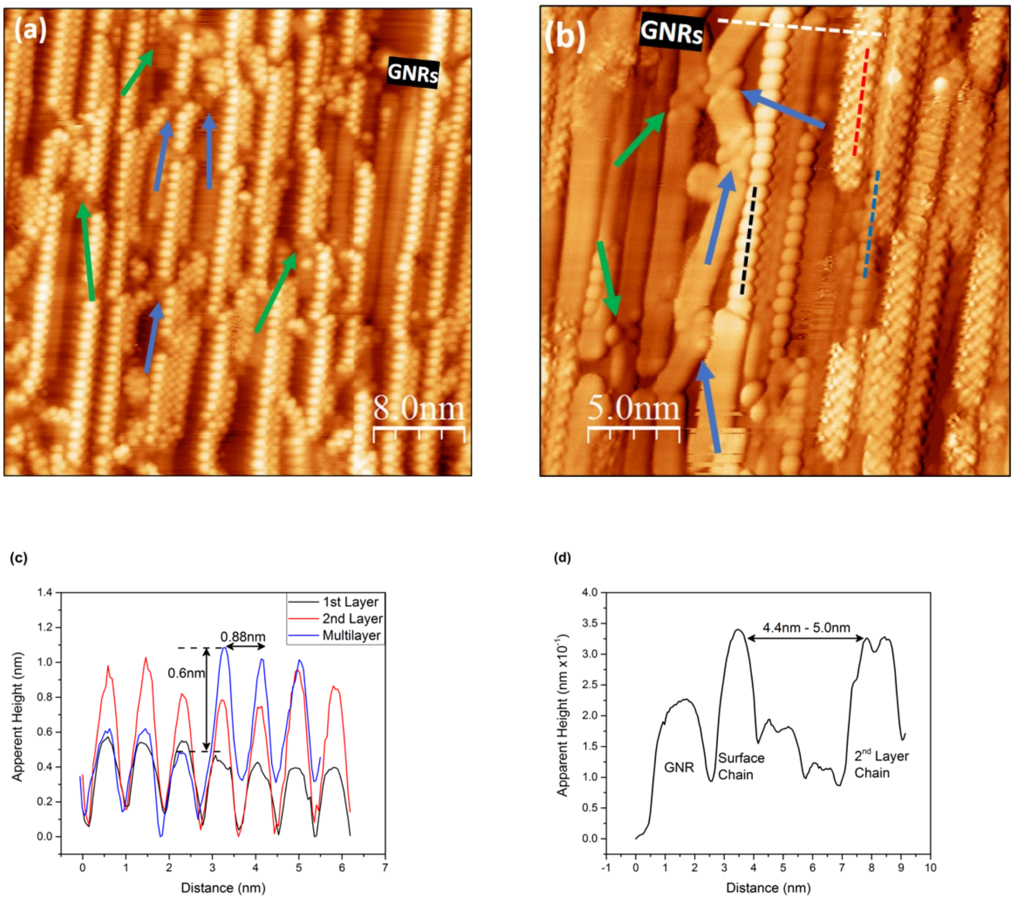

***Figure 3.28**: Porphyrin Functionalised chains and ribbons. (a) 40 nm × 40 nm (V=1.28 V, I=53 nA). (b) 25 nm × 25 nm (V=-0.10 V, I=0.10 nA) (c) Line Profiles taken of (b). (d) Line profile taken of (b).*

Figures 3.29 (a) and (b) show porphyrin functionalised 7-AGNRs on the Au(788) surface following complete cyclodehydrogenation after annealing the sample at 400 °C. The surface coverage is approximately 1 ML and preferential alignment of the functionalised nanoribbons along the $[01\bar{1}]$ direction can be clearly seen. To quantify the templating effect of the vicinal Au(788) surface the distribution of angles at the AGNR-porphyrin-AGNR junction is measured from a series of images in figure 3.30 (a) – (f) and compared to those measured on the Au(111) surface.

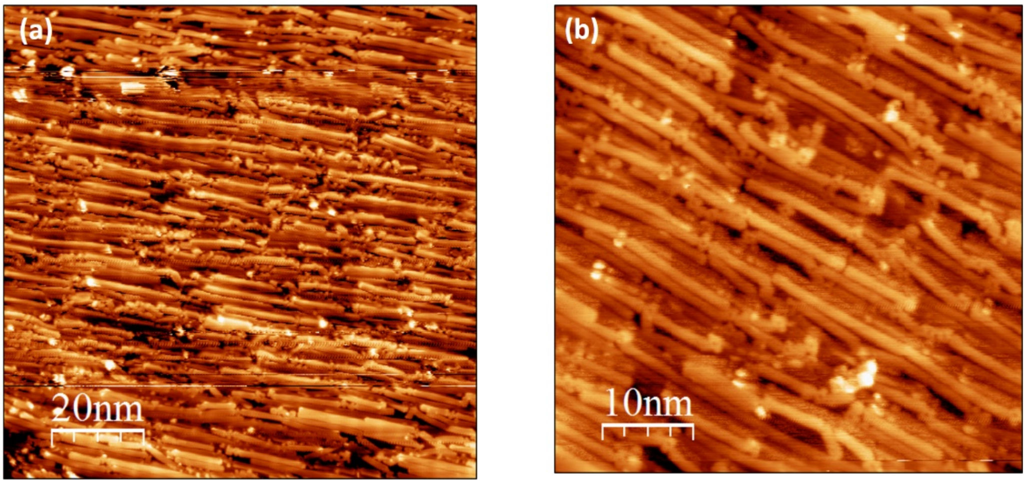

Figure 3.29: *Porphyrin functionalized GNRs on Au(788). (a) 100 nm × 100 nm (V=-1.0 V, I=1.0 nA) (b) 50 nm × 50 nm (V=2.2 V, I=0.95 nA)*

Distinguishing the angles formed at the heterojunctions in relation to the models outlined in figures 3.17, 3.18 and 3.19 can be challenging as some orientations cannot be resolved. As a compromise, angles of similar size are grouped together. Group 1 are linear/offset junctions with an angle of 180° and are highlighted with blue arrows in the figures. Junctions which form angles between 179° - 150° are collected in Group 2 and are shown with green arrows. Group 3 junctions are those with angles in the range 149° – 130° and are highlighted with yellow arrows while Group 4 junctions are those with angles of less than 129° and are shown in white. The angle of the junction predicted in the models is an approximation and, discounting the position of the fluoranthene unit, other factors including the surface index ((111) vs. (788)) and the presence of other GNRs which can obstruct and/or distort the growth of neighbouring ribbons and can contribute to the final structure of the functionalised ribbon. Junctions which cannot be identified, porphyrin-porphyrin junctions and ribbons terminated with a porphyrin are not included in the statistics. Histograms of both distributions are shown in figures 3.31 (a) and (b). Explicit identification of heterojunction angles on the Au(111) surface is included in Appendix A. In figure 3.30 (c) a triply fused porphyrin is seen highlight in the white box. This results from the removal hydrogen atoms from the phenyl rings during dehydrogenation allowing for 7-AGNR to bond to the porphyrin. This is similar to the fusing of 7-AGNRs to form 14- to 21-AGNRs and can happen if the annealing temperature exceeds that required for dehydrogenation of the phenyl rings. This triply fused porphyrin junction was not included in the statistics and is indicated here to highlight the formation of this type of junction.

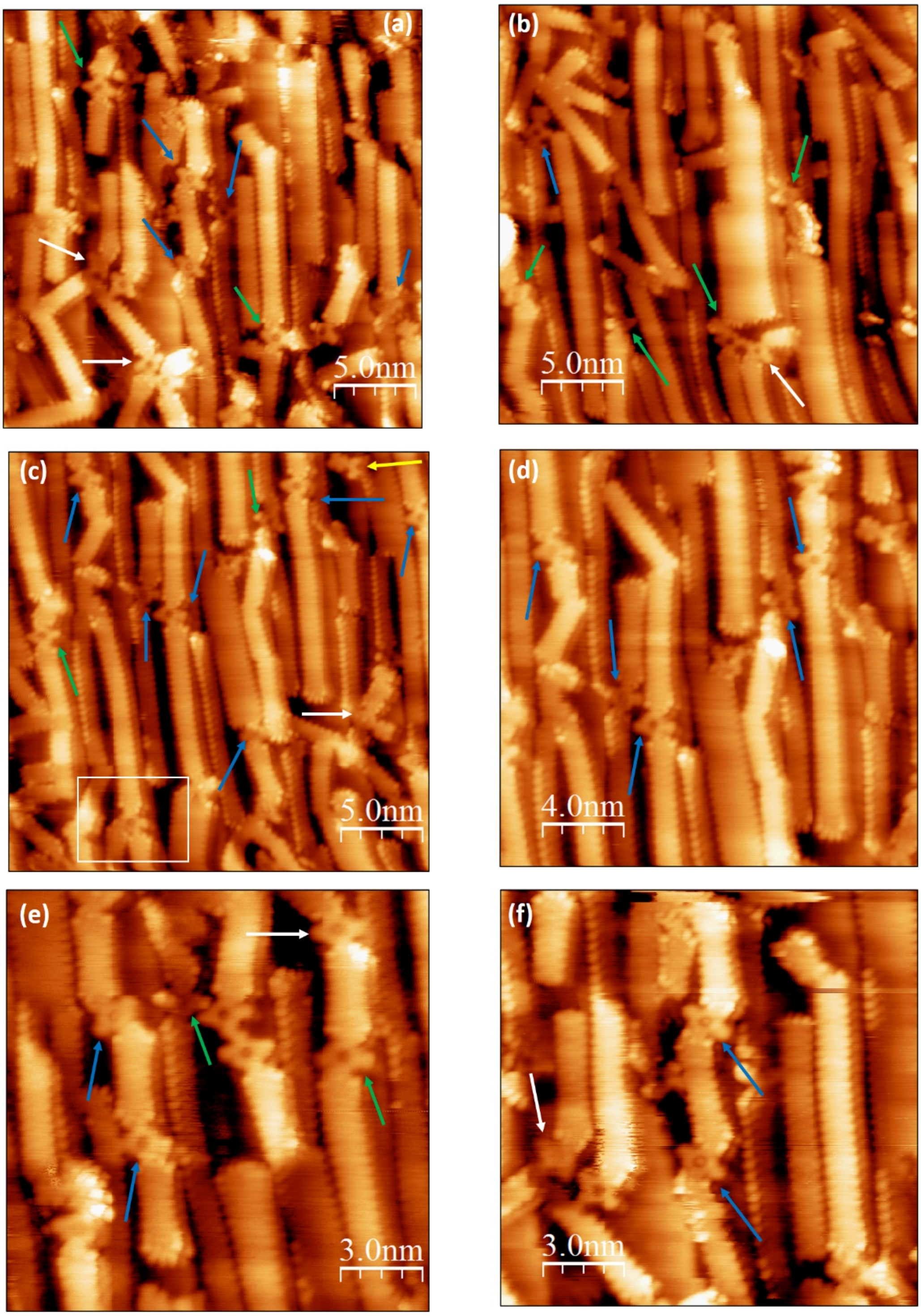

Figure 3.30: *Porphyrin-7-AGNR heterojunctions on Au(788). (a) 25 nm × 25 nm (V=0.53 V, I=0.23 nA). (b) 25 nm × 25 nm (V=0.54 V, I=0.23 nA). (c) 25 nm × 25 nm (V=0.54 V, I=0.23 nA). (d) 20 nm × 20 nm (V=0.53 V, I=0.23 nA) (e) 15 nm × 15 nm (V=0.54 V, I=0.36 nA). (f) 15 nm × 15 nm (V=0.54 V, I=0.23 nA).*

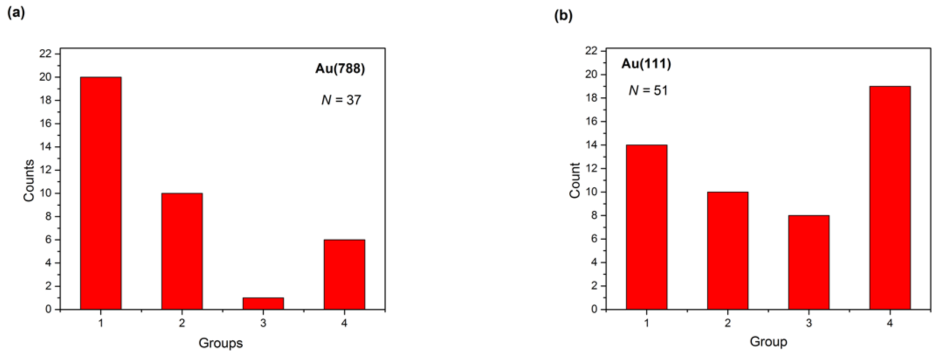

Figure 3.31: Histograms of heterojunction angles. (a) Au(788) and (b) Au(111)

The number of heterojunctions included in the statistics for the Au(788) and Au(111) surfaces are 37 and 51 respectively. Group 1 junctions account for 54% of all counted junctions on the Au(788) surface while the same group accounts for only 27% of junctions on the Au(111) crystal. The number of Group 2 junctions is the same for both surfaces but represents 27% and 20% of junctions for the (788) and (111), respectively. Groups 3 and 4, the smallest angle junctions, increase significantly from 19% on Au(788) to 53% on the Au(111) surface. There is significant difference between the junctions formed on both surfaces and the templating effect of the vicinal Au(788) surface explains the alignment of the porphyrin-7-AGNR structures, however it is important to note that the surface coverage for the Au(788) surface is 1.00-0.92 ML for the regions included in the statistics and between 0.46 ML and 0.62 ML for the Au(111) surface. The surface coverage has been shown to impact the length ribbons can grow on the Au(111) surface with less dense regions giving rise to longer AGNRs. However, the opposite is true for ribbons on the Au(788) surface as shown in the histograms in figure 3.32. Comparing monolayer coverage of functionalised 7-AGNRs on Au(788) and Au(111) shows that a greater proportion (~33%) of structures on the Au(788) surface are over 21 nm and the longest measured ribbon is 69 nm ± 2 nm. For the Au(111) surface approximately 25% of structures are over 21 nm and the longest is 31 nm ± 2 nm. This result combined with the better alignment of structures on the Au(788) surface suggest the vicinal gold surface is better than the Au(111) will lend itself to both transfer and angle dependent characterisation techniques.

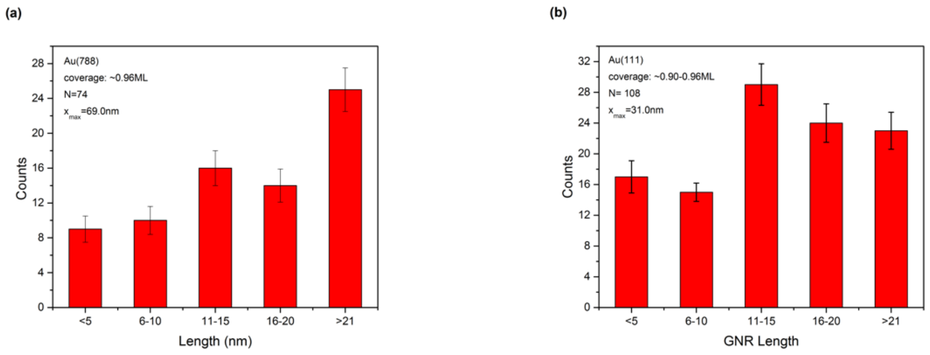

Figure 3.32: *Histograms of functionalised 7-AGNR length. (a) Au(788) (b) Au(111)*

3.4 Conclusions

This chapter described the formation of Ni-porphyrin functionalised 7-AGNR on the Au(111) and Au(788) surfaces. First, Ni-DBTPP was deposited on the Au(111) surface and annealing the sample induced dehalogenation and the formation of porphyrin chains. This also resulted in the formation of 2x1 reconstruction.

Multiple self-assemblies of DBBA molecules including hexamer “florets” were observed on the Au(111) surface following monolayer co-deposition of DBBA and Ni-DBTPP. Porphyrin functionalised 7-AGNRs wee formed through on-surface synthesis on Au(111). Longer nanostructures were found to form in regions with a low-density of deposited material as opposed to shorter structures which formed in the high-density regions and nanostructures in all regions were multidirectional.

Porphyrin functionalised 7-AGNRs were also formed on the Au(788) surface to take advantage of the templating effect of the vicinal surface. At 0.5 ML surface coverage nanostructures were not aligned and did not grow over 5 nm in length. However, monolayer coverage on the Au(788) surface yielded longer and more aligned functionalised ribbons than the Au(111).

3.5 References

1. Cai, J. *et al.* Atomically precise bottom-up fabrication of graphene nanoribbons. *Nature* **466**, 470–473 (2010).

2. Grill, L. *et al.* Nano-architectures by covalent assembly of molecular building blocks. *Nat. Nanotechnol.* **2**, 687–691 (2007).

3. Saywell, A., Schwarz, J., Hecht, S. & Grill, L. Polymerization on stepped surfaces: Alignment of polymers and identification of catalytic sites. *Angew. Chemie - Int. Ed.* **51**, 5096–5100 (2012).

4. Lafferentz, L. *et al.* Controlling on-surface polymerization by hierarchical and substrate-directed growth. *Nat. Chem.* **4**, 215–220 (2012).

5. Carpy, T. A Scanning Tunnelling Microscopy and Spectroscopic Study of Bromine Functionalised Molecules on Metal Surfaces. *Ph.D Thesis DCU* (2015).

6. Doyle, C. An investigation of the structural and electronic properties of covalently bonded molecular networks on metal surfaces formed through debromination reactions. *Ph.D Thesis DCU* 232 (2013).

7. Fortuna, S. *et al.* Molecule-Driven Substrate Reconstruction in the Two-Dimensional Self-Organization of Fe-Phthalocyanines on Au(110). *J. Phys. Chem. C* **116**, 6251–6258 (2012).

8. Guaino, P., Carty, D., Hughes, G., McDonald, O. & Cafolla, A. A. Long-range order in a multilayer organic film templated by a molecular-induced surface reconstruction: Pentacene on Au(110). *Appl. Phys. Lett.* **85**, 2777–2779 (2004).

9. Tian, G. *et al.* Effects of monolayer Bi on the self-assembly of DBBA on Au(111). *Surf. Sci.* **665**, 89–95 (2017).

10. Simonov, K. A. *et al.* Synthesis of armchair graphene nanoribbons from the 10,10′-dibromo-9,9′-bianthracene molecules on Ag(111): the role of organometallic intermediates. *Sci. Rep.* **8**, 3506 (2018).

11. Shen, Y. *et al.* Chiral Self-Assembly of Nonplanar 10,10′-Dibromo-9,9′-bianthryl Molecules on Ag(111). *Langmuir* **33**, 2993–2999 (2017).

12. Tian, Q. *et al.* Electronic structure evolution at DBBA/Au(111) interface W/O Bismuth insertion layer. *Synth. Met.* **251**, 24–29 (2019).

13. Kolmer, M. *et al.* Polymerization of Polyanthrylene on a Titanium Dioxide (011)-(2×1) Surface. *Angew. Chemie Int. Ed.* **52**, 10300–10303 (2013).

14. Xiao, Z. *et al.* Ab initio investigation of the cyclodehydrogenation process for polyanthrylene transformation to graphene nanoribbons. *npj Comput. Mater.* **5**, 1–6 (2019).

15. Berner, N. C. *et al.* Intermolecular dehalogenation reactions on passivated germanium(001). doi:arXiv:1505.06031

16. Jacobse, P. H. *et al.* One Precursor but Two Types of Graphene Nanoribbons: On-Surface Transformations of 10,10′-Dichloro-9,9′-bianthryl on Ag(111). *J. Phys. Chem. C* **123**, 8892–8901 (2019).

17. Rousset, S., Repain, V., Baudot, G., Garreau, Y. & Lecoeur, J. Self-ordering of Au(111) vicinal surfaces and application to nanostructure organized growth. *J. Phys. Condens. Matter* **15**, 3363–3392 (2003).

Chapter 4: Porphyrin Functionalised (4,1) chiral-GNRs on Au(111) and Au(788)

4.1 Introduction

The formation of porphyrin functionalised 7-AGNR has been demonstrated in chapter 3. However, due to the position of the halogen atoms on DBBA molecules the junction at the porphyrin has two degrees of freedom and forms a fluoranthene unit which is hypothesised to reduce conductivity in the device. A solution to this problem is to design a GNR forming precursor molecule that forms a 6-membered ring, triphenylene, on bonding to dehalogenated porphyrins. Narita *et al.* synthesised 6,16-dibromo-9,10,19,20-tetraoxa-9a,19a- diboratetrabenzo[a,f,j,o] perylene (OBO) which has bromine at the 6 and 16 positions (see section 2.6.1). The OBO molecule is a precursor for (4,1) chiral GNRs. The OBO molecule, the porphyrin-GNR heterojunction and the triphenylene unit are shown in figure 4.1.

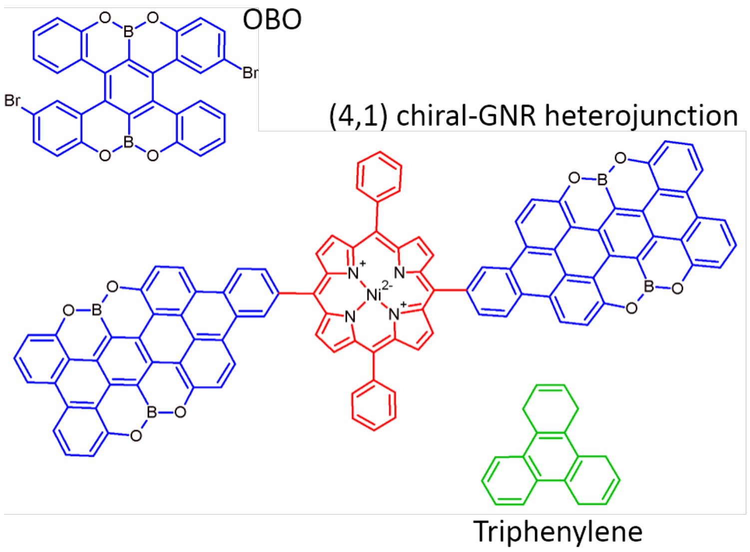

Figure 4.1 *OBO molecule, (4,1) chiral heterojunction and triphenylene unit*

4.2 Experimental Details

The formation of porphyrin functionalised GNRs was conducted in stages. First, (4,1) chiral-GNRs were formed on Au(111) using 6,16-dibromo-9,10,19,20-tetraoxa-9a,19a-diboratetrabenzo (OBO) precursor molecules. The molecules were evaporated from a homemade K-cell at 240 °C for 60 minutes to achieve ~1.0 monolayers (ML) on the Au(111) crystal. Surface coverage was verified using STM and XPS. The gold substrate was sequentially annealed at 120 °C, 215 °C, and 400 °C for between 15 to 20 minutes to activate self-assembly, polymerisation, and cyclo-dehydrogenation reactions, respectively. The process is illustrated in figure 4.2. Following each annealing stage, the substrate was allowed cool to room temperature and STM images were taken. XPS spectra of the C 1*s*, Br 3*p,* B 1*s* and O 1*s* and wide scans were acquired at each stage to track the development of OBO precursors from self-assembly through polymerisation to (4,1) chiral-GNR formation. High surface coverage of OBO is required to achieve sufficient photoelectron counts for fitting data. Subsequent lower surface coverage depositions did not yield enough counts for robust XPS analysis and therefore are not included in the discussion. All XPS spectra were acquired at normal emission angle. In addition to normal emission spectra, 60° off-angle XPS experiment was conducted for increased surface sensitivity following the anneal at 120 °C. The improved statistics of this spectrum offered a better signal-to-noise ratio compared to normal emission spectra. This spectrum was used to fit the individual carbon constituents with a proposed model. A 0.5ML of OBO was also deposited on the Au(111) to investigate the self-assembly and ribbon formation of OBO on a less densely packed surface. The OBO was sublimated at the same temperature as described previously for 30 minutes.

To form porphyrin functionalised GNRs on Au(111) a simultaneous co-deposition of OBO precursors molecules and porphyrins were evaporated from K-Cells at the same temperatures and duration as mentioned previously for individual depositions. The sample was annealed to 250 °C for 10 minutes to induce dehalogenation and allowed cool to room temperature then annealed to 400 °C for 10 minutes to cyclo-dehydrogenate the GNRs. STM measurements were taken of functionalised GNRs on Au(111). The simultaneous co-deposition of OBO and Ni-DBTPP procedure was repeated for the Au(788) surface and STM images were taken.

Lastly, to investigate alignment strategies of (4,1) CGNR in isolation on the Au(788) surface two deposition strategies where implemented. The first protocol deposited approximately a monolayer of OBO on the surface from a K-Cell at 240 °C for 60 minutes and annealed the surface to 400 °C to thermally activated the formation of GNRs. The second protocol included two separate depositions of approximately 0.5 ML each by evaporating OBO from a K-Cell at 240 °C for 30 minutes and subsequently annealing the sample at 400 °C for 10 minutes after each deposition to instigate GNR formation.

Prior to all depositions the Au(111) and Au(788) crystals were prepared by argon sputtering and annealing cycles as outlined in section 2.5. Cleanliness of the crystals was verified by STM and XPS.

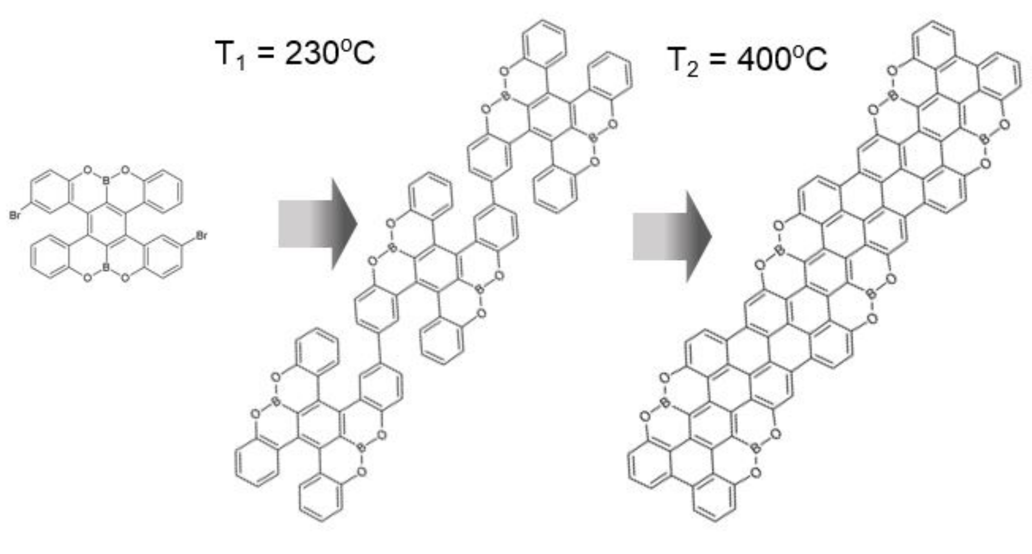

Figure 4.2: *Graphene nanoribbon formation from OBO molecules. Dehalogenation occurs at 200 °C forming chains. Cyclo-dehydrogenation begins at 315 °C and is complete at 400 °C*

4.3 Results and Discussion

4.3.1 Formation of OBO doped (4,1) chiral-GNRs

Figure 4.3(a) displays a large area (200 nm × 200 nm) STM image of the pristine Au(111) surface. Four terraces can be seen with no artefacts or remnants of organic material from previous experiments visible at step edges. The $22 \times \sqrt{3}$ "herringbone" surface reconstruction can be seen and three prominent crystal plane directions; $[1\bar{1}0]$, $[10\bar{1}]$, $[01\bar{1}]$ are identified. Similarly, in the 80 nm × 80 nm image in figure 4.3(b) the clean gold surface is visible, and the surface reconstruction can be clearly seen. The gold surface is imaged in figure 4.3(c) after OBO deposition and annealing the crystal to 120 °C to instigate self-assembly. In the 100 nm × 60 nm image in figure 4.3(d) OBO molecules are seen to occupy two domains separated by the superimposed grey box in the image. The directions of self-assembly align with the $[10\bar{1}]$ and $[01\bar{1}]$ crystal plane directions. Figure 4.3(e) shows a 30 nm × 30 nm image with chemical model of OBO overlaid. The OBO molecules are not easily imaged due to either STM tip geometry or to thermal vibrations. While detailed structure of the monomers is not attainable the outline of most molecules can be identified. As in figure 4.3(d), two directions of self-assemble appear at 60° to each other suggesting the crystal plane directions of the Au(111) substrate influence the direction of alignment and molecular diffusion. In the lower half of figure 4.3(e) the rows of molecules appear to bend. This is most likely due to strain in the STM tip which causes the image to "drift". Figure 4.3(f) is an illustration of the chemical model in figure 4.3(e) highlighting the 60° angle separation.

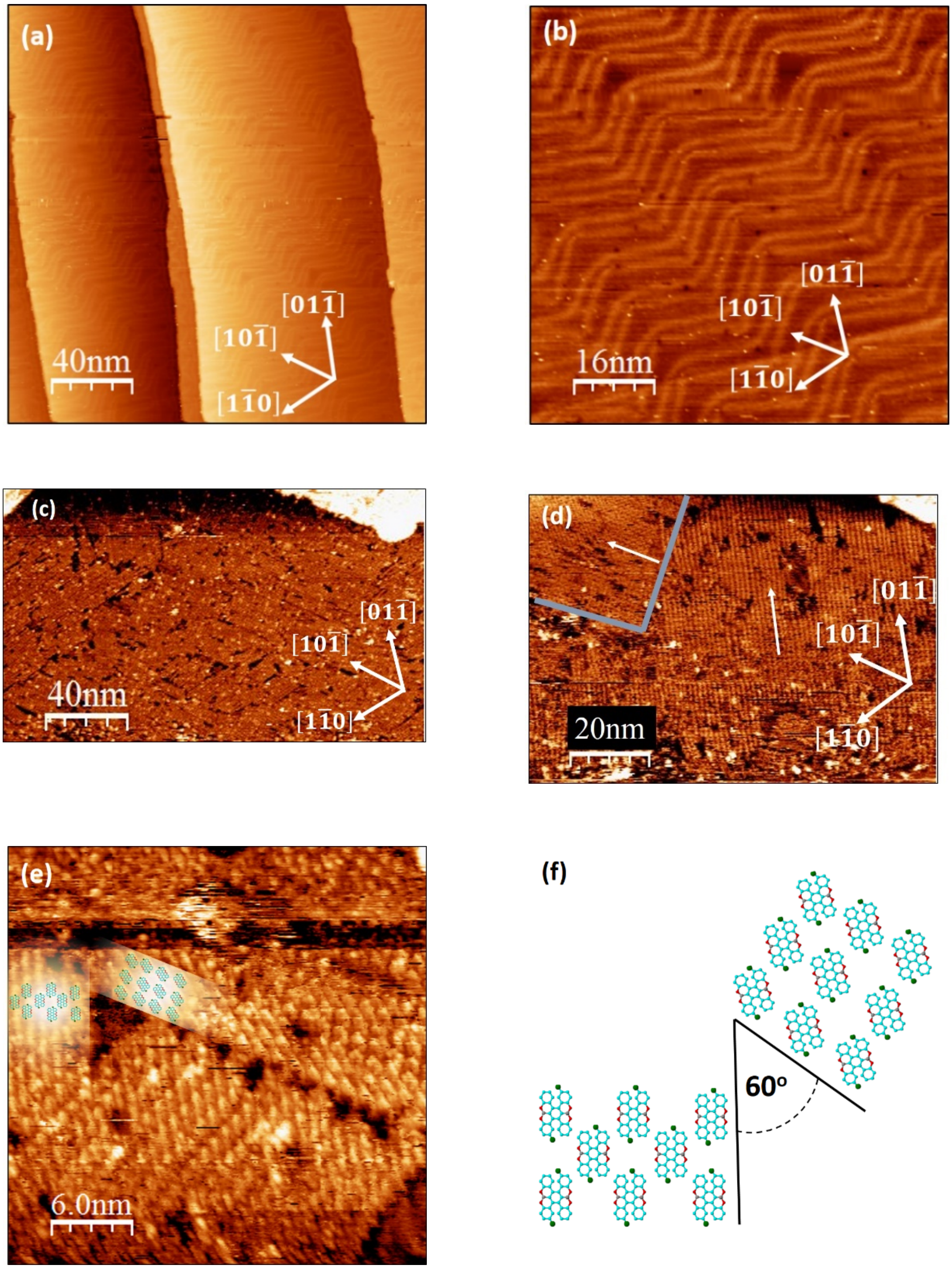

***Figure 4.3**: Clean Au(111) surface and OBO molecules on Au(111): (a) 200 nm × 200 nm image of clean Au(111) surface (V=-1.0 V, I=0.1nA) (b) 80 nm × 80 nm of Au(111) showing 22x$\sqrt{3}$ surface reconstruction (V=-1.0 V, I=0.1 nA) (c) 200 nm × 100 nm image showing monolayer OBO coverage (V_t=1.0 V, I_t=0.1 nA) (d)100 nm × 60 nm OBO self-assembly alignment along the $[10\bar{1}]$ and $[01\bar{1}]$ crystal directions (V=1.5 V, I=0.1 nA) (e) 30 nm × 30 nm image of rows of self-assembled OBO precursors with chemical structure overlaid (V=1.0 V, I=0.1 nA) (f) Enlarged chemical model from (e).*

Images in figure 4.4 show smaller areas than those shown in figure 4.3 allowing for specific alignments and interactions to be ascertained. In figure 4.4 (a), monomers are seen to self-assemble into rows along the long axis of the OBO molecule. The OBO molecule is rotated by approximately 30° to the direction of self-assembly as highlighted by the dashed white lines in figure 4.4 (a). Wang *et al.* observed two drivers for self-assembly among OBO molecules; Br--H and O--H interactions [1]. The Br--H interactions dominate the self-assembly in figure 4.4 (a). Adjacent rows of monomers appear to have two ways of aligning; parallel and anti-parallel as identified in figure 4.4 (a). In figure 4.4 (b) two pairs of anti-parallel rows converge at a 60° degree angle. The surface is not visible, so the crystal plane direction is uncertain. However, from figures 4.3 (c) and (d) it is highly likely that the rows in figure 4.4 (b) are along two of the three prominent directions of the Au(111) surface. The lattice parameters of the closed packed OBO unit cell are shown in figure 4.4 (c). The unit cell forms a rectangular lattice with lattice vectors **a** and **b** equal to 1.1 nm ±0.05 nm and 1.2 nm ±0.05 nm, respectively. Lattice vector values are calculated from the average of twenty measurements. Figure 4.4 (d) is the same image as 4.4 (c). The circled areas highlight intermolecular bonds formed between O--H of adjacent molecules as mentioned previously. Interestingly, the presence of the O--H bonds does not appear to reduce the separation between adjacent molecules. O--H bonds are only observed in rows of molecules with parallel packing and not in rows with anti-parallel packing. Using the dimensions of the OBO molecule given in section 2.6.1 the area of each molecule is ~1.0 nm^2. This value is used to estimate the density of OBO molecules on the surface for a ~1 ML deposition. Using a 4 nm x 4 nm grid on several images of closed packed self-assembled OBO there are approximately nine molecules per 16 nm^2. From repeat measurements the packing fraction of closed packed OBO is between 53 and 60%. Regions with anti-parallel alignment have lower density than parallel aligned rows. Figure 4.4 (e) and (f) show chemical models of Br--H and O--H interactions.

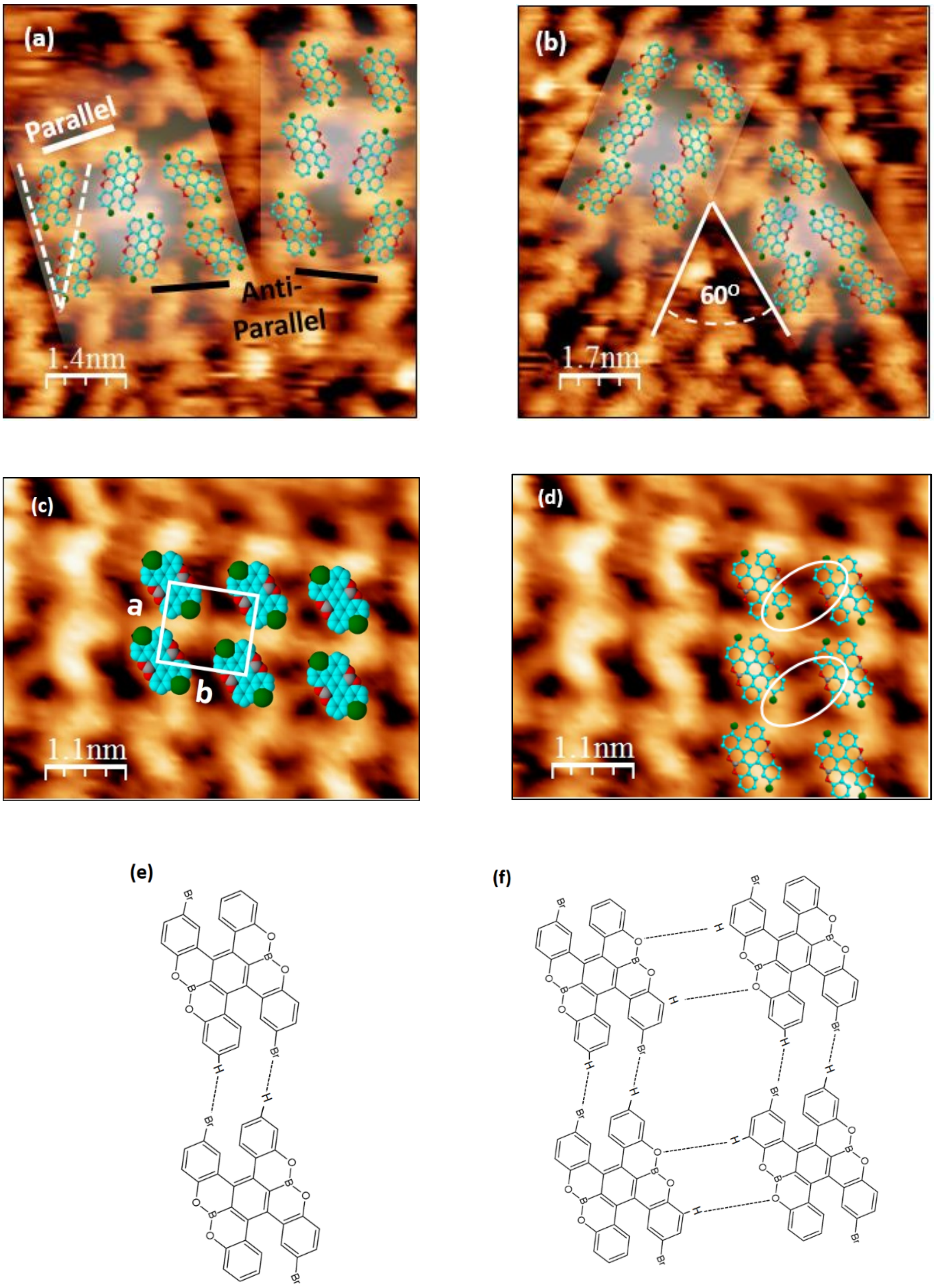

***Figure 4.4**: OBO self-assembly and assembly models. (a) 7 nm × 7 nm image of OBO. (b) 8.5 nm × 8.5 nm.(c) 5.5 nm × 5.5 nm with lattice vectors a=1.1 nm b=1.2 nm. (d) 5.5 nm × 5.5 nm showing H--O bonds between adjacent precursors. All STM images taken with same parameters (V=2.0 V, I=0.1 nA). (e)Model of self-assembly through Br- -H driven interactions (f) Model of combined H--O and Br--H driven self-assembly.*

After annealing the substrate at 215 °C for 15 minutes to instigate aryl-aryl coupling of OBO monomers and allowing the crystal to cool to room temperature STM images were taken. Figure 4.5 (a) shows a large area (200 nm x 200 nm) coverage of OBO polymer chains. The STM imaging conditions are such that the Au(111) reconstruction is faintly visibly underneath the material. Two pairs of dashed black lines are used to guide the eye along the corrugation lines of the 3x√23 surface reconstruction. As with molecular self-assembly the polymer chains appear to grow along the three prominent directions of the gold crystal. On the left-hand side of the image is a terrace. The chains are unconfined by the 1.5Å step-edge of the terrace and grow over the step. In figure 4.5 (b) is a 25 nm × 25 nm showing close-packed parallel rows of OBO chains growing along the $[10\bar{1}]$ direction. A ball and stick model of parallel chains is overlaid on the image. The unique shape of the chains is a result of the protruding phenyl rings due to steric hindrance of hydrogen atoms between neighbouring OBO units and is indicative of (4,1) chiral-GNR precursor chains. Figure 4.5 (c) shows a 10 nm × 7 nm magnified portion of the outlined section in figure 4.b (b). The image shows seven parallel OBO chains with chemical model overlaid. The dashed white line is a line profile shown in figure 4.5 (d). The line profile is of three benzene ring protrusions from three OBO units. The image in figure 4.5 (c) is heavily filtered such that apparent height measurements do not provide reliable information. Instead, only lateral measurements can be taken with confidence. The distance between each protrusion is 1.20 nm ±0.05 nm. This is in agreement with 1.18 nm measured from the chemical model and similar to the 1.12 nm value reported by Wang *et al.* [2].

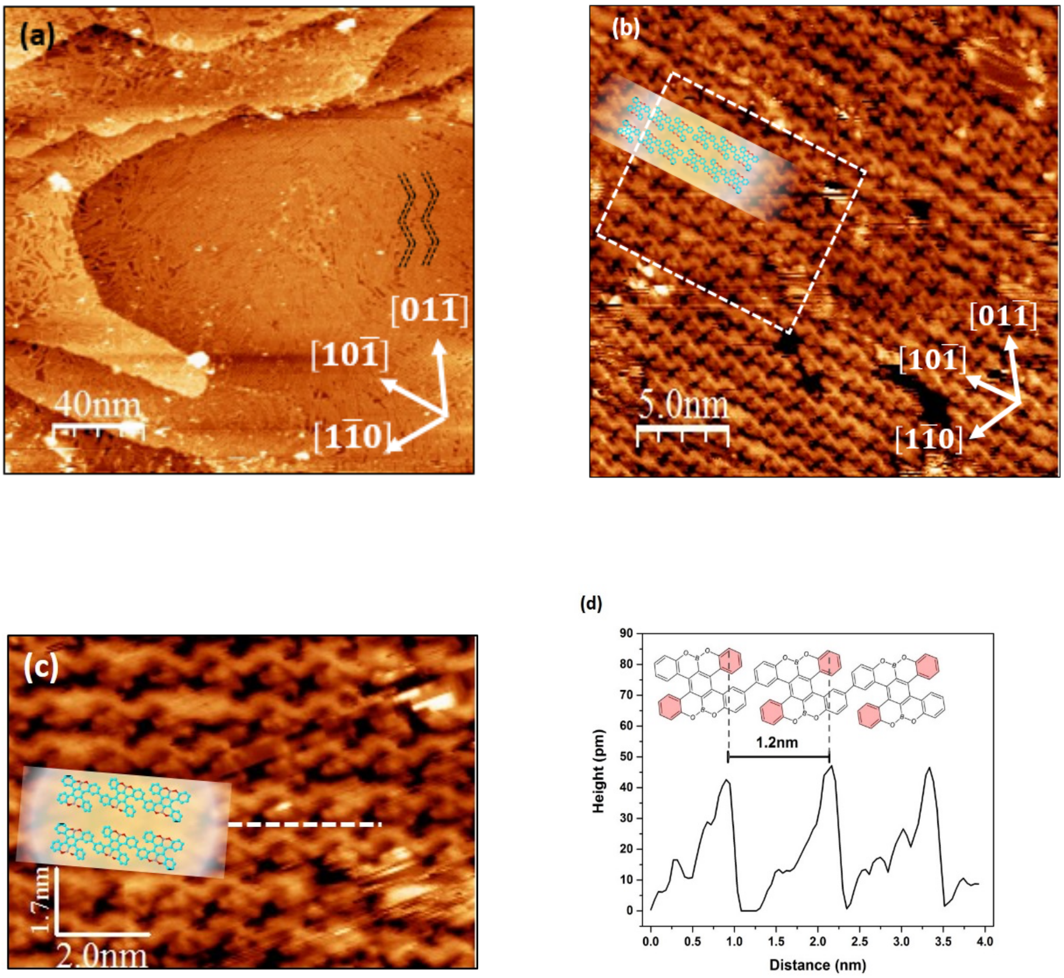

***Figure 4.5**: High density OBO Chains: (a) 200 nm × 200 nm image showing high coverage of polymer chains (V=0.87 V, I=0.28 nA) (b) 25 nm × 25 nm image of OBO chains with chemical model overlaid (V=1.05 V, I=0.27 nA). (c) 2.0 nm × 1.7 nm magnified segment of (b) showing distinct features in OBO chains with chemical model overlaid. (d) profile segment highlighted in (c) displaying 1.2 nm separation between protrusions on OBO chain.*

OBO doped (4,1) CGNR were observed on the Au(111) surface after annealing the sample at 400 °C for 15 minutes. Figure 4.6 (a) shows a large area image with GNR covering the surface with the underlying reconstruction visible. The surface is remains mostly covered in GNRs. The bright spots indicate regions with high density of states, usually found at the ends of GNRs. In the 30 nm × 30 nm image in 4.6 (b) there is some evidence of material desorbed from the surface most likely while in the OBO monomer phase. All ribbons are still aligned in one of the three prominent planes, $[10\bar{1}]$ in this case. A histogram of GNR lengths is shown in figure 4.6 (c). The length of 212 GNRs from figure 4.6 (a) were measured. The majority of GNRs are over 31 nm in length with the median length is between 31-40 nm. The shortest GNRs tend to be at the intersections between two domains of growth. High-resolution image of four OBO doped (4,1) CGNR are shown in figure 4.6 (d). Three OBO GNRs are overlaid on the image, two of the ribbons are in parallel alignment while the ribbon at the bottom of the image has the opposite chirality to the other two. These alignments are discussed in more detail later in this section. Figure 4.6 (d) was acquired with a negative bias on the STM tip meaning electrons tunnelled from the tip to empty states in the ribbon. The outer edges of the GNRs are brightest compared to the dark lobes in the interior indicating more filled states exist at the edges while the empty states reside in the interior of the ribbon.

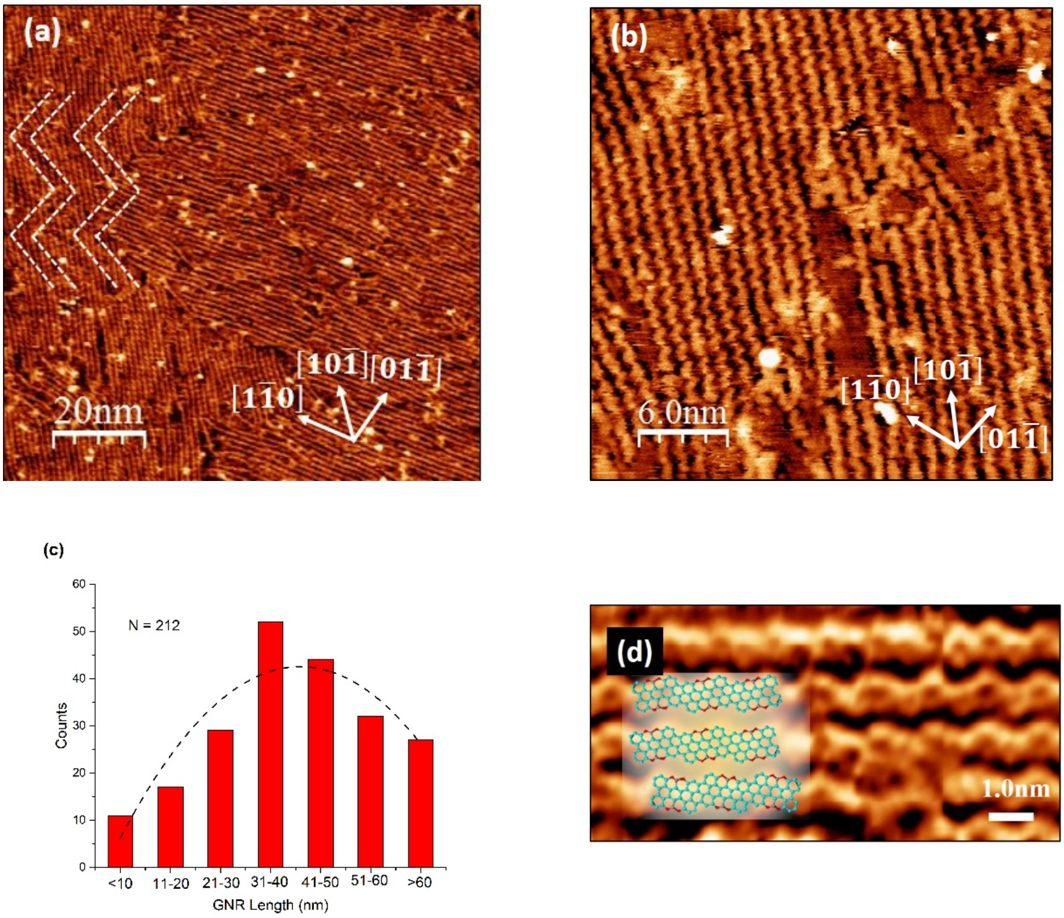

***Figure 4.6**: High Density OBO GNRs: (a) 100 nm × 100 nm of ribbons. The Au(111) surface reconstruction is visible underneath GNRs (V=0.85 V, I=0.1 nA) (b) 30 nm × 30 nm image shows unidirectional growth of GNRs with areas of desorbed material (V=0.74 V, I=0.1 nA). (c) Histogram of GNR lengths taken from (a). (d) 10 nm × 5 nm showing four parallel GNRs with differing chirality and dark lobes on body of GNR (V=-0.8 V, I=0.25 nA)*

4.3.2 XPS of OBO doped (4,1) chiral-GNR formation

X-ray photoelectron spectra were taken of the clean gold surface and after 1 hour of OBO deposition. Survey spectra from 0 – 800 eV are shown in figure 4.7. All prominent peaks are identified and labelled. The gold peaks are the strongest in both spectra. It is important to note the spectra from the clean gold sample has evidence of carbon, oxygen and tantalum present which suggests the sample is not pristine, however STM images of the gold surface provide evidence to the contrary. The sample holder is made of tantalum and may have oxidised and have adventitious carbon present after exposure to atmosphere which would account for the presence of C and O [3]. Attempts to eradicate the signal from Ta holder by adjusting the sample position and repeat Ar$^+$ bombarding were unable to completely remove organics and oxides from the spectra. As a compromise, the background carbon signal was subtracted from spectra after OBO deposition. Following deposition there is a significant increase in the C 1*s* peak compared to clean sample.

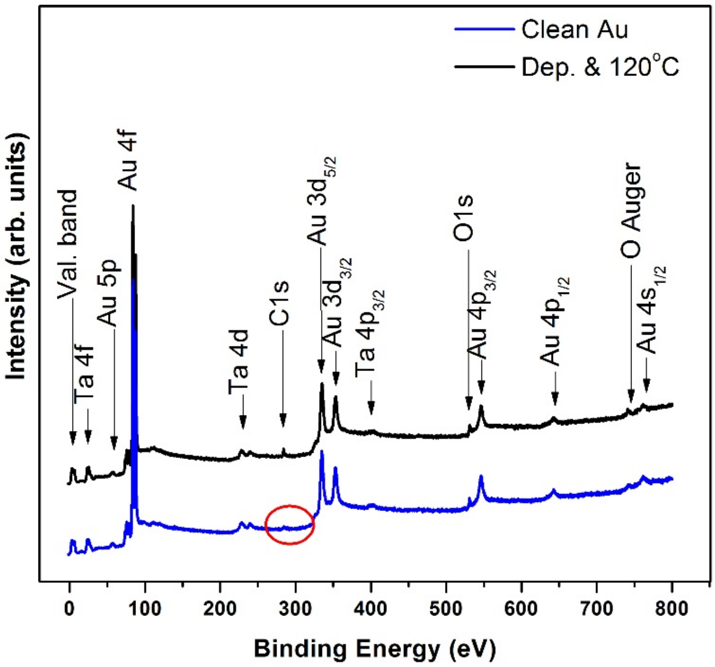

***Figure 4.7**: Wide scan of clean Au surface and OBO on Au(111). Red circle highlights trace amount of carbon on the clean gold spectra.*

Figure 4.8 shows the C 1*s* peak and the Au 4*d* doublet of the clean gold sample and post deposition. The presence of a carbon signal in the clean gold spectrum is more easily identifiable than in figure 4.7. The ratio of the C 1*s* to the Au $4d_{5/2}$ peak, in conjunction with STM images provided a rule-of-thumb for subsequent OBO deposition rates. Using C 1*s* and Au 4*d* peak maximums and subtracting the baseline gives a carbon to gold ratio of 1:13 which corresponds to approximately one monolayer. This rule-of-thumb is only applicable to the XPS system used to acquire this data.

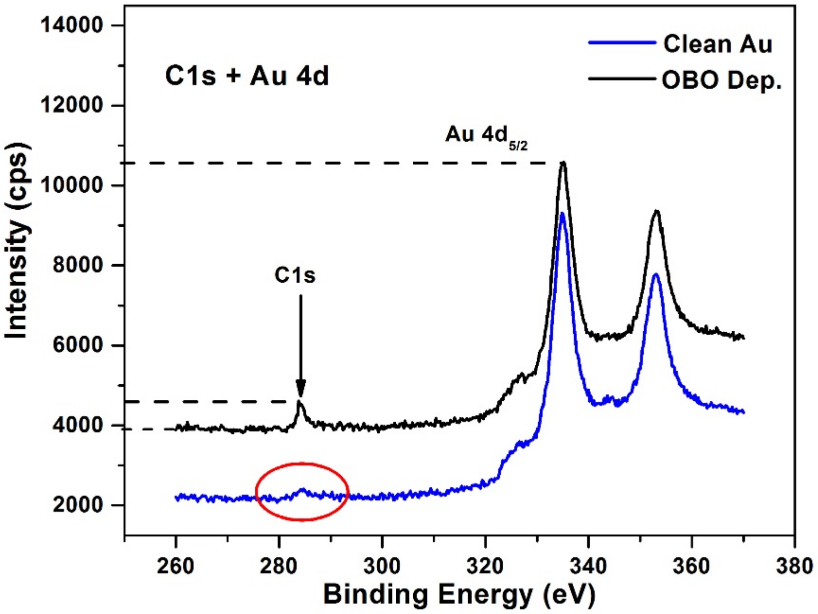

Figure 4.8: *XPS of C 1s and Au 4d*

Further evidence that the presence of oxygen in the data is due to the tantalum sample holder is provided by the O 1*s* spectra in figure 4.9. The O 1*s* from the clean gold spectrum is fit with one line-shape owing to surface oxide(s) on the Ta. The FWHM of the fitted peak is 1.9eV which is larger than the 1.0eV resolution of the spectrometer. The width of the peak is put down to amorphous oxides on the Ta sample holder. After OBO deposition another oxygen component is present at higher binding energy. Table 4.1 shows values for peak areas and area uncertainties.

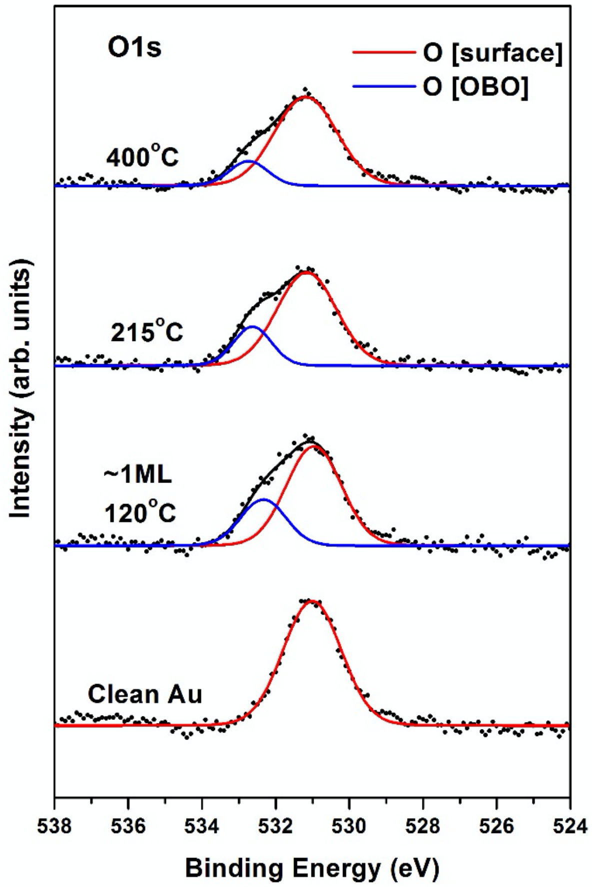

***Figure 4.9**: O1s spectra from the clean sample and OBO deposition*

***Table 4.1**: Areas and uncertainties of O1s*

	O 1*s* [Surface]	**Uncertainty**	**O 1*s* [OBO]**	**Uncertainty**
Clean	1.00	±0.01	--	--
OBO dep & 120 °C	0.90	±0.01	0.29	±0.01
215 °C	0.84	±0.01	0.21	±0.01
400 °C	0.80	±0.01	0.13	±0.01

All oxygen spectra are normalised to the surface oxide after OBO deposition. Both the surface oxide and the OBO is removed by annealing the sample however the OBO desorbs from the surface at a higher rate than the Ta oxide and complete removal of surface oxides was not achievable.

Figure 4.10 (a) shows the 60° off-angle spectrum and of the Br 3*p* and B 1*s* peaks after a 60-minute OBO deposition and annealing the sample at 120 °C for 15 minutes. Figure 4.10 (b) shows normal emission spectra after higher temperature annealing. Off-angle XPS experiments offer greater sensitivity which is useful for interpreting normal emission spectra. Due to the relatively small amount of bromine and boron present in the OBO molecule long scan times of >3hours were needed to acquire sufficient electron counts with adequate signal to noise ratio. In spite of these efforts the off-angle spectrum and normal emission spectra was smoothed to improve peak definition using 5-point and 11-point 2nd order Savitzky-Golay filter, respectively. In figure 4.10 (a), the B 1*s* peak at 190.5 eV (red line) is fit with one curve as boron is present in only one chemical environment in the OBO molecule. To fit the bromine 3*p* curve two doublet peaks are used at 184.3 eV (green line) and 181.4 eV (blue line) each with a spin-orbit splitting of 6.9 eV, in line with other studies [4,5]. The presence of two bromine peaks is indicative of bromine existing in two separate environments. There are two possible reasons for this which will each be discussed in turn. Firstly, the two bromine states could arise due to double or multilayer OBO deposition whereby one peak is associated with OBO in contact with the gold surface and the other due to π-π interactions of bi- or multilayer stacking of precursors. Energy shifts resulting from stacking has been observed and is reported in the literature [6,7]. In such cases the binding energy difference between surface molecules and stacked molecules is approximately 1 eV. However, in figure 4.10 (a) the shift in energy between bromine peaks is 3.0 eV. Also, for the multilayer explanation to be true another peak associated with boron should be present and no evidence of an additional boron peak is seen. The other explanation for the bromine peaks is a result of dissociation of bromine from the OBO molecule upon annealing at 120 °C. Wang *et al.*[1] report complete dehalogenation of OBO at 200 °C, however, the dehalogenation process may commence at lower temperatures as demonstrated by Simonov *et al.* in their study of DBBA on Au(111)[8].

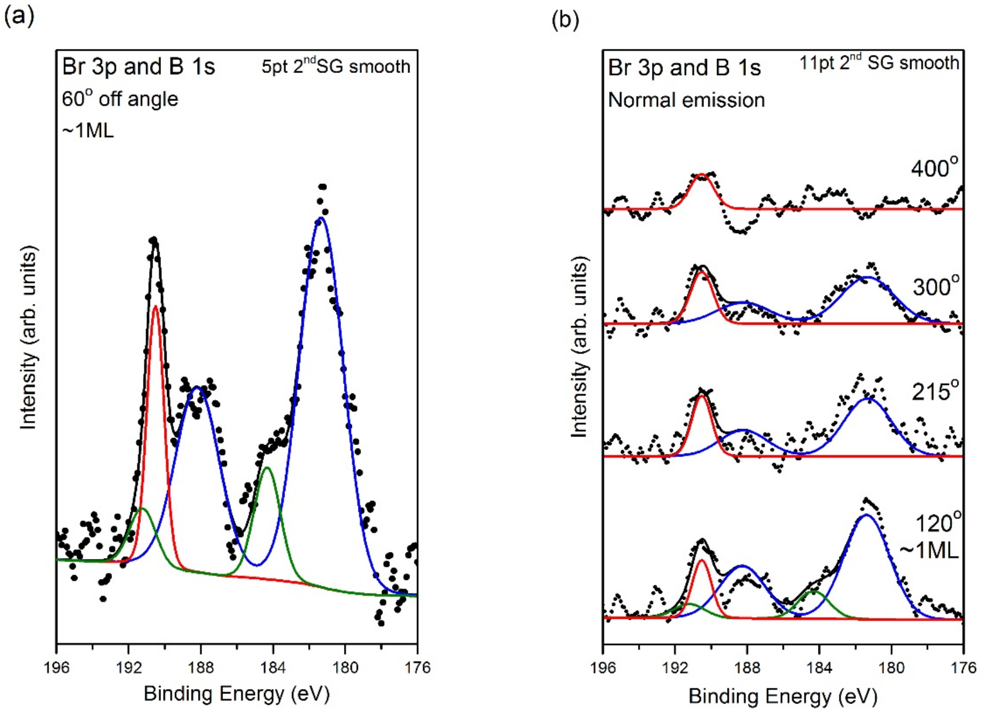

***Figure 4.10**: XPS of Br 3p and B 1s (a) 60° Off angle and (b) normal emission XPS data of Br 3p and B 1s with monolayer coverage of OBO molecules. (a) is taken after annealing at 120 °C for 15 minutes and (b) spectra as labelled.*

The data here supports the partial dehalogenation hypothesis. The question then arises which of the Br 3*p* doublet peaks in figure 4.10 (a) is due to OBO and which to the dissociated bromine on the gold surface. The area and the binding energy position of each component in conjunction with other XPS spectra and STM data suggests the doublet centred at 184.3eV is due to bromine present in the OBO molecule and the larger peak at 181.3eV is cleaved bromine on the gold surface. To validate this point, figure 4.10 (b) shows the evolution of the Br 3*p* and B 1*s* peaks with increasing temperature. The 120 °C spectrum is fit with the same Gaussian and Lorentzian values as used in figure 4.10 (a) and has two bromine peaks present. As the temperature is increased the higher binding energy peak is removed while the peak at 181.3 eV reduces with higher temperatures until complete removal at 400 °C. This suggests bromine completely dissociates from the molecule at 215 °C in line with Wang *et al.* and is removed from the surface at 400 °C. Further evidence of dissociated bromine on the surface can be seen in the STM images in figure 4.5 (b) and (c) where bright spots in between OBO polymer chains are likely due to individual bromine atoms on the surface.

The 60° off-angle spectrum of carbon 1*s* and the normal emission data is shown in figure 4.11 (a) and (b) respectively. The C 1*s* peak is fit with five Voight line shapes. The model used to fit the C 1*s* peak is based on carbon existing in five chemical environments in the OBO molecule therefore the C 1*s* envelope is comprised of five individual components.

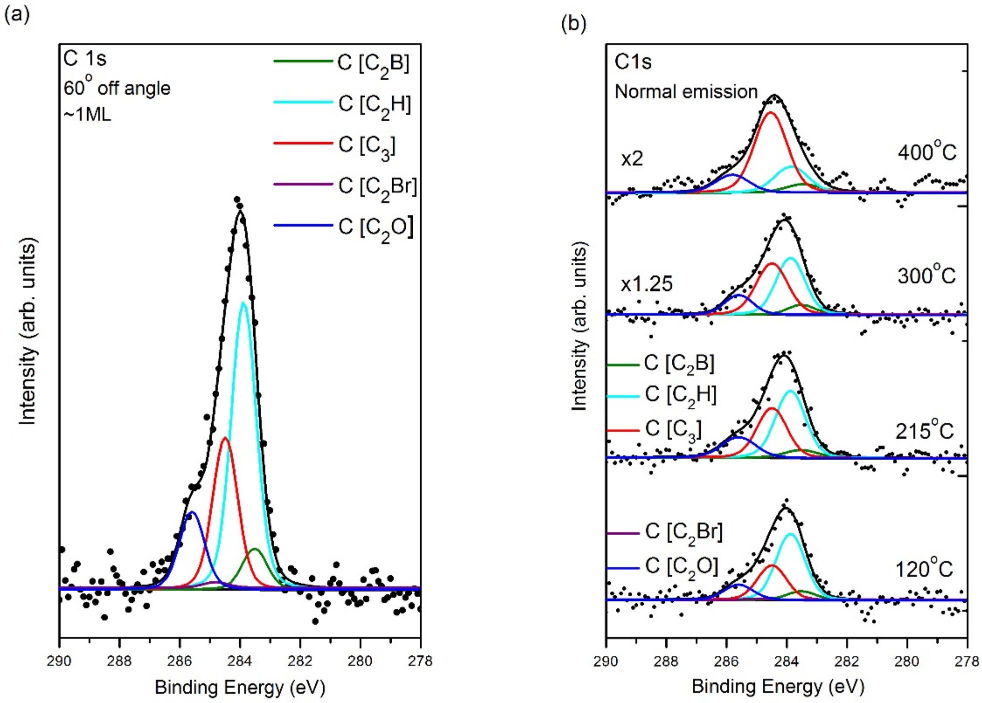

Figure 4.11: *XPS of C 1s (a) 60° Off angle and (b) normal emission XPS data of C 1s with ML of OBO. (a) is taken after annealing at 120 °C for 15 minutes and (b) spectra as labelled.*

Each OBO molecule has the chemical formula $C_{30}H_{14}B_2Br_2O_4$. The total area of the peak is the summed total of the thirty carbon atoms in OBO and the area of the individual line shapes is proportional to each carbon component accordingly. For a fully intact OBO molecule two carbon atoms are bonded to boron and two to bromine so the height and area of these components are equal. Likewise, there are four carbon atoms bond to oxygen therefore the oxygen component has twice the area of the boron component as shown by the green and blue line shapes in figure 4.11 (a). Similarly, triple bonded carbon and double bonded carbon with hydrogen are fit with an area according to the number of bonds in the molecule; eight and 14 respectively. Each OBO molecule has two bromine atoms however, the molecules are partially dehalogenated at 120 °C when the first XPS spectrum was acquired. The amount of bromine still attached to the OBO molecule can be determined from the 60° off-angle spectrum of Br 3*p* in figure 4.10 (a). Using the ratio of the areas of the Br-Au component at 181.3 eV to the Br-C component at 184.3eV in the Br 3*p* peak shows 86% of the bromine is thermally cleaved from OBO and adsorbed on the surface while 14% is remains bonded to OBO. Consequently, the Br-C component in figure 4.11 (a) is fit with an area 14% of its predicted value for a fully intact OBO molecule.

The binding energy position of each fit in figure 4.11 is estimated using the electronegativity of the element bonded to the carbon such that elements with lower electronegativity result in the spectral component having lower binding energy compared to elements with the greater electronegativity. The spectrums in figure 4.11 are fit by fixing the areas of each component and allowing the binding energy values to vary to acquire the line of best fit. A table of the electronegativity values and C 1*s* binding energies of each components in the OBO molecule is shown in table 4.2.

Table 4.2*: Electronegativity of five elements in OBO and their binding energy in the C 1s peak*

Element	***Electronegativity***	***C 1s component Binding Energy (eV)***
B	2.04	283.5
H	2.20	283.9
C	2.55	284.5
Br	2.96	284.8
O	3.44	285.6

In Table 4.3 each components predicted area based on the proposed model is shown together with the measured areas from the data and the uncertainty associated with each curve fit. The uncertainties are calculated using the covariant matrix method discussed in chapter 2 and the discrepancy between the model and measured values is also presented. The proposed model fits well with the experimental data for all components except the C_3 and the C_2Br components. However, the large discrepancy between the model and the data for these components can be understood by referring to figure 4.10 (a). The proposed model is based on the OBO retaining the halogen atoms but as discussed previously 86% of bromine is detached from the molecule. Taking this result into account the experimental value for C_2Br in table 4.3 supports the conclusion that only 14% of bromine remains bonded to OBO. Likewise, the discrepancy of the C_3 component is due to a finite probability that these debrominated carbon sites having sufficient energy to form triply bond carbon in the first stage of polymerisation. As no large-scale OBO chain formation is observed in the STM images it is possible that the polymerisation is rare at this temperature and located at regions of higher catalytic energy i.e. step-edges [9].

Table 4.3: *Modelled and measured areas for components in the C 1s 60^o off-angle spectrum*

Component	**#C**	**Model Area**	**Expt. Fit**	**Uncertainty (±)**	**Discrepancy**
C_2B	2	0.067	0.067	0.006	<0.000
C_2H	14	0.467	0.467	0.004	<0.000
C_3	8	0.267	0.323	0.005	0.056
C_2Br	2	0.067	0.009	0.001	0.058
C_2O	4	0.133	0.135	0.007	0.002

Using this model, the 120 °C normal emission spectra in figure 4.11 (b) was fit in the same fashion. As the molecules dehalogenate and form chains and dehydrogenate forming planar (4,1) chiral-GNRs the C 1*s* envelope also evolves reflecting the changing environment of carbon atoms. The number of carbon atoms in an OBO molecule segment at each stage of GNR formation following the different annealing temperatures is shown in table 4.4. All spectra in figure 4.11 (b) are normalised to the 120 °C data. Due to material desorbing from the surface the 300 °C and 400 °C spectrums are multiplied by 1.25 and 2, respectively for reading convenience. A table of the modelled and measured areas is presented in table 4.5. The model proposes that at 120 °C fully intact OBO molecules with bromine self-assemble on the surface and these molecules complete dehalogenate to form chains at 215 °C. At 300 °C a combination of chains and ribbons exists in a 1:1 ratio. Finally, complete cyclo-dehydrogenation is achieved at 400 °C.

Table 4.4: *Number of carbon atoms in OBO molecule associated to each stage of GNR formation*

Component	Molecules	Chains	Ribbons
C_2B	2	2	2
C_2H	14	14	6
C_3	8	10	18
C_2Br	2	0	0
C_2O	4	4	4

Table 4.5: *Modelled and fit areas for components in C 1s peak*

	Molecules 120 °C		**Chains 215 °C**		**Chains/ Ribbons 300 °C**		**Ribbons 400 °C**	
	Model	**Expt.**	**Model**	**Expt.**	**Model**	**Expt.**	**Model**	**Expt.**
C_2B	0.067	0.065	0.067	0.063	0.067	0.067	0.067	0.067
C_2H	0.467	0.504	0.467	0.459	0.400	0.402	0.200	0.198
C_3	0.267	0.310	0.342	0.342	0.400	0.398	0.600	0.598
C_2Br	0.067	0.009	0	0	0	0	0	0
C_2O	0.113	0.111	0.133	0.137	0.133	0.134	0.133	0.136

The discrepancy between the model and the data will be discussed for each temperature regime. The values for oxygen and boron components are unchanged and consistent with the model throughout the experiment. However, the C-H and C-C=C components do change after each anneal and these components are the indicators for each stage of GNR formation. At 120 °C the model predicted OBO molecules to remain intact with bromine atoms attached but, as with the off-angle analysis, deviation from the predicted value for the bromine component can be understood by looking at the Br 3*p* spectra in figure 4.10 (a) whereby 86% of bromine is removed from the molecule. This also affects the values for the C-C=C carbon component as there is the possibility dehalogenated bromines forming short chains which would account for the larger value for the C_3 in table 4.5. The model matches well with experiment values for the 215 °C regime indicating that the precursor molecules have completely debrominated and molecules have successfully diffused to form chains and the process of cyclo-dehydrogenation has yet to occur. At 300 °C it is predicted that half of the chains would cyclo-dehydrogenate resulting in equal amounts of chains and ribbons and the results in the table support the model. The small discrepancy can be ignored as it is within the uncertainty of measurements. The final temperature regime of 400 °C is expected to yield only ribbons based on STM observations yet the XPS data reveals a ratio of 60:40 of ribbons to chains. This is roughly in agreement with previous studies where ribbons are reported at 450 °C [10]. However, in the experiments described herein most of the material desorbed from the surface at 450 °C resulting in low signal to noise spectra rendering XPS measurements inconclusive. It is possible that annealing the surface at 400 °C for a longer duration may complete cyclo-dehydrogenation without desorbing as much material. What these results show is chain and nanoribbon formation from OBO monomers at lower temperatures than previously described in the literature. A summary of the results are presented in table 4.6

***Table 4.6**: Summary of XPS results highlight the stage of GNR development at each temperature*

	Molecules	**Chains**	**Ribbons**
120 °C	**14%**	**86%**	**0%**
215 °C	**0%**	**100%**	**0%**
300 °C	**0%**	**50%**	**50%**
400 °C	**0%**	**0%**	**100%**

4.3.3 (4,1) chiral-graphene nanoribbons from 0.5 ML Deposition

In preparation for synthesising porphyrin functionalised (4,1) chiral-graphene nanoribbons the Au(111) surface was cleaned by Ar^+ bombardment and annealing as outlined in the procedure in chapter 2. To understand the effect surface coverage has on the growth of (4,1) CGNR on Au(111) approximately 0.5 ML of OBO was deposited on surface. The 0.5 ML was estimated by reducing the deposition time by half from the previous deposition that yielded ~1 ML. Chains were formed by annealing the surface to 300 °C. Using information from section 4.3.2 the surface was annealed at 400 °C for 15 minutes to form fully cyclo-dehydrogenated OBO ribbons. At room temperature and with half monolayer coverage the individual molecules cannot be imaged by STM due to their movement on the surface therefore results from chain formation onwards are presented. Figure 4.12 shows two large scale image of OBO chains on Au(111). The surface coverage is estimated between 45-55% coverage. In both images the chains appear to preferentially grow perpendicularly from the step-edges. This is consistent with previous studies as the step-edge acts as a barrier for diffusing molecules creating a seeding site. Although in figure 4.12 (a), there is one domain of chains in the centre of the image that is not in contact with a step-edge.

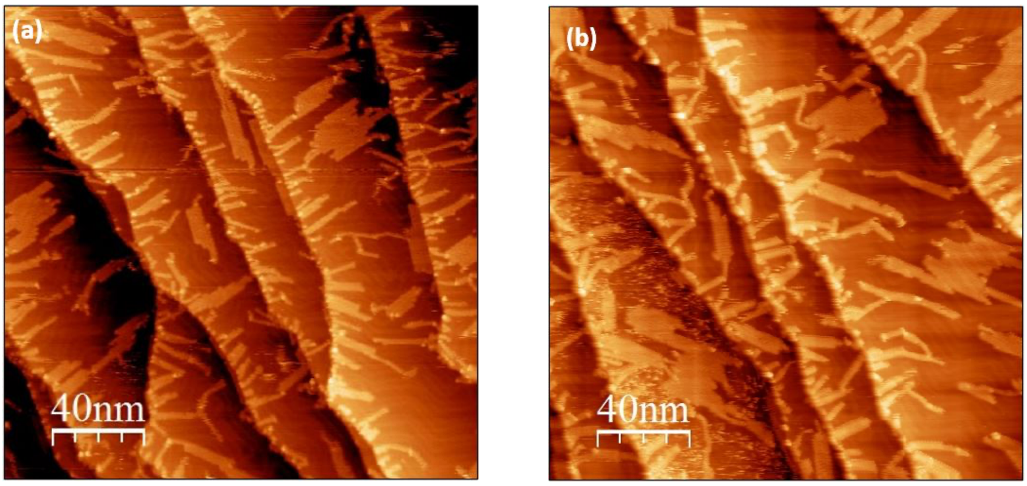

Figure 4.12: *OBO Chains on Au(111). (a) and (b) 200 nm × 200 nm image of different regions of OBO chains on Au(111) showing approximately 0.5 ML coverage. (V=-1.6 V, I=0.2 nA)*

OBO chains can align parallel to each other in three identifiable alignments: homochiral 1, homochiral 2 and heterochiral as shown in figure 4.13 (a), (b) and (c), respectively. Homochiral OBO chains (and ribbons) are such that their orientation with respect to the surface is the same and heterochiral structures have opposing orientation. The variation among homochiral structures is due to the steric hindrances between hydrogen atoms of adjacent chains and only two stable homochiral alignments are seen.

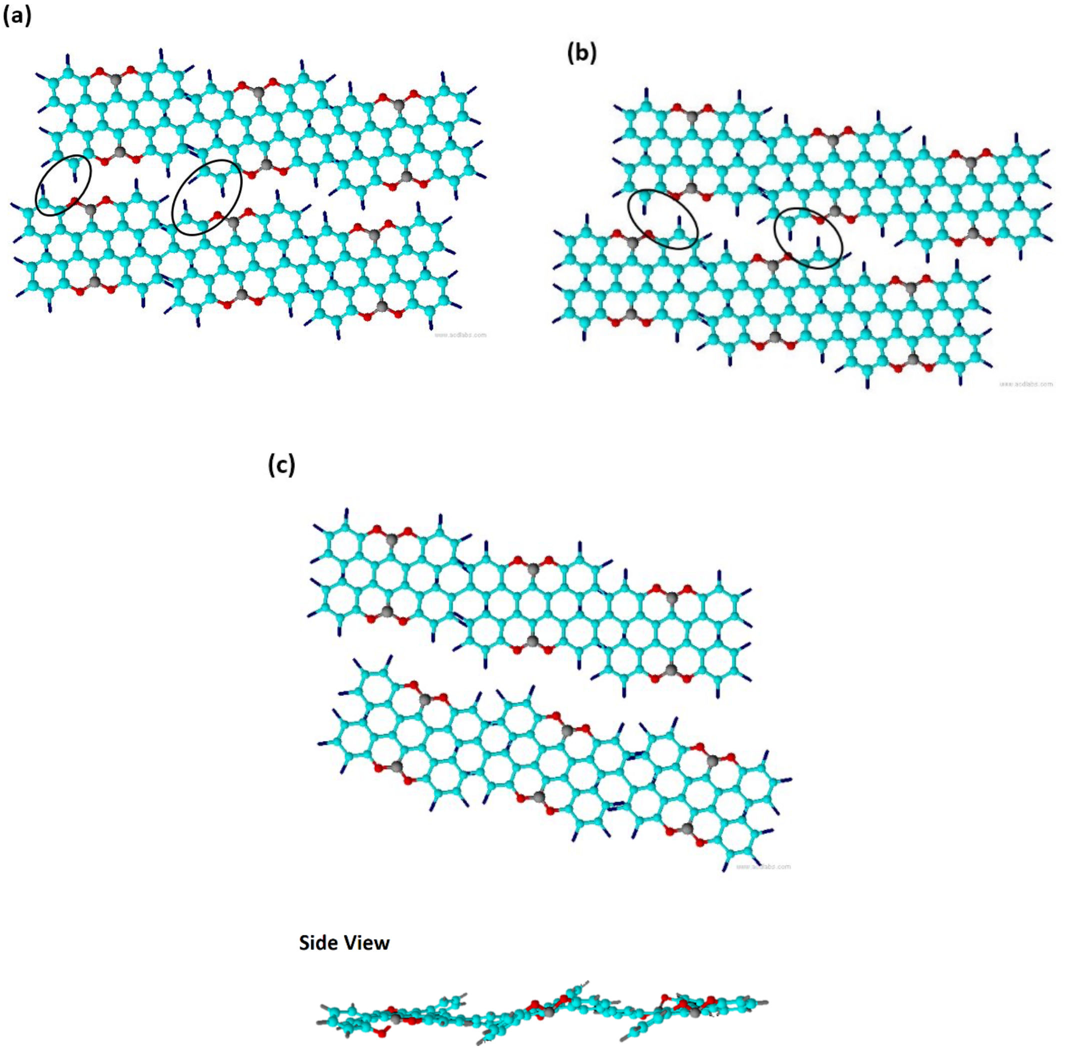

Figure 4.13: Chirality of OBO chains. Chemical models of (a) Homochiral 1, (b) Homochiral 2 and (c) Heterochiral OBO chain alignments with hydrogen atoms shown in navy.

STM images of OBO chains are shown in figure 4.14. The difference in the appearance of these chains to the previous chains in figure 4.5 (b) and (c) is due to the imaging parameters. The images in figure 4.4 were captured with +1.05 V and 0.28 nA whereas the images in figure 4.14 were acquired with -0.82 V and current of 0.42 nA. The increase in current brings the tip closer to the surface and conversely, the reduction in voltage decreases the separation between the tip and the surface. Add to this the reversal of polarity where, with a negative bias on the tip electrons tunnel from filled states to empty states in the sample. In figure 4.14 (a) the domain of chains is ten units wide. As discussed in section 4.3.1 the bright spots are due to protruding benzene segments that are raised off the surface as a result of hydrogen repulsion between sections of the OBO molecule. The inset of figure 4.14 (a) illustrates this and from Chemsketch software the distance between protrusions is on average 1.18nm and indicative of OBO chains. The area enclosed by the white dashed box is shown in figure 4.14 (b). The two homochiral alignments are identified in figure 4.14 (b). The two alignments can be distinguished by measuring the distance between protrusions in adjacent chains. The distance for the homo 1 orientation is 0.65 nm and 0.82 nm for the homo 2 alignment. The distance was measured from the STM image 4.14 (b) and ten measurements were taken from both the homochiral 1 and homochiral 2 regions to compile an average value. The line profiles are shown in figure 4.15 and show the average values of 0.62 nm and 0.85 nm are in good agreement with predicted measurements from Chemsketch.

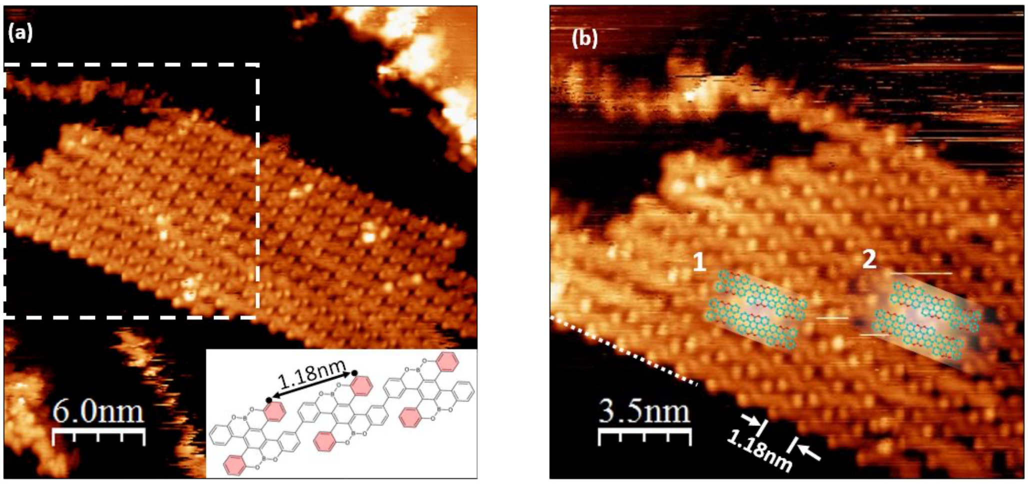

***Figure 4.14**: STM of OBO chains. (a) 36 nm × 36 nm and (b) 17.5 nm × 17.5 nm of OBO chains after annealing at 300 °C (V=-0.82 V, I=0.28 nA)*

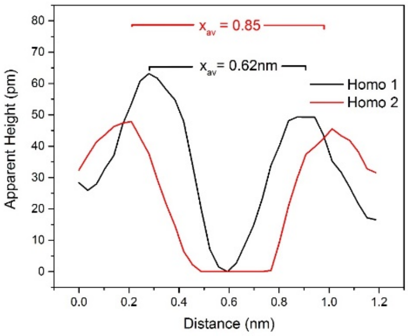

***Figure 4.15**: Line profiles of separation between adjacent benzene ring protrusions for homo 1 and homo 2 alignments*

After annealing at 400 °C for 15 minutes, the chains cyclo-dehydrogenate to form (4,1) CGNRs as shown in figure 4.16 (a). At this lower density coverage GNRs can are observed to grow along and across the step-edges of the Au(111) surface. The majority of the ribbons grow in straight, parallel rows while there is some evidence of ribbons bending when encountering a boundary with other ribbons. In figure 4.16 (b), 5 parallel ribbons are shown labelled as rows 1-5. Row 1 appears unambiguously as one continuous ribbon whereas row 2 appears to be two ribbons of opposite chirality that meet at the region circled in the yellow. The interface of two ribbons appears brighter than the surrounding regions, possibly a result of the ribbons overlapping or a result of higher density of states at the ribbons ends as is observed in 7-wide armchair GNRs [11]. The ribbon in row 1 and the ribbon in the top portion of row 2 have homochiral alignment while the bottom portion of row 2 has heterochiral alignment with row 1. The STM imaging conditions are insufficient to determine the edge structure of the ribbon in the third row however it is apparent that there is a gap corresponding to two OBO molecule units between the top and bottom ribbons. Rows 4 and 5 contain ribbons that have heterochiral alignment. The presence of multiple orientations of ribbons suggests that at lower surface coverage the GNRs are do not form high density packed structures. Histograms of the lengths of GNRs from figure 4.16 (a) are compiled in figure 4.15 (c), ribbons that extend beyond the area of the image were not included in the statistics. The line profiles in figure 4.16 (b) and the white line profile taken from figure 4.14 (b) are shown in figure 4.16 (d) where the difference in length between protruding benzene rings of OBO chains and the distance between the step of (4,1) CGNRs are shown to be 0.89 nm ±0.1 nm for ribbons and

1.18 nm ±0.1 nm for chains. The reduction of the separation of protrusions is due to cyclo-dehydrogenation of the chain and the planarization of the ribbon.

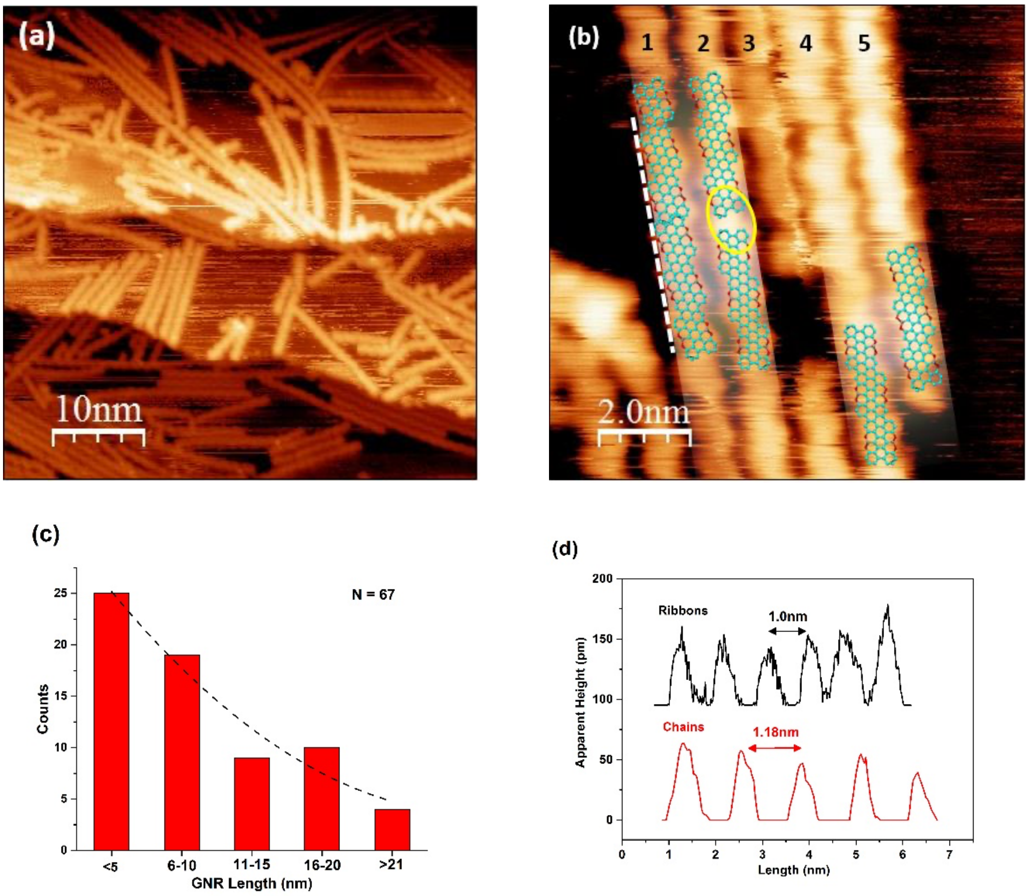

Figure 4.16: *(4,1) chiral GNR on Au(111): histograms and line profiles. (a) 50 nm × 50 nm image of GNRs along and across Au(111) step-edges. V=0.98 V, I=0.49 nA. (b) 10 nm × 10 nm image of 5 parallel GNRs. V=1.00 V, I=0.10 nA. (c) Histograms of GNR lengths taken from (a). (c) Line profiles from (b) and figure 4.13 (b) showing the distance between step of OBO ribbons and chains.*

4.3.4 Porphyrin functionalised (4,1) chiral GNRs on Au(111)

The OBO molecules and Ni-DBTPP were deposited simultaneously onto the Au(111) surface while samples were heated to 200 ºC to initiate dehalogenation on contact. The evaporation conditions aimed to achieve a surface coverage of 0.6ML with a ratio of 3:2 OBO to porphyrin. While it is difficult to ascertain the ratio, the total material sublimated produced a surface coverage of 50-77%. The wide range of surface coverage is due to local variations in the density of material possibly due to the position of the sample with respect to the evaporation cells during a co-deposition. Figure 4.17 (a) shows a large-scale image of material on the surface. Three islands of material are highlighted and can be identified as OBO chains. This is because OBO chains form straight rigid structures while porphyrin chains form non-rigid structures owing to the number of degrees of freedom at the bonding site. In the highlighted region in the top right of figure 4.17 (a) non-rigid chains can be seen to grow from the OBO island that can be evidence of porphyrin chains. Outside of the highlighted regions the material is less densely packed and interacts weakly with the surface making identification of the species of molecule challenging. Figure 4.17 (b) unambiguously shows the presence of both OBO and porphyrin chains. Region 1 shows a large domain of OBO chains forming at the lower part of the step-edge. The OBO chains show the characteristic 1.2 nm spacing between protruding benzene rings. In region 2, a 4-porphyrin chain is connected to an OBO chain and forms a fan-like "Christmas Tree" shape as discussed previously in section 3.3.1. The effect is caused by the molecules moving on the surface faster than the scan speed of the STM tip. Porphyrins appear to align along the higher part of the step-edge and form nucleation sites as seen in regions 3 and 4. Particularly in region 4 an OBO chain is linked to a porphyrin on the step-edge. Long porphyrin chains are seen growing parallel side by side in region 5.

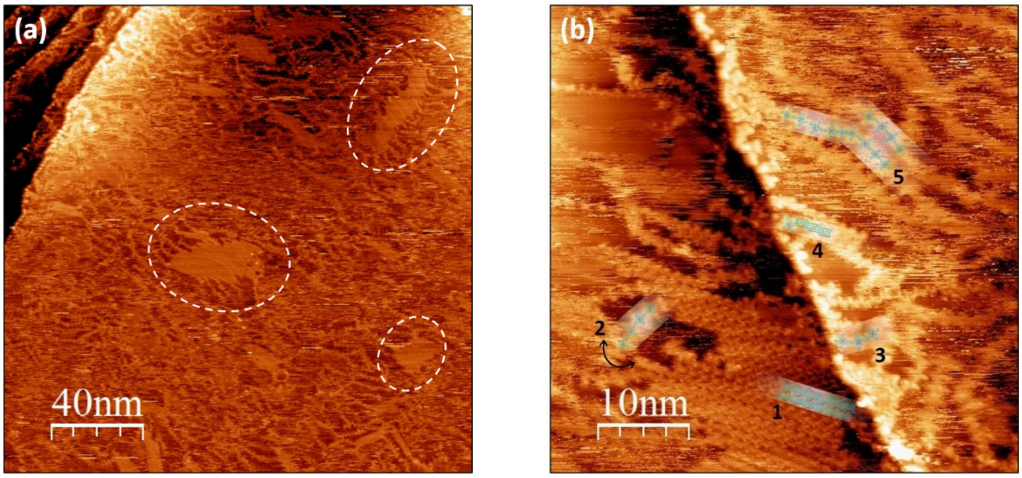

***Figure 4.17**: OBO and Porphyrin on Au(111). (a) 200nm × 200nm (V=1.0V, I=0.1nA). (b) 50nm × 50nm (V=0.9V, I=0.1nA)*

The sample was annealed at 250 °C for 10 minutes to encourage diffusion of both OBO and porphyrin molecules that had not formed into chains while not instigating cyclo-dehydrogenation. In figure 4.18 (a) the 200 nm × 200 nm image shows material on three terraces. Again, large islands of OBO chains are highlighted in the image. There appears to be phase separation between both species of molecules with OBO chains self-assembling into densely packed domains and porphyrins forming long, non-rigid chains. The gold surface has reconstructed into a 2 × 1 lattice as first mentioned in section 3.3.1. A feature of this reconstruction is the appearance of apparent troughs on the surface clearly seen in figure 4.18 (b). The cause of this surface phenomena is unknown however the troughs are possibly caused by stress in the 2 × 1 reconstruction where a discontinuation of the gold surface atoms occurs. Whether or not the troughs are due to the presence of the porphyrin or OBO is unclear, but it is apparent the porphyrins diffuse into the troughs and form meandering chains along them.

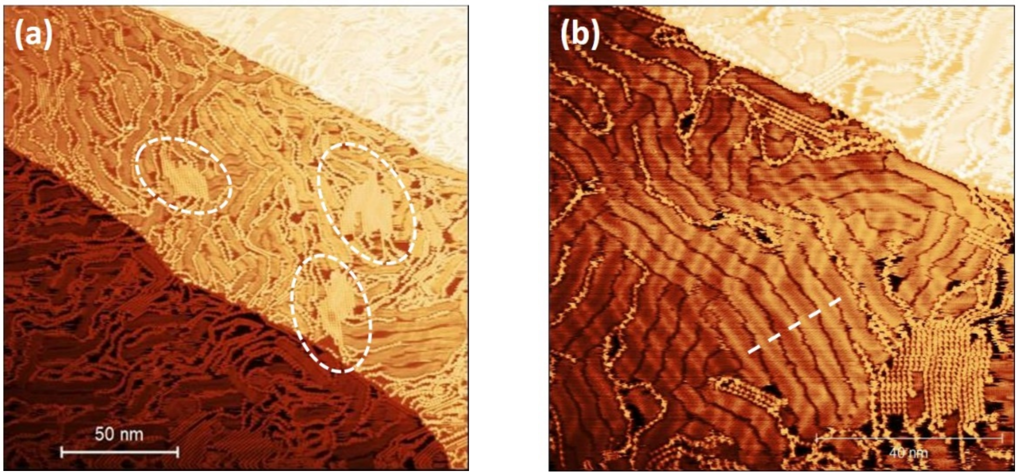

Figure 4.18: *OBO domains and porphyrin chains. (a) 200 nm × 200 nm (V=1.1 V, I=0.1 nA*

Another unusual feature of the surface in figure 4.18 (b) is the visibility of the 22×√3 so-called "herringbone" surface reconstruction associated with Au(111) surface. Figure 4.19 shows the line profile taken from figure 4.18 (b), the separation between neighbouring troughs is 4.8 nm ±0.2 nm and the gap between corrugation lines of the Au(111) is ~2.2 nm in agreement with studies on the gold crystal [12]. It should be noted that the line profile is taken perpendicular to the gold troughs and not to the reconstruction lines. An explanation for the existence of 2 × 1 reconstruction remains an open question.

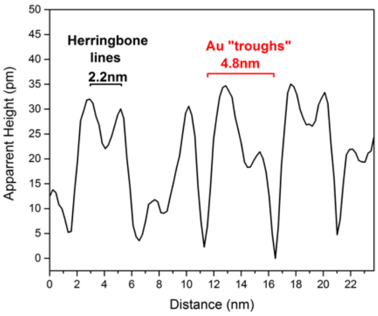

Figure 4.19: *Line profile of Au(111) reconstruction lines and surface troughs*

Figure 4.20 (a) shows a different region of the gold sample that was subject to the same deposition and annealing procedure. Imaged with a positive tip bias an array of equidistant features is visible. Unlike OBO chains which are seen to group into high density domains and form straight rigid structures, these features are well-spaced and have slight deviations in their direction of growth and seem to align parallel to the step-edges and do not grow from the step-edges. They also do not resemble porphyrin chains as there is no evidence of phenyl rings perpendicular to the central axis as is normally seen with Ni-TPP chains. In figure 4.20 (b) a 20 nm × 20 nm area from figure 4.20 (a) shows four such rows of material and provides some resolution into the internal structure of the features. The step-like chiral nature of OBO chains is not seen but the width of each row is 1.2 nm ±0.2 nm, which agrees with the length of individual OBO molecules. The internal structure revealed in the STM image also matches with non-planar OBO molecules. From the line profile in figure 4.19 (c), the distance between the centre of each row is approximately 4.8 nm, the same as the separation between the troughs in the gold surface. It is fair to conclude that the rows of material are comprised of OBO molecules self-assembled side by side in the troughs created on the gold surface. In this case OBO molecules are not covalently bonded to each other despite the removal of bromine during dehalogenation and instead, they follow the grooves of the gold surface. To our knowledge self-assembled dehalogenated OBO molecules have not been reported in the literature. One possible reason for this alignment of OBO molecules is due the amount of time the sample was left idle. The images in figure 4.20 were acquired 48 hours after figures 4.18. Dehalogenated OBO molecules could be in low density area of the surface and not diffuse to bond to other dehalogented OBO molecules. However, in the preceding 48 hours at room temperature the solo molecules still diffuse on the surface but without the catalytic effect of the hot surface to provide enough energy to overcome the chemical energy required to form polymer chains [13]. Instead, the molecules relax into the troughs formed in the 2 × 1 gold reconstruction and over time the number of individual OBO molecules builds up and form these long tendrils.

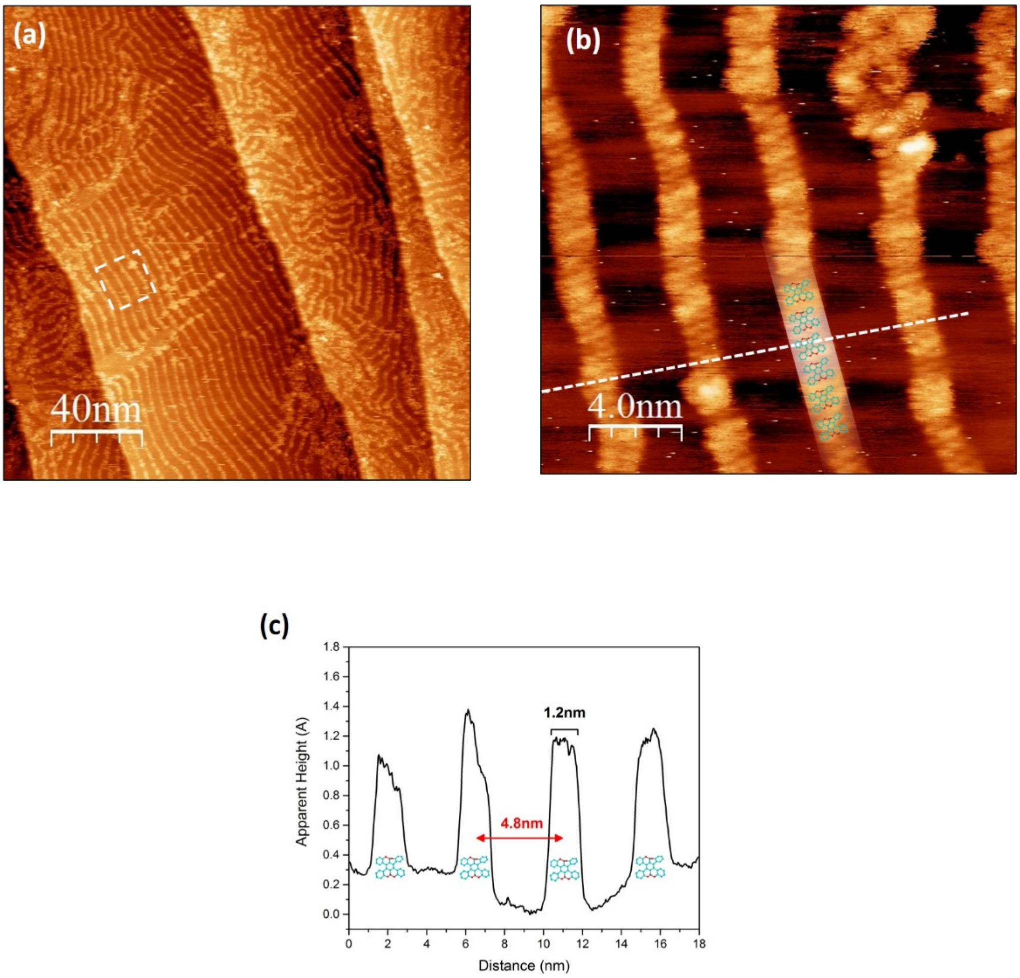

Figure 4.20: *OBO self-assembly on Au(111). (a) 200 nm × 200 nm (V=1.0 V, I=0.09 nA) (b) 20 nm × 20 nm (V=0.6 V, I=0.05 nA). (c) Line profile of self-assembled material in (b).*

The junction between the porphyrin and the OBO chains can form in one of two ways. One structure occurs when OBO molecules are in the same orientation with respect to the surface and the bottom debrominated site and the top debrominated site of the OBO molecule bond to the porphyrin phenyl rings as shown in the dehalogenation image in figure 4.21 and referred to as trans-OBO orientation. The other formation is cis-OBO orientation and happens when the OBO molecules have the opposite orientation with respect to the surface and bond to the porphyrin as shown in figure 4.21. Upon cyclo-dehydrogenation a triphenylene unit is formed between the debrominated phenyl ring of the porphyrin and the OBO molecule, unlike the fluoranthene unit formed by 7-AGNR and porphyrin heterojunctions discussed in chapter 3. The dehydrogenation process also leads to the formation of 5-sided rings between the porphyrin macrocycle and the triphenylene unit. This bending at the junction results in five unique configurations defined by the angle between the graphene nanoribbons with the porphyrin at the vertex. For the trans-OBO orientation there are two angles possible; 170.5° and 174.1° as shown in figure 4.20. While for cis-OBO orientation there are three angular arrangements, 80.2°, 164.1° and 165.6°. The phenyl rings at the 5 and 15 position on the porphyrin macrocycle also dehydrogenate forming five member rings with the macrocycle. This further increases the number of possible configurations for OBO ribbons and porphyrins with 15 in total. All possible configurations of a porphyrin integrated into a (4,1) CGNR are shown in figures 4.21 and 4.22.

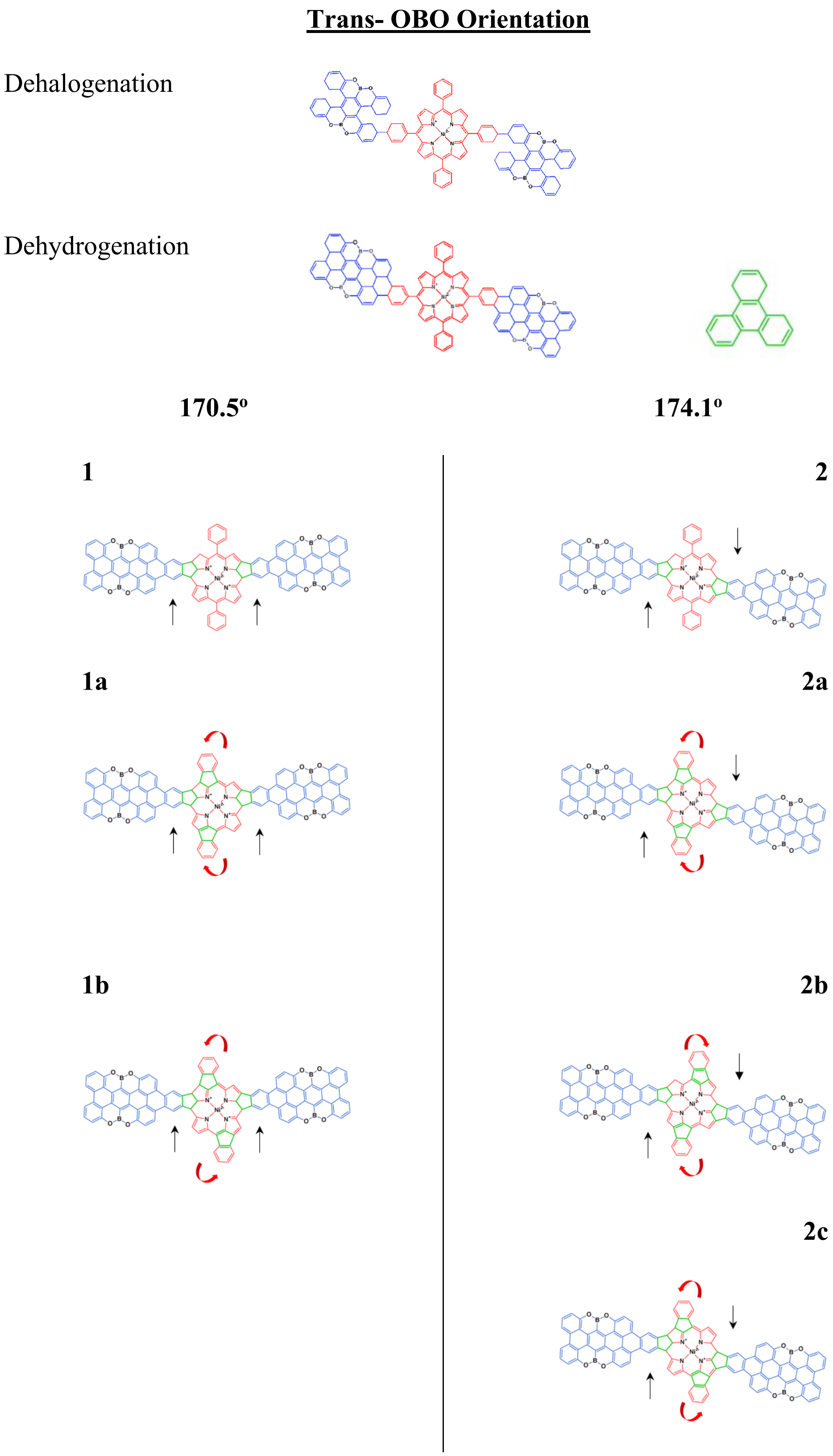

Figure 4.21: Configurations of trans-porphyrin functionalised (4,1) CGNR

Cis- OBO Orientation

Dehalogenation

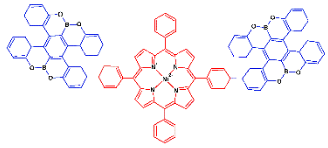

Dehydrogenation

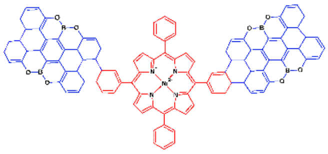

80.2°

3

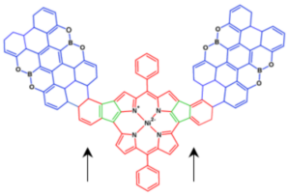

3a

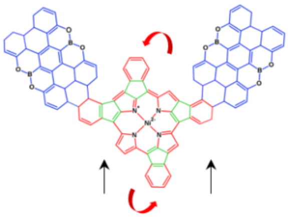

3b

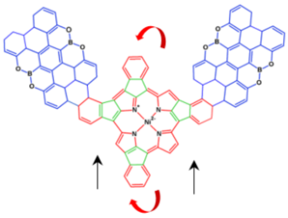

164.1°

4

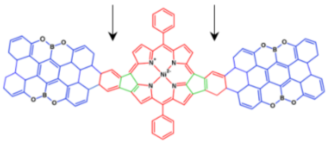

4a

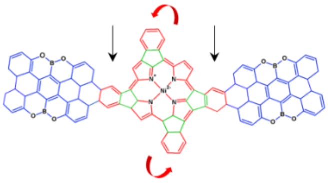

4b

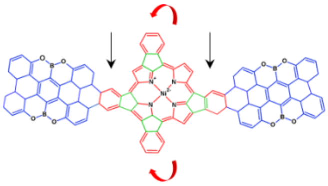

160.6°

5

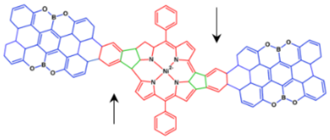

5a

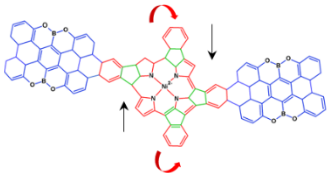

5b

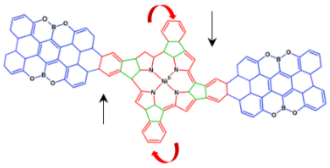

5c

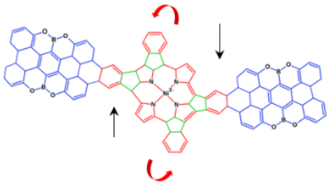

Figure 4.22: *Configurations of cis-porphyrin functionalised (4,1) CGNR*

Hetero-junction structures between OBO ribbons and porphyrin molecules are formed on the Au(111) by annealing the surface at 400 °C as the cyclo-dehydrogenation process was previously found to be complete at this temperature. Figure 4.23 (a) shows a 50 nm × 50 nm image of OBO chains on the Au(111) crystal. The 2 × 1 surface reconstruction is clearly seen and with three distinct directions which forms rows at 60° with respect to each other. Certain regions of the GNRs appear brighter than others. This is mostly likely due to the higher density of states found at the end of ribbons [11]. However, one bright spot at the centre of the image is highlighted by white box. A closer image is shown in figure 4.23 (b). This can unambiguously be identified as a triply fused heterojunction with (4,1) CGNRs connected to the debrominated phenyl rings at the usual 10 and 20 positions on the porphyrin but also with a ribbon bonded to the phenyl ring at the 15 (or 5) position. In order for such a structure to form the outermost hydrogen of the phenyl ring in question must be removed allowing for a nearby ribbon to attach to the radical. The dehydrogenation of outer hydrogens on 7-AGNRs is reported in the literature at temperatures ~450 °C but there is no report of similar occurring for porphyrins. A 5 nm × 5 nm image is shown in figure 4.23 (c) with a bright spot in the centre surrounded by four bright lobes. The image was acquired with a positive bias on the tip which suggests these bright lobes are attributable to high local density of states (LDOS) at the HOMO of the heterojunction. It is fair to say the bright lobe in the centre is associated to the nickel core of the porphyrin however the four lobes cannot be attributed to any specific atom but are possibly associated with the five membered rings. From figure 4.23 (c) the chemical model is shown in (d) which has the same configuration as model 2a in figure 4.21 with the additional ribbon attached at the 15 (5) position.

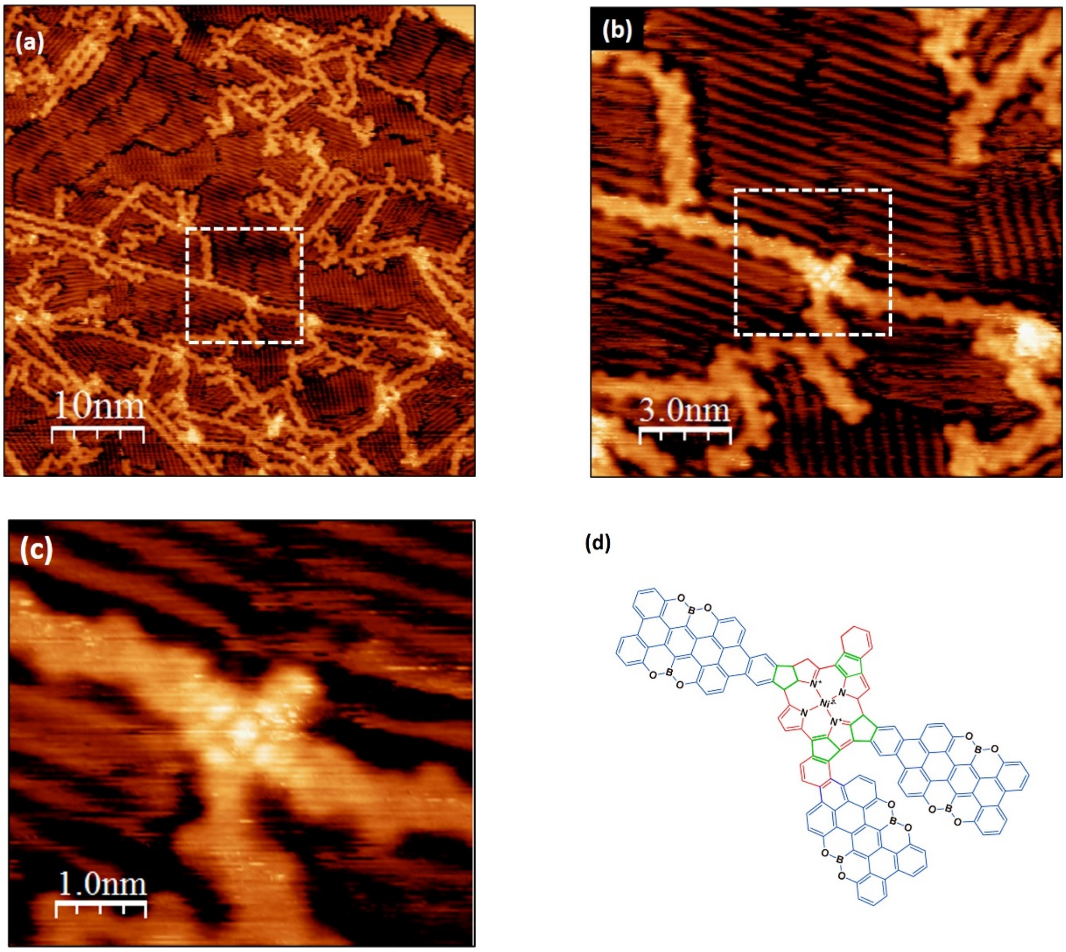

Figure 4.23*: Porphyrin functionalised (4,1) chiral-GNRs on Au(111). (a) 50 nm × 50 nm. (b) 15 nm × 15 nm. (c) 5 nm × 5 nm (d) Chemical model of triply fused heterojunction. All STM images acquired at V=-0.6 V, I=0.2 nA*

The images in figure 4.24 (a), (b), (c) and (d) shows a collection of large area STM images. At this level exact heterojunction configurations cannot be identified; however, blue arrows are used to direct the eye to suspected porphyrins. Under the tip bias conditions in figure 4.23 the nickel atom appeared as a bright spot but under different bias the porphyrin centre can appear empty.

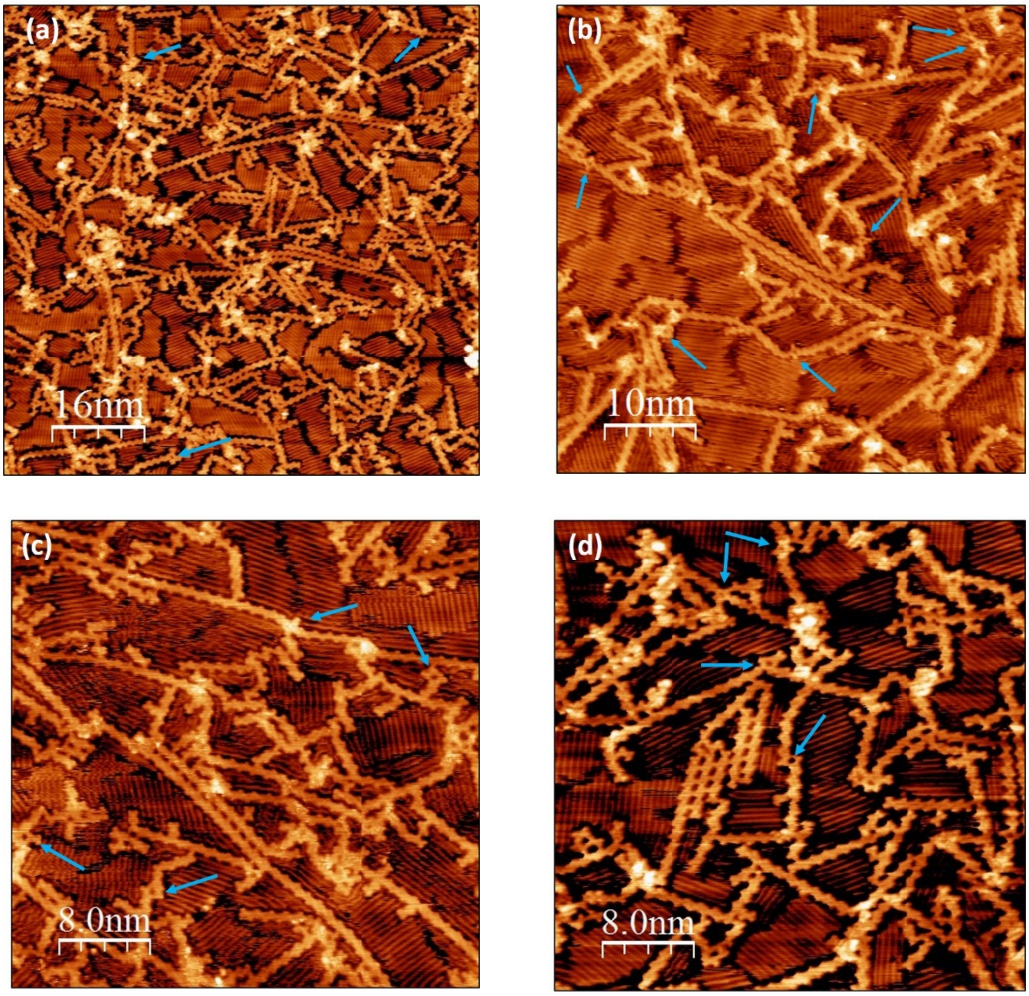

Figure 4.24*: Porphyrin functionalised ribbons on Au(111). (a) 80 nm × 80 nm (V=-0.4 V, I=0.25 nA). (b) 50 nm × 50 nm (V=-0.4 V, I=0.3 nA) (c) 40 nm × 40 nm (V=-0.4 V. I=0.3 nA) (d) 40 nm × 40 nm (V=-0.4 V. I=0.3 nA)*

Figure 4.25 shows various hetero-junction configurations. Green arrows are used to identify cis-OBO orientation type 1 and yellow arrows highlight trans-OBO orientation type 2. In figure 4.25 (a) one porphyrin is identified in cis- type 1 configuration. Figure 4.25 (b) shows a 14 nm long OBO ribbon with two integrated porphyrins in trans- type 2 orientation separated by three OBO units. Figures 4.25 (c) and (d) are composite images formed by combining the STM image and its derivative. In figure 4.25 (c) a trans- type 2 orientation is seen, and single bonded porphyrins are highlighted by the blue arrows. The junctions circled in white are triple bonds similar to that shown in figure 4.23 (c) however, with this tip bias the porphyrin core appears dark. In figure 4.25 (d) a single cis- type 1 junction is shown.

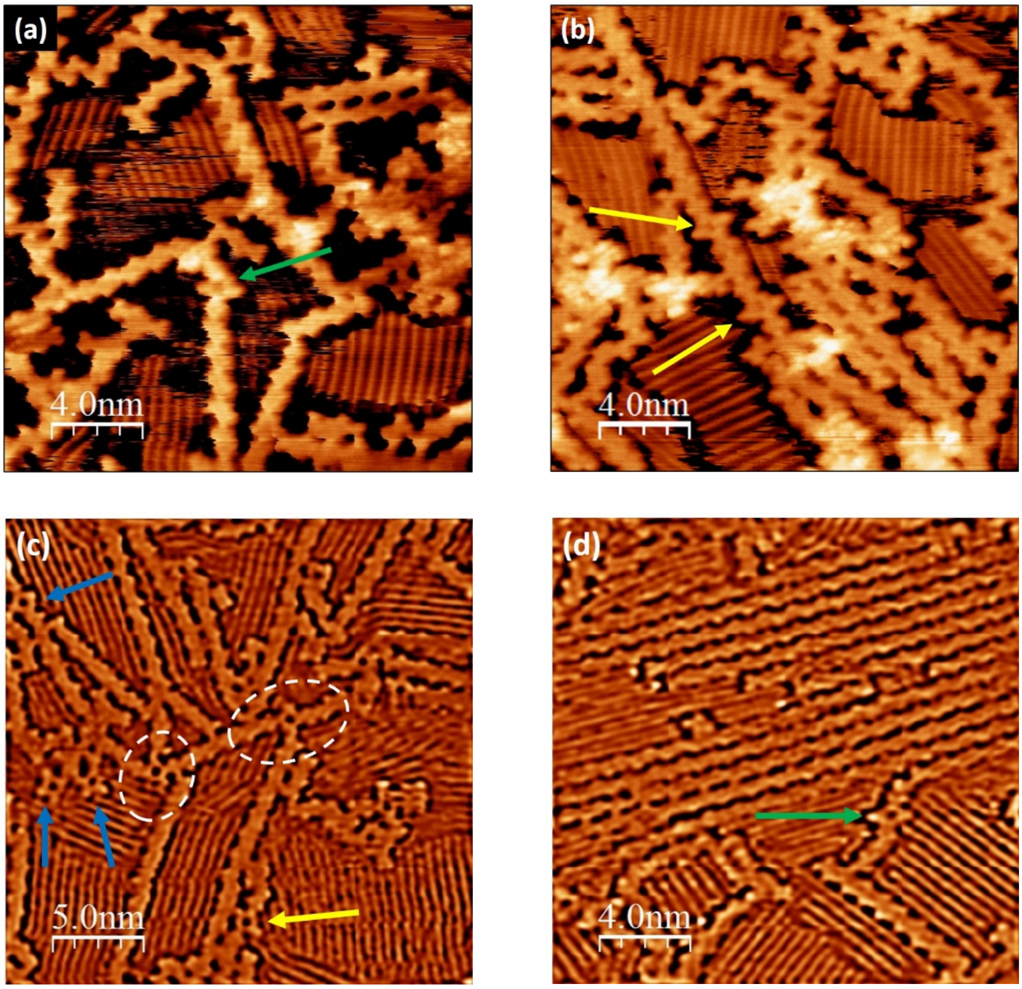

***Figure 4.25**: Heterojunction identification on Au(111). (a) 20 nm × 20 nm (V=-0.4 V. I=0.3 nA) (b) 20 nm × 20 nm (V=-0.4 V. I=0.3 nA) (c) 25 nm × 25 nm (d) 20 nm × 20 nm*

4.3.5 Porphyrin functionalised (4,1) chiral GNRs on Au(788)

As with the formation of porphyrin functionalised (4,1) CGNRs on the Au(111) surface the same deposition and annealing stages were repeated for the Au(788) surface. The Au(788) vicinal surface has 4.0 nm wide terraces separated by step-edges. These narrow terraces have been shown to confine the diffusion of precursor molecules and thus influence the direction of growth of polymers [14, 15]. Alignment of GNRs is desirable when transferring structures onto semiconducting surfaces and for area averaging characterisation techniques specifically angular resolvable photoelectron spectroscopy (ARPES) and Raman spectroscopy.

Figure 4.26 shows porphyrin functionalised (4,1) CGNRs on the Au(788) surface. As with the Au(111) various configurations of heterojunctions are possible. In figure 4.26 (a) three configurations are identified. The blue arrow shows a one-sided junction and the yellow shows trans- type 2 and the pink arrow shows a cis-type 3 junction that forms a 80° angle. A ribbon approximately 40 nm in length is seen to grow along the step-edge, two white circles highlight the two ends of the ribbon. The GNR appears to be discontinuous because the nearby ribbons on both ends have the opposite chirality which inhibit its extended growth. In figure 4.26 (b) trans- type 2 and cis- type 3 orientations are seen alongside unidentifiable heterojunctions. Ribbons also appear to grow both along and across the step-edges. Figure 4.26 (c) is a composite image of height and derivative. In the white highlighted area two porphyrins integrated into GNRs appear to bond to each other at the 5 and 20 position. In the circled area in figure 4.26 (d) three porphyrins are shown bonded to each other in chain like form growing along then across the step-edge. At this surface coverage, estimated at less than 50%, the ribbons are not exclusively confined in parallel rows along the terraces as many GNRs are growing across the step-edges many ribbons can be seen to grow across the step-edges. The angle at which the ribbons cross the step edge appears to be limited to 60°, 90°, and 150° with respect to the step-edge, the reason for this remains an open question. There is also evidence of 2 × 1 surface reconstruction on the terraces as previously seen on Au(111) in section 3.3.1 which proves the phenomena is not specific to one crystal plane.

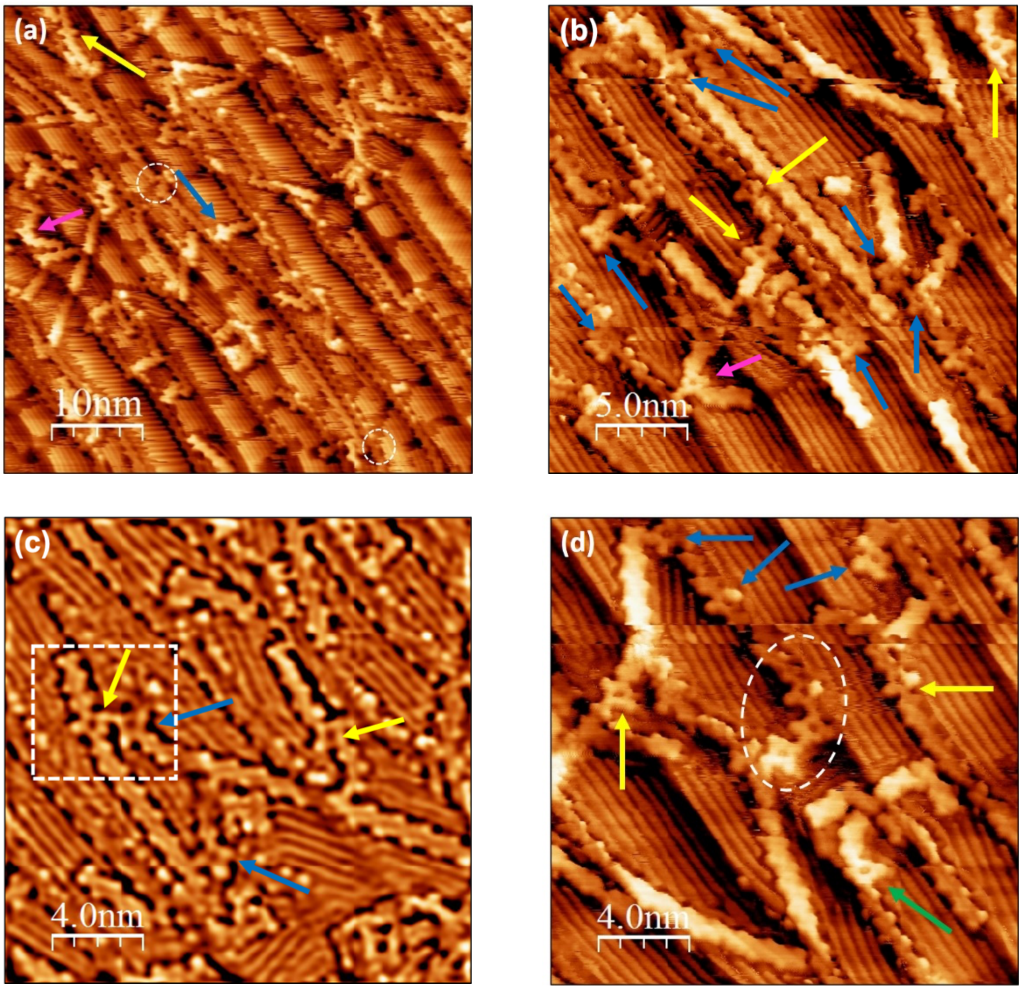

Figure 4.26: *Porphyrin functionalised (4,1) CGNRs on the Au(788). (a) 50 nm × 50 nm (V=-0.4 V. I=0.3 nA). (b) 25 nm × 25 nm (V=-0.4 V. I=0.25 nA). (c) 20 nm × 20 nm (d) 20 nm × 20 nm (V=-0.4 V. I=0.25 nA)*

4.3.6 Formation of aligned (4,1) chiral GNRs on Au(788)

To investigate methods for achieving alignment of (4,1) CGNR without integrated porphyrins on Au(788), two deposition strategies where implemented. The first protocol deposited approximately a monolayer of OBO on the surface and annealed the surface to thermally activate the formation of GNRs. The second protocol included two separate depositions of approximately 0.5 ML each, and subsequently annealing the sample at 400 °C after each deposition to instigate GNR formation. The results from the first protocol are shown in figure 4.27. The image in figure 4.27 (a) shows deposited OBO molecules on the Au(788) surface. The adsorbents image poorly and individual molecules are difficult to identify. However, the surface coverage can be estimated at approximately a monolayer. A line profile average of figure 4.27 (a) is shown in (b) and the rows of material have a mean separation of 4.0 nm which coincides with the separation of step-edges on the Au(788) surface. Figures 4.27 (c) and (d) show (4,1) CGNR following dehalogenation and cyclo-dehydrogenation. The ribbons are disordered on the surface with many ribbons seen growing across the step-edges. To quantify the degree-of-alignment the ribbons are classified into three categories; aligned, angled, and perpendicular and labelled 1, 2, and 3 respectively, in figure 4.29 (a). Aligned ribbons grow along the step-edges, angled ribbons grow across the step-edge at a 60° or 150° angle and perpendicular ribbons cross the step-edge at 90°. Histograms of the degree-of-alignment together with histograms for length are collected from figure 4.27 (c) and (d) shown in figure 4.30.

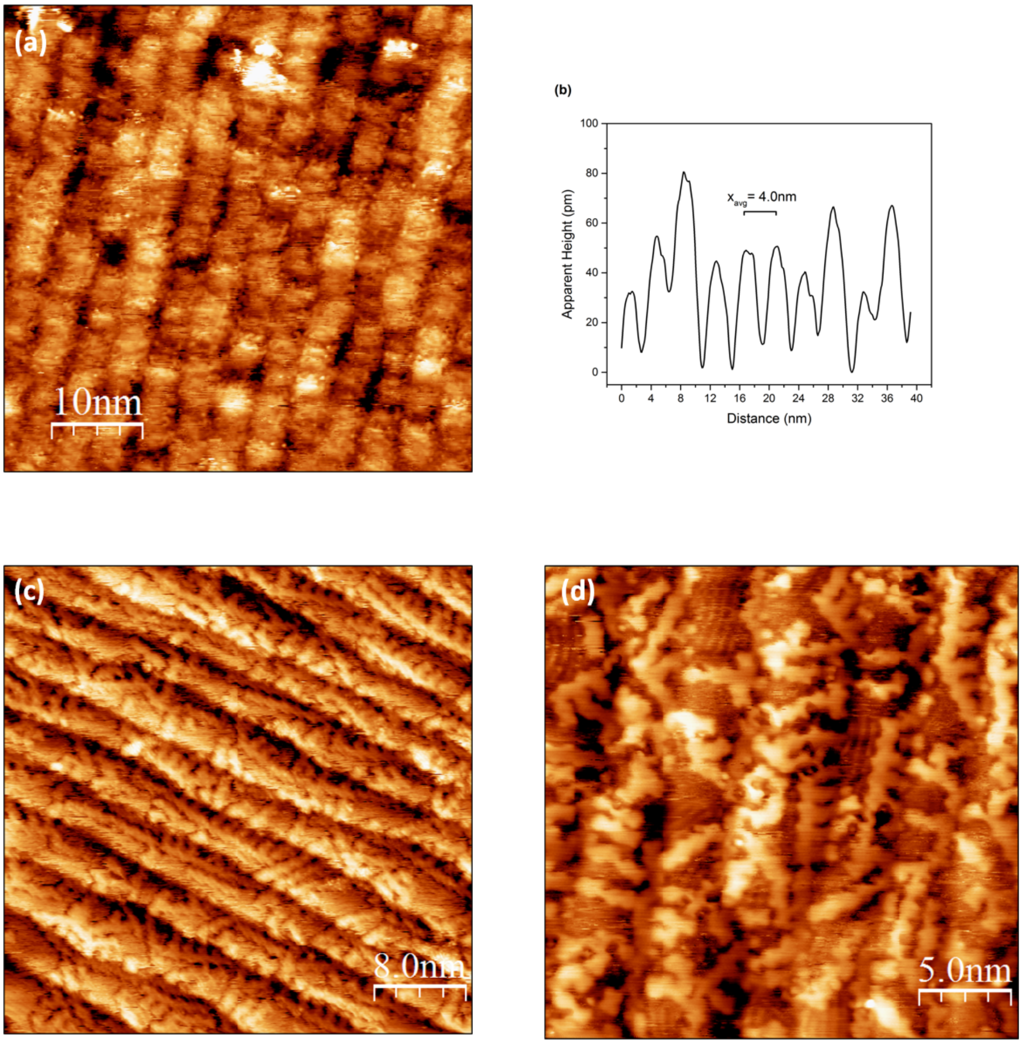

Figure 4.27: *Monolayer OBO deposition on Au(788). (a) 50 nm × 50 nm OBO molecules on Au(788) (V=-0.96 V, I= 1.0 nA). (b) Line profile average of (a) with spacing of 4.0 nm (c) 40 nm × 40 nm (4,1) CGNRs (V=-0.01 V, I=1.0 nA). (d) 25 nm × 25 nm (4,1) CGNRs (V=-1.00 V, I=0.2 nA).*

The sample was cleaned, and 0.5 ML of material was deposited. The OBO molecules cannot be imaged on the surface at this coverage as the molecules diffuse on the surface. Forming chains reduces the amount of diffusion and allows the polymers structures to be imaged. Figure 4.28 (a) shows OBO chains predominantly aligned along the step-edge while some chains are angled and perpendicular to the step-edge. The local surface coverage of OBO chains is estimated at ~0.4 ML A line profile from 4.28 (a) is shown in (b) and the characteristic benzene ring protrusion distance of 1.2 nm for OBO chains is identified. After annealing the sample at 400 °C for 10 minutes (4,1) CGNRs form on the surface as shown in figures 4.28 (c) and (d).

As with the monolayer coverage in figures 4.27 the ribbons appear uniformly distributed between aligned, angled, and perpendicular.

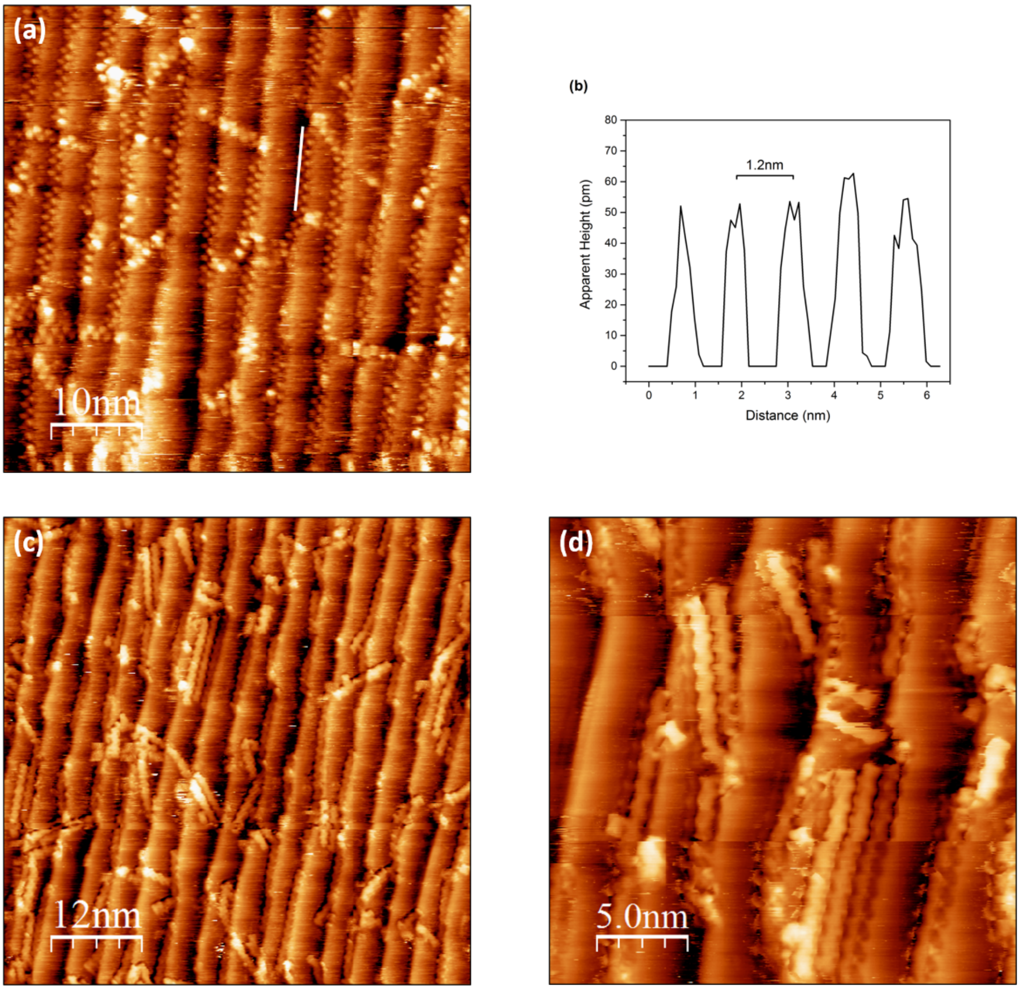

***Figure 4.28**: OBO chains and (4,1) CGNRs on Au(788). (a) 40 nm × 40 nm images of chains (V=-0.74 V, I=25 pA). (b) Line profile taken from (a). (c) 60 nm × 60 nm image of CGNRs (V=0.56 V, I=56 pA). (d) 25 nm × 25 nm image of CGNRs (V=-0.53 V, I=56 pA).*

Once the ribbons were formed on the Au(788) surface a second 0.5ML of OBO was deposited. The surface has approximately a monolayer surface coverage and the confinement restricts the movement of precursors and the individual OBO molecules can be imaged as seen in figure 4.29 (a). Chemical models of the (4,1) CGNR are overlayed specific ribbons to highlight the three angles the ribbons can grow with respect to the $[10\bar{1}]$ direction on the Au(788) crystal. Regions **a** and **b** highlight individual OBO molecules which appear to preferentially nucleate on the step-edges. Interestingly, the molecules in region **a** lie at an angle and the molecules in region **b** are perpendicular. This may explain why ribbons are observed to cross step-edges at defined angles. Figure 4.29 (b) was acquired after annealing the sample to 200 °C for the second time and OBO chains and CGNRs are observed in parallel rows. Similarly, figures 4.29 (c) and (d) were captured after the sample was annealed at 400 °C and display predominantly straight, aligned (4,1) CGNRs. The surface coverage estimated for the 100 nm × 100 nm area in figure 4.29 (c) is 0.8 ML. Histograms of the length and degree-of-order are compiled from figure 4.29 (c) and presented in figure 4.30.

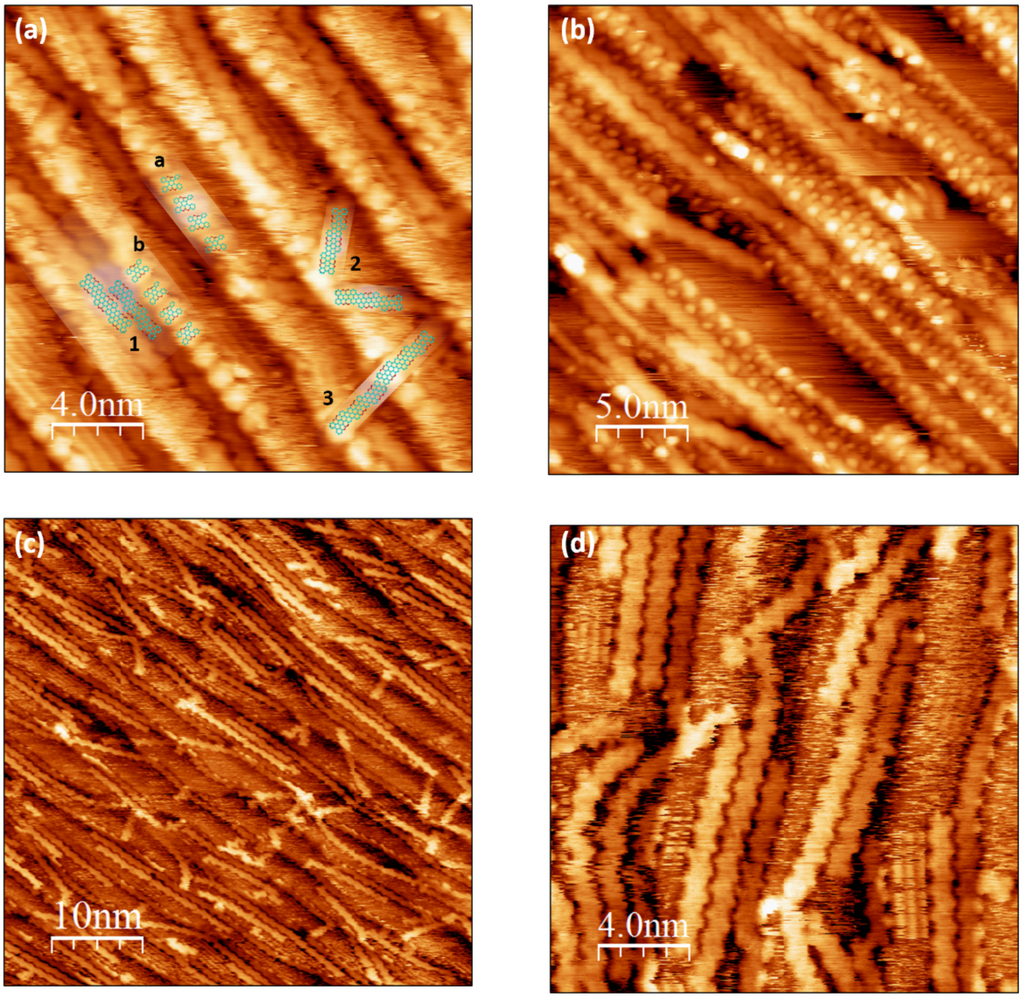

Figure 4.29*: 2nd Deposition of OBO on Au(788). (a) 16 nm × 16 nm OBO molecules with CGNRs (V=-0.5 V, I= 0.1 nA) (b) 25 nm × 25 nm OBO chains with CGNRs (V=-1 V, I=1.0 nA), (c) 100 nm × 100 nm High density aligned (4,1) CGNRs (V=-0.5 V, I=1.0 nA) (d) 16 nm × 16 nm (V=-0.5 V, I=1.0 nA)*

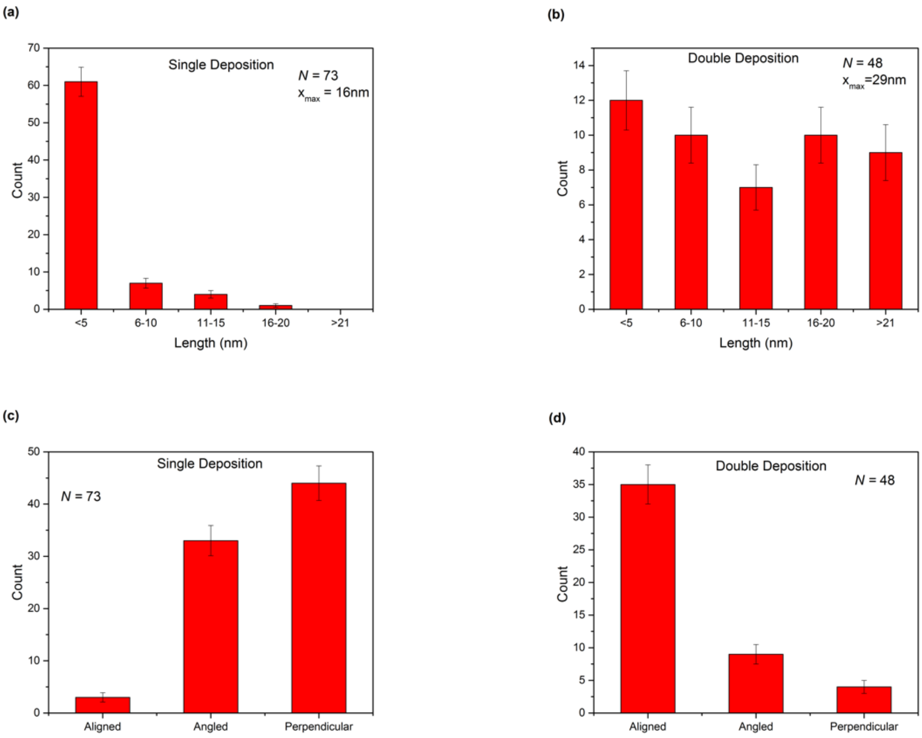

Figure 4.30: *Histograms of degrees-of-alignment and length of (4,1) CGNR. (a) Length of CGNRs after single deposition. (b) Length of CGNRs after double deposition. (c) Measure of alignment after single deposition (d) Measure of alignment after double deposition.*

Comparing the histograms of length for the single- and double depositions it is clear the double deposition results in longer ribbons. 83% of the ribbons after single deposition are 5 nm or less while its only 25% for this category after double deposition. There are no ribbons over 21 nm observed for a single deposition and the longest ribbon is 16 nm ±0.5 nm. Conversely, the longest CGNR measured after a double deposition is 29 nm ±0.5 nm and 19% of ribbons are over 21 nm. The double deposition method with intermediate ribbon formation results in a greater number of long ribbons. Looking at the degree-of-alignment histograms, there is a significant increase from 4% to 73% in the number of aligned CGNRs for the double deposition. Likewise, only 10% of ribbons are perpendicular to the step-edge compared to 62% after the single deposition. The double deposition protocol is successful method for achieving long, aligned (4,1) chiral GNRs on the Au(788) surface.

4.4 Conclusions

In this chapter, (4,1) chiral GNRs and porphyrin functionalised CGNRs are formed via on-surface synthesis on the Au(111) and Au(788) surfaces. The precursor molecule for (4,1) CGNR, OBO, was deposited on the Au(111) surface and the stages of self-assembly, polymerisation and ribbon formation are described using STM. XPS was used to track the evolution of the carbon environment in OBO from molecules to chains to ribbons and a model was proposed that accurately fit the photoemission data.

During the formation of porphyrin functionalised (4,1) CGNRs on the Au(111) OBO molecules were observed to nucleate in the troughs on the surface following 2×1 surface reconstruction during the polymerisation stage. Nanostructures on the Au(111) surface were multidirectional and displayed a wide range of angles.

A co-deposition of OBO and Ni-DBTPP on the Au(788) surface did not result in unidirectional functionalised (4,1) CGNRs. However, a deposition protocol was developed for OBO molecules to achieve highly aligned and long (4,1) CGNRs on the Au(788) surface.

4.5 References

1. Wang, X. Y. *et al.* Bottom-Up Synthesis of Heteroatom-Doped Chiral Graphene Nanoribbons. *J. Am. Chem. Soc.* **140**, 9104–9107 (2018).
2. Wang, X. et al. Supporting Information for Bottom-Up Synthesis of Heteroatom-Doped Chiral Graphene Nanoribbons. *J. Am. Chem. Soc.* 1–23 (2018).
3. Miller, D. J., Biesinger, M. C. & McIntyre, N. S. Interactions of CO2 and CO at fractional atmosphere pressures with iron and iron oxide surfaces: one possible mechanism for surface contamination? *Surf. Interface Anal.* **33**, 299–305 (2002).
4. Petitto, S. C., Marsh, E. M. & Langell, M. A. Adsorption of Bromobenzene on Periodically Stepped and Nonstepped NiO(100). *J. Phys. Chem.* **110**, (2006).
5. Koch, S. *et al.* Amplified cross-linking efficiency of self-assembled monolayers through targeted dissociative electron attachment for the production of carbon nanomembranes. *Beilstein J. Nanotechnol* **8**, 2562–2571 (2017).
6. Xiao, Z. *et al.* Ab initio investigation of the cyclodehydrogenation process for polyanthrylene transformation to graphene nanoribbons. *npj Comput. Mater.* **5**, 1–6 (2019).
7. Doyle, C. An investigation of the structural and electronic properties of covalently bonded molecular networks on metal surfaces formed through debromination reactions. *Ph.D Thesis DCU* 232 (2013).
8. Simonov, K. A. *et al.* Effect of Substrate Chemistry on the Bottom-Up Fabrication of Graphene Nanoribbons: Combined Core-Level Spectroscopy and STM Study. *J. Phys. Chem. C* **118**, (2014).
9. Saywell, A., Schwarz, J., Hecht, S. & Grill, L. Polymerization on stepped surfaces: Alignment of polymers and identification of catalytic sites. *Angew. Chemie - Int. Ed.* **51**, 5096–5100 (2012).
10. Wang, X.-Y., Narita, A., Zhang, W., Feng, X. & Mü, K. Synthesis of Stable Nanographenes with OBO-Doped Zigzag Edges Based on Tandem Demethylation-Electrophilic Borylation. *J. Am. Chem. Soc.* **138**, 9021–9024 (2016).
11. Jacobse, P. H. *et al.* One Precursor but Two Types of Graphene Nanoribbons: On-Surface Transformations of 10,10′-Dichloro-9,9′-bianthryl on Ag(111). *J. Phys. Chem. C* **123**, 8892–8901 (2019).
12. Takeuchi, N., Chan, C. T. & Ho, K. M. Au(111): A theoretical study of the surface reconstruction and the surface electronic structure. *Phys. Rev. B* **43**, (1991).
13. Blankenburg, S., Cai, J., Ruffieux, P., Jaafar, R. & Passerone, D. Intraribbon Heterojunction Formation in Ultranarrow Graphene Nanoribbons. *ACS Nano* **6**, 2020–2025 (2012).
14. Merino-Díez, N. *et al.* Switching from Reactant to Substrate Engineering in the Selective Synthesis of Graphene Nanoribbons. *J. Phys. Chem. Lett.* **9**, 2510–

2517 (2018).

15. De Boni, F. *et al.* Templating Effect of Different Low-Miller-Index Gold Surfaces on the Bottom-Up Growth of Graphene Nanoribbons. *ACS Appl. Nano Mater.* **3**, 11497–11509 (2020).

Chapter 5: Summary and Future Work

5.1 Summary of Thesis

The work presented in this thesis describes the formation of porphyrin functionalised graphene nanoribbons (GNRs) on the Au(111) and Au(788) surfaces through on-surface synthesis In chapter 1, the properties and shortcomings of graphene are introduced as the motivation for and current state-of-art in the field of on-surface. Chapter one introduces the work of Grill *et al*.[1] in forming covalently bonded networks of molecules and describes how this advance laid the groundwork for the growth of atomically precise GNRs described in the seminal work by Cai *et al*.[2] It was shown that the bandgap and other electronic, magnetic and chemical properties of GNRs can be tailored by controlling the width, edge-shape, and by the inclusion of dopants. A review of the wide range of GNRs that research groups have formed using bespoke precursor molecules is discussed in reviews by Taleriz [3] and Zhou [4]. Open questions are raised in terms of large-area electronic characterisation and the issue of transferring GNR structures from metallic to semiconductor surfaces for device fabrication.

In chapter 2, the experimental techniques employed in acquiring and analysing the data are discussed. The use of scanning tunnelling microscopy and X-ray photoemission spectroscopy are standards in the field and their operation from a theoretical and practical standpoint is addressed. The precursor molecules 10,10′-dibromo-9,9′-bianthracene (DBBA), 6,16-dibromo-9,10,19,20-tetraoxa-9a,19a-diboratetrabenzo[a,f,j,o] perylene (OBO) and nickel-dibromo-tetra-phenyl-porphyrin (Ni-DBTPP) are described as are the experimental procedures for sample preparation and molecular deposition. The surface structure of the gold crystals is discussed in relation to their use for OSS.

In chapter 3, the deposition of DBBA on the Au(111) and Au(788) surfaces in conjunction with Ni-DBTPP to form porphyrin functionalised 7-carbon-wide armchair GNRs (7-AGNR) is described. The transformation from self-assembled precursor molecules to functionalised GNRs was tracked with STM. The formation of porphyrin networks and chain-like structures was also observed. The possible orientations and formation of 5-membered fluoranthene units at the 7-AGNR-porphryin heterojunction are discussed and identified for both gold surfaces. The vicinal Au(788) surface was shown to have a strong impact on unidirectional growth of GNRs.

Chapter 4 describes the (4,1) chiral GNRs formed using the OBO precursor, this precursor was used to address the issue of 5-membered ring formation at the GNR-porphyrin heterojunction. The various (4,1) chiral GNR-porphyrin structures are identified and grown on the Au(111) and Au(788) surfaces and the formation of the triphenylene segment in place of the fluoranthene unit is noted. The evolution of the deposited OBO from self-assembled molecules through polymerisation and GNR formation was observed with STM and XPS. For XPS in particular, the chemical environment of the carbon components of the C1s peak is observed to change as the system evolves from molecules to chains and ribbons in good agreement with the predicted model.

5.2. Current State of the Art

Since the work in this thesis was carried out there have been some notable advances made in growth and applications of GNRs. There are three prominent research groups working in this area; (1) the group lead by Peña across several Spanish institutions, (2) the Crommie group based out of UC Berkley and (3) the multi-group collaboration of Fasel, Ruffieux, and Mullen at Swiss Federal Laboratories for Materials Science and Technology (Empa). Notwithstanding the efforts made by the three leading groups, others have also made significant contributions and some of these are highlighted in the following sections.

5.2.1 Bandgap tuning by edge state engineering

Bandgap and transport property engineering is a critical component for device fabrication and has seen an explosion in the number of exotic edge-shapes and dopant incorporated GNR structures. In a paper closely related to the work in this thesis, Senkovskiy *et al.* [5] deposited 9,10-bis(10-bromoanthracen-9-yl)-9,10-dihydro-9,10-diboraanthracene, Figure 5.1(b), on the Au(111) and Au(788) surface, this molecule, similar to DBBA with the addition of boron, forms 7-AGNR with substituted boron atoms along the longitudinal axis of the ribbon. By achieving alignment on the Au(788) surface they used area averaged techniques such as ARPES, NEXAFS, Raman spectroscopy to probe the electronic structure and found that the boron doping had little effect on the electron effective mass but it did change the valence band-1 energy level by 110 meV and drastically affected the Raman spectra compared to pristine 7-AGNR. They also deconvolved the C 1*s* XPS data in a similar fashion to the XPS data in chapter 4 by identifying specific carbon atom environments within their structures. As well as including dopants, porous structures can have a significant effect on the band structure of GNRs. Pawlak *et al.* [6] combined both doping and porosity to grow nitrogen doped porous 9-AGNRs on the Ag(111) surface resulting in a bandgap of 2.2 eV. Another challenge that faces the field is the formation of narrow GNRs. In 2020, Zuzak *et al.*[7] successfully grew 5-AGNR on Au(111) with an organometallic intermediate formed between chlorine atoms on the precursor molecule and gold atoms from the surface in a similar process as observed by Simonov *et al.* [8].

The Empa group have mostly focused on the impact that mixed edge topography has on the band structure of GNRs, specifically the edge states. Using 2,6-dibromo-1,5-diphenylnaphthaleneas, Figure 5.1. (a), a precursor molecule they formed a non-planar, chiral GNR with a *pseudo*-combination of armchair and cove edges having a bandgap of ~1.6 eV on Au(111) [9].

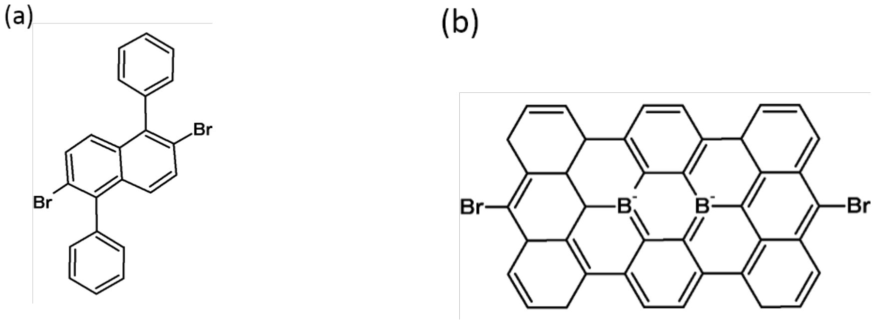

Figure 5.1: *Precursor molecules (a) 2,6-dibromo-1,5-diphenylnaphthalene (b) 9,10-bis(10-bromoanthracen-9-yl)-9,10-dihydro-9,10-diboraanthracene*

This group recently achieved a GNR with periodic zig-zag and singular armchair units composed of capes and coves as shown in figure 5.2 (a) [10]. Figures 5.2 (b) and (c) show STM images of the polymeric structure and the final cove-cape, zigzag GNRs (cc-ZGNR). With remarkable resolution, figure 5.2 (d) shows the constant height non-contact AFM of the cc-ZGNR. They found that with this edge shape topological magnetic states were localized at the zig-zag segment while the cove-cape portion were non-magnetic, a promising discovery for spintronic based devices. They also observed that the placement of the cape at opposite sides of the ribbon in either, symmetric or staggered positions drastically changes the band structure. In relation to the work in this thesis they found that breaking carbon bonds had a significant effect on the aromaticity and electronic transport properties. Following on from this work, the Empa team formed a mixed edge structure of mostly armchair topology but with periodic capes consisting of a 3-carbon zig-zag edge. They transferred the mixed-edge GNRs onto NaCl crystals on the gold surface using the STM tip [11] to electronically and magnetically isolate them the metallic surface. They then observed well-defined spin-states localised at the zig-zag capes. A result that has promising results for extending GNR research into the spintronic domain.

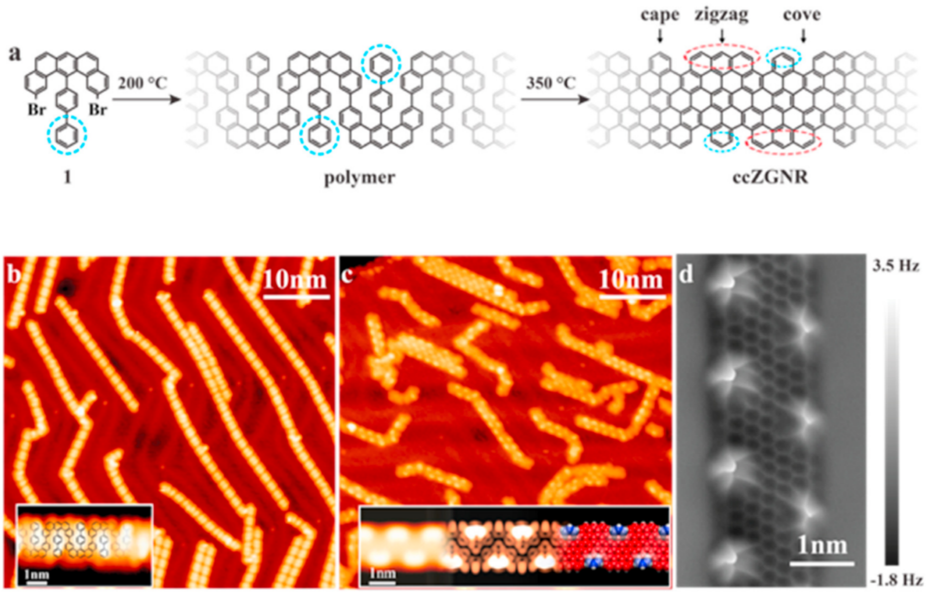

Figure 5.2: *cc-ZGNRs on Au(111)* [8]

5.2.2 Developments in porphyrin integration

A key issue noted in this thesis that requires further study is the affect the 5-membered ring formed between the phenyl ring and the porphyrin macrocycle has on the transport properties of the heterostructure. To address this issue, the group at Empa synthesised a modified free-base porphyrin with adjoining anthryl and brominated anthryl units (figure 5.3 (a)) and formed GNR/porphyin hybrids of specific dimensions on Au(111) with no 5 membered ring at the GNR/por. heterojunction as shown in figure 5.3 (b). The aromaticity of the heterojunction is accompanied by the dehydrogenation of the CH_3 groups from the phenyl rings which also form aromatic rings with the porphyrin macrocycle potentially maintaining the transport properties of the nanostructure. The highly non-planar geometry of the porphyrin was beneficial for surface diffusion. The group found dehalogenation and dehydrogenation of the dimers occurs at 200 °C and 350 °C, respectively. In figure 5.3, STM (c)(d) and nc-AFM (e) images show unambiguously formed GNR/porphyrin hybrid consisting of two free-base porphyrins connected by 7-AGNR. The tailored geometry of the precursors results in rigid junction at the halogen sites. Ten such hybrid structures can be seen in figure 5.3 (c) while six precursors can also be seen that did not polymerize with other monomers and instead dibrominated. In figure 5.3 (d) high resolution STM shows the highly planar structure and exact geometry as outlined in the molecular drawing in 5.3 (b) following cyclo-dehydrogenation. The nc-AFM image in 5.3 (e) again shows the high level of coordination between the two functionalised porphyrins with a triply fused carbons at the 7-AGNR/por. junction. One drawback of the asymmetric bis-anthracene functionalised porphyrin is that it results in porphyrin capped rather than integrated nanostructures, limiting their possible applications. Zhang *et al*. have recently synthesised a symmetric 5,15-bis-anthracene porphyrin [13], however it lacks halogenated sites, and it remains to be seen if this porphyrin can be modified to support Ullmann coupling for on-surface synthesis of GNR nanostructures.

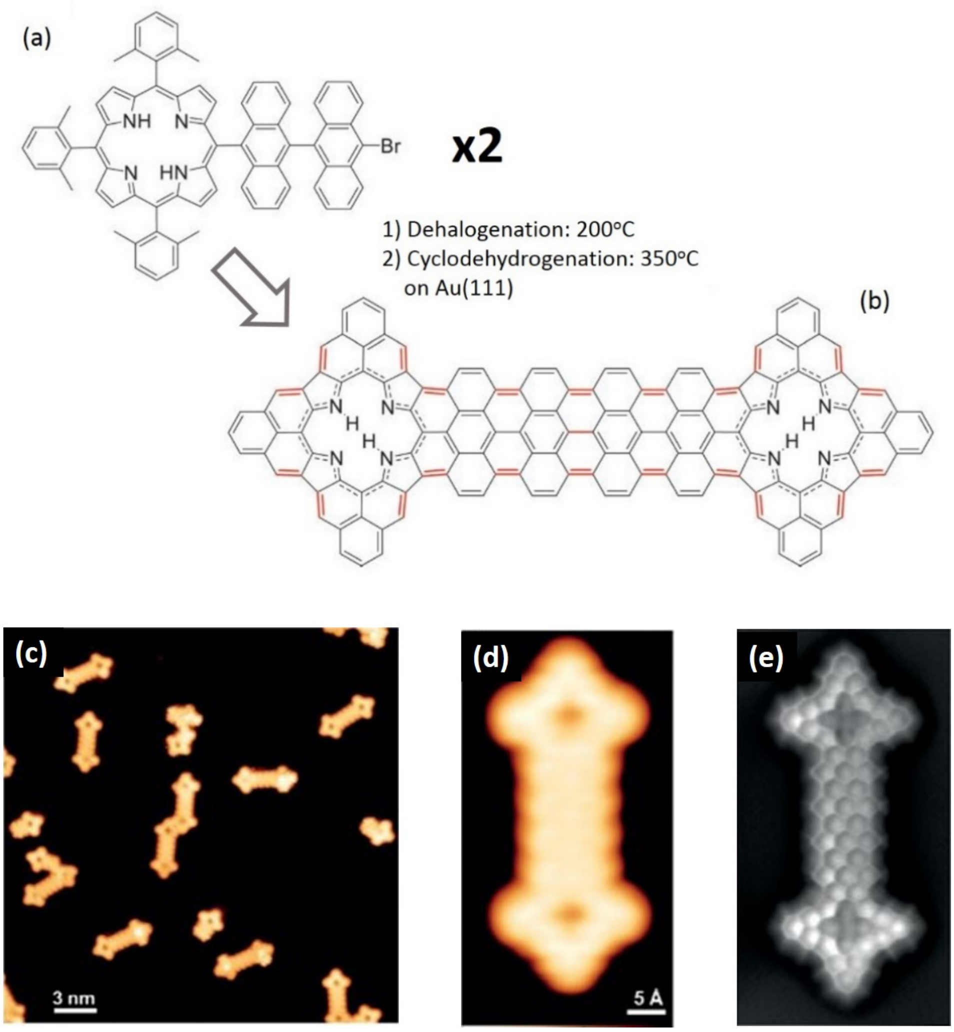

***Figure 5.3**: Triply-fused 7-AGNR/Por hybrid. (a) Chemical drawing of synthesised precursor (b) Chemical drawing of hybrid. (c) 24 nm × 24 nm STM image of hybrid device (d) 1.5nm × 4.0nm STM image of single GNR/Por. hybrid (V=-0.5 V, I=0.02 nA) (e) nc-AFM image of (d) showing chemical bonding within structure* [12]

5.2.3 Transfer techniques

For functional devices to be realised it is necessary that the GNRs are transferred onto or grown on semiconducting surfaces. Transfer was been achieved in 2018 by Ohtomo *et al.*[14] using an etchant free technique as mentioned in section 1.3.3 and by Bennet *et al.* using a PMMA polymer to transfer CVD grown 7-AGNR from the Au(111) surface to SiO_2 [15]. The Empa group reported a transfer technique [16][17] using etchants that results in high quality GNRs with less tears and defects than other studies [18] GNRs were grown via on-surface synthesis on an Au(111) on a mica substrate. Raman spectroscopy confirmed that the GNRs width and edge-shapes were preserved during transfer unlike when using PMMA.

The Crommie group have recently reported two breakthroughs in terms of transfer methods. The first involves matrix assisted direct (MAD) transfer which combines on-surface synthesis and solution-based synthesis [19]. This approach provides the benefit of atomically precise edge geometry from the cyclo-dehydrogenation process during OSS and the controllability of GNR length and functionalization of GNR end groups associated with solution-based production. Polymer precursors for chevron GNRs are formed in solution then mixed with a matrix, pyrene, and under UHV using a fibreglass applicator transferred the polymer-matrix mix onto the Au(111) surface. Annealing the surface at 420 °C desorbed the matrix elements and induced cyclo-dehydrogenation causing the polymer to form chevron GNRs on the surface of relatively uniform length. They compared these results with direct contact transfer without matrix and found the pyrene had a strong influence on the controllability of the length. The group successfully transferred polymer chains that formed chevron-GNRs and N_4-doped 7-AGNRs on Au(111) and also on highly orientated pyrolytic graphite. As the authors note, this technique opens the possibility for more complex GNR structures unachievable by current techniques.

Combining the ability to control length and direction is highly desirable for device fabrication. In a second recent breakthrough, the Crommie group also demonstrated a transfer-free method of growing GNRs on SiO_2/Si [20]. They grew a 100 nm thin film of gold on the SiO_2/Si surface through e-beam evaporation. They deposited DBBA precursors and formed 7-AGNR through the standard OSS protocol and through gentle wet etching removed the gold leaving the GNRs adhered to the

SiO_2/Si substrate as outlined in figure 5.4 (a). Annealing the sample at 480 °C under UHV reduced the roughness as seen in figure 5.4 (b) and (c). XRD results show that after e-beam deposition the gold surface is poly-crystalline with evidence for (111), (200), (220) and (311) crystal planes present. The annealing stage not only reduces surface roughness but reconstructs the surface to a pure Au(111) structure as seen in the XRD data in figure 5.4 (d). This approach to forming GNRs on semiconducting surfaces provides an accessible route for most research groups.

Controllability of length is an important parameter to control integrating GNRs into lithographically patterned integrated circuits as is the control of the direction of growth. In chapter three the use of the vicinal Au(788) surface was shown to form unidirectional GNRs. Similarly, De Boni *et al.*[21] compared the role low Miller index gold surfaces; Au(111), Au(110) and Au(100), and their role during GNR formation from 4,4″-dibromo-p-terphenyl (DBTP) precursor molecules. They found the Au(111) surface had poor templating effect on directional growth and this allowed the DBTP precursors to form 6-, 9-, 12-, and 15-AGNRs. The corrugated Au(100) surface with terraces 1.44 nm wide and step-heights of 0.07 nm restricted lateral fusion and resulted in only 6-AGNR and 9-AGNR growth along the [011] direction while the narrow terraces of the Au(110) crystal limited the width to only 6-AGNR.

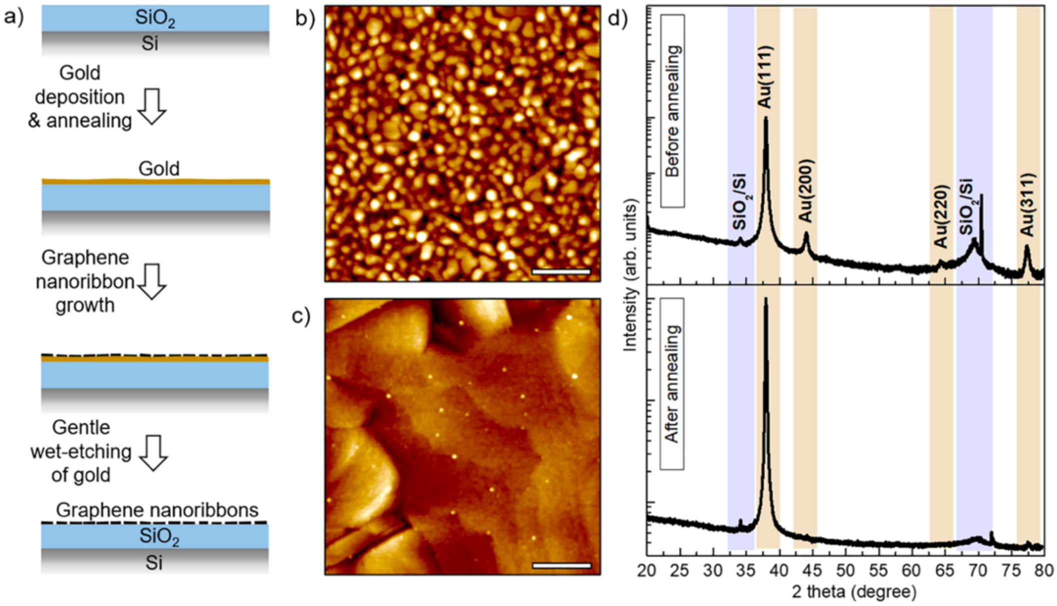

Figure 5.4: *Transfer-free method* [15]

5.2.4 GNR Devices

Incorporating GNRs into FET device architectures is a goal of this field of research. Several groups have been successful in forming molecular devices through on-surface synthesis and FETs with GNRs in the channel region with an on/off ratio of ~10^3 have been demonstrated by Bennet *et al.* as discussed in the section 1.2.2 [15]. The Crommie group improved on their previous result and used the transfer-free method discussed in section 5.2.3 and the standard solution-based transfer technique to fabricate FETs using the 7-AGNR as the channel material [20]. The lithographically prepatterned architecture employed Pd electrodes and a HfO_2 high-k dielectric between the source and drain and the tungsten back gate. The results from I-V measurements for the standard transfer method show an on/off ratio of ~10^5 and an I_{on} of ~60 nA, the highest recorded current for a 7-AGNR, although this was only observed for hole transport. The same experiments for the transfer free method showed a lower on/off ratio of ~10 and a maximum on-current of 30nA with both electrons and holes acting as charge carriers. Though comparisons are made, a true characterisation of the devices is hard to realise as the number of GNRs in the channel region is unknown and different for both FETs.

The use of GNRs in FETs is not limited to high-speed switches or sensor and GNR based quantum dots offer a new field of research from single photon emission, single electron transistor, spintronic devices and quantum computing. Exploring the use of GNRs as quantum dots is steadfastly underway. The group at Empa have grown 5-AGNR via on-surface synthesis and transferred it to form the device shown in figure 5.5 [22]. The 5-AGNR bridges a gap between two sheets of graphene each connected to titanium coated gold electrodes on SiO_2.

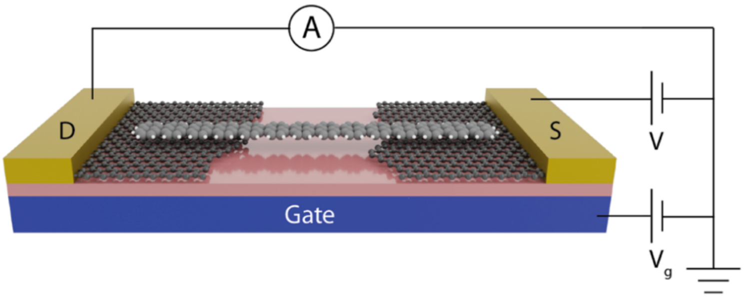

Figure 5.5: *A 5-AGNR FET device with graphene contacts* [16].

At room temperature they observed metallic like *I-V* curves suggesting the bandgap of the 5-AGNR in the specific device set-up is very small. They also found the large variance in resistance for several devices which they attribute to the number of GNRs bridging the graphene gap between electrodes. As seen in the work by Mutlu *et al.*[20] this unknown parameter has a significant effect on the device properties. It also stands that forming better contacts between electrodes and GNRs is vital for optimal device operation. For quantum dot characterisation cryogenic temperatures are required. By cooling the device to 13 K they observed the presence of two quantum dots at the GNR-graphene junction that exhibited single electron transistor behaviour.

Research is also underway to explore other *sp*^{2} hybridized graphene-like carbon allotropes. This could have far reaching applications and specifically help solve the problem of high contact resistance between GNRs and graphene or metallic electrodes in devices. Fan *et al.* [23] used 4,4″-dibromo-2,2′,2″,5,5′,5″-hexafluoro-1,1′:4′,1″- terphenyl (DHTP) precursor molecule in a hierarchical Ullman coupling, as first demonstrated by the Grill group [24], to form 1-dimensional polymeric chains through OSS dehalogenation and HF zipping [25] as shown in figure 5.6. The intrinsic selectivity of the chains means that it only fuses to chains of the same chirality creating a network with four and eight membered rings that exhibits metallic properties. Biphenylene could possibly be adapted to allow for covalently bonded GNRs to grow from edges improving the contact resistance between GNRs and electrodes

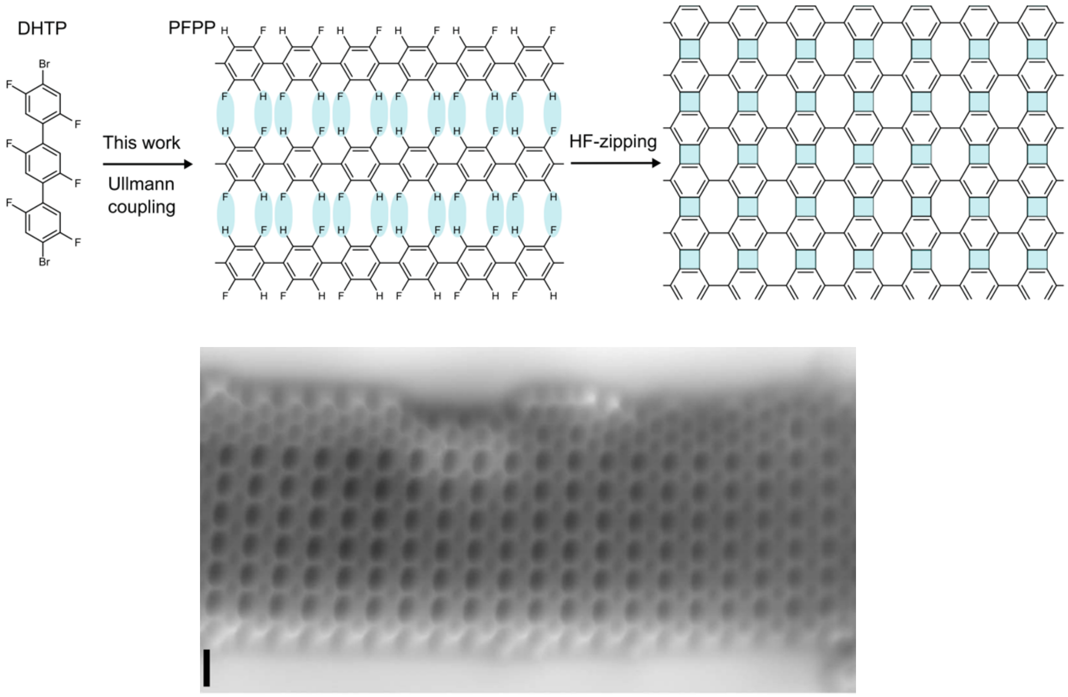

Figure 5.6: *Steps toward biphenylene through Ullmann coupling and HF-zipping and nc-AFM of biphenylene sheet (scale bar: 5nm)*

5.3 Future Work

Several questions relating to the work in this thesis remain open for future research. The reordering of the gold surface into the (2×1) reconstruction is observed in the presence of DBBA, OBO and NiDBTPP after heating the sample to 200 °C. A temperature dependent study with variable temperature STM could provide an explanation for this phenomena. Another important aspect of the work in this thesis that would benefit from further study is measuring the HOMO-LUMO energy separation at the heterojunctions between the porphyrin and 7-AGNRs and (4,1) CGNR. STM *I-V* spectroscopy studies would provide useful data to confirm or disconfirm the hypothesis the 5-memebered rings result in reduced electrical conductivity.

5.4 References

1. Grill, L. *et al.* Nano-architectures by covalent assembly of molecular building blocks. *Nat. Nanotechnol.* **2**, 687–691 (2007).
2. Cai, J. *et al.* Atomically precise bottom-up fabrication of graphene nanoribbons. *Nature* **466**, 470–473 (2010).
3. Talirz, L. Ruffieux, P. Fasel, R. On-Surface Synthesis of Atomically Precise Graphene Nanoribbons. *Adv. Mater.* **28**, 6222–6231 (2016).
4. Zhou, X. & Yu, G. Modified Engineering of Graphene Nanoribbons Prepared via On-Surface Synthesis. *Adv. Mater.* **32**, 1–24 (2020).
5. Senkovskiy, B. V. *et al.* Boron-Doped Graphene Nanoribbons: Electronic Structure and Raman Fingerprint. *ACS Nano* **12**, 7571–7582 (2018).
6. Pawlak, R. *et al.* Bottom-up Synthesis of Nitrogen-Doped Porous Graphene Nanoribbons. *J. Am. Chem. Soc.* **142**, 12568–12573 (2020).
7. Zuzak, R. *et al.* On-Surface Synthesis of Chlorinated Narrow Graphene Nanoribbon Organometallic Hybrids. *J. Phys. Chem. Lett.* **11**, 10290–10297 (2020).
8. Simonov, K. A. *et al.* Synthesis of armchair graphene nanoribbons from the 10,10′-dibromo-9,9′-bianthracene molecules on Ag(111): the role of organometallic intermediates. *Sci. Rep.* **8**, 3506 (2018).
9. Keerthi, A. *et al.* On-surface Synthesis of a Chiral Graphene Nanoribbon with Mixed Edge Structure. *Chem. - An Asian J.* **15**, 3807–3811 (2020).
10. Shinde, P. P. *et al.* Graphene nanoribbons with mixed cove-cape-zigzag edge structure. *Carbon N. Y.* **175**, 50–59 (2021).
11. Söde, H. *et al.* Electronic band dispersion of graphene nanoribbons via Fourier-transformed scanning tunneling spectroscopy. *Phys. Rev. B* **91**, 45–49 (2015).
12. Mateo, L. M. *et al.* On-Surface Synthesis and Characterization of Triply Fused Porphyrin–Graphene Nanoribbon Hybrids. *Angew. Chemie - Int. Ed.* **59**, 1334–1339 (2020).
13. Zhang, P. *et al.* Bis-Anthracene Fused Porphyrin as an Efficient Photocatalyst: Facile Synthesis and Visible-Light-Driven Oxidative Coupling of Amines. *Chem. - A Eur. J.* **26**, 16497–16503 (2020).
14. Ohtomo, M., Sekine, Y., Hibino, H. & Yamamoto, H. Graphene nanoribbon field-effect transistors fabricated by etchant-free transfer from Au(788). *Appl. Phys. Lett.* **112**, (2018).
15. Bennett, P. B. *et al.* Bottom-up graphene nanoribbon field-effect transistors. *Appl. Phys. Lett.* **103**, 253114 (2013).
16. Passi, V. *et al.* Field-Effect Transistors Based on Networks of Highly Aligned, Chemically Synthesized N = 7 Armchair Graphene Nanoribbons. *ACS Appl. Mater. Interfaces* **10**, 9900–9903 (2018).
17. Borin Barin, G. *et al.* Surface-Synthesized Graphene Nanoribbons for Room

Temperature Switching Devices: Substrate Transfer and ex Situ Characterization. *ACS Appl. Nano Mater.* **2**, 2184–2192 (2019).

18. Hallam, T., Berner, N. C., Yim, C. & Duesberg, G. S. Strain, Bubbles, Dirt, and Folds: A Study of Graphene Polymer-Assisted Transfer. *Adv. Mater. Interfaces* **1**, 1400115 (2014).

19. McCurdy, R. D. *et al.* Synergetic Bottom-Up Synthesis of Graphene Nanoribbons by Matrix-Assisted Direct Transfer. *J. Am. Chem. Soc.* **143**, 4174–4178 (2021).

20. Mutlu, Z. *et al.* Transfer-Free Synthesis of Atomically Precise Graphene Nanoribbons on Insulating Substrates. *ACS Nano.* **15**, 2635−2642 (2021).

21. De Boni, F. *et al.* Templating Effect of Different Low-Miller-Index Gold Surfaces on the Bottom-Up Growth of Graphene Nanoribbons. *ACS Appl. Nano Mater.* **3**, 11497–11509 (2020).

22. El Abbassi, M. *et al.* Controlled Quantum Dot Formation in Atomically Engineered Graphene Nanoribbon Field-Effect Transistors. *ACS Nano* **14**, 5754–5762 (2020).

23. Fan, Q. *et al.* Biphenylene Sheet: A Nonbenzenoid Carbon Allotrope. *ChemRxiv* **856**, 852–856 (2020).

24. Bronner, C. *et al.* Hierarchical On-Surface Synthesis of Graphene Nanoribbon Heterojunctions. *ACS Nano.* **12**, 2193−2200 (2018).

25. Kolmer, M. *et al.* Fluorine-programmed nanozipping to tailored nanographenes on rutile TiO2 surfaces. *Science (80-.).* **363**, 57–60 (2019).

Appendix A: 7-AGNR/porphyrin heterojunctions on the Au(111) surface

Identification of 51 heterojunctions on the Au(111) used for the statistics in figure 3.31.

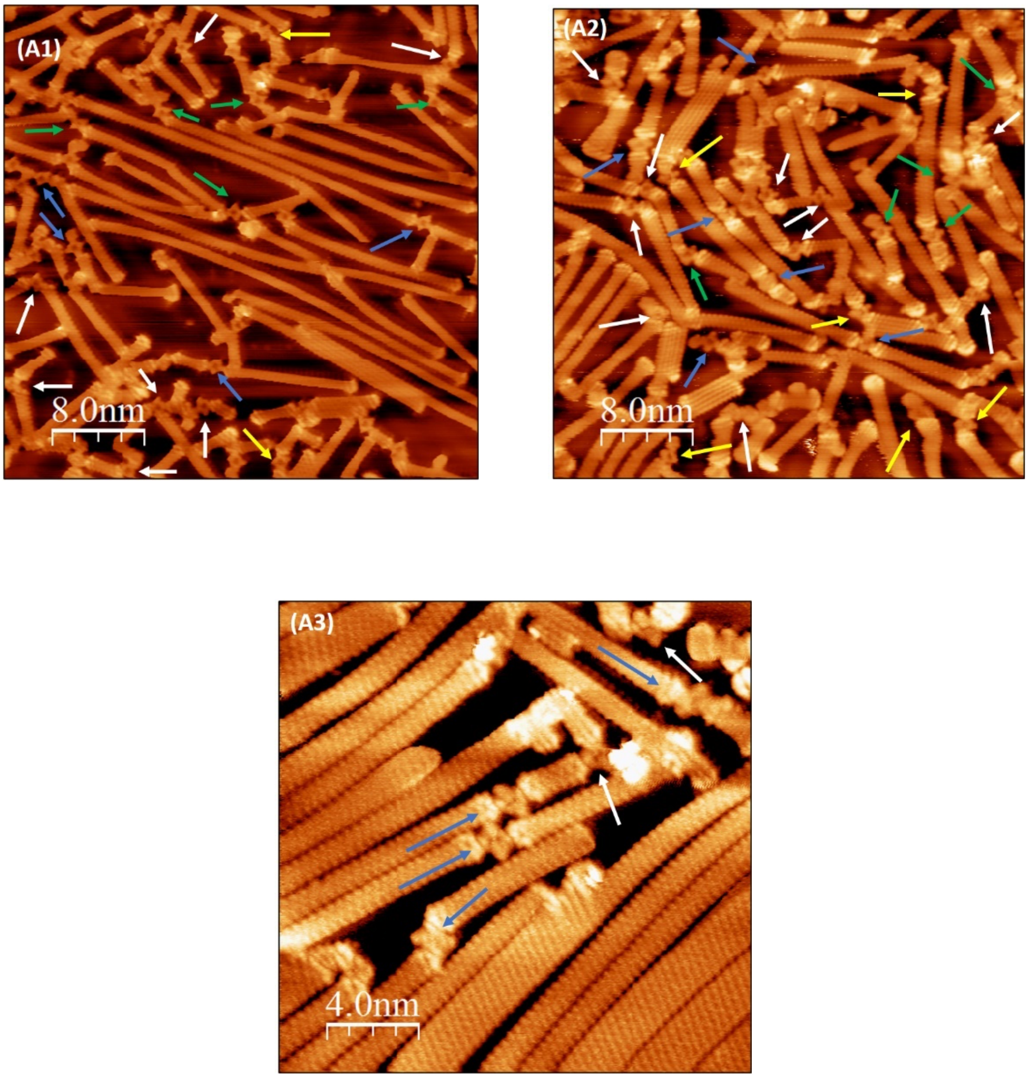

Figure A: *Porphyrin Functionalised 7-AGNR on Au(111) (A1) 40 nm × 40 nm (V=0.50 V, I=77 pA). (A2) 40 nm × 40 nm (V=0.031 V, I=0.37 nA) (A3) 20 nm × 20 nm (V=-0.61 V, I=77 pA)*